

**FEASIBILITY ASSESSMENT  
OF INNOVATIVE ISOLATION BEARING SYSTEM  
WITH SHAPE MEMORY ALLOYS**

**A Dissertation Submitted in Partial Fulfilment of the Requirements  
for the Master Degree in**

**Earthquake Engineering**

**By**

**GABRIELE ATTANASI**

**Supervisors:**

**Prof. GREGORY L. FENVES**

**Prof. FERDINANDO AURICCHIO**

**April, 2008**

**Istituto Univeritario di Studi Superiori  
Università degli Studi di Pavia**

The dissertation entitled “Feasibility Assessment of Innovative Isolation Bearing System with Shape Memory Alloys”, by Gabriele Attanasi, has been approved in partial fulfilment of the requirements for the Master Degree in Earthquake Engineering.

**Gregory L. Fenves** \_\_\_\_\_

**Ferdinando Auricchio** \_\_\_\_\_

## ABSTRACT

The objective of this work is to investigate the feasibility of a new seismic isolation device concept based on the superelastic effect given by shape memory alloys.

Seismic isolation is one of the most effective options for passive protection of structure, which modifies the structural global response and improves performance, in particular regularizing the structural response, shifting the fundamental period of vibration and increasing global energy dissipation.

Shape memory alloys (SMAs) are characterized by unique mechanical properties due to solid-solid transformation between phases of the alloy. They show high strength and strain capacity, high resistance to corrosion and to fatigue. Regarding the stress-strain constitutive law, the nonlinear hysteresis due to the superelastic effect, that for particular range of temperature can be described like a flag shape relation, avoids residual deformation, provides some hysteretic energy dissipation and limits the maximum transmitted force.

An isolation bearing system based on SMA superelastic effect is intended to provide the nonlinear characteristics of yielding devices, limiting the induced seismic force and providing additional damping characteristics, together with recentering properties to reduce or eliminate the cumulative damage. Nevertheless, flag-shape hysteresis is characterized by less energy dissipation with respect to other isolation device technology force-displacement relations, therefore its effectiveness has to be investigated.

In this work the dynamic response of the proposed innovative SMA isolation devices has been compared with equivalent traditional bearing response through dynamic time history analyses. Results show that force and displacement demands in the two systems are quite similar for medium to high flag shape dissipation capability.

*Keywords:* Seismic isolation, shape memory alloys, superelastic effect.

## ACKNOWLEDGEMENTS

I wish express sincere gratitude to various people who provided me with assistance, support and friendship during the time in which my studies and research lasted and in particular:

- my supervisors, professor Gregory Fenves and professor Ferdinando Auricchio for their invaluable guidance and patient supports over this time;
- all the ROSE course teachers for everything I learned in this experience and the classmates I have encountered during my study at ROSE for the good time we had together;
- engineer Cesare Crosti from *Agom International* and engineer Francesco Butera from *Saes Getters* for their help in providing data to perform this work;
- professor Stefano Pampanin from *University of Canterbury* for his suggestions, guidance and encouragements over the past two years;
- professor Athol Carr from *University of Canterbury*, professor Constantin Christopoulos from *University of Toronto* and professor Steve Kramer from *University of Washington* for their generous help and suggestions when I met them in Pavia;
- finally, Laura, Mum, Dad, my sister Elena and all my friends, for their unwavering supports.

## TABLE OF CONTENTS

ABSTRACT	i
ACKNOWLEDGEMENTS	ii
TABLE OF CONTENTS	iii
LIST OF FIGURES	ix
LIST OF TABLES	xxiv
1. INTRODUCTION	1
1.1 Earthquake Engineering in Context . . . . .	1
1.2 Seismic Isolation . . . . .	2
1.3 Advanced Material Application in Seismic Engineering . . . . .	2
1.4 Dissertation Objectives and Outline . . . . .	3
2. SEISMIC ISOLATION	5

iii

2.1	Introduction . . . . .	5
2.2	Fundamental Concepts . . . . .	5
2.2.1	Response Regularization . . . . .	5
2.2.2	Period Shift . . . . .	6
2.2.3	Energy Dissipation . . . . .	7
2.3	Base Isolated Structure Dynamics . . . . .	8
2.4	Bearing Devices . . . . .	10
2.4.1	Low and High Damping Laminated Rubber Bearings . . . . .	10
2.4.2	Lead Rubber Bearings . . . . .	11
2.4.3	Friction Pendulum Devices . . . . .	14
3.	DESIGN PROCEDURE FOR ISOLATED STRUCTURES	16
3.1	Introduction . . . . .	16
3.2	Main features of the Direct Displacement Based design . . . . .	16
3.2.1	Simulation of equivalent nonlinear Single Degree of Freedom system	17
3.2.2	Effective stiffness consideration . . . . .	18
3.2.3	Equivalent damping evaluation . . . . .	20
3.2.4	Design displacement spectra and structural base shear . . . . .	20
3.3	Displacement Based Design of Isolated Structures . . . . .	22
3.3.1	Base-Isolated Rigid Structures . . . . .	23
3.3.2	Base-Isolated Flexible Structures . . . . .	24

3.4	Comments on Equivalent Linear System Concept . . . . .	26
3.4.1	Initial stiffness formulation . . . . .	27
3.4.2	Mathematic Derivation of the Equivalent Damping Expression for a Linear SDOF System . . . . .	27
3.4.3	Period Shift in Secant Stiffness Formulation . . . . .	31
3.4.4	Period Shift in Other Formulations . . . . .	33
3.4.5	Elastic damping component . . . . .	34
3.4.6	Conclusions on Equivalent Linear System Concept Evaluation . . . . .	35
4.	SHAPE MEMORY ALLOYS . . . . .	36
4.1	Introduction . . . . .	36
4.2	Basics About Shape Memory Alloys . . . . .	36
4.2.1	Shape Memory and Superelastic Effects . . . . .	36
4.2.2	Other Mechanical Properties of Shape Memory Alloys . . . . .	38
4.2.3	Potentials of SMA in Seismic Engineering Applications . . . . .	39
5.	FEASIBILITY OF SMA TECHNOLOGY FOR SEISMIC ISOLATION APPLICA- TION . . . . .	40
5.1	Introduction . . . . .	40
5.2	SMA Technology Isolation Device Design . . . . .	42
5.2.1	Goal of the Design Process . . . . .	42
5.2.2	Reference Isolator Device . . . . .	42
5.2.3	Equivalent SMA Isolator Device . . . . .	45

5.3	Flag-Shape Hysteresis Reduction Factor Estimation Using the Equivalent Damping Approach . . . . .	46
5.3.1	Hysteretic damping component estimation . . . . .	47
5.3.2	Reduction Factor Computation . . . . .	50
5.3.3	Conclusions about Reduction Factors Estimation using Equivalent Damping . . . . .	52
5.4	Effective Seismic Response Evaluation of Different Hysteresis Isolation Devices . . . . .	53
5.4.1	Validation Strategy through Time-History Analysis . . . . .	53
5.4.2	Ground Motion for the Time History Analyses . . . . .	64
5.5	Rigid Superstructure Approach Time History Analyses Results . . . . .	68
5.5.1	Evaluation of Results Considering SMA Model with Largest Dissipation Capability . . . . .	68
5.5.2	Evaluation of Result Sensibility to Model Dissipation Ratio . . . . .	74
5.5.3	Evaluation of Result Sensibility to Second Hardening Effect . . . . .	86
5.6	Flexible Superstructure Approach Time History Analyses Results . . . . .	100
5.6.1	Simplified Design Procedure Structure . . . . .	100
5.6.2	Time History Analysis Isolation System Modeling . . . . .	104
5.6.3	Evaluation of Results considering different SMA Dissipation Capabilities . . . . .	105
5.7	Time History Analysis Result Evaluation . . . . .	112

5.7.1	Dissipation Capability and Influence in Reducing Force and Displacement Demand . . . . .	112
5.7.2	Recentering Capability . . . . .	112
5.7.3	Displacement Limitation Considering the Second Hardening effect . . . . .	113
6.	CONCLUSIONS . . . . .	114
	REFERENCES . . . . .	116
A.	GROUND MOTION RECORDS USED IN THE TIME HISTORY ANALYSES . . . . .	119
A.1	Artificial Ground Motion Generation . . . . .	119
A.1.1	Ground motion 1 . . . . .	120
A.1.2	Ground motion 2 . . . . .	121
A.1.3	Ground motion 3 . . . . .	122
A.1.4	Ground motion 4 . . . . .	123
A.1.5	Ground motion 5 . . . . .	124
A.1.6	Ground motion 6 . . . . .	125
A.1.7	Ground motion 7 . . . . .	126
A.2	Near Field Ground Motion Scaling . . . . .	127
A.2.1	Ground motion 8 . . . . .	128
A.2.2	Ground motion 9 . . . . .	130
A.2.3	Ground motion 10 . . . . .	132
A.2.4	Ground motion 11 . . . . .	134
A.2.5	Ground motion 12 . . . . .	136

A.2.6	Ground motion 13	138
A.2.7	Ground motion 14	140
<b>B.</b>	<b>RIGID SUPERSTRUCTURE TIME HISTORY RESULTS SUMMARY</b>	<b>142</b>
B.1	No second hardening model	143
B.1.1	$\beta = 0.95$	143
B.1.2	$\beta = 0.75$	146
B.1.3	$\beta = 0.55$	149
B.1.4	$\beta = 0.35$	152
B.1.5	$\beta = 0.15$	155
B.2	Second hardening model	158
B.2.1	$\beta = 0.95$	158
B.2.2	$\beta = 0.75$	161
B.2.3	$\beta = 0.55$	164
B.2.4	$\beta = 0.35$	167
B.2.5	$\beta = 0.15$	170
<b>C.</b>	<b>FLEXIBLE SUPERSTRUCTURE TIME HISTORY RESULTS SUMMARY</b>	<b>173</b>

## LIST OF FIGURES

2.1	Displacement response spectra for different damping factor values experiencing the El Centro (1940) ground motion. . . . .	6
2.2	Acceleration response spectra for different damping factor values experiencing the El Centro (1940) ground motion. . . . .	7
2.3	Isolated system dynamic model and parameters. . . . .	8
2.4	Laminated low damping rubber bearing structure. . . . .	11
2.5	Laminated low damping rubber bearing (LDRB) force-displacement relation. . . . .	11
2.6	Laminated high damping rubber bearing (HDRB) force-displacement relation. . . . .	12
2.7	Lead rubber bearing (LRB) force-displacement relation . . . . .	12
2.8	Hysteresis model for a lead rubber bearing (LRB). . . . .	13
2.9	Friction pendulum system (FPS) device cross sections. . . . .	14
2.10	Force-displacement FPS result from experimental dynamic tests. . . . .	14

3.1	Equivalence between a MDOF having estimated the lateral forces deformed shape and a SDOF of parameters $m_e$ and $h_e$ . . . . .	17
3.2	Effective stiffness concept for a bilinear force displacement relation envelope. . . . .	19
3.3	Equivalent viscous damping estimation as a function of the displacement ductility. . . . .	20
3.4	Displacement design spectra for different damping ratios. . . . .	21
3.5	Summary of DDBD equivalent SDOF base shear computation. . . . .	22
3.6	Base isolated rigid structure design: equivalent displacement profile. . . . .	23
3.7	Base isolated rigid structure model: displacement profile and equivalent SDOF parameters. . . . .	24
3.8	Base isolated flexible structure model: displacement profile and equivalent SDOF parameters. . . . .	25
3.9	Viscous damper hysteresis loop. . . . .	29
3.10	Linear spring and viscous damper in parallel hysteresis loop. . . . .	29
3.11	Dissipated energy $E_D$ and strain energy $E_{S0}$ . . . . .	30
3.12	Equivalent system concept as applied in secant equivalent stiffness. . . . .	31
3.13	Elastic damping force evaluation for a nonlinear hysteresis. . . . .	34
4.1	Idealized stress-strain curve for shape memory effect. . . . .	37
4.2	Idealized stress-strain curve for superelastic effect. . . . .	37
4.3	Stress-strain hysteresis of superelastic NiTi bars. . . . .	38
4.4	Temperature dependent force-displacement response of superelastic NiTi. . . . .	39
5.1	Parameters for the SMA superelastic model. . . . .	41

5.2	Experimental force-displacement characterization of LRB 500 isolator. . . . .	43
5.3	LRB elastoplastic model parameters. . . . .	44
5.4	LRB 500 force-displacement relations experimental and modeling comparison. . . . .	45
5.5	SMA model parameters. . . . .	46
5.6	Hysteretic damping component computation for LRB device. . . . .	48
5.7	Hysteretic damping component computation for SMA device. . . . .	48
5.8	Hysteretic damping ratio comparison for elastoplastic and flag-shape model considering constant $r$ and $\beta$ values. . . . .	49
5.9	Hysteretic damping ratio for elastoplastic model as a function of ductility and hardening. . . . .	51
5.10	Hysteretic damping ratio for flag-shape model as a function of ductility and $\beta$ factor. . . . .	51
5.11	Far field and near field equivalent damping reduction factor for elastoplastic and flag-shape models. . . . .	52
5.12	Spectra selection procedure for isolated structure. . . . .	55
5.13	Time history analysis procedure for displacement and force demand in a isolated structure system. . . . .	56
5.14	Analysis model for rigid superstructure base isolation. . . . .	57
5.15	Analysis model for flexible superstructure base isolation. . . . .	58
5.16	Base shear horizontal displacement relation for lead rubber bearing isolation device. . . . .	58
5.17	Base shear horizontal displacement relation for shape memory alloy isolation device. . . . .	59

5.18	Base shear horizontal displacement relation for equivalent linear elastic with secant stiffness isolation device. . . . .	59
5.19	Energy components in a t.h.a. for a linear elastic system. . . . .	62
5.20	Energy components in a t.h.a. for a elastoplastic system. . . . .	62
5.21	Energy components in a t.h.a. for a flag-shape system. . . . .	63
5.22	Displacement and acceleration elastic design spectra from Eurocode 8. . . . .	64
5.23	Displacement and acceleration elastic design spectra from Eurocode 8 modified ( $T_D = 4s$ ). . . . .	64
5.24	Acceleration and displacement elastic design spectra for spectra compatible artificial ground motions. . . . .	65
5.25	Acceleration and displacement elastic design spectra for original near fault ground motion record. . . . .	66
5.26	Modified acceleration and displacement elastic design spectra for near fault ground motion record. . . . .	67
5.27	Flag-shape hysteresis considering parameter $\beta = 0.95$ . . . . .	69
5.28	Displacement demand values normalized to the linear elastic displacement demand for artificial ground motions. . . . .	70
5.29	Displacement demand values normalized to the linear elastic displacement demand for near fault ground motions. . . . .	70
5.30	Force demand values normalized to the linear elastic displacement demand for artificial ground motions. . . . .	71
5.31	Force demand values normalized to the linear elastic displacement demand for near fault ground motions. . . . .	71
5.32	System absorbed energy for artificial ground motions. . . . .	72

5.33	System absorbed energy for near fault ground motions. . . . .	72
5.34	System absorbed energy for artificial ground motions normalized respect input energy. . . . .	73
5.35	System absorbed energy for near fault ground motions normalized respect input energy. . . . .	73
5.36	Displacement-time response from an artificial event. . . . .	75
5.37	Displacement-time response from an artificial event. . . . .	75
5.38	Residual displacements in lead rubber bearing elastoplastic model. . . . .	75
5.39	Elastoplastic hysteresis and flag-shape hysteresis $\beta = 0.95$ . . . . .	76
5.40	Flag-shape hysteresis $\beta = 0.75$ and $\beta = 0.55$ . . . . .	76
5.41	Flag-shape hysteresis $\beta = 0.35$ and $\beta = 0.15$ . . . . .	76
5.42	Displacement demand values for different dissipation parameter $\beta$ for artificial ground motions. . . . .	77
5.43	Displacement demand values for different dissipation parameter $\beta$ for near fault ground motions. . . . .	77
5.44	Displacement demand values for different dissipation parameter $\beta$ normalized to linear elastic system response for artificial ground motions. . . . .	78
5.45	Displacement demand values for different dissipation parameter $\beta$ normalized to linear elastic system response for near fault ground motions. . . . .	78
5.46	Force demand values for different dissipation parameter $\beta$ for artificial ground motions. . . . .	79
5.47	Force demand values for different dissipation parameter $\beta$ for near fault ground motions. . . . .	79

---

5.48	Force demand values for different dissipation parameter $\beta$ normalized to linear elastic system response for artificial ground motions. . . . .	80
5.49	Force demand values for different dissipation parameter $\beta$ normalized to linear elastic system response for near fault ground motions. . . . .	80
5.50	Absorbed energy values for different dissipation parameter $\beta$ for artificial ground motions. . . . .	81
5.51	Absorbed energy values for different dissipation parameter $\beta$ for near fault ground motions. . . . .	81
5.52	Input energy values for different dissipation parameter $\beta$ for artificial ground motions. . . . .	82
5.53	Input energy values for different dissipation parameter $\beta$ for near fault ground motions. . . . .	82
5.54	Input normalized energy values for different dissipation parameter $\beta$ for artificial ground motions. . . . .	83
5.55	Input normalized energy values for different dissipation parameter $\beta$ for near fault ground motions. . . . .	83
5.56	Absorbed energy values for different dissipation parameter $\beta$ normalized respect the input energy for artificial ground motions. . . . .	84
5.57	Absorbed energy values for different dissipation parameter $\beta$ normalized respect the input energy for near fault ground motions. . . . .	84
5.58	SMA simplified hysteresis model with second hardening. . . . .	87
5.59	Flag-shape hysteresis with second hardening $\beta = 0.95$ . . . . .	88
5.60	Flag-shape hysteresis $\beta = 0.95$ . . . . .	88
5.61	Elastoplastic hysteresis and flag-shape hysteresis with second hardening $\beta = 0.95$ . . . . .	89
5.62	Flag-shape hysteresis with second hardening $\beta = 0.75$ and $\beta = 0.55$ . . . . .	89

5.63	Flag-shape hysteresis with second hardening $\beta = 0.35$ and $\beta = 0.15$ . . . . .	89
5.64	Displacement demand values for different dissipation parameter $\beta$ considering second hardening for artificial ground motions. . . . .	91
5.65	Displacement demand values for different dissipation parameter $\beta$ considering second hardening for near fault ground motions. . . . .	91
5.66	Displacement demand values for different dissipation parameter $\beta$ considering second hardening normalized to linear elastic system response for artificial ground motions. . . . .	92
5.67	Displacement demand values for different dissipation parameter $\beta$ considering second hardening normalized to linear elastic system response for near fault ground motions. . . . .	92
5.68	Force demand values for different dissipation parameter $\beta$ considering second hardening for artificial ground motions. . . . .	93
5.69	Force demand values for different dissipation parameter $\beta$ considering second hardening for near fault ground motions. . . . .	93
5.70	Force demand values for different dissipation parameter $\beta$ considering second hardening normalized to linear elastic system response for artificial ground motions. . . . .	94
5.71	Force demand values for different dissipation parameter $\beta$ considering second hardening normalized to linear elastic system response for near fault ground motions. . . . .	94
5.72	Absorbed energy values for different dissipation parameter $\beta$ considering second hardening for artificial ground motions. . . . .	95
5.73	Absorbed energy values for different dissipation parameter $\beta$ considering second hardening for near fault ground motions. . . . .	95
5.74	Input energy values for different dissipation parameter $\beta$ considering second hardening for artificial ground motions. . . . .	96

5.75	Input energy values for different dissipation parameter $\beta$ considering second hardening for near fault ground motions. . . . .	96
5.76	Input normalized energy values for different dissipation parameter $\beta$ considering second hardening for artificial ground motions. . . . .	97
5.77	Input normalized energy values for different dissipation parameter $\beta$ considering second hardening for near fault ground motions. . . . .	97
5.78	Absorbed energy values for different dissipation parameter $\beta$ normalized respect the input energy for artificial ground motions. . . . .	98
5.79	Absorbed energy values for different dissipation parameter $\beta$ normalized respect the input energy for near fault ground motions. . . . .	98
5.80	Flexible superstructure frame system geometric outline. . . . .	100
5.81	Capacity curve from structure pushover analysis. . . . .	103
5.82	Capacity spectrum analysis of the simulated design frame. . . . .	104
5.83	Maximum relative displacement demand mean values from artificial ground motions. . . . .	108
5.84	Maximum relative displacement demand mean values from near fault ground motions. . . . .	108
5.85	Maximum total acceleration demand mean values from artificial ground motions.	109
5.86	Maximum total acceleration demand mean values from near fault ground motions.	109
5.87	Maximum shear demand mean values from artificial ground motions. . . . .	110
5.88	Maximum shear demand mean values from near fault ground motions. . . . .	110
5.89	Maximum relative displacement demand standard deviation. . . . .	111
5.90	Maximum acceleration floor demand standard deviation. . . . .	111

5.91	Maximum shear demand standard deviation. . . . .	111
A.1	Ground motion 1. . . . .	120
A.2	Ground motion 1 spectra. . . . .	120
A.3	Ground motion 2. . . . .	121
A.4	Ground motion 2 spectra. . . . .	121
A.5	Ground motion 3. . . . .	122
A.6	Ground motion 3 spectra. . . . .	122
A.7	Ground motion 4. . . . .	123
A.8	Ground motion 4 spectra. . . . .	123
A.9	Ground motion 5. . . . .	124
A.10	Ground motion 5 spectra. . . . .	124
A.11	Ground motion 6. . . . .	125
A.12	Ground motion 6 spectra. . . . .	125
A.13	Ground motion 7. . . . .	126
A.14	Ground motion 7 spectra. . . . .	126
A.15	Original ground motion 8. . . . .	128
A.16	Original ground motion 8 spectra. . . . .	128
A.17	Scaled ground motion 8. . . . .	129
A.18	Scaled ground motion 8 spectra. . . . .	129
A.19	Original ground motion 9. . . . .	130

A.20 Original ground motion 9 spectra. . . . .	130
A.21 Scaled ground motion 9. . . . .	131
A.22 Scaled ground motion 9 spectra. . . . .	131
A.23 Original ground motion 10. . . . .	132
A.24 Original ground motion 10 spectra. . . . .	132
A.25 Scaled ground motion 10. . . . .	133
A.26 Scaled ground motion 10 spectra. . . . .	133
A.27 Original ground motion 11. . . . .	134
A.28 Original ground motion 11 spectra. . . . .	134
A.29 Scaled ground motion 11. . . . .	135
A.30 Scaled ground motion 11 spectra. . . . .	135
A.31 Original ground motion 12. . . . .	136
A.32 Original ground motion 12 spectra. . . . .	136
A.33 Scaled ground motion 12. . . . .	137
A.34 Scaled ground motion 12 spectra. . . . .	137
A.35 Original ground motion 13. . . . .	138
A.36 Original ground motion 13 spectra. . . . .	138
A.37 Scaled ground motion 13. . . . .	139
A.38 Scaled ground motion 13 spectra. . . . .	139
A.39 Original ground motion 14. . . . .	140

A.40	Original ground motion 14 spectra. . . . .	140
A.41	Scaled ground motion 14. . . . .	141
A.42	Scaled ground motion 14 spectra. . . . .	141
B.1	Displacement demand values normalized to the linear elastic displacement demand for artificial ground motions. . . . .	143
B.2	Displacement demand values normalized to the linear elastic displacement demand for near fault ground motions. . . . .	143
B.3	Force demand values normalized to the linear elastic displacement demand for artificial ground motions. . . . .	144
B.4	Force demand values normalized to the linear elastic displacement demand for near fault ground motions. . . . .	144
B.5	System absorbed energy for artificial ground motions. . . . .	145
B.6	System absorbed energy for near fault ground motions. . . . .	145
B.7	Displacement demand values normalized to the linear elastic displacement demand for artificial ground motions. . . . .	146
B.8	Displacement demand values normalized to the linear elastic displacement demand for near fault ground motions. . . . .	146
B.9	Force demand values normalized to the linear elastic displacement demand for artificial ground motions. . . . .	147
B.10	Force demand values normalized to the linear elastic displacement demand for near fault ground motions. . . . .	147
B.11	System absorbed energy for artificial ground motions. . . . .	148
B.12	System absorbed energy for near fault ground motions. . . . .	148

B.13 Displacement demand values normalized to the linear elastic displacement demand for artificial ground motions. . . . .	149
B.14 Displacement demand values normalized to the linear elastic displacement demand for near fault ground motions. . . . .	149
B.15 Force demand values normalized to the linear elastic displacement demand for artificial ground motions. . . . .	150
B.16 Force demand values normalized to the linear elastic displacement demand for near fault ground motions. . . . .	150
B.17 System absorbed energy for artificial ground motions. . . . .	151
B.18 System absorbed energy for near fault ground motions. . . . .	151
B.19 Displacement demand values normalized to the linear elastic displacement demand for artificial ground motions. . . . .	152
B.20 Displacement demand values normalized to the linear elastic displacement demand for near fault ground motions. . . . .	152
B.21 Force demand values normalized to the linear elastic displacement demand for artificial ground motions. . . . .	153
B.22 Force demand values normalized to the linear elastic displacement demand for near fault ground motions. . . . .	153
B.23 System absorbed energy for artificial ground motions. . . . .	154
B.24 System absorbed energy for near fault ground motions. . . . .	154
B.25 Displacement demand values normalized to the linear elastic displacement demand for artificial ground motions. . . . .	155
B.26 Displacement demand values normalized to the linear elastic displacement demand for near fault ground motions. . . . .	155

B.27 Force demand values normalized to the linear elastic displacement demand for artificial ground motions. . . . . 156

B.28 Force demand values normalized to the linear elastic displacement demand for near fault ground motions. . . . . 156

B.29 System absorbed energy for artificial ground motions. . . . . 157

B.30 System absorbed energy for near fault ground motions. . . . . 157

B.31 Displacement demand values normalized to the linear elastic displacement demand for artificial ground motions. . . . . 158

B.32 Displacement demand values normalized to the linear elastic displacement demand for near fault ground motions. . . . . 158

B.33 Force demand values normalized to the linear elastic displacement demand for artificial ground motions. . . . . 159

B.34 Force demand values normalized to the linear elastic displacement demand for near fault ground motions. . . . . 159

B.35 System absorbed energy for artificial ground motions. . . . . 160

B.36 System absorbed energy for near fault ground motions. . . . . 160

B.37 Displacement demand values normalized to the linear elastic displacement demand for artificial ground motions. . . . . 161

B.38 Displacement demand values normalized to the linear elastic displacement demand for near fault ground motions. . . . . 161

B.39 Force demand values normalized to the linear elastic displacement demand for artificial ground motions. . . . . 162

B.40 Force demand values normalized to the linear elastic displacement demand for near fault ground motions. . . . . 162

B.41 System absorbed energy for artificial ground motions. . . . . 163

B.42 System absorbed energy for near fault ground motions. . . . . 163

B.43 Displacement demand values normalized to the linear elastic displacement demand for artificial ground motions. . . . . 164

B.44 Displacement demand values normalized to the linear elastic displacement demand for near fault ground motions. . . . . 164

B.45 Force demand values normalized to the linear elastic displacement demand for artificial ground motions. . . . . 165

B.46 Force demand values normalized to the linear elastic displacement demand for near fault ground motions. . . . . 165

B.47 System absorbed energy for artificial ground motions. . . . . 166

B.48 System absorbed energy for near fault ground motions. . . . . 166

B.49 Displacement demand values normalized to the linear elastic displacement demand for artificial ground motions. . . . . 167

B.50 Displacement demand values normalized to the linear elastic displacement demand for near fault ground motions. . . . . 167

B.51 Force demand values normalized to the linear elastic displacement demand for artificial ground motions. . . . . 168

B.52 Force demand values normalized to the linear elastic displacement demand for near fault ground motions. . . . . 168

B.53 System absorbed energy for artificial ground motions. . . . . 169

B.54 System absorbed energy for near fault ground motions. . . . . 169

B.55 Displacement demand values normalized to the linear elastic displacement demand for artificial ground motions. . . . . 170

B.56 Displacement demand values normalized to the linear elastic displacement demand for near fault ground motions. . . . . 170

B.57 Force demand values normalized to the linear elastic displacement demand for artificial ground motions. . . . .	171
B.58 Force demand values normalized to the linear elastic displacement demand for near fault ground motions. . . . .	171
B.59 System absorbed energy for artificial ground motions. . . . .	172
B.60 System absorbed energy for near fault ground motions. . . . .	172
C.1 Ground motion 1 results (artificial). . . . .	174
C.2 Ground motion 2 results (artificial). . . . .	175
C.3 Ground motion 3 results (artificial). . . . .	176
C.4 Ground motion 4 results (artificial). . . . .	177
C.5 Ground motion 5 results (artificial). . . . .	178
C.6 Ground motion 6 results (artificial). . . . .	179
C.7 Ground motion 7 results (artificial). . . . .	180
C.8 Ground motion 8 results (near fault). . . . .	181
C.9 Ground motion 9 results (near fault). . . . .	182
C.10 Ground motion 10 results (near fault). . . . .	183
C.11 Ground motion 11 results (near fault). . . . .	184
C.12 Ground motion 12 results (near fault). . . . .	185
C.13 Ground motion 13 results (near fault). . . . .	186
C.14 Ground motion 14 results (near fault). . . . .	187

## LIST OF TABLES

5.1	Nominal design properties of reference LRB device. . . . .	43
5.2	Elastoplastic model parameters for LRB 500. . . . .	44
5.3	Flag-shape model parameters for SMA bearing equivalent to LRB 500. . . . .	45
5.4	Reduction factor coefficients for artificial ground motions. . . . .	86
5.5	Reduction factor coefficients for near fault ground motions. . . . .	86
5.6	Flag-shape model parameters for SMA bearing with hardening. . . . .	87
5.7	Frame model geometric properties. . . . .	101
5.8	Modal properties from not isolated structure analysis. . . . .	102
5.9	Modal properties from isolated structure analysis. . . . .	102
5.10	Base shear and control point displacements from pushover analysis. . . . .	103
A.1	Artificial ground motion generation parameters. . . . .	119

A.2 Near field ground motions. . . . . 127

A.3 Near field ground motions scaling factors. . . . . 127

## 1. INTRODUCTION

### 1.1 EARTHQUAKE ENGINEERING IN CONTEXT

A large proportion of the population in the world lives in seismic hazard regions and are at risk from earthquakes of varying severity and frequency of occurrence. Every year earthquakes cause significant loss of life and damage to property.

Progress in design and assessment methods of civil structures traditionally followed major earthquakes, whenever the need of improving the safety level of engineering structures became evident.

When it was realized in the 1950s and 1960s that structures can survive levels of response accelerations apparently exceeding the ultimate strength level, concept of *ductility* was formalized and began to be adopted, attributing to the structures the capacity of deforming inelastically without significant strength loss, thus surviving high level earthquakes. It was also understood that a general improvement of the structural response could be obtained by modifying the structural dynamic characteristics and dissipating the seismic energy during the earthquakes. Consequently, *capacity design principles* (also known as *failure-mode-control approach*) were developed, based on the designing the structure in order to get a predetermined post elastic mechanism, independent from the seismic intensity and in which selected ductile components are designed to withstand several cycles under reversed loading well beyond yield, while other members are supposed to remain to their elastic or low ductility range. These principles were applied more effectively as long as a number of performance-based design methods were developed, involving that damage variable limits are not exceeded during the earthquake occurrence.

## 1.2 SEISMIC ISOLATION

In this context, seismic isolation is a technology which mitigates the earthquake effects on buildings and their potentially vulnerable contents. The concept of protecting a structure from the damaging effects of an earthquake introducing a support isolating the building from the shaking ground is quite old, but research continues for effective, economical, and reliable seismic isolation systems.

Advantages in seismic isolation are evident: first, the level of damage is more safely controlled and confined to generally well-replaceable spots; then, an isolation system not only damps and reduces the action demand of the global structure, but also limits the force transmittable to the superstructure.

However, design of isolated structures has some particular concerns. Practical isolation systems must balance between the extent of force isolation and acceptable relative displacements across the isolation system during earthquakes. Acceptable displacements in conjunction with a large degree of force isolation can be reached by providing damping, as well as flexibility in the isolator. In such a case, both the forces transmitted and the deformation within the structure are reduced, and the seismic design of the superstructure will be considerably simplified, apart from the service connections need to accommodate the large displacements across the isolating layer.

A full and extensive description of seismic isolation can be found in standard texts like (Naeim and Kelly 1999), (Skinner, Robinson, and McVerry 1993) and (Chopra 2006).

## 1.3 ADVANCED MATERIAL APPLICATION IN SEISMIC ENGINEERING

Major developments have occurred in the last years about investigation on *advanced material* properties. The term *advanced* in civil structure context refers to a capability in increasing the structural performance and safety, the building design life time and its serviceability respect traditional materials. Seismic isolation can be considered an important example of an advanced technology from this point of view.

A key aspect to move towards the improved structural behavior technology is the development of this advanced materials, which can be integrated in structural innovative systems to provide better responses.

Some examples of smart materials are *Shape Memory Alloys* (also referred as *SMA*), which are a class of materials that have unique properties, including Youngs modulus-temperature relations, shape memory effects, superelastic effects, and high damping characteristics (Song, Ma, and

Li 2006). These unique properties, which have led to numerous applications in the biomedical and aerospace industries, are currently being evaluated for applications in the area of seismic resistant design and retrofitting (Desroches and Smith 2003).

## **1.4 DISSERTATION OBJECTIVES AND OUTLINE**

The aim of this work is to investigate the possibility of applying Shape Memory Alloys to isolation devices for buildings and bridges. We want to evaluate their response properties and compare them with traditional isolation bearing ones.

The outline of the dissertation is summarized below.

- Chapter 2 presents the main features of seismic isolation, starting from its theoretical formulation and evaluating the benefits it is supposed to provide and the main issues to be considered. This chapter concludes with a summary description of the most common isolation devices.
- Chapter 3 describes the design procedure for isolated structures, underlines the steps and their importance following a displacement based design approach and reports on comment about formulation of the design method.
- Chapter 4 is an introduction to Shape Memory Alloy materials and it provides basic information about its hysteretic and mechanical properties.
- Chapter 5 is the core of the investigation and it contains the following aspects:
  - section 5.1: the force-displacement constitutive model which we consider for the shape memory alloy isolation device;
  - section 5.2: the design of a SMA isolation device to get equivalent properties with respect to an actual reference device;
  - section 5.3: an estimation of the SMA device hysteretic reduction factor using the equivalent damping traditional approach and conclusion about the feasibility of the procedure;
  - section 5.4: the general presentation of the seismic response procedure to characterize the different device responses through time history analyses;
  - section 5.5 and section 5.6: respectively, the rigid and the flexible superstructure model time history analysis results;

- section 5.7: the general remarks on the time history analysis results.
- Chapter 6 summarizes the main conclusions of the investigation.

## **2. SEISMIC ISOLATION**

### **2.1 INTRODUCTION**

This chapter introduces the subject of seismic isolation. It briefly describes the main concepts, evaluates the advantages in using this method and presents the isolated system dynamic behavior. Moreover, it reports the most common seismic isolation bearing devices.

### **2.2 FUNDAMENTAL CONCEPTS**

Seismic isolation is a technique for reduce the seismic risk in different types of structures, like buildings and bridges. The goal in using seismic isolation is to modify the global response and improve the structural performance. We summarize in this section some of the most important issues about the topic are reported. An extensive description of the topic can be found in (Skinner, Robinson, and McVerry 1993), (Naeim and Kelly 1999) and (Priestley, Calvi, and Kowalsky 2007).

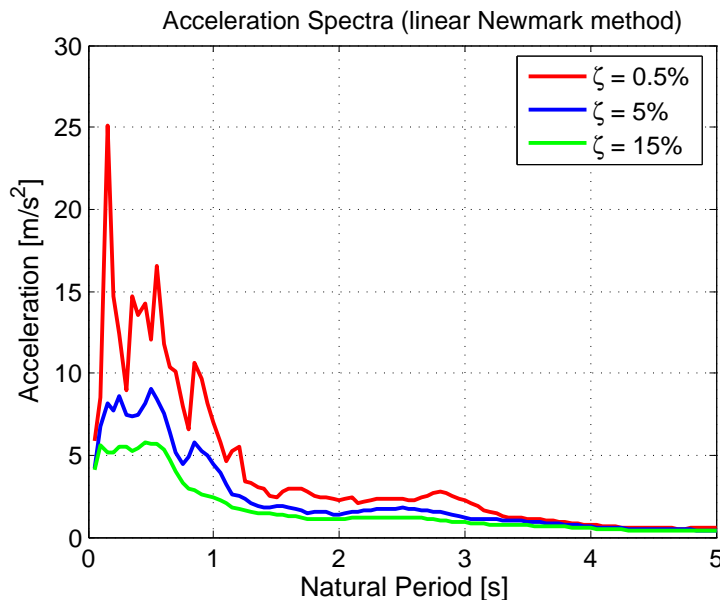
#### ***2.2.1 Response Regularization***

Isolation is a design method to regularize the response and to modify the relative effective stiffness and strength in the structure. The isolation system affects the global structural behavior because it has the same effect of an additional stiffness in series respect the superstructure stiffness. In fact, isolation layer is more flexible with respect to the rest of the structure, hence it absorbs a large part of the displacement demand. If we design the isolators in a correct way, providing enough displacement capacity, we can take advantage of this in the protection of the superstructure. Since the displacement demand of the superstructure is small, we can assure its

elastic response. Moreover, if we use nonlinear isolation system devices, the maximum base shear transmitted to the superstructure is limited and capacity design can be performed. In this way we assure that all the nonlinear and dissipating phenomena occur at the isolation level and we avoid any brittle failure mode.

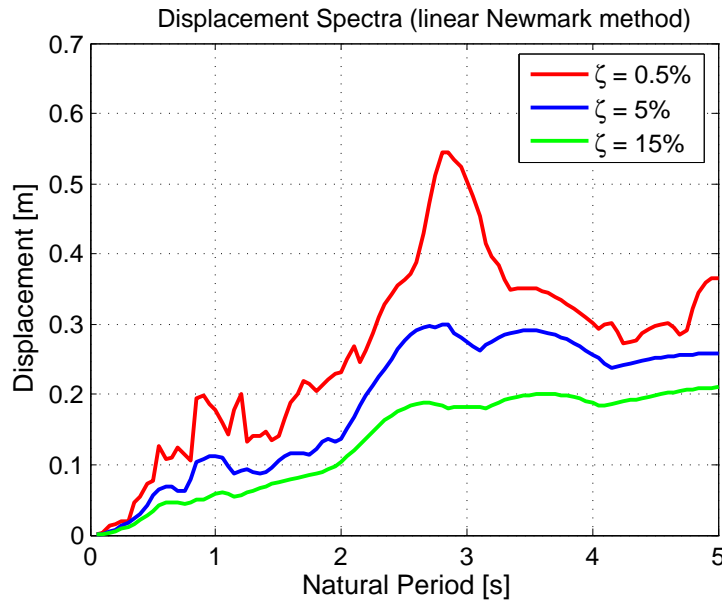
### 2.2.2 Period Shift

A change in global structure stiffness shifts the fundamental period of vibration. Since the isolation layer is more flexible than the superstructure, the fundamental period of the isolated structure is increased with respect to the one in the not isolated condition, inferring to either the displacement or the acceleration demand. The isolation system affects strongly the properties of the first mode of vibration. In an isolated structure this is very different from all the other modes and it is even more important than in the not isolated case. The vertical profile of the horizontal displacements is approximately rectangular, with equal motions for all the masses. In fact, fundamental mode is characterized by a large participating mass, almost equal to the total mass. Therefore the isolation system determines the first period and damping of an isolated structure, and these, in their turn, control the structure seismic response.



**Figure 2.1:** displacement response spectra for different damping factor values experiencing the El Centro (1940) ground motion.

Displacement and acceleration response spectra are shown respectively in Fig.(2.1) and in Fig.(2.2). Maximum accelerations are greatest when the first vibrational period of the structure is in the short period range. In the other hand, displacement demand is high for long periods.



**Figure 2.2:** acceleration response spectra for different damping factor values experiencing the El Centro (1940) ground motion.

Effectiveness of damping is reducing both acceleration and displacement ordinate.

Seismic isolation induces the elongation of fundamental mode period and this is a primary reason for effectiveness of the method. It leads to a reduction in the inertia load acting on the structure and to an increase in the demand of displacements, occurring anyway mostly at the level of the isolators. Usually higher modes producing deformations in the structure are essentially not excited by the ground motion.

### 2.2.3 Energy Dissipation

The presence of isolation system increases the global energy dissipation capacity of the structure. This helps to reduce the displacement demand as shown in Fig.(2.1). Usually we refer to the assumption according to which different structural elements contribute to the overall energy dissipation as a function of their displacements. Hence if the structural displacement demand is all localized in the isolation system and the superstructure is rigid, the isolation devices determines the energy dissipation; otherwise, if superstructure deforms, the energy is dissipated according to the isolation and to structure dissipation contributions.

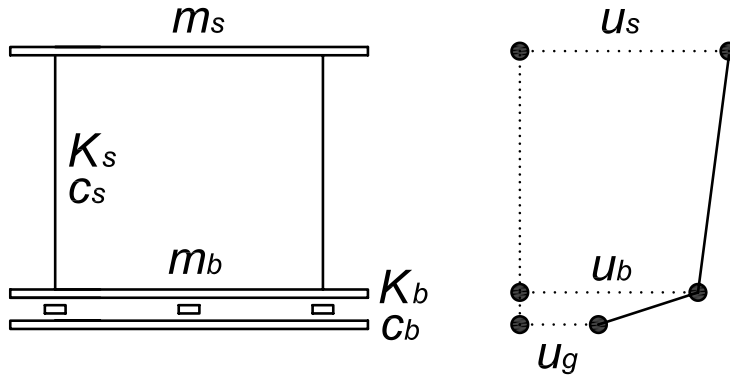
## 2.3 BASE ISOLATED STRUCTURE DYNAMICS

The linear theory of seismic isolation has been described in detail in (Naeim and Kelly 1999). This section presents the two mass isolated structural model as shown in Fig.(2.3). The mass  $m_s$  represents the superstructure and the mass  $m_b$  is the mass of the storey levels above the isolation system. The superstructure stiffness and damping are  $k_s$  and  $c_s$  and the stiffness and damping of the isolation system are  $k_b$  and  $c_b$ . Absolute displacements of the two masses are  $u_s$  and  $u_b$ ;  $u_g$  is the ground displacement.

For the sake of simplicity we take into account as independent variables the relative displacements, being:

$$\begin{aligned} v_b &= u_b - u_g \\ v_s &= u_s - u_b \end{aligned} \quad (2.1)$$

The definition in (2.1) is particular feasible because the relative degrees of freedom are representing respectively the isolation system displacement  $v_b$  and the superstructure drift  $v_s$ .



**Figure 2.3:** isolated system dynamic model and parameters.

The equation of motion of the system in terms of the quantities in (2.1) is given by:

$$\mathbf{M}\ddot{\mathbf{v}} + \mathbf{C}\dot{\mathbf{v}} + \mathbf{K}\mathbf{v} = \mathbf{M}\mathbf{r}\ddot{u}_g \quad (2.2)$$

which can be rewritten as:

$$\begin{aligned} \begin{bmatrix} m_s + m_b & m_s \\ m_s & m_s \end{bmatrix} \begin{Bmatrix} \ddot{v}_b \\ \ddot{v}_s \end{Bmatrix} + \begin{bmatrix} c_b & 0 \\ 0 & c_s \end{bmatrix} \begin{Bmatrix} \dot{v}_b \\ \dot{v}_s \end{Bmatrix} + \begin{bmatrix} k_b & 0 \\ 0 & k_s \end{bmatrix} \begin{Bmatrix} v_b \\ v_s \end{Bmatrix} = \\ = \begin{bmatrix} m_s + m_b & m_s \\ m_s & m_s \end{bmatrix} \begin{Bmatrix} 1 \\ 0 \end{Bmatrix} \ddot{u}_g \end{aligned} \quad (2.3)$$

Defining the mass ratio  $\gamma$  as:

$$\gamma = \frac{m_s}{m_s + m_b} \quad (2.4)$$

the natural frequencies  $\omega_b$  and  $\omega_s$  are given by:

$$\omega_b^2 = \frac{k_b}{m_s + m_b} \quad \omega_s^2 = \frac{k_s}{m_s} \quad (2.5)$$

and it is assumed that the following relation is valid:

$$\epsilon = \frac{\omega_b^2}{\omega_s^2} = O(10^{-2}) \quad (2.6)$$

damping factors  $\xi_b$  and  $\xi_s$  are defined by:

$$2\omega_b\xi_b = \frac{c_b}{m_s + m_b} \quad 2\omega_s\xi_s = \frac{c_s}{m_s} \quad (2.7)$$

the system dynamic equations (2.3) therefore become:

$$\begin{aligned} \gamma\ddot{v}_s + \ddot{v}_b + 2\omega_b\xi_b\dot{v}_b + \omega_b^2v_b &= -\ddot{u}_g \\ \ddot{v}_s + \ddot{v}_b + 2\omega_s\xi_s\dot{v}_s + \omega_s^2v_s &= -\ddot{u}_g \end{aligned} \quad (2.8)$$

as  $\omega_1$  and  $\omega_2$  are the natural frequencies of the two structural modes as expressed in (2.5), they can be also computed as:

$$\begin{aligned} \omega_1^2 &= \frac{1}{2(1-\gamma)} \left\{ \omega_b^2 + \omega_s^2 - \sqrt{(\omega_b^2 - \omega_s^2)^2 + 4\gamma\omega_b^2\omega_s^2} \right\} \\ \omega_2^2 &= \frac{1}{2(1-\gamma)} \left\{ \omega_b^2 + \omega_s^2 + \sqrt{(\omega_b^2 - \omega_s^2)^2 + 4\gamma\omega_b^2\omega_s^2} \right\} \end{aligned} \quad (2.9)$$

and to first order in  $\epsilon$  are given by:

$$\begin{aligned} \omega_1^2 &= \omega_b^2 (1 - \gamma\epsilon) \\ \omega_2^2 &= \frac{\omega_s^2}{1 - \gamma} (1 + \gamma\epsilon) \end{aligned} \quad (2.10)$$

while the mode shapes normalized in the isolation system displacement component are:

$$\phi^{(1)} = \begin{Bmatrix} 1 \\ \epsilon \end{Bmatrix} \quad \phi^{(2)} = \begin{Bmatrix} 1 \\ -\frac{1}{\gamma}[1 - (1 - \gamma)\epsilon] \end{Bmatrix} \quad (2.11)$$

analysis leads to express modal masses as:

$$M_1 = (m_s + m_b) (1 + 2\gamma\epsilon) \quad M_2 = (m_s + m_b) \frac{(1 - \gamma)[1 - 2(1 - \gamma)\epsilon]}{\gamma} \quad (2.12)$$

and participation factors can be expressed as:

$$\Gamma_1 = 1 - \gamma\epsilon \quad \Gamma_2 = \gamma\epsilon \quad (2.13)$$

The results in (2.13) reveal the basic concept which an isolation system relies: the participation factor of the second mode, responsible for the structural deformation, is of the order of magnitude of  $\epsilon$  and if the two frequencies are well separated, as assumed in (2.6), it may be very small.

Since the participation factor of the second mode is very small, it is also almost orthogonal to the earthquake input: this means that in any case the input energy associated to the second mode structural frequency will not be inferred to the structure. The isolation system works in fact by deflecting energy through its orthogonality property rather than by absorbing it.

Nevertheless energy absorption is another component of the isolation system. Modal damping ratios depend on the superstructural and on the isolator damping coefficients. When they can be treated separately, and the energy dissipation can be described just by linear viscous damping, the following simple relationships are found:

$$\xi_1 = \xi_b \left( 1 - \frac{3}{2}\gamma\epsilon \right) \quad \xi_2 = \frac{\xi_s + \gamma\xi_b\sqrt{\epsilon}}{\sqrt{1-\gamma}} \left( 1 - \frac{\gamma\epsilon}{2} \right) \quad (2.14)$$

which demonstrates that if the  $\epsilon$  is small enough the damping coefficient of the fundamental mode is the damping coefficient of the isolation system.

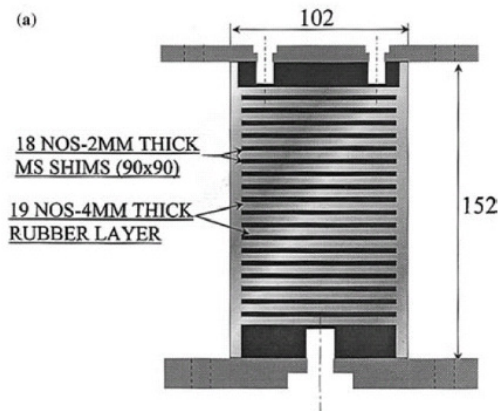
## 2.4 BEARING DEVICES

In this section we present a summary of the most common seismic isolation bearing devices. Bearings are designed to transmit the vertical load and to dissipate energy through friction, viscous damping or hysteretic damping. Usually they are designed to reduce or control the horizontal force and displacement demand.

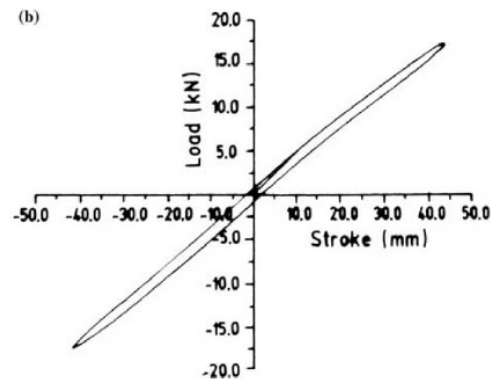
### 2.4.1 *Low and High Damping Laminated Rubber Bearings*

In laminated rubber bearings steel plates are inserted in a vulcanized piece of rubber to confine the rubber laterally and reducing its tendency to bulge, as shown in Fig.(2.4). Hence, shims increase the vertical stiffness and improve stability under horizontal forces.

This type of bearing shows a substantially linear response and the rubber properties controls essentially the dissipation. Low dissipation rubber provides a force-displacement relation as shown in Fig.(2.5), while high dissipation rubber gives the response shown in Fig.(2.6). The fundamental property of this type of bearing is the dependance between vertical load capacity, period of vibration and displacement capacity.



**Figure 2.4:** laminated low damping rubber bearing structure [from (Jain and Thakkar 2005)].



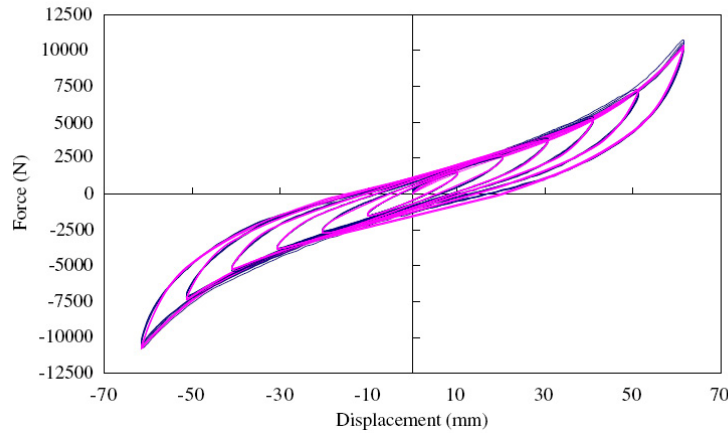
**Figure 2.5:** laminated low damping rubber bearing (LDRB) force-displacement relation [from (Jain and Thakkar 2005)].

Maximum displacement capacity of this class of bearings is limited by either plan or height dimensions: typical design capacities for medium seismicity areas range in the order of 200 mm with ultimate capacities up to 300 mm. The only damping source is the viscous one and it is of the order of 5% for normal rubber and in the order of 15%-20% for high dissipating rubber. Given the constitutive force displacement relation quasi-elastic, the devices are usually characterized by recentering capacity and almost constant stiffness.

The failure is usually related to instability due to large displacements, either in the form of Euler instability or as roll-out instability (Priestley, Calvi, and Kowalsky 2007).

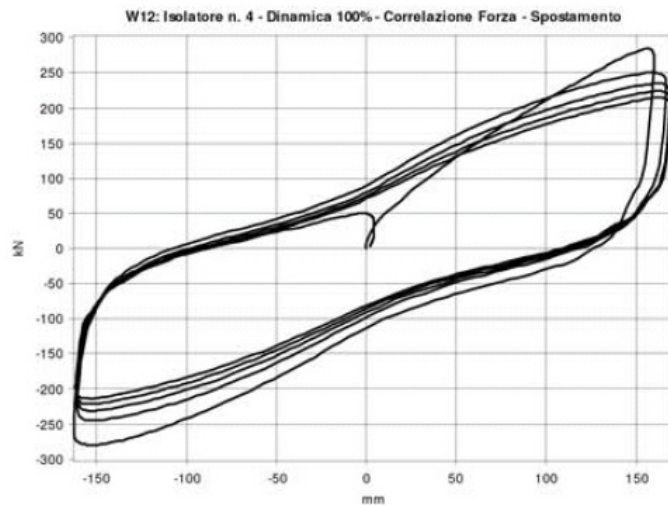
### 2.4.2 Lead Rubber Bearings

Lead rubber bearings are low damping laminated rubber devices with a lead plug inserted in the core. The aim of the lead addition is to increase both the stiffness at relatively low horizontal



**Figure 2.6:** laminated high damping rubber bearing (HDRB) force-displacement relation [from (Tsai, Chiang, Chen, and Lin 2003)].

force levels and the energy dissipation capacity. The resulting horizontal force-displacement relation curve is shown in Fig.(2.7). It can be interpreted as a combination of the linear response of the rubber bearing and of the elasto-perfectly plastic response of a confined lead plug. Hence we can describe it using an elastoplastic model with hardening, as presented in Fig.(2.8).

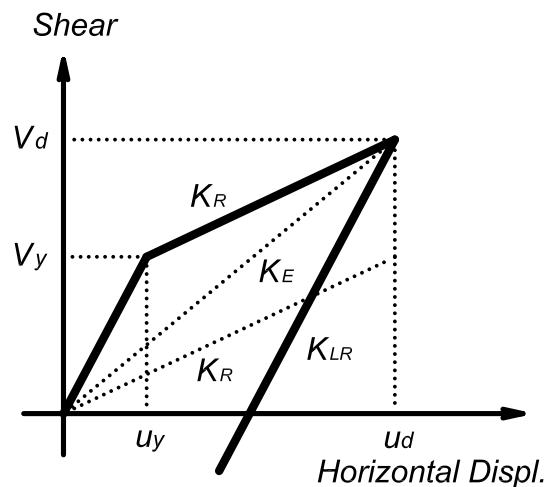


**Figure 2.7:** lead rubber bearing (LRB) force-displacement relation [courtesy *AGOM Internazionale srl*].

Maximum displacement is still governed either by the allowable shear strain in the rubber or by the global stability of the device under vertical load. Post-yielding stiffness corresponds to the mere rubber stiffness and the unloading branch of the force-displacement curve is approximately parallel to the initial stiffness branch, up to yielding of the lead plug in the opposite

direction. Referring to typical geometries and proportions between lead plug and rubber, the yield force is in the range of one half of the ultimate force and the post-yield stiffness in the range of one tenth of the initial one. Displacement capacity, response at failure, sensitivity to vertical input are similar to those described for the case of rubber bearings. Given the same geometry, the initial stiffness of a lead rubber bearing system  $K_{LR}$  is approximately 10 times higher than the one of a rubber bearing  $K_R$ . This involves that the initial period of vibration is shorter by a factor of about 3 or 4; after yielding, the LRB stiffness is similar to that of the rubber device.

Referring to Fig.(2.8), the elastoplastic system can be characterized considering the secant stiffness  $K_E$  to the design displacement. In this case the stiffness is about two times larger than the rubber bearing one. If we take into account the secant stiffness to compute the natural period, we estimate a value which is almost the double of the one computed based on the initial stiffness, because the ultimate displacement secant stiffness is approximately the 20% of the initial one.

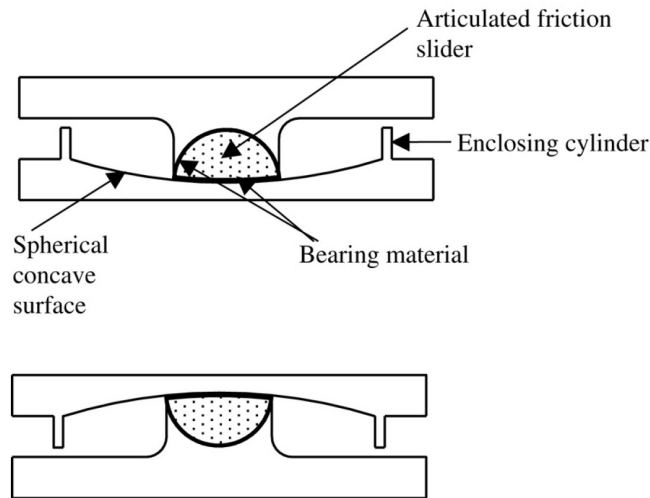


**Figure 2.8:** hysteresis model for a lead rubber bearing (LRB).

From the previous discussion is evident that the device has significant hysteretic dissipation. Recentering capacity of lead rubber bearings depends on the ratio between post-yield and initial stiffness and on the ratio between ultimate and yield strength. A larger tendency to recenter is shown if the hardening is high, but residual displacements depend mainly on the loading history and they usually are not negligible.

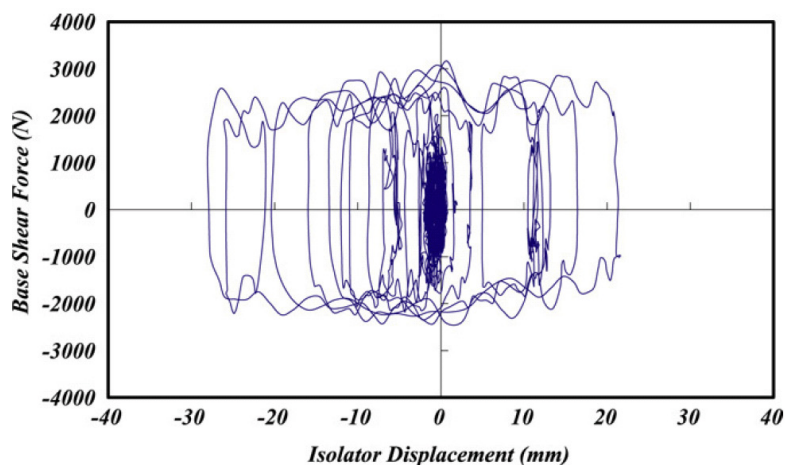
### 2.4.3 Friction Pendulum Devices

The friction pendulum system (*FPS*) is conceptually based on the properties of pendulum motion (Christopoulos and Filiatrault 2006) and (Priestley, Calvi, and Kowalsky 2007). The struc-



**Figure 2.9:** double configuration friction pendulum system (FPS) device cross sections [from (Ates, Dumanoglu, and Bayraktara 2005)].

ture is supported on an articulated teflon-coated load element sliding on the inside of a spherical surface as shown in Fig.(2.9), hence any horizontal displacement is implying a vertical uplift of the supported weight. If friction force is neglected, the system equation of motion is similar to



**Figure 2.10:** force-displacement FPS result from experimental dynamic tests. [from (Tsai, Lu, Chen, Chiang, Yang, and Lin 2008)].

that of a pendulum with equal mass and length given by the radius of curvature of the spherical

surface. The expected force-displacement relation is rigid for horizontal loads lower than the resisting friction force and proportional to the ratio between the seismic weight and the radius of curvature for larger loads. An example of FPS force-displacement relation is reported in Fig.(2.10).

Theoretically, the approach does not have a displacement limit, but for the physical size of the bearing related to possibility of manufacturing the devices. It exhibits favorable self centering properties based on the effect of the weight.

## **3. DESIGN PROCEDURE FOR ISOLATED STRUCTURES**

### **3.1 INTRODUCTION**

In this chapter we look at the typical procedure for the design of seismic isolation structures. There are two possible main approaches to design a seismic resistant structure, the *force based* and the *displacement based* approaches. The force based one is traditionally used in seismic design, but in the last years researches have underlined several lacks in this approach (Priestley, Calvi, and Kowalsky 2007). Nowadays, we think it is not very suitable for seismic isolation system design. Hence in this work we only take into account and follow a displacement-based procedure.

The chapter presents the general main concepts of DDBD in section 3.2, then specializes the design procedure description for isolated structures in 3.3. Finally some general comments on the DDBD and its application to innovative systems are reported in 3.4.

### **3.2 MAIN FEATURES OF THE DIRECT DISPLACEMENT BASED DESIGN**

The *Direct Displacement Based Design (DDBD)* is a particular formulation of *Performance Based Design*. Following this approach we target the design process to achieve a given performance limit state for the design conditions. Hence, for a given seismic intensity, displacement based designed structures are characterized by uniform risk.

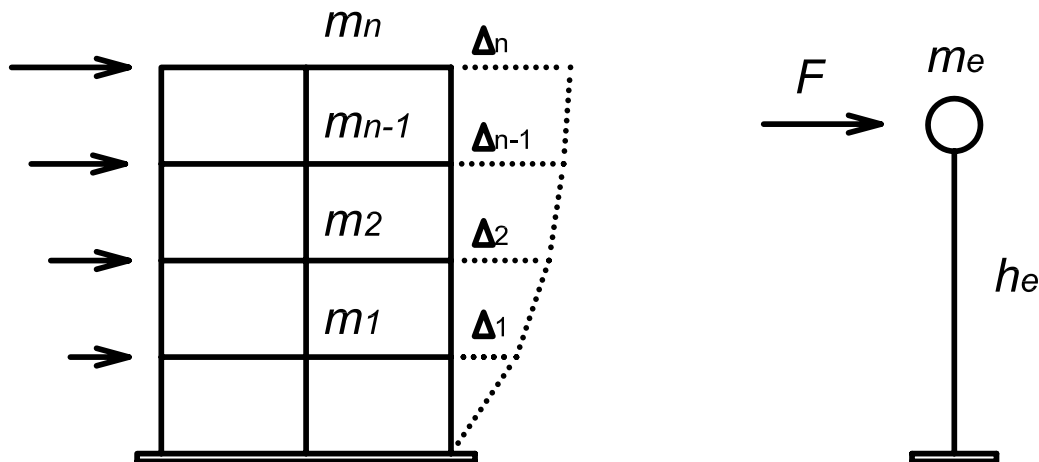
In fact, the most representative parameters related to structural damage, and therefore to performance, are strains: since strains are directly dependent on drifts and displacements, this approach is based on the assumption that the design displacements have to control the seismic design. For different limit states we consider different levels of acceptable damage and different

levels of corresponding displacements. Then, we define the required strength at several locations to get the design displacement capacity and avoid development of non ductile inelastic deformation mechanisms.

The fundamental steps on which the DDBD is based are briefly reported below; a systematic description of the procedure can be found in (Priestley, Calvi, and Kowalsky 2007).

### 3.2.1 Simulation of equivalent nonlinear Single Degree of Freedom system

The displacement based design consists firstly in modeling the structure (usually a multi-degree of freedom system, *MDOF*) with an equivalent *single degree of freedom* system (*SDOF*), characterized by an equivalent mass ( $m_e$ ) lumped at an equivalent height ( $h_e$ ), as shown in Fig.(3.1).



**Figure 3.1:** equivalence between a MDOF having estimated the lateral forces deformed shape and a SDOF of parameters  $m_e$  and  $h_e$ .

If we assume that the fundamental mode of vibration is the most important for the structure, because it is characterized by a participating modal mass significantly greater with respect to other modes, the approximation is acceptable. This assumption is reasonable for almost all the existing structures, hence the equivalent system is able to describe characteristics of a wide range of real buildings.

Moreover, if the previous assumption is satisfied, we can also assume that the deformed shape under horizontal loads reproduces the first mode of vibration; usually the shape depends on the structural system, but in general it is known, at least in an approximated form. Therefore we can estimate the deformed shape  $\Delta$  of a general structure with  $N_{fl}$  floors and mass  $m$  at each storey;  $\Delta$  is a vector having  $N_{fl}$  components corresponding to the displacements of each floor (as shown in Fig.(3.1)).

Given the previous, the generalized displacement coordinate is defined as:

$$\Delta_d = \frac{\sum_{j=1}^{N_{fl}} m_j \Delta_j^2}{\sum_{j=1}^{N_{fl}} m_j \Delta_j} \quad (3.1)$$

and the effective mass is:

$$m_e = \frac{\sum_{j=1}^{N_{fl}} m_j \Delta_j}{\Delta_d} \quad (3.2)$$

which is also called *base shear effective modal mass* because it is the lumped SDOF mass producing a base shear for the first mode of vibration which is the same of the original MDOF with distributed mass.

The effective height is given by:

$$h_e = \frac{\sum_{j=1}^{N_{fl}} m_j \Delta_j h_j}{\sum_{j=1}^{N_{fl}} m_j \Delta_j} \quad (3.3)$$

and can be interpreted as the height of the resultant of the lateral forces to produce at the base of the SDOF a bending moment equal to the base moment of original MDOF.

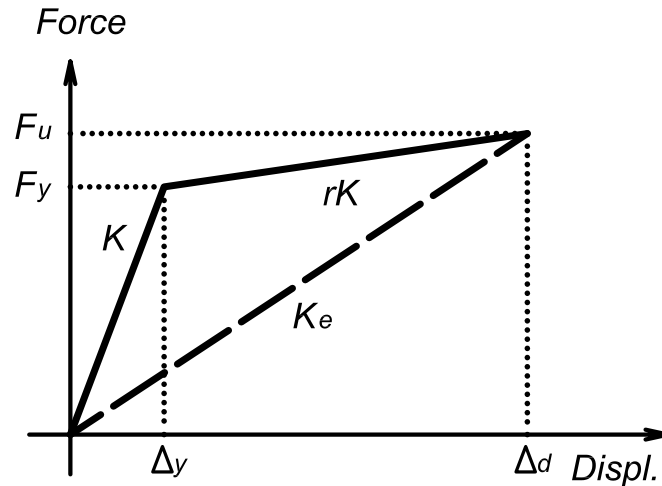
Hence the limit of this approximation is that the equivalence between the MDOF and the SDOF system is only in terms of base bending moment and shear.

### 3.2.2 *Effective stiffness consideration*

The DDBD approach describes the SDOF system lateral force-displacement response envelope using a bilinear curve. As shown in Fig.(3.2), we consider an initial elastic stiffness  $K$  and a post yielding stiffness which is a fraction  $rK$  of the previous.

In a *force-based* design approach, even if the system is characterized by a nonlinear hysteresis like the one shown in Fig.(3.2), we would compute the structural period and the percentage of the elastic damping just referring to pre-yielding stiffness  $K$ . Eventually, through refinements of the method, we could take into account the nonlinearity of the constitutive relation and the second stiffness, but modal properties are usually considered constant and computed only from the initial stiffness.

On the other hand, the *Direct Displacement Based Design* approach assumes that the most significant structural stiffness is the secant stiffness at the maximum design displacement  $\Delta_d$ , that



**Figure 3.2:** effective stiffness concept for a bilinear force displacement relation envelope.

is the *effective stiffness*  $K_e$  shown in Fig.(3.2). This implies that fundamental mode properties are computed considering  $K_e$ , regardless the initial stiffness  $K$ .

The design displacement  $\Delta_d$  is a function of the limit state condition we are interested in. We evaluate it using the equation (3.1). Considering the real structure properties such as materials and cross sections, we compute the displacement that would occur in the control point of the SDOF when the limit state condition is reached in any of the structural elements. Hence the control point displacement is related to structural performance.

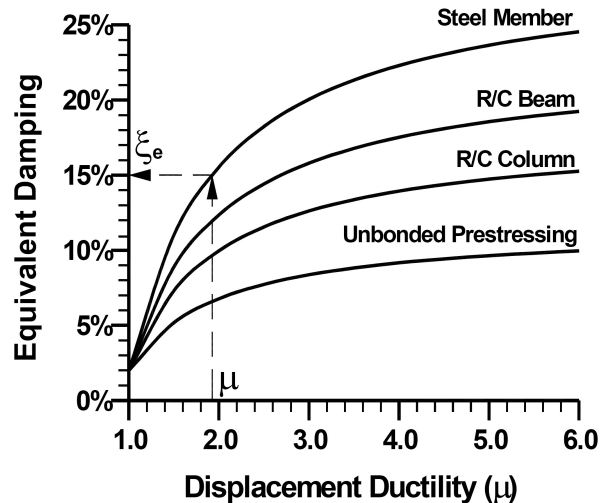
Still referring to SDOF control point, we also compute the loss of linearity displacement  $\Delta_y$ , corresponding to the first yielding in the structure. Then the displacement ductility of the equivalent system is given by:

$$\mu = \frac{\Delta_d}{\Delta_y} \quad (3.4)$$

The system displacement ductility is useful to determine the damping parameter of the equivalent SDOF system, because it is leading information about the "magnitude" of the nonlinearity of the system. Nevertheless, as a matter of the effective stiffness conception, it makes no difference, but for damping computation (as reported in the following section), to consider two systems with the same design displacement  $\Delta_d$  with different yielding displacements  $\Delta_y$  and different ductility  $\mu$ .

### 3.2.3 Equivalent damping evaluation

In displacement based design procedure we simplify the structure modeling it as a SDOF system with a linear elastic stiffness equal to the effective stiffness. Nevertheless, we cannot neglect real inelastic properties because they are related to energy dissipation. Therefore we use an equivalent viscous damping ratio which is representative of the elastic damping and of the hysteretic energy absorbed during the real response.



**Figure 3.3:** equivalent viscous damping estimation as a function of the displacement ductility [from (Grant, Blandon, and Priestley 2005)]; there are different relations for different structural systems.

In some researches (such as (Grant, Blandon, and Priestley 2005)) empirical relations between the equivalent damping ratio for different structural system and the design displacement ductility have been developed as shown in Fig.(3.3).

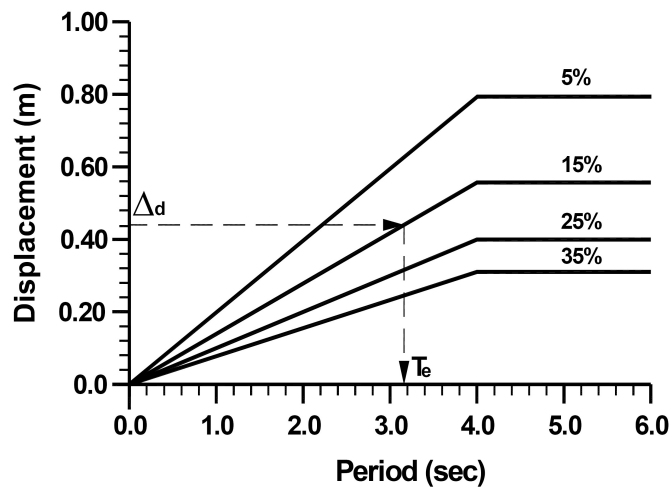
### 3.2.4 Design displacement spectra and structural base shear

As we know an estimation of the system equivalent damping ratio, we compute the design spectra as a function of the damping itself. The effectiveness of damping is in reducing the displacement ordinates, and usually spectra are provided for a given damping ratio, normally the 5% of the critical one. We can get an estimation of the relative damping ratio spectra multiplying the original spectra ordinates by a factor  $R_{\xi}$ . This is a reduction factor increasing as the equivalent viscous damping increases. It differs as a function of the seismic input properties we consider, but in one of the most common formulation we can estimate it for the far field

events as (Priestley, Calvi, and Kowalsky 2007):

$$R_{\xi} = \sqrt{\frac{10}{5 + \xi}} \quad (3.5)$$

Using the design displacement for our structure and referring to the design spectra for the given damping, we compute the effective structural period  $T_e$  as shown in Fig.(3.4).



**Figure 3.4:** displacement design spectra for different damping ratios (reported on the curves) and computation of the effective structural period given the design displacement [from (Dwairi, Kowalsky, and Nau 2007)].

According to the previous assumption, the effective stiffness  $K_e$  is given by:

$$K_e = \frac{4\pi^2 m_e}{T_e^2} \quad (3.6)$$

and the base shear of the structure:

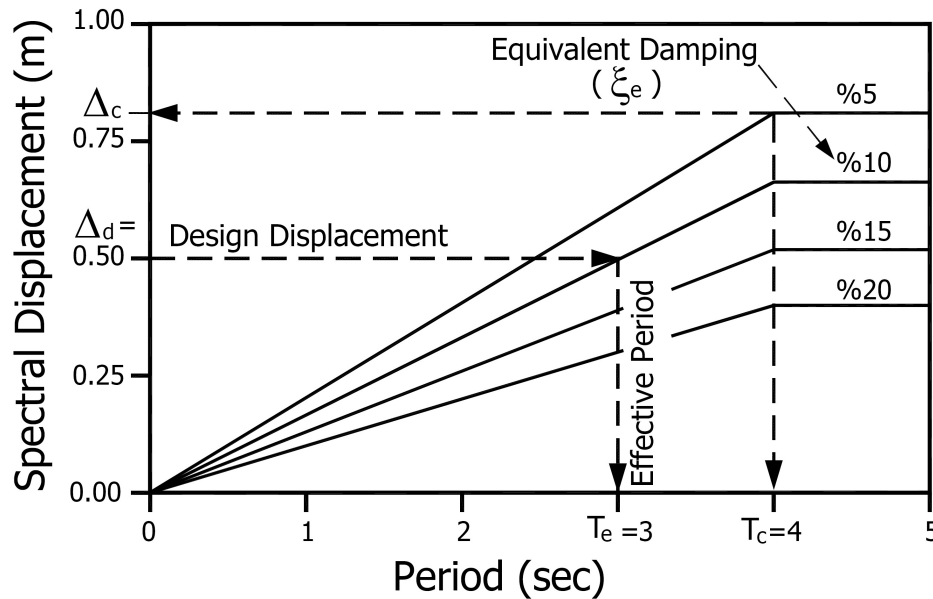
$$V_{base} = K_e \Delta_d \quad (3.7)$$

Given the base shear, we can find the design actions in all the structural elements.

As a final summary of the DDBD procedure, the following equation directly computes the equivalent SDOF base shear:

$$V_{base} = \frac{4\pi^2 m_e}{\Delta_d} \left( \frac{\Delta_c}{T_c} \right)^2 R_{\xi}^2 \quad (3.8)$$

being  $\Delta_c$  and  $T_c$  the coordinate of the corner period in the design displacement spectra. The procedure for the determination of the base shear is summarized graphically in Fig.(3.5).



**Figure 3.5:** DDBD equivalent SDOF base shear computation: summary of the procedure [from (Dwairi, Kowalsky, and Nau 2007)].

### 3.3 DISPLACEMENT BASED DESIGN OF ISOLATED STRUCTURES

Given the displacement based approach for the structural design, the problem of base isolated structures is just a particular case in the framework of the general concepts described above.

The design displacement is usually computed assuming the elastic response in the superstructure and all the essential nonlinear phenomena taking place in the isolation system. This means that *structural displacement* is regularized in the structure, because large part of the displacement demand is expected to occur at the isolation level and the maximum relative displacement of the superstructure is supposed to be smaller than the yielding one.

The basic *capacity design* concept also affects the design, because the isolation system works even as a force limiting mechanism. Since it is more flexible than the superstructure and more ductile, it avoids any possible *brittle failure*, provided that we take into account the foundation protection. The *limiting force* is given either by the smaller value between the base shear  $V_{base}$ , related to the structural fundamental period increased, and the limiting shear capacity of the isolation system, if any.

The isolation system increases the *energy dissipation* because a uniformly distributed inelastic demand occurs in a large number of ductile elements, which are the seismic isolation bearings.

As a function of the different structural properties, the design of isolated structure can be performed assuming the superstructure *rigid* or *flexible*. For both the cases which are described

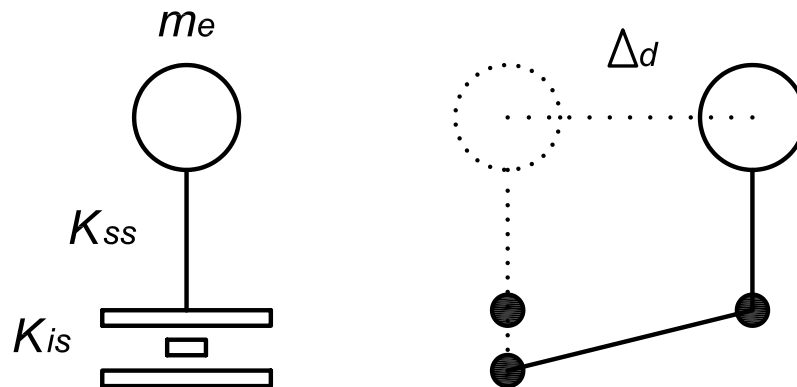
below, we follow the design procedures presented in (Priestley, Calvi, and Kowalsky 2007).

### 3.3.1 Base-Isolated Rigid Structures

For small buildings or tanks, fundamental period of base-isolated structure is several times larger than fixed-base structure. Hence the isolation system horizontal stiffness  $K_{is}$  is several times smaller than the superstructure stiffness  $K_{ss}$ :

$$K_{is} \gg K_{ss} \quad (3.9)$$

When relation (3.9) is verified, the assumption of rigid superstructure is reasonable. Therefore we can perform separate design for superstructure and isolation system, assuming that all the displacement is occurring only at the isolation level, as shown in Fig.(3.6).



**Figure 3.6:** base isolated rigid structure design: equivalent displacement profile.

In this case the superstructure affects the isolation system design only as an additional mass: it is usually designed just considering the non-seismic load combination and assuming that it responds elastically to the seismic actions filtered by the isolation system.

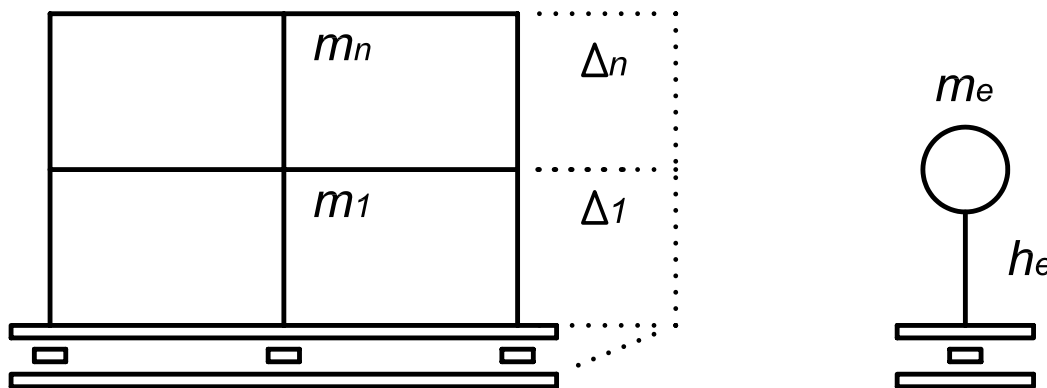
Looking at Fig.(3.7), which reproduces the fundamental mode of vibration of the system, we conclude that all the mass of the superstructure participates in the fundamental mode of vibration, hence:

- the effective mass of the isolated system  $m_e$  is given by the total mass of the superstructure, that is the sum on all the storey levels ( $N_{fl}$ ) of the storey masses  $m_j$ :

$$m_e = \sum_{j=1}^{N_{fl}} m_j \quad (3.10)$$

- the equivalent height of the system, knowing the deformed shape, is given by one half of the total superstructure height  $h_{tot}$  because this moves rigidly on the isolated surface:

$$h_e = \frac{h_{tot}}{2} \quad (3.11)$$



**Figure 3.7:** base isolated rigid structure model: displacement profile and equivalent SDOF parameters.

The isolation system provides reduction of forces and increasing of global displacements in the structure, but also some energy dissipation in terms of viscous damping or hysteretic behavior. Since the superstructure is characterized by a small drift, we can assume its contribution to the global dissipation negligible. Therefore the equivalent global damping is given by the equivalent viscous damping of the isolators.

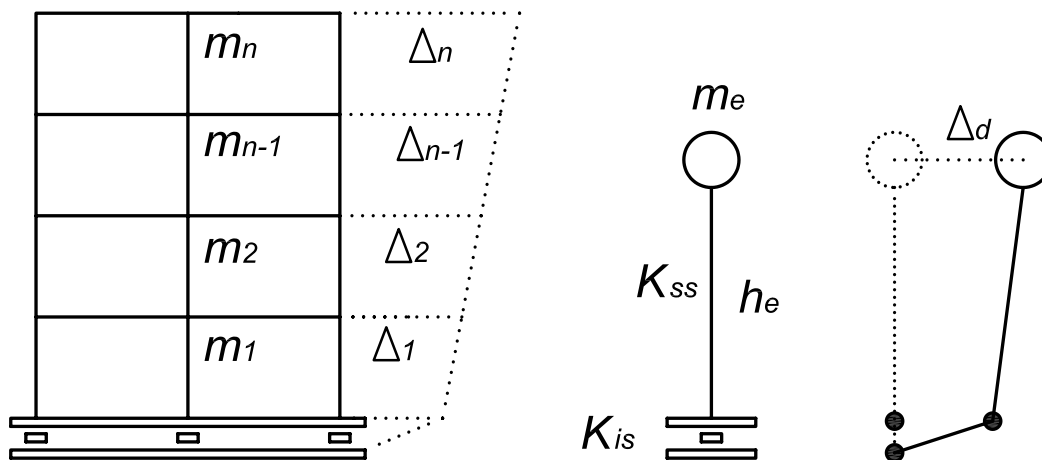
$$\xi_{e,is} \simeq \xi_{e,sys} \quad (3.12)$$

The design displacement  $\Delta_d$  usually does not depend on drift limits or superstructural material strain limits, but it is affected by the properties of the isolators.

Knowing  $\xi_{is}$  we can refer to the relative displacement spectra and find the design equivalent period  $T_e$  as shown in Fig.(3.4). Finally we compute the base shear using formulas (3.6) and (3.7).

### 3.3.2 Base-Isolated Flexible Structures

If the period of the isolated structure is not several times longer (at least 3 times according to (Priestley, Calvi, and Kowalsky 2007)) than the one of the fixed-base structure, the superstructure cannot be considered rigid respect the isolation level, but we have to take into account the flexibility, as shown in Fig.(3.8).



**Figure 3.8:** base isolated flexible structure model: displacement profile and equivalent SDOF parameters.

Hence in the design procedure we have to consider the superstructure deformed profile. Since the superstructure response is supposed to be elastic, displacements of the structural members are not critical and can be evaluated in a simplified manner considering usually a linear deformed shape.

Knowing the deformed shape and recalling the (3.2) and the (3.3), we compute the effective height  $h_e$ , and the effective mass  $m_e$ . In general the equivalent height is quite close to the value we had in the rigid superstructure approach, at one half of the total height, even if the deformability of the superstructure leads to a value a bit larger than the previous; moreover, the equivalent mass is close to the total mass. In fact isolation system increases the participation coefficient of the structure to the first mode of vibration and higher modes are not very important even in the case of flexible superstructure.

We compute the global design displacement as a sum of the isolation system displacement and of the superstructure displacement:

$$\Delta_{d,sys} = \Delta_{d,is} + \Delta_{d,ss} \quad (3.13)$$

Regarding the equivalent viscous damping of the system, again because of the flexibility of the superstructure, we are not allowed to assume that it is equal to the one of the isolation system. Assuming that the dissipation of an element is proportional to its displacement, global damping can be estimated as the sum of the two contributions weighted by the displacements occurring in the superstructure and in the isolation system (Priestley, Calvi, and Kowalsky 2007), using

an expression like:

$$\xi_{e,sys} = \frac{\xi_{e,is} \Delta_{d,is} + \xi_{e,ss} \Delta_{d,ss}}{\Delta_{d,is} + \Delta_{d,ss}} \quad (3.14)$$

Usually the isolation system equivalent damping  $\xi_{e,is}$  is larger than the superstructure one  $\xi_{e,ss}$ , hence the (3.14) implies that if the structural deformation  $\Delta_{d,ss}$  is a large fraction of the total one  $\Delta_{d,sys}$ , the effectiveness of isolation system in dissipating energy is significantly reduced.

To proceed with the design we follow the usual procedure starting with the design displacement

$$\Delta_d = \Delta_{d,sys} \quad (3.15)$$

and with the displacement spectra relative to the global viscous damping coefficient  $\xi_{e,sys}$ , to find the equivalent period  $T_e$  and the base shear  $V_{base}$  through formulas (3.6) and (3.7).

### 3.4 COMMENTS ON EQUIVALENT LINEAR SYSTEM CONCEPT

The direct displacement based design is characterized by use of auxiliary SDOF structure, which reproduces the structural response of the multiple degree of freedom system in base shear and overturning moment evaluation assuming fundamental mode response. Given the definition of the SDOF in terms of equivalent height  $h_e$  and equivalent mass  $m_e$  as shown in Fig.(3.1), we assume that it can be modeled using a linear stiffness, representative of the secant to the design displacement. Moreover, this design stiffness is a function of the effective damping in the structure, which is assumed to represent the effects of the dissipations and of all the nonlinearities in the system.

Therefore, the equivalent secant stiffness and the equivalent viscous damping play a very important role in the DDBD approach. Anyway, in the most common cases, we base the design procedure on the equivalent damping computation through *approximate charts*, like the one shown in Fig.(3.3). Then we reduce the displacement spectra ordinates using *approximate* and *simplified reduction factors* like the one presented in (3.5).

Previous investigations prove that this approach produces good results in acceptable structural design, for which the previous *approximate* models have been calibrated. Nevertheless we want to focus on something new, which is a new device using an advanced material with a nonlinear force-displacement relation which is not very common in traditional seismic engineering design field. Hence we have to evaluate in detail the models we are supposed to use in order to judge if they are suitable or not even for our advanced material device design. Of course this does not mean to want to propose changes in the DDBD formulation, but rather have a critical look at its main assumption. In order to perform this evaluation we concern about the basis of the *equivalent linear structure concept*.

### 3.4.1 *Initial stiffness formulation*

The equivalent linear system concept has been proposed for the first time by Jacobsen (Jacobsen 1930). In his work an equivalent linear system with effective damping was proposed to approximate the steady state response of a damped nonlinear system. Advantages in using the linear equation instead a nonlinear one are mainly related to the simplification of the equation, provided that the equivalent viscous damping is feasible to represent the effects of all the sources of dissipation in the structure. In his first formulation anyway the equivalent viscous damping concept considers a linear SDOF system characterized by the initial stiffness of the real system.

The original basic assumptions in (Jacobsen 1930) were:

- both systems have the same initial period: therefore the stiffness of the linear system is equal to the initial stiffness of the nonlinear system;
- both systems undergo harmonic steady state response given by a constant amplitude sinusoidal function of the form  $p(t) = p_0 \sin(\omega_n t)$ , being  $\omega_n$  the natural frequency of the system, which is at resonance;
- the goal is to get a linear system which is going to dissipate the same amount of energy per cycle than the original nonlinear one.

In structural design cases, these assumptions are not typically met. During real earthquakes the frequency content is varied, hence quite far from the hypothesis of a single excitation frequency and of course the response is not harmonic. Moreover, maximum displacement is often reached before the transient response damps out.

### 3.4.2 *Mathematic Derivation of the Equivalent Damping Expression for a Linear SDOF System*

Provided that the single degree of freedom system is characterized by a linear force-displacement relation a mathematical derivation of the equivalent damping expression can be performed, as reported in (Chopra 2006). Looking at a single degree of freedom system, characterized by a mass  $m$ , a stiffness  $k$  and a damping coefficient  $c$ , being  $u(t)$ ,  $\dot{u}(t)$  and  $\ddot{u}(t)$  respectively the displacement, the velocity and the acceleration of the system, function of time, the dynamic equation of motion is given by:

$$m\ddot{u}(t) + c\dot{u}(t) + ku(t) = p(t) \quad (3.16)$$

Considering a steady state condition due to the external load  $p(t) = p_0 \sin(\omega t)$  being the external load frequency  $\omega$  and the system fundamental frequency  $\omega_n$ , the energy dissipated by the viscous damping  $E_D$  in one cycle of harmonic vibration is:

$$\begin{aligned} E_D &= \int_0^{\frac{2\pi}{\omega}} c \dot{u}^2(t) dt = c \int_0^{\frac{2\pi}{\omega}} [\omega u_0 \cos(\omega t - \phi)] dt = \\ &= \pi c \omega u_0^2 = 2\pi \xi \frac{\omega}{\omega_n} k u_0^2 \end{aligned} \quad (3.17)$$

in which the energy dissipated is proportional to the square of the amplitude of motion  $u_0$  and is increasing linearly with the increasing of the excitation frequency.

On the other side, the external force inputs an energy to the system which for each cycle of vibration is given by:

$$\begin{aligned} E_I &= \int_0^{\frac{2\pi}{\omega}} p(t) \dot{u}(t) dt = \int_0^{\frac{2\pi}{\omega}} p_0 \sin(\omega t) [\omega u_0 \cos(\omega t - \phi)] dt = \\ &= \pi p_0 u_0 \sin(\phi) \end{aligned} \quad (3.18)$$

It can be demonstrated that the two energy quantities are equal at the steady state  $u_0$  while  $E_I(u^*) > E_D(u^*)$  for  $u^* < u_0$  and  $E_I(u^*) < E_D(u^*)$  for  $u^* > u_0$ . When steady state is reached,  $\phi = 90$  and equation (3.18) become:

$$E_I = \pi p_0 u_0 \quad (3.19)$$

Equating (3.17) with (3.19) we get:

$$u_0 = \frac{p_0}{c \omega_n} \quad (3.20)$$

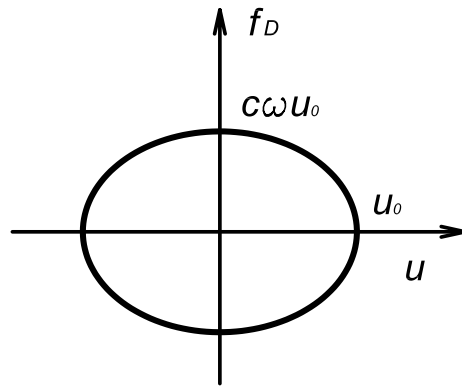
The graphical interpretation of the energy dissipated in viscous damping can be found expressing the damping force  $c \dot{u}(t) = f_D(t)$  as:

$$\begin{aligned} c \dot{u}(t) = f_D(t) &= c \omega u_0 \cos(\omega t - \phi) = \\ &= c \omega \sqrt{u_0^2 - u(t)^2} \sin^2(\omega t - \phi) = c \omega \sqrt{u_0^2 - [u(t)]^2} \end{aligned} \quad (3.21)$$

which leads to:

$$\left( \frac{u(t)}{u_0} \right)^2 + \left( \frac{f_D(t)}{c \omega u_0} \right)^2 = 1 \quad (3.22)$$

This is the equation of the hysteresis loop that in the plane displacement-force is an ellipse, as shown in Fig.(3.9).

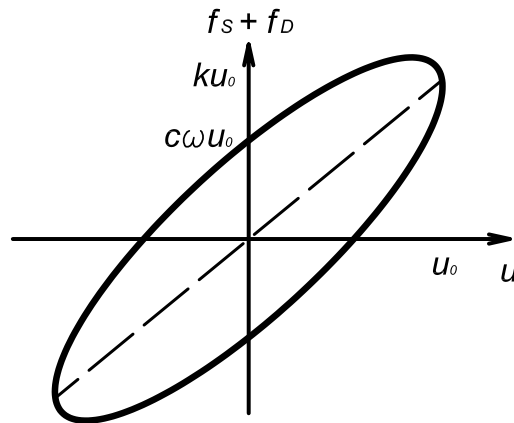


**Figure 3.9:** viscous damper hysteresis loop.

If we want to analyze the expression of the total resisting force, which means elastic resisting force  $f_S$  plus damping resisting force  $f_D$ , we would have:

$$ku(t) + c\dot{u}(t) = f_S + f_D = ku + c\omega\sqrt{u_0^2 - [u(t)]^2} \quad (3.23)$$

and the relative hysteresis loop, having in parallel two elements, a viscous damper and a linear stiffness usually defined as *Kelvin model* is shown in Fig.(3.10).



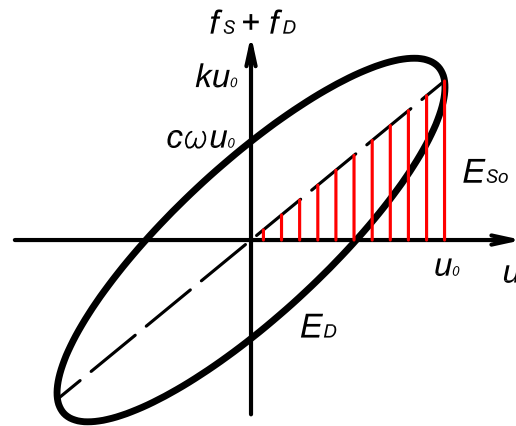
**Figure 3.10:** linear spring and viscous damper in parallel (Kelvin model) hysteresis loop.

In both the cases, the area enclosed in the ellipse is equal to the dissipated energy and is given by:

$$E_D = \pi(u_0)(c\omega u_0) = \pi c\omega u_0^2 \quad (3.24)$$

which is the same expressed previously. Referring to equation (3.17), it can be rearranged as:

$$\xi = \frac{E_D}{4\pi \frac{\omega}{\omega_n} k u_0^2} \quad (3.25)$$



**Figure 3.11:** dissipated energy  $E_D$  and strain energy  $E_{S_0}$  in a Kelvin model.

Looking at the hysteresis loop of the total resisting force in Fig.(3.11), we recognize that the strain energy which is dissipated at each cycle of motion is the lined area, which can be expressed as:

$$E_{S_0} = \frac{ku_0^2}{2} \quad (3.26)$$

and substituting the (3.26) into the (3.25) it is possible to express the specific damping factor, in case of resonance,  $\omega = \omega_n$ , as:

$$\xi = \frac{E_D}{2\pi E_{S_0}} \quad (3.27)$$

that can also be interpreted as:

$$\xi = \frac{1}{2\pi} \left( \frac{\text{Work done in half a cycle}}{\text{Work done under skeleton curve}} \right) \quad (3.28)$$

in which the skeleton curve considered in the previous is a curve given by the positive and by the negative envelope of the hysteresis cycles.

This procedure is commonly applied to model the damping in MDOF systems assuming that, regardless the constitutive law we are considering, the dissipated energy is given by the area enclosed in the hysteresis and the strain energy is defined as a function of the maximum force and displacement in the system.

As a conclusion of the analytical derivation of the expression, it is clear that this widely used formula in (3.27) is formally correct only for the cases in which the following hypothesis are verified:

- steady-state condition

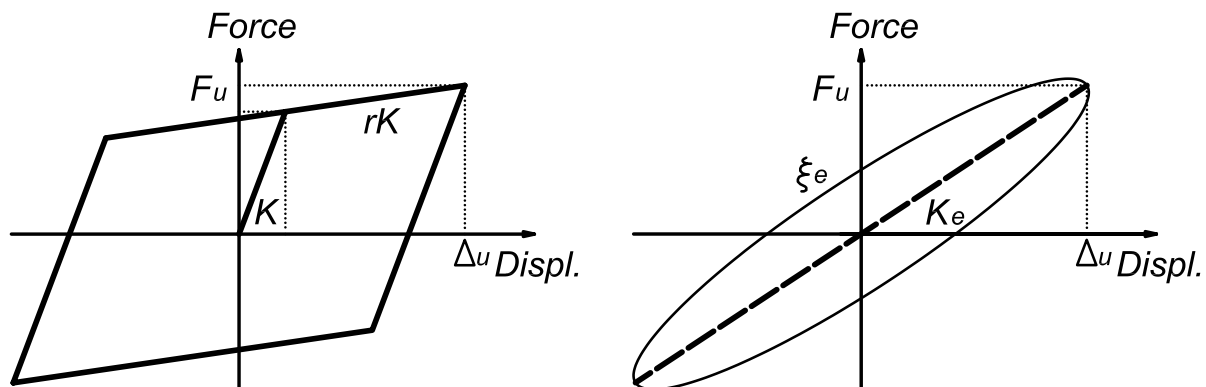
- resonance
- maximum displacement cycle

Therefore every application in other conditions is formally an approximation bringing some larger or smaller amount of error.

### 3.4.3 Period Shift in Secant Stiffness Formulation

Rosenblueth and Herrera (Rosenblueth and Herrera 1964) modified the Jacobsen's approach (Jacobsen 1960) equating the energy dissipated in a cycle of nonlinear hysteresis with the same quantity for a linear viscoelastic system at resonance: in this formulation they modeled the equivalent linear system considering an *effective stiffness* given by the secant stiffness to the point of maximum displacement on the hysteresis loop.

For the sake of simplicity the representation of the maximum response of a nonlinear system by a linear viscous elastic system results to be extremely favorable. Even if this approach leads to significant errors, it has been widely used in the past as a first order level of approximation to estimate the damping of an equivalent SDOF system for design purpose (Priestley, Calvi, and Kowalsky 2007), and constitutes the basis of several code design procedures.



**Figure 3.12:** equivalent system concept as applied in secant equivalent stiffness: original non-linear system (left); equivalent SDOF with additional damping (right).

As a matter of the use of a stiffness  $K_e$  which is typically smaller than the initial one  $K$ , as shown in Fig.(3.12), this procedure is characterized by a period shift, constant for all the hysteresis relations.

Considering the displacement ductility  $\mu$  as defined in equation (3.4), the period shift of the

equivalent system is:

$$\frac{T_e}{T} = \sqrt{\frac{\mu}{1 + r\mu - r}} \quad (3.29)$$

being  $T$  the period computed through the initial stiffness of the real stiffness.

Given the assumption of use a SDOF characterized by the use of the secant stiffness, previous investigations have developed optimized methods to compute the hysteretic contribution for the equivalent viscous damping in the equivalent linear system. Some of the most relevant are presented in the following.

- (Gulkan and Sozen 1974). Using experimental results and Takeda's hysteretic model, it was suggested to compute equivalent damping for reinforced concrete columns considering the following expression:

$$\xi_{hyst} = 0.2 \left( 1 - \frac{1}{\sqrt{\mu}} \right) \quad (3.30)$$

Results of this approach with experimental data and with Jacobsens approach have been compared, and found them to be in good agreement.

- (Dwairi, Kowalsky, and Nau 2007). The hysteretic component of the response can be estimated by the expression:

$$\xi_{hyst} = C \frac{\mu - 1}{\mu\pi} \quad (3.31)$$

in which  $C$  is a function of the hysteresis rule. In this analysis authors have investigated the following force-displacement relation: elastoplastic, two different kinds of Takeda's hysteresis and flag-shape.

- (Grant, Blandon, and Priestley 2005). The hysteretic contribution has been estimated considering a formula like:

$$\xi_{hyst} = a \left( 1 - \frac{1}{\mu^b} \right) \left( 1 + \frac{1}{(T_e + c)^d} \right) \quad (3.32)$$

in which the response is period dependent and parameters  $c$  and  $d$  are also function of the period, while parameters  $a$  and  $b$  are function of the hysteresis. The authors have considered in their work the elastoplastic relation, two Takeda's hysteresis, a Ramberg-Osgood and a flag-shape force-displacement relation.

### 3.4.4 Period Shift in Other Formulations

Other contributions have been based on the computation of optimized period shift and of optimized equivalent viscous damping. Therefore in this class of cases the equivalent SDOF is *not characterized by the equivalent secant stiffness* to the maximum displacement point. The following results are reported:

- (Iwan and Gates 1979). Applying a statistical regression to different hysteresis models and considering different ground motions, minimizing the mean square of the error between nonlinear and linear systems, the estimations of effective period and damping have been computed as a function of the ductility:

$$\frac{T_e}{T} = 1 + 0.121 (\mu - 1)^{0.939} \quad (3.33)$$

$$\xi_{hyst} = 0.0587 (\mu - 1)^{0.371} \quad (3.34)$$

- (Kwan and Billington 2003). Following the same approach of the previous work, effective period and damping were estimated for models able to represent ductile steel and reinforced concrete structures as:

$$\frac{T_e}{T} = 0.8\sqrt{\mu} \quad (3.35)$$

$$\xi_{hyst} = (0.352\mu - 1) \xi_v + \frac{0.717\mu - 1}{\pi \mu} \quad (3.36)$$

- (Miranda and Lin 2003). Starting from several time histories analysis results, the authors expressed the new relation in terms of strength ratio  $R$  which is the ratio of the maximum lateral seismic force respect the yielding strength of the structure:

$$R = m \frac{S_a}{F_y} \quad (3.37)$$

being  $m$  the mass of the system,  $S_a$  the spectral acceleration and  $F_y$  the yielding force. Estimations of equivalent period shift and damping are:

$$\frac{T_e}{T} = 1 + (R^{1.8} - 1) \left( 0.027 + \frac{0.01}{T^{1.6}} \right) \quad (3.38)$$

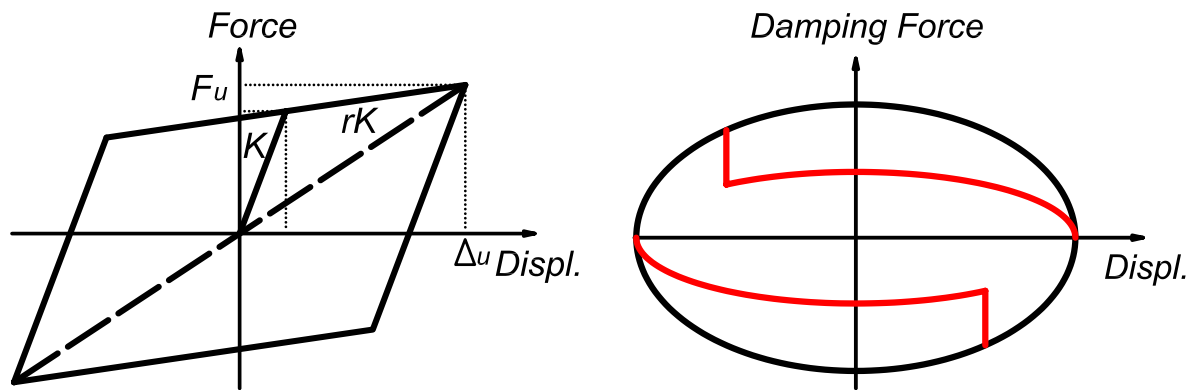
$$\xi_{hyst} = (R - 1) \left( 0.02 + \frac{0.002}{T^{2.4}} \right) \quad (3.39)$$

### 3.4.5 Elastic damping component

The elastic damping is used in the inelastic time history analysis to represent damping not captured by the hysteretic model. The damping coefficient in the equation of motion (3.16) is a function of the stiffness of the system:

$$c = 2\xi\sqrt{mk} \quad (3.40)$$

therefore the damping force depends on which is the stiffness we consider. In most inelastic analysis the initial stiffness is adopted in all the analysis. In the formulation of the DDBD given in (Grant, Blandon, and Priestley 2005) and (Priestley, Calvi, and Kowalsky 2007) it is suggested to use the tangent stiffness to compute the damping coefficient in (3.40).



**Figure 3.13:** elastic damping force evaluation (right) for a nonlinear hysteresis (left).

If we consider a damping coefficient proportional to the initial stiffness, this choice leads to a constant  $c$  coefficient and a circular damping force in the displacement-damping force plane as shown in Fig.(3.9) and in the external envelope of Fig.(3.13). If we consider a tangent stiffness proportional damping, it leads to a not constant  $c$  coefficient computed as a function of the tangent stiffness  $k_t$  like:

$$c = A + \beta k_t \quad (3.41)$$

in which  $A$  and  $\beta$  are constants different as a function of the damping model adopted. Graphically it is producing a damping force as a function of the displacement represented by the internal envelope of Fig.(3.13).

Because of this, (Priestley, Calvi, and Kowalsky 2007) introduced a correction factor  $\kappa$  to change the influence of the elastic damping in the equivalent damping expression considering the different assumption in using initial or tangent stiffness proportional elastic damping:

$$\xi_e = \kappa\xi_v + \xi_{hyst} \quad (3.42)$$

the parameter  $\kappa$  is a function of the displacement ductility and of the hysteresis. For practical design it is acceptable to consider a constant value for elastic damping  $\xi_v$  between the 2% and the 5% and an unitary value for parameter  $\kappa$ .

### ***3.4.6 Conclusions on Equivalent Linear System Concept Evaluation***

The use of the equivalent single degree of freedom system in displacement based design is a feasible strategy to simplify the design problem.

The previous investigation underlines anyway that this is not the only possibility to model a linear system equivalent to the original system. In particular, researches have stated the following conclusions:

- to characterize an equivalent SDOF system the effective stiffness can be computed considering different models; every model is characterized by different damping evaluation expressions;
- even if we decide to use the secant stiffness, different damping relations exist and most of them have been computed considering statistical regression;
- if we use the Jacobsen method to compute the hysteretic damping, which has been demonstrated to be theoretically grounded, we have to consider that in seismic engineering most of the base assumptions are not verified;
- uncertainties are related also to the damping elastic component computation.

In this context, a further difficulty exists for innovative systems.

Let us assume that given a new hysteresis relation we want to characterize it considering the *secant stiffness*, because this is more related to the structural information than other methods and we want to be consistent with the DDBD. Still, there are no evidences that the relations presented in the previous sections are working for the new case. In fact they have been computed using numerical regression and are not suitable for a different of systems (we typically cannot use statistical regression data to perform extrapolations).

The only way we have in general to estimate the effective damping is the Jacobsen hysteresis-area based method; in this case anyway we know that the original assumptions lead some errors.

Because of the previous, as a general conclusion of the chapter, we decide to follow the DDBD procedure for the isolation system design considering the secant stiffness. Nevertheless we also need to investigate the suitability of effective damping models evaluation for the new system.

## 4. SHAPE MEMORY ALLOYS

### 4.1 INTRODUCTION

Shape memory alloy (*SMA*) is a novel functional material with increasing applications in many areas, recently also in response control of civil structures (Song, Ma, and Li 2006).

SMA's have demonstrated energy dissipation capabilities, large elastic strain capacity, hysteretic damping, good high and low-cycle fatigue resistance, recentering capabilities and excellent corrosion resistance. All of these characteristics give SMA's great potential for use within seismic resistant design and retrofit applications.

In this chapter we present an overview of the SMA physical and mechanical properties, summarizing the last years research results (Desroches and Smith 2003).

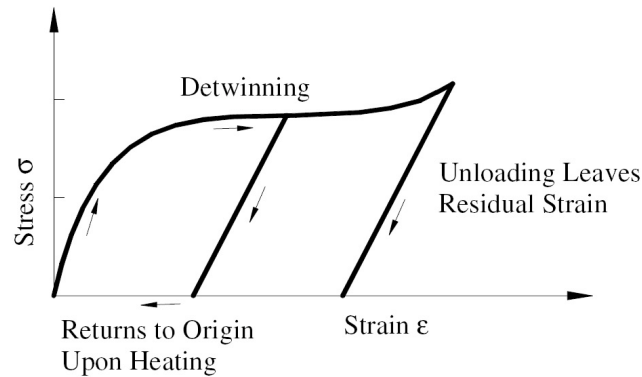
### 4.2 BASICS ABOUT SHAPE MEMORY ALLOYS

The first record of the shape memory transformation was the observation of a reversible phase transformation in the gold-cadmium (AuCd), but the shape memory effect was discovered in the nickel -titanium (the material was named *Nitinol*). Since then, many types of shape memory alloys have been discovered. Among the various alloys, Nitinol possesses superior thermo-mechanical and thermo-electrical properties and is the most commonly used SMA. In this work, SMA's are referred to as Nitinol SMA's.

#### 4.2.1 *Shape Memory and Superelastic Effects*

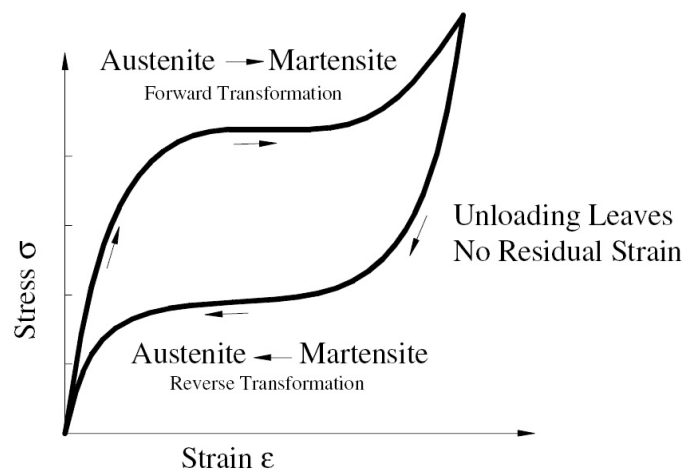
The most important properties showed by the SMA are the *shape memory* and the *superelastic effects*. These unique properties are the result of reversible phase transformations of SMA's.

There are two crystal structure phases in SMAs: the austenite one, stable in high temperature, and the martensite one, stable in low temperature. The austenite has a body-centered cubic crystal structure, while the martensite has a parallelogram structure (which is asymmetric).



**Figure 4.1:** idealized stress-strain curve for shape memory effect [from (Desroches and Smith 2003)].

In its low temperature phase, SMAs exhibit the shape memory effect (SME). When SMAs in martensite are subjected to external stress, they deform through a so-called detwinning mechanism. Originally in its martensitic form, the SMAs are easily deformed to several percent strain. Unloading results in a residual strain, as shown in Fig.(4.1) and reported in (Desroches and Smith 2003).



**Figure 4.2:** idealized stress-strain curve for superelastic effect [from (Desroches and Smith 2003)].

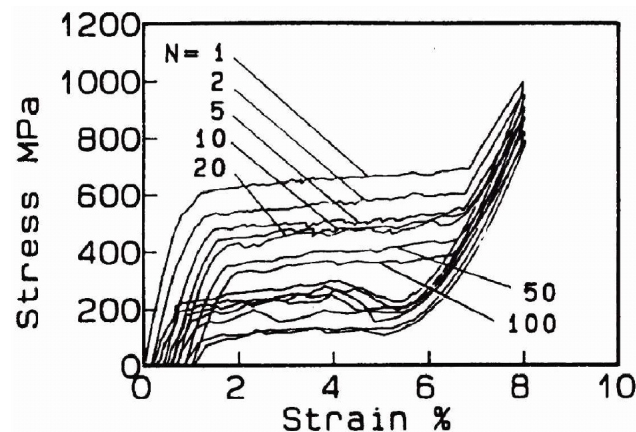
Heating the previously deformed specimen above a determined temperature results in phase transformation, and a recovering of the original shape (removal of the residual strain).

In its high temperature form, SMAs exhibit a superelastic effect. Originally in austenitic phase, martensite is formed upon loading beyond a certain stress level, resulting in the stress plateau shown in Fig.(4.2), reported in (Desroches and Smith 2003). However, upon unloading, the martensite becomes unstable, resulting in a transformation back to austenite and the recovery of the original, undeformed shape.

#### 4.2.2 Other Mechanical Properties of Shape Memory Alloys

The other mechanical properties of SMAs, as well as how they vary under different conditions, need to be understood before evaluating the potential and effectiveness of SMAs within seismic retrofit applications.

(a) **Cyclical Behavior Properties.** Fig.(4.3) shows a stress-strain diagram of a Nitinol SMA wire in its Austenitic phase subjected to cyclical loads. Several observations could be made from the figure.

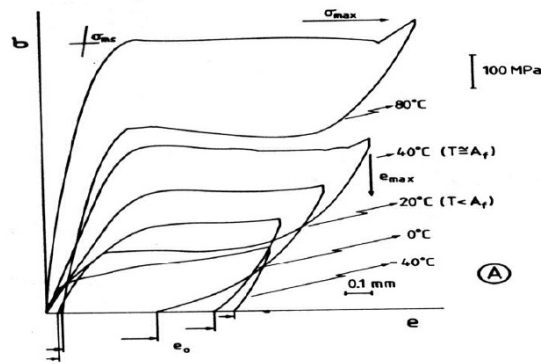


**Figure 4.3:** stress-strain hysteresis of superelastic NiTi bars [from (Kaounides 1995)].

First, repeated cyclical loading leads to gradual increases in the residual strains. This results from the occurrence of microstructural slips during the stress-induced martensitic transformation, which causes residual strains and internal stresses. The other observation is that the forward transformation stress decreases for increasing number of cycle. This also occurs because of the microstructural slips, which inhibits the formation of stress-induced martensite upon additional cycling. As a result, the martensitic forward transformation stress is reduced. Following the same logic, the stress required to induce the reverse transformations is also reduced by repeated cycling. However, the reduction in the reverse transformation is less than that in the

forward phase transformation. The degradation of the cyclical properties of the SMAs, known as fatigue, can be improved. In fact training, which consists of pre-cycling of the specimen, decreases the fatigue effect, as demonstrated in (Desroches and Smith 2003).

**(b) Temperature Effects.** Temperature is likely the single most important factor when predicting the behavior of shape memory alloys. The shape memory process is a thermo-elastic process, meaning that a decrease in temperature is equivalent to an increase in stress. Therefore, as the temperature decreases, an increase in stress results, thereby a lower stress value is required to induce transformation, as shown in Fig.(4.4). A specimen tested at low temperature will exhibit the shape memory effect, while the same specimen tested at a high temperature may exhibit the superelastic effect. This can pose significant design issues if the operating temperature of SMAs is not known within a reasonable bound.



**Figure 4.4:** temperature dependent force-displacement response of superelastic NiTi [from (Strnadel, Ohashi, Ohtsuka, Ishihara, and Miyazaki 1995)].

### 4.2.3 Potentials of SMA in Seismic Engineering Applications

The unique properties of shape memory alloys make them an ideal candidate for use as devices for seismic resistant design and retrofit. Experimental and analytical studies of shape memory alloys show that they are an effective mean of improving the response of buildings and bridges subjected to seismic loading. The re-centering potential of superelastic shape memory alloys is one of the most important characteristic that can be exploited for applications in earthquake engineering. The ability to undergo cyclical strains greater than 6%, with minimal residual strain (typically less than 1%), has been shown to be useful as bracing elements in buildings, and as restraining elements in bridges. Furthermore, the recentering capabilities appear to be independent of the diameter of the specimen and insensitive to the strain rate of the loading (Song, Ma, and Li 2006).

## 5. FEASIBILITY OF SMA TECHNOLOGY FOR SEISMIC ISOLATION APPLICATION

### 5.1 INTRODUCTION

The objective of this chapter is to investigate the possibility of using *shape memory alloys* in seismic isolation devices and to evaluate its effectiveness in reaching the structural design goals, compared with traditional isolation devices.

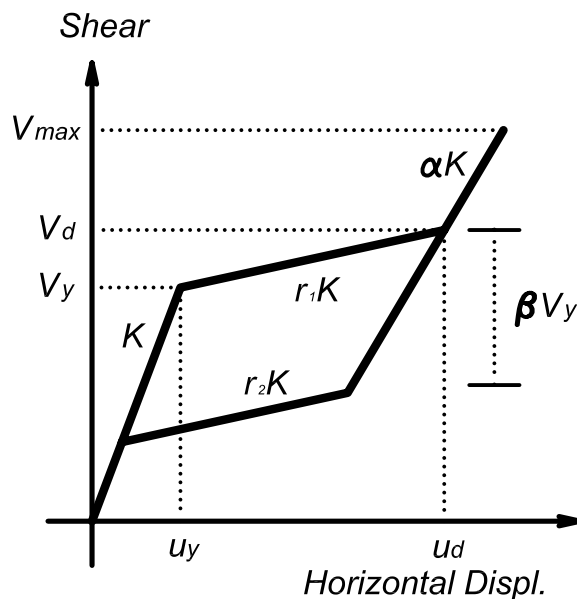
The term *shape memory alloys device* refers to a bearing systems characterized by a non-linear horizontal force-displacement relation which can be described by a *flag-shape* hysteresis.

We assume a bearing system is used to provide a horizontal base shear as a function of displacement like the one shown in Fig.(5.1). This force-displacement relation is supposed to be given by the superelastic effect of shape memory alloys eventually coupled with other sources of stiffness.

The key parameters characterizing the nonlinear behavior of the device (Fig.(5.1)) are:

- $K$ : initial lateral stiffness for the system, relative to the first shape memory alloy stiffness contribution and, eventually, to the other stiffness sources;
- $V_y$ : lateral force corresponding to the reaching of the device linear limit; it can be interpreted as the shear that produces the initial transformation in the shape memory alloys;
- $u_y$ : lateral displacement corresponding to reaching of the linear limit of the force-displacement relation for the device;
- $V_d$ : lateral force corresponding to reaching of the end of plateau limit; it can be interpreted as the shear at the end of transformation in the shape memory alloys;
- $u_d$ : lateral displacement corresponding to reaching of the end of plateau limit;

- $r_1K$ : lateral stiffness for the system after reaching the shape memory alloy elastic limit loading, taking also in account, eventually, the other stiffness sources;  $r_1$  is the fraction of the loading second stiffness respect the first one;
- $\alpha K$ : lateral stiffness for the system after reaching the shape memory alloy second elastic limit at the end of the phase transformation;  $\alpha$  is the fraction of the unloading second stiffness respect the initial one;
- $r_2K$ : lateral stiffness for the system after reaching the shape memory alloy elastic limit unloading, taking also in account, eventually, the other stiffness sources;  $r_2$  is the fraction of the unloading second stiffness respect the initial one;
- $\beta V_y$ : the lateral force difference between the level of force at which the first transformation (when it is loaded) occurs and the level of force at which the second transformation (when it is unloaded) occurs;  $\beta$  is the fraction of the  $V_y$  lateral force;
- $V_{max}$ : the maximum lateral force which the device can stand without breaking.



**Figure 5.1:** parameters for the SMA superelastic force-displacement model.

The device we consider behaves in the same way both in tension and in compression, which implies the force-displacement relation is symmetric respect the origin between first and third quadrant.

In order to define the main features, underline the drawbacks and eventually be able to examine the advantages of an isolation system characterized by a lateral force-lateral displacement

relation as the one shown in Fig.(5.1), we want to compare the response we can get from a system with this hysteresis with the one we would get if we were considering one of the "classic" isolation bearing systems. In order to perform this, we consider as a reference parameter the response of a lead rubber bearing (*LRB*).

## **5.2 SMA TECHNOLOGY ISOLATION DEVICE DESIGN**

To evaluate the advisability in using a SMA technology in seismic base isolation we assume to be able to design and manufacture a SMA bearing based on the superelastic effect for the horizontal force-displacement relation. At this first stage of work, since we are still investigating the feasibility of the concept, the device has been defined just in terms of hysteresis rule, without analyzing the real technology able to provide that hysteresis. The practical design of an actual isolation bearing device with suitable properties would be a further step if this numerical investigation provides good results.

### ***5.2.1 Goal of the Design Process***

We perform the research taking into account a SMA bearing device with *equivalent* properties respect an existing nonlinear isolator. Obviously the SMA is characterized by a different force-displacement relation with respect to traditional isolation bearings, but it has the same yielding and design forces, and the same yielding and design displacements with respect to a traditional device. Therefore in this context, the concept of equivalence involves that the two different nonlinear hysteresis are characterized by the same initial and second stiffness and the same yielding force and strength. This choice affects the secant stiffness computation according the DDBD approach design philosophy; hence even effective periods are the same and from a DDBD point of view the only difference between the traditional bearing and the actual isolation device is the hysteretic energy dissipation.

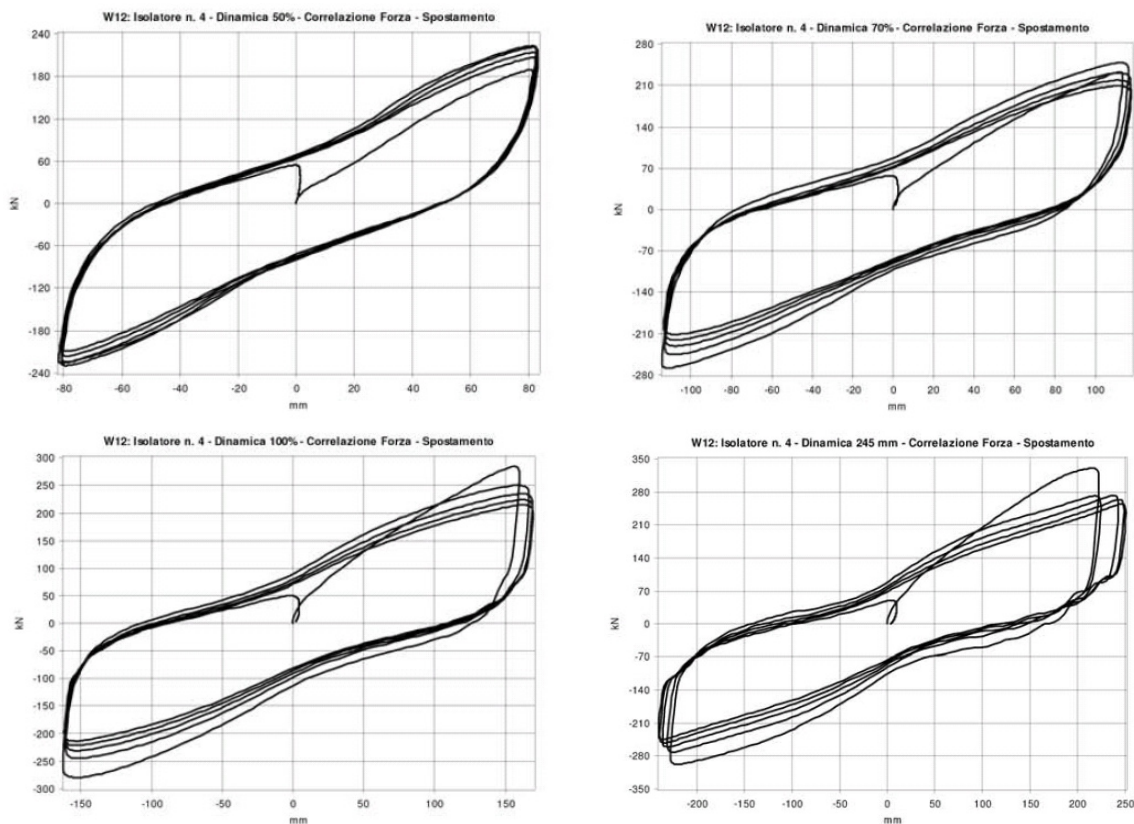
### ***5.2.2 Reference Isolator Device***

The isolator we consider as a starting point for the referring parameters is an actual lead rubber bearing, which has been fully characterized by an experimental campaign. It is produced by *AGOM International srl* and the nominal parameters used for the design purpose are listed in Tab.(5.1). For the practical design, following the displacement based design approach, in

**Table 5.1:** nominal design properties of reference lead rubber bearing diameter 500 mm (courtesy *AGOM International srl*).

<i>LRB 500</i>	
diameter	<b>500 mm</b>
effective horizontal stiffness	<b>1.62 kN/mm</b>
seismic comb. vertical load	<b>1653 kN</b>
seismic design displacement	<b>162 mm</b>
hysteretic damping ratio	<b>28%</b>

Tab.(5.1) the property definition of the devices is based on the secant stiffness and the equivalent damping coefficient.



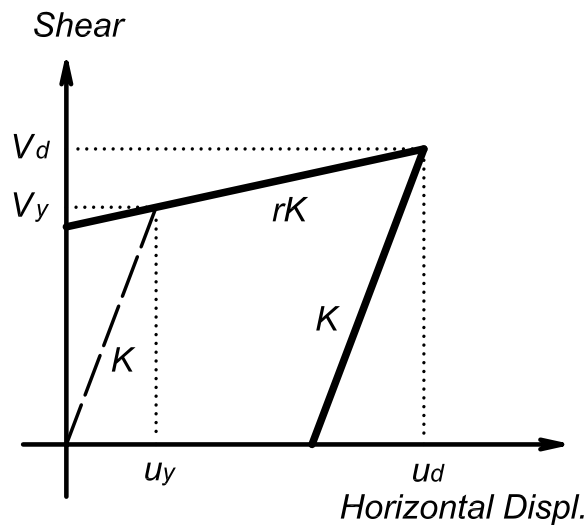
**Figure 5.2:** force-deformation relations for LRB 500 from experimental tests at different displacement levels: 50% (top left), 70% (top right), 100% (bottom left), 150% (bottom right) of the design displacement (courtesy *AGOM International srl*).

Results of experimental tests carried on the bearings are shown in Fig.(5.2). Looking at this figure, we can conclude that the lead core contribution provides a large and highly dissipating hysteresis. In fact this device is characterized by a nominal hysteretic damping equal to 28% (as reported in Tab.(5.1)) which is the damping computed from the hysteresis area evaluation,

following the approach given in formula (3.27) and recalling Fig.(3.11).

**Table 5.2:** elastoplastic model parameters for lead rubber bearing diameter 500 mm [following the symbols in Fig.(5.3)] (courtesy *AGOM International srl*).

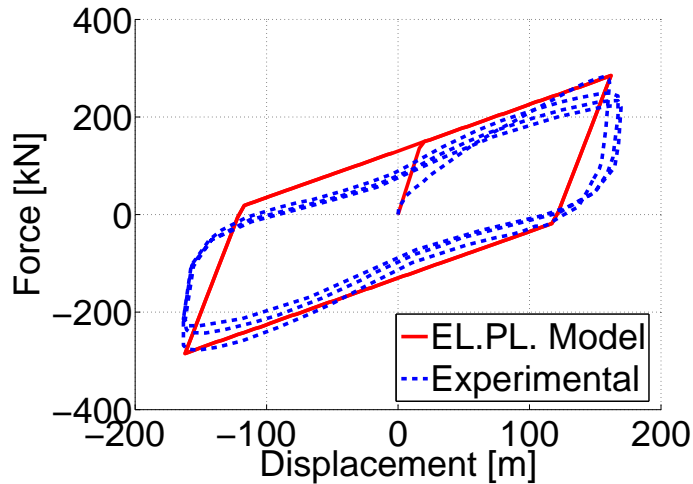
<b>LRB 500</b>		
yielding shear	$V_y$	<b>147 kN</b>
design shear	$V_d$	<b>262 kN</b>
yielding displacement	$u_y$	<b>17.5 mm</b>
design displacement	$u_d$	<b>162 mm</b>
initial stiffness	$k$	<b>8.4 kN/mm</b>
second stiffness	$rk$	<b>0.8 kN/mm</b>



**Figure 5.3:** LRB elastoplastic model parameters.

The behavior of this device is usually described considering an elasto-plastic force-displacement relation (as already we mentioned in section 2.4.2). Hence in addition to properties in Tab.(5.1), the manufacturer provides parameters reported in Tab.(5.2) to model the isolator using a non-linear elastoplastic force-displacement relation.

A plot of the force-displacement relation of the model and comparison with experimental test results is shown in Fig.(5.4). Elastoplastic model is clearly an approximation of the real behavior of the isolator. In particular, the comparison with the experimental results shows that the elastoplastic model does not estimate the initial stiffness nor the degradation well. However, for the representation of the general characteristics of the devices, the adopted model is acceptable, being exact in terms of secant stiffness at the design displacement and giving a good estimation, even if not exact, of the hysteretic energy dissipated and of residual displacements.



**Figure 5.4:** force-deformation relations for LRB 500: comparison of experimental test and elastoplastic model (experimental data and model parameters have been provided by *AGOM International srl*).

### 5.2.3 Equivalent SMA Isolator Device

We simulate the idealized design of an equivalent SMA isolator considering the properties of the lead rubber bearing in previous subsection. Starting from the elastoplastic model of the actual device as described in Tab.(5.2) we use an *equivalent* flag-shape model referring to the hysteresis in section 5.1. Consistently with Fig.(5.1), we describe SMA device force-displacement relation using parameters summarized in Tab.(5.3).

**Table 5.3:** flag-shape model parameters for SMA bearing equivalent to LRB diameter 500 mm [parameters as shown in Fig.(5.5)].

<i>SMA eq. LRB500</i>		
yielding shear	$V_y$	<b>147 kN</b>
design shear	$V_d$	<b>262 kN</b>
yielding displacement	$u_y$	<b>17.5 mm</b>
design displacement	$u_d$	<b>162 mm</b>
initial stiffness	$k$	<b>8.4 kN/mm</b>
second stiffness	$rk$	<b>0.8 kN/mm</b>

With respect to model in Fig.(5.1) we consider  $r_1 = r_2 = r$ , which means that the device has the same stiffness for loading and unloading in the flag-shape plateau, and  $\alpha = 1$ , which means the final stiffness is the same as the initial. Moreover we assume a large ductility available in the flag-plateau, so that the final hardening occurs far away from the area of displacement we

care about. Fig.(5.5) depicts the force-deformation relationship based on Fig.(5.1) given these assumptions.

Finally, we take into account different *dissipation* capabilities of the flag-shape hysteresis. Hence we introduce the  $\beta$  parameter, measure of the ratio of dissipation, which is a free parameter according to which investigate differences in the response.

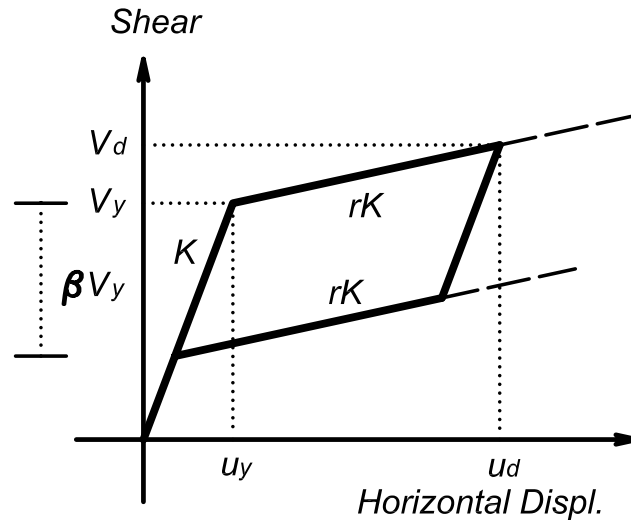


Figure 5.5: SMA model parameters.

### 5.3 FLAG-SHAPE HYSTERESIS REDUCTION FACTOR ESTIMATION USING THE EQUIVALENT DAMPING APPROACH

Consistent with previous method presentation, we follow the DDBD procedure to evaluate the design and the response of the ideal SMA isolation system and comparison with actual LRB. In this context, the damping modeling and estimation is a key point in the isolation devices design because it strongly affects the structural displacement demand. Moreover in our analysis and comparison, we consider two systems with the same secant stiffness, because the design displacement and shear are the same, and initial and second stiffness are also the same; hence in a displacement based approach the most important difference is given by the damping ratio.

Hysteretic damping estimation of elastoplastic model is very common in DDBD. On the other hand, a procedure to estimate the hysteretic damping for a flag shape relation is more difficult to find in literature. Investigations on flag-shape consistently with the SDOF secant stiffness formulation have been performed in (Dwairi, Kowalsky, and Nau 2007) and in (Grant, Blandon, and Priestley 2005). However, we think these damping relations are not applicable in this analysis because of the statistical regression procedure used to derive them. In fact in these

investigations, flag-shape force-displacement relation is used to model other structural applications than the isolation one. Rather they used it to model hybrid post-tensioned systems. Formally they are characterized by the same hysteresis but also by a range of ductility and  $\beta$  factor completely different with respect to the case we consider for seismic isolation. In the regressions for post-tensioned applications the ductility demand is supposed to be smaller than the isolation ductility demand; in the case of hybrid system the  $\beta$  value is limited in order to guarantee a restoring force for rocking, while in the isolation we accept larger values to increase the dissipation.

Therefore, considering that the relations are highly nonlinear, the extrapolation, that is the application of those to an interval larger than the one for which they have been computed, is not valid. The only reasonable way to estimate the hysteresis about the different reduction factor due to the dissipation between the elastoplastic and the flag-shape model is to follow the equivalent area-based procedure presented in section 3.4.

### 5.3.1 *Hysteretic damping component estimation*

The two hysteresis have been described in the previous pictures: the elastoplastic model in Fig.(5.3), the flag-shape model in Fig.(5.5).

Considering expression (3.27) we can have a first order estimation of the differences between the effective damping:

$$\xi_{hyst} = \frac{2}{\pi} \frac{A_1}{A_2} \quad (5.1)$$

in which  $A_1$  is the area of the hysteresis skeleton curve and  $A_2$  is the area of the rectangle enveloping the hysteresis relation, as represented in Fig.(5.6) and Fig.(5.7). Defining the displacement ductility again as a function of the design and yielding displacements:

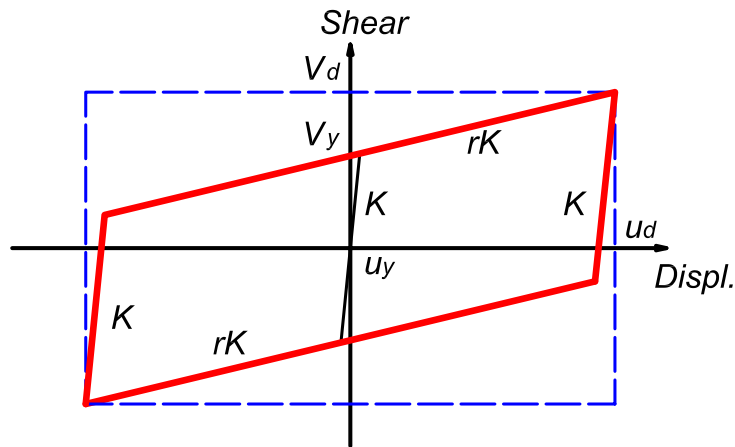
$$\mu = \frac{u_d}{u_y} \quad (5.2)$$

we compute the damping coefficient for the two cases.

For the elastoplastic model, referring to Fig.(5.6):

$$\begin{aligned} A_1 &= 2F_y(1-r) \cdot 2(\mu-1)u_y \\ A_2 &= 4\mu u_y [F_y + rk(\mu-1)u_y] \end{aligned} \quad (5.3)$$

$$\xi_{hystEP} = \frac{2}{\pi} \frac{(\mu-1)(1-r)}{\mu(1+r\mu-r)} \quad (5.4)$$

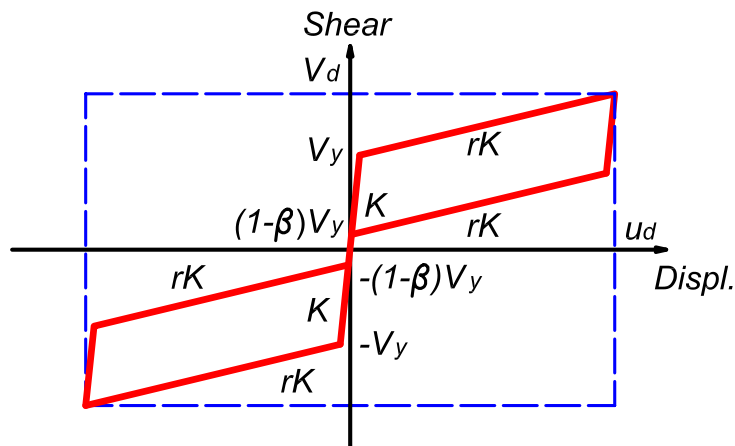


**Figure 5.6:** hysteretic damping component computation for LRB device following the area-based approach.

For the Flag-shape, referring to Fig.(5.7):

$$\begin{aligned} A_1 &= 2(\mu - 1)u_y \beta F_y(1 - r) \\ A_2 &= 4\mu u_y [F_y + rk(\mu - 1)u_y] \end{aligned} \quad (5.5)$$

$$\xi_{hystFS} = \frac{1}{\pi} \frac{\beta(\mu - 1)(1 - r)}{\mu(1 + r\mu - r)} \quad (5.6)$$

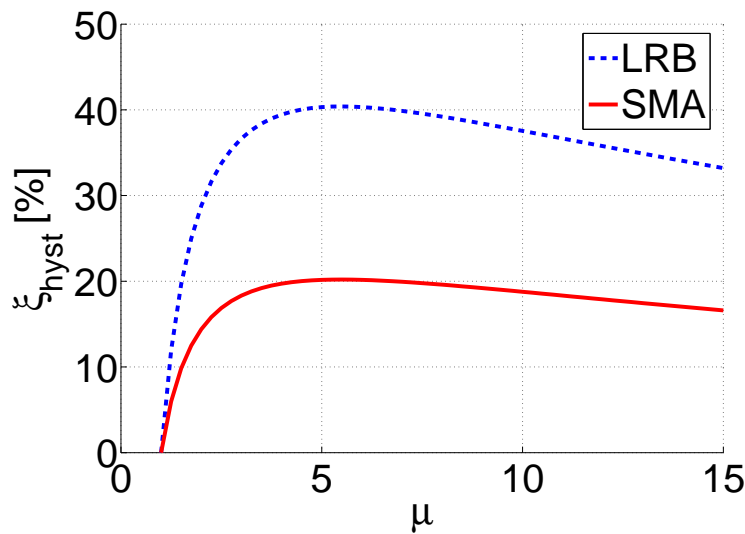


**Figure 5.7:** hysteretic damping component computation for SMA device following the area-based approach.

From the comparison of expressions (5.4) and (5.6), we conclude that the ratio between the two is a function of  $\beta$  if all the other parameters are kept constant in the two models. For  $\beta = 1$  formula (5.6) gives a damping ratio which is one half of the one given by the (5.4). This is shown in Fig.(5.8), in which for a constant  $r$  value and considering  $\beta = 1$ , we plot the hysteretic damping component computed according to the (5.4) and (5.6) as a function of displacement ductility  $\mu$ , up to the value  $\mu = 15$ .

Fig.(5.8) is unexpected if compared to Fig.(3.3). Fig.(3.3), limited to  $\mu = 6$ , shows a monotonically increasing damping coefficient with the ductility, while in the Fig.(5.8) the damping ratio decreases for high ductility values. Actually, the two plots (Fig.(3.3) and Fig.(5.8)) report the same behavior in the range of ductility  $\mu < 6$ . Moreover Fig.(5.8) underlines that the equivalent damping computed considering the area-based approach increases up to a  $\mu = 5$ , remains more or less constant till  $\mu = 6$  and then decreases. It seems odd that for large ductility the equivalent damping is smaller than for low ductility; probably the applicability of the approach have to be limited to the smaller  $\mu$  range.

In general this concept works for normal structure design, which are expected to experience a displacement ductility usually not larger than 6. Nevertheless, in an isolation system device we have to take into account even significantly larger ductility demands and in these cases the described approach results seem to be unrealistic.



**Figure 5.8:** hysteretic damping ratio comparison for elastoplastic and flag-shape model considering  $r = 5\%$  and  $\beta = 1$  from equations (5.4) and (5.6).

Fig.(5.9) shows the influence of hardening ratio  $r$  and ductility  $\mu$  in hysteretic component of damping ratio for the elastoplastic model. The same graph represents also the analogous result for flag-shape hysteresis, provided to multiply all the ordinates for a coefficient equal to  $\alpha_{fs} = 0.5\beta$ . Looking at Fig.(5.9), we can conclude that the ductility at which the damping value is maximum increases if the hardening ratio decreases; if  $r$  were very small, a system would experience no damping decreasing even for large  $\mu$  values. As a general comment concerning Fig.(5.9), if we change  $r$  and  $\mu$  we also change the secant stiffness of the system, so the graphs are applicable to the specified case just for the pointed hardening and ductility values. To evaluate the influence of dissipation parameter  $\beta$  in flag-shape and considering constant hard-

ening  $r = 0.05$ , we report the hysteretic component of damping ratio for flag-shape hysteresis in Fig.(5.10) as a function of ductility and of the  $\beta$  factor. From this we conclude that the  $\beta$  parameter does not influence the maximum damping ductility of the system.

### 5.3.2 Reduction Factor Computation

As described in section 3.2, referring to equation (3.5), we can use the equivalent damping to estimate a reduction coefficient for the design spectra.

There are several expression for the reduction factor. We follow the approach in (Priestley, Calvi, and Kowalsky 2007): two formulas are reported as a function of the seismic source distance with respect to the site.

For far field events we refer to the following:

$$R_{\xi 1} = \left( \frac{10}{5 + \xi_e} \right)^{0.5} \quad (5.7)$$

while for near field events we compute the reduction using:

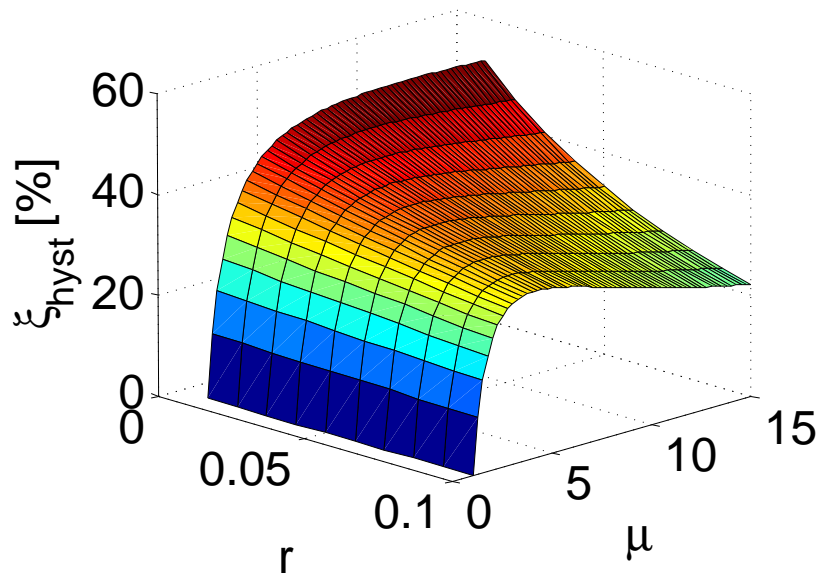
$$R_{\xi 2} = \left( \frac{10}{5 + \xi_e} \right)^{0.25} \quad (5.8)$$

In which  $\xi_e$  is given by the viscous elastic and hysteretic damping components:

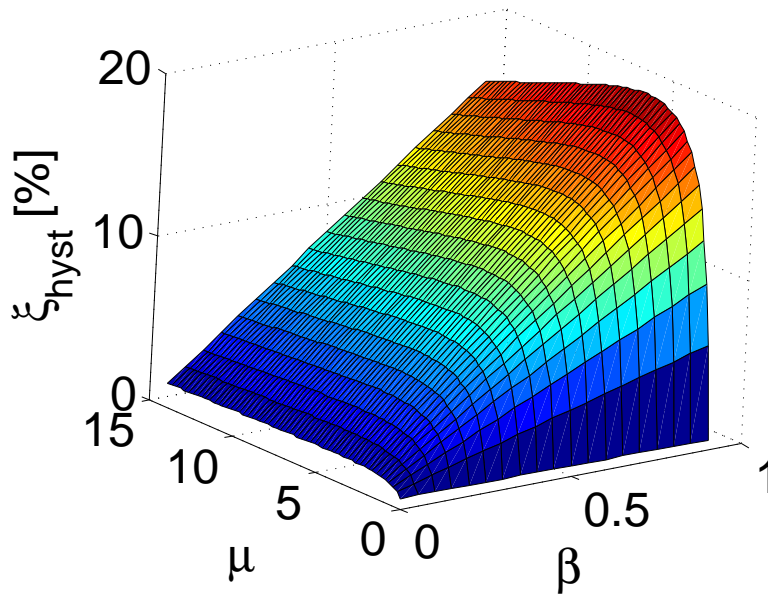
$$\xi_e = \xi_v + \xi_{hyst} \quad (5.9)$$

Hence, given the estimation of the hysteretic damping as a function of ductility in the previous section (formulas (5.4), (5.6) and Fig.(5.8)), we input those values in the expressions (5.7) and (5.8) to find the reduction factor coefficient. The aim is to perform a system comparison, between the elastoplastic model and the flag shape model, in terms of reduction factors. We consider  $r = 0.05$  and  $\beta = 1$  and a constant elastic viscous damping component equal to  $\xi_v = 5\%$ . The reduction factor  $R_{\xi}$  as a function of ductility  $\mu$  is reported in Fig.(5.11).

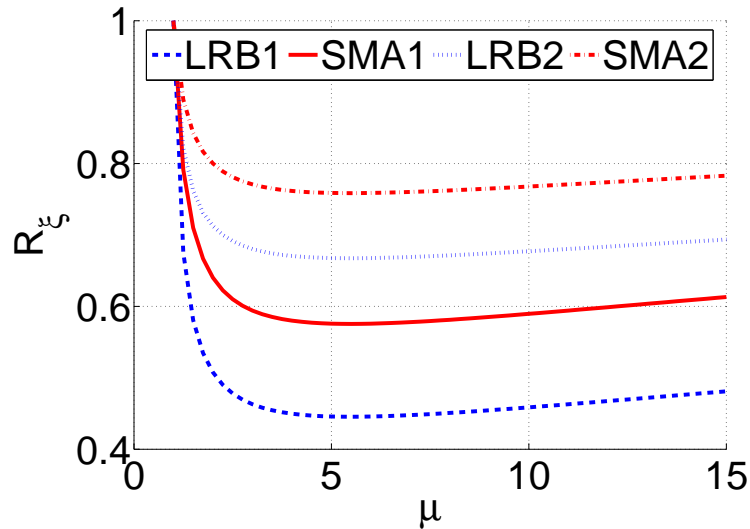
Still, the reduction factor increases up to a particular value of ductility, which is a function of the  $r$  parameter, and then decreases. This actually seems to make no sense and since isolator devices experience large displacement values, we think this approach does not work very well in seismic isolation.



**Figure 5.9:** hysteretic damping ratio for elastoplastic model computed from equation (5.4) as a function of ductility  $\mu$  and hardening  $r$ ; multiplying the ordinates by the coefficient  $\alpha_{fs} = 0.5\beta$  we get the same graph for the flag-shape model.



**Figure 5.10:** hysteretic damping ratio for flag-shape model computed from equation (5.6) as a function of ductility  $\mu$  and  $\beta$  factor, for  $r = 0.05$ .



**Figure 5.11:** far field and near field equivalent damping reduction factor for elastoplastic and flag-shape models; the far field values are named (1) while near field are named (2) in the legend.

In addition, we look at the comparison between a flag-shape model and an elastoplastic model equivalent damping estimation. The SMA response results in a larger displacement demand and in a larger force demand. Hence, if the equivalent damping concept were exact, the flag shape constitutive relation would significantly reduce the advantages of isolation.

### 5.3.3 Conclusions about Reduction Factors Estimation using Equivalent Damping

The approach described in the previous sections leads to the conclusion that an isolation device based on a SMA technology and flag-shape hysteresis is always supposed to be significantly less favorable in terms of displacement and force demand respect to a similar system based on elastoplastic hysteresis. This is because the damping reduction factor computed considering the hysteresis results to be significantly lower for SMA flag shape force displacement relation respect to LRB elastoplastic relation. Even if the flag-shape force-displacement relation is the more possible dissipating one, the SMA reduction factor is one half of the LRB one. If  $\beta = 0.5$  which is a more reasonable value, SMA reduction factor is one fourth on the LRB one.

Nevertheless, we do not have evidences of the suitability of the approach itself to determine the hysteretic energy dissipation for flag-shape force-displacement relation with high ductility demand.

Moreover the fact that the effective damping and the reduction factor are decreasing for large ductility values it seems far from the physics of the problem.

As a matter of fact, the conclusion that a SMA technology isolation device is not suitable for the structural purpose, based on the approximate computation of the reduction factor given the estimation of the hysteretic damping, from our point of view is a superficial judgement. Therefore we want to investigate it in more detail.

## **5.4 EFFECTIVE SEISMIC RESPONSE EVALUATION OF DIFFERENT HYSTERESIS ISOLATION DEVICES**

To investigate the response of a shape memory alloy isolator device and to compare it with the response of an equivalent classical lead rubber bearing, we perform time history analysis.

When we use the equivalent damping reduction factor approach to estimate demands for a flag-shape force displacement relation characterized by a large ductility, we find some uncertainties about the problem feasibility. Therefore we consider the analysis of the demand envelopes from time histories compatible ground motions the best way to check the response properties.

### ***5.4.1 Validation Strategy through Time-History Analysis***

The traditional spectra selection procedure is summarized in graph of Fig.(5.12).

Starting from information about local seismicity it is possible to get the 5% damping ratio design spectra; on the other hand, we take into account the superstructure, focusing on masses and geometry in order to estimate the deformed shape and to be able to produce a feasible structural model. These elements let us to pre-design an isolation system. Considering the isolation system and the information about the superstructure, we can create a global structural model. Then we evaluate the effective period from the secant stiffness and the damping reduction factor from equivalent damping ratio. From the last one we obtain the equivalent damping design spectra, while using the effective period we estimate the system displacement and the force demands. Finally we check comparing the demand with the capacity of the system and, eventually, we change the base isolation system properties if the design is not verified.

In the case of the SMA isolation devices, characterized by flag-shape hysteresis, the suitability of the concept of equivalent damping is not clear. Hence we decide to perform time history analysis and to follow the logical procedure shown in graph of Fig.(5.13).

The procedure is the same than the previous until the definition of the isolation system. Then

we model the isolator either as a secant stiffness linear system and as a real hysteresis system. From the 5% damping ratio design spectra we get spectra compatible ground motions. We use those to perform time history analyses for equivalent linear elastic system and for real hysteresis nonlinear systems. At this point we compare the time history analysis results of the different models to underline analogies and differences between flag-shape hysteresis and elastoplastic one also respect to the effective stiffness linear elastic model.

The ratio between the nonlinear hysteresis response and the secant stiffness linear elastic one provides the *real* reduction factor for the nonlinear system.

**(a) Previous Investigations on Flag-Shape System Dynamic Response and Interest in this Research.** Some authors investigated about the dynamic response of SDOF systems characterized by flag-shape force-displacement relation. The research has been mainly performed in order to investigate the response of post-tensioned concrete element but some of the conclusions are interesting even for our point of view.

A study (Priestley and Tao 1993) compared the seismic response of SDOF systems exhibiting a bilinear elastic hysteresis to that of bilinear elastoplastic systems. The bilinear elastic hysteresis considered represents the extreme case of the flag-shape hysteresis with no energy dissipation, therefore in our case systems are expected to exhibit some energy dissipation and to perform better with respect the bilinear elastic systems. Nevertheless the conclusion was that "despite the total lack of hysteretic energy absorption in the bilinear elastic model, displacement for medium to long period structures with such force-displacement response would be less than 35 percent larger than that of elastoplastic system with the same period". It was also recognized therefore that the increase in maximum displacement, and consequently in maximum force, under seismic load varies greatly depending on the natural period of the system.

Moreover, an extensive and interesting investigation about flag-shape model response have been performed in (Christopoulos 2004). Beside the mathematic formulation of the flag-shape dynamic response derived by the author, SDOF time histories have been performed to evaluate the sensitivity of displacement and force demand considering as free parameters the initial system stiffness, the hardening coefficient  $r$ , the energy dissipation coefficient  $\beta$  and the strength reduction factor. Response was compared to response of analogous elastoplastic system too.

The general conclusion of this work is that given an elastoplastic system is possible to find "at least one flag-shape hysteretic system of similar initial period and strength ratio that can achieve equal or smaller displacement ductility. In general intermediate values of  $r$  and  $\beta$  are sufficient to achieve this performance level".

The same author performed some MDOF system analysis of moment resistant frame structures

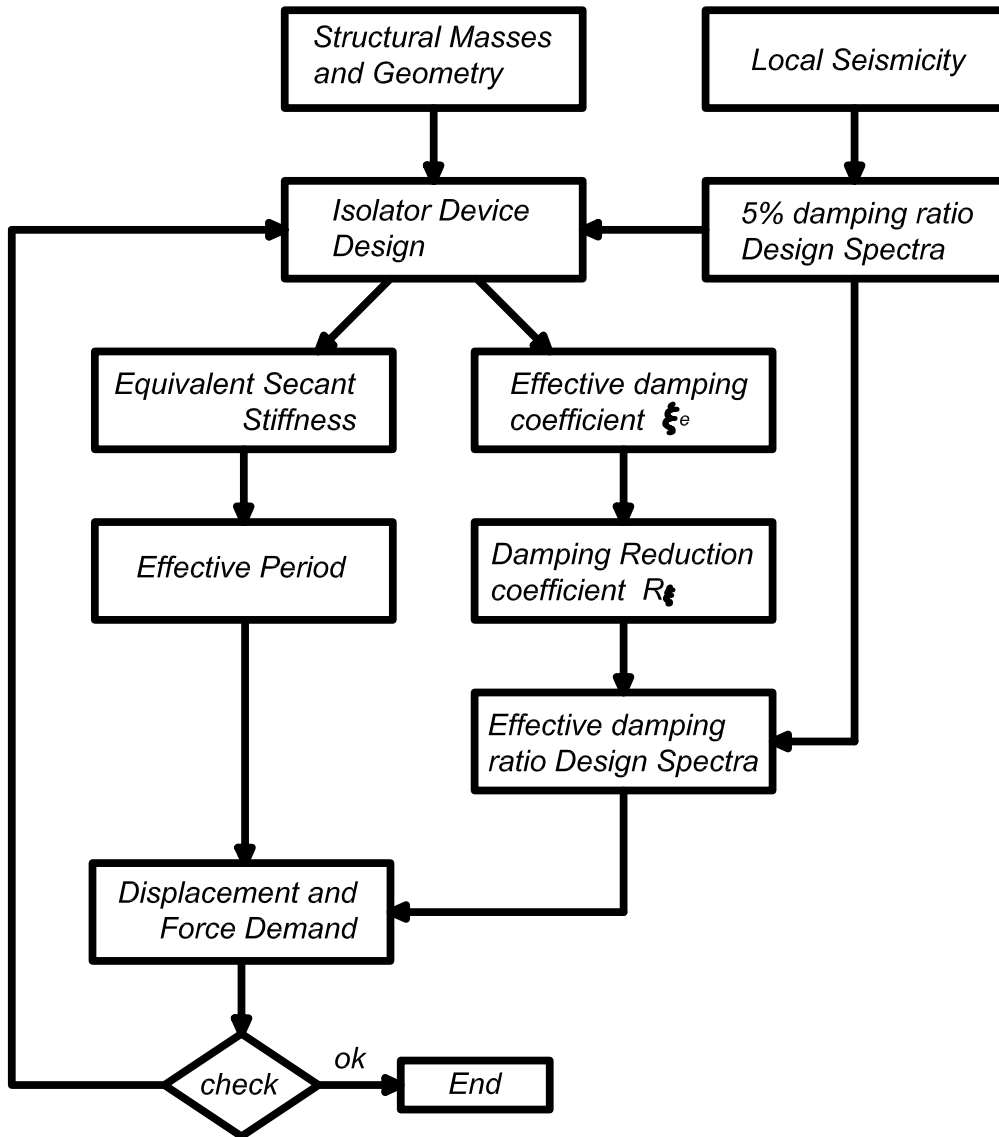
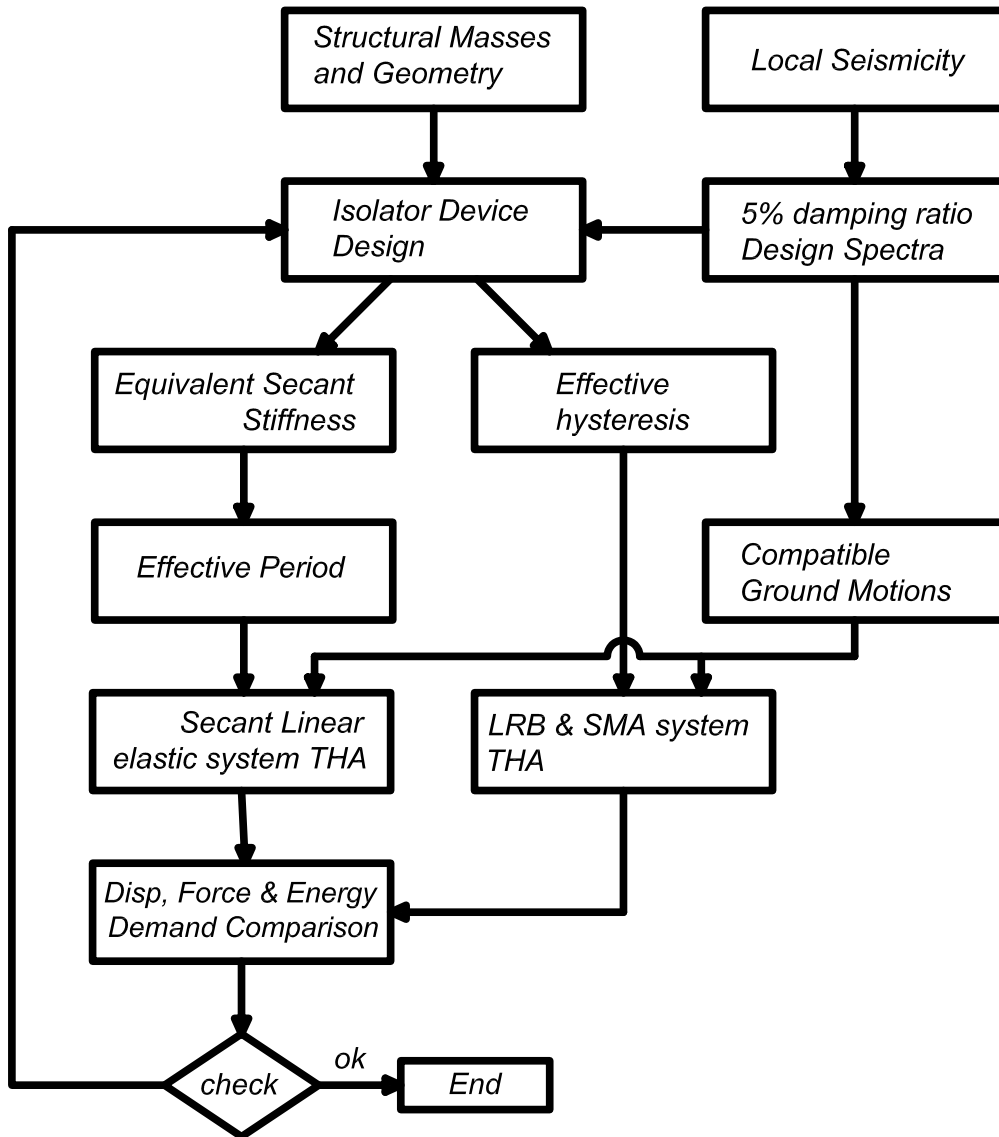


Figure 5.12: spectra selection procedure for isolated structure.



**Figure 5.13:** time history analysis procedure for displacement and force demand in a isolated structure system.

characterized by post-tensioned energy dissipative connections with flag shape hysteresis. In general even in the MDOF the shape-flag model response was quite good if compared with elastoplastic connection.

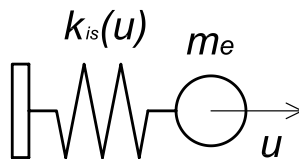
In general, previous investigations are very interesting because they state the principle that even if a force-displacement relation is characterized by a less energy dissipation hysteresis, it can perform in terms of ductility (and therefore displacements) like a more dissipating one.

Given the principles reported in the previous section, we want to check if these conclusions are valid also in the response of an isolation system.

In the previous research (Christopoulos 2004), both the initial stiffness and the strength reduction factor were free parameters. In our case on the contrary we need to guarantee a response similar to the actual isolator device indeed, therefore those parameters are fixed as defined in Tab.(5.2). For the same reason the mass is given, because it is related to the vertical capacity of the bearings which is defined in Tab.(5.1) and therefore the period is fixed. Considering the initial stiffness the period of our device is  $T_{k_0} = 0.89s$ . If we consider the secant stiffness to the design displacement point, the period is  $T_e = 2.02s$ . Since the structural period has been demonstrated to be an issue (Priestley and Tao 1993) and given that the previous research results were based on the initial period  $T_{k_0}$ , we have to check if our case can be considered a long-period condition in which the flag-shape hysteresis is well performing.

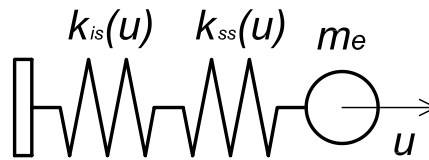
**(b) Structural Models for Time History Analysis.** To investigate analogies and differences, advantages and disadvantages of the two isolation systems, we consider two structural configurations, to reproduce either the base isolation of rigid structure (according to the condition described in section 3.3.1) and the base isolation of flexible structure (as described in section 3.3.2).

Concerning the first, the single degree of freedom has been characterized by a total mass computed from the seismic combination vertical load on every isolator reported in Tab.(5.1) and a stiffness as shown in Fig.(5.14).



**Figure 5.14:** analysis model for rigid superstructure base isolation.

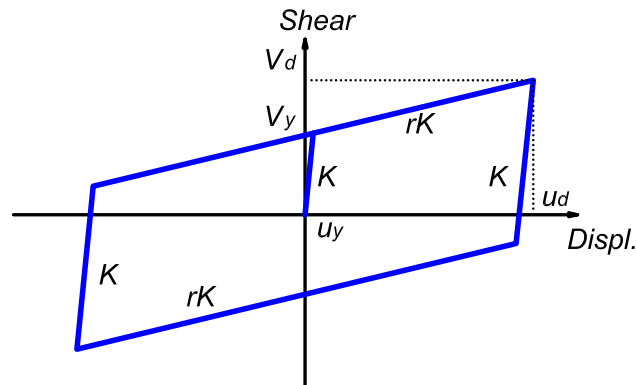
Regarding the flexible structure approach, we perform a design of a flexible structure and evaluate the response of the system considering the response in series of the isolator system and of the superstructure as shown in Fig.(5.15).



**Figure 5.15:** analysis model for flexible superstructure base isolation.

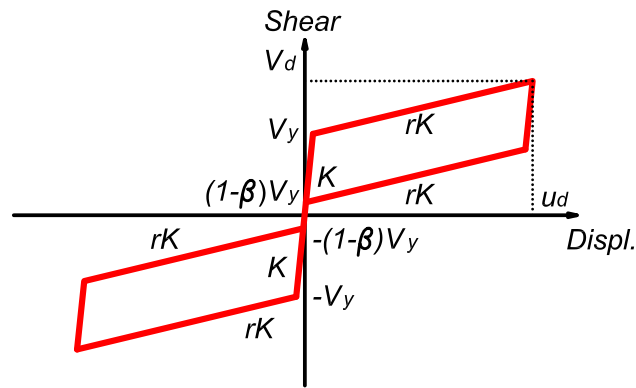
In the analysis we consider three hysteresis rules for the isolation system ( $k_{is}$ ), subjected to the same seismic input:

- Elasto-plastic model (Fig.(5.16)). The elastoplastic model is representative of the real lead rubber bearing device and the parameters we use are those reported in Tab.(5.2).

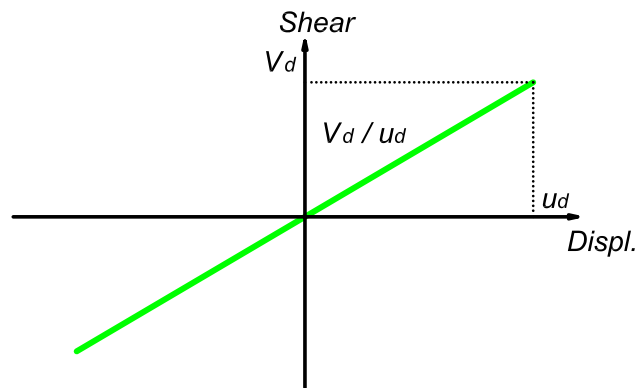


**Figure 5.16:** base shear horizontal displacement relation for lead rubber bearing isolation device.

- Flag-shape model (Fig.(5.17)). The flag-shape model reproduces the shear-horizontal displacement relation of the shape memory alloy device characterized by the design properties reported in Tab.(5.3). We target a device that performs like the real LRB system in the sense of equivalent shear and displacement capacity and initial and second stiffness.
- Linear elastic model (Fig.(5.18)). Considering the design displacement  $u_d$  and the design shear  $V_d$ , which are the same for the previous models, we carry out the analysis of the equivalent linear system, considering a secant stiffness which it is the same of the model reported in Tab.(5.1).



**Figure 5.17:** base shear horizontal displacement relation for shape memory alloy isolation device.



**Figure 5.18:** base shear horizontal displacement relation for equivalent linear elastic with secant stiffness isolation device.

In all the models we consider only the elastic damping component given by the total system and assumed to be equal to  $\xi_{sys} = \xi_v = 5\%$ . We neglect the additional damping component provided by the isolator hysteresis. To perform a comparison, the damping coefficient is constant in all the models and it is referred to the secant stiffness, constant in the all of them.

From a qualitative point of view, we expect that the nonlinear dynamic time history analysis (*THA*) comparison between elastoplastic model and flag-shape model is characterized by the following results:

- the flag-shape hysteresis has more frequent stiffness changes within one non linear cycle than the elastoplastic hysteresis;
- the flag-shape hysteresis returns to zero force and displacement point at every cycle whereas yielding of the elastoplastic system at every cycle may lead residuals;
- inherent dissipation of flag-shape hysteresis is smaller with respect to elastoplastic.

(c) **Energy Balance Analysis.** The aim of these analyses is to compare the response of elastoplastic model and of flag-shape model with respect to the response of linear elastic secant stiffness.

According to the equivalent stiffness principle we assume that a viscoelastic system is able to reproduce the demand of an inelastic system. For the design we refer to the response of the equivalent elastic system and then we reduce it by a coefficient which is taking into account the hysteretic damping component.

Uncertainties about the estimation of hysteretic damping component suggest to consider the force and displacement system response and to evaluate hysteresis dissipation considering an energetic approach. In this research we follow the formulation presented in (Christopoulos and Filiatrault 2006).

Considering the fundamental equilibrium dynamic equation (3.16) for a general multi degree of freedom system, we can write:

$$\mathbf{M}\ddot{\mathbf{x}}(t) + \mathbf{C}\dot{\mathbf{x}}(t) + \mathbf{F}_r(t) = -\mathbf{M}\mathbf{r}\ddot{x}_g(t) \quad (5.10)$$

in which:

- $\mathbf{M}$  is the global mass matrix;
- $\mathbf{C}$  is the global viscous damping matrix;
- $\ddot{\mathbf{x}}(t)$ ,  $\dot{\mathbf{x}}(t)$ ,  $\mathbf{x}(t)$  are respectively the vectors of global accelerations, velocities and displacement relative to the moving base at time  $t$ ;
- $\mathbf{F}_r(t)$  is the vector of global nonlinear restoring force at time  $t$ ;
- $\mathbf{r}$  is the influence vector, which represents the displacements of masses resulting from static application of a unit ground displacement;
- $\ddot{x}_g$  is the horizontal acceleration of the ground at time  $t$ .

Computing the work done by each contribution over an increment of the global displacement vector  $d(\mathbf{x})$  and integrating, it is possible to obtain the energy formulation of the (5.10):

$$\int d\mathbf{x}^T \mathbf{M}\ddot{\mathbf{x}}(t) + \int d\mathbf{x}^T \mathbf{C}\dot{\mathbf{x}}(t) + \int d\mathbf{x}^T \mathbf{F}_r(t) = - \int d\mathbf{x}^T \mathbf{M}\mathbf{r}\ddot{x}_g(t) \quad (5.11)$$

Recalling the relations:

$$\begin{aligned} d\mathbf{x}(t) &= \dot{\mathbf{x}}(t)dt \\ d\dot{\mathbf{x}}(t) &= \ddot{\mathbf{x}}(t)dt \end{aligned} \quad (5.12)$$

and substituting in the previous:

$$\int \dot{\mathbf{x}}(t)^T \mathbf{M} d\dot{\mathbf{x}}(t) + \int \dot{\mathbf{x}}(t)^T \mathbf{C} d\mathbf{x}(t) + \int d\mathbf{x}^T \mathbf{F}_r(t) = - \int d\mathbf{x}^T \mathbf{M} \mathbf{r} \ddot{x}_g(t) \quad (5.13)$$

which is the final form for the energy formulation. The different terms are representative of the different energy contributions:

- kinetic energy at time  $t$ :

$$E_{ki}(t) = \int \dot{\mathbf{x}}(t)^T \mathbf{M} d\dot{\mathbf{x}}(t) = \frac{1}{2} \dot{\mathbf{x}}(t)^T \mathbf{M} \dot{\mathbf{x}}(t) \quad (5.14)$$

- viscous damping dissipated energy up to time  $t$ :

$$E_{da}(t) = \int \dot{\mathbf{x}}(t)^T \mathbf{C} d\mathbf{x}(t) \quad (5.15)$$

- absorbed energy up to time  $t$ :

$$E_{ab}(t) = \int d\mathbf{x}^T \mathbf{F}_r(t) \quad (5.16)$$

- introduced energy up to time  $t$ :

$$E_{in}(t) = - \int d\mathbf{x}^T \mathbf{M} \mathbf{r} \ddot{x}_g(t) \quad (5.17)$$

We can compute the same quantities in the discrete time integration schemes considering the analogous approximate expressions:

- kinetic energy at time  $t$ :

$$E_{ki}(t) = \frac{1}{2} \dot{\mathbf{x}}(t)^T \mathbf{M} \dot{\mathbf{x}}(t) \quad (5.18)$$

- viscous damping dissipated energy up to time  $t$ :

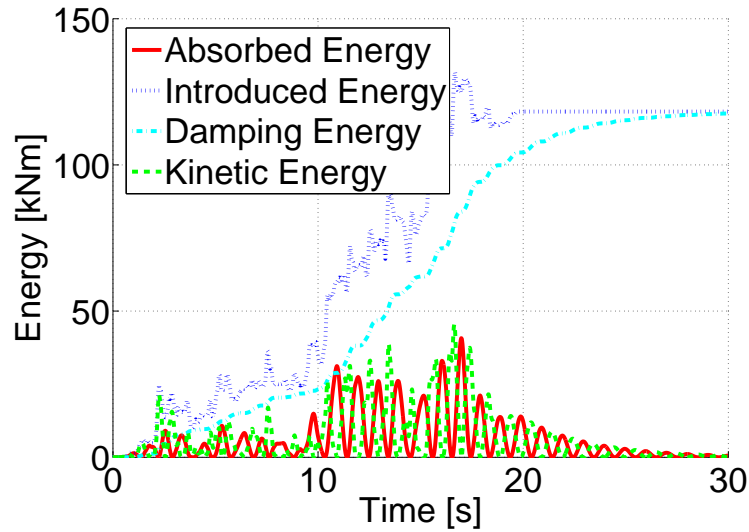
$$E_{da}(t) = E_{da}(t - \Delta t) + \frac{1}{2} [\dot{\mathbf{x}}(t - \Delta t) + \dot{\mathbf{x}}(t)]^T \mathbf{C} [\mathbf{x}(t) - \mathbf{x}(t - \Delta t)] \quad (5.19)$$

- absorbed energy up to time  $t$ :

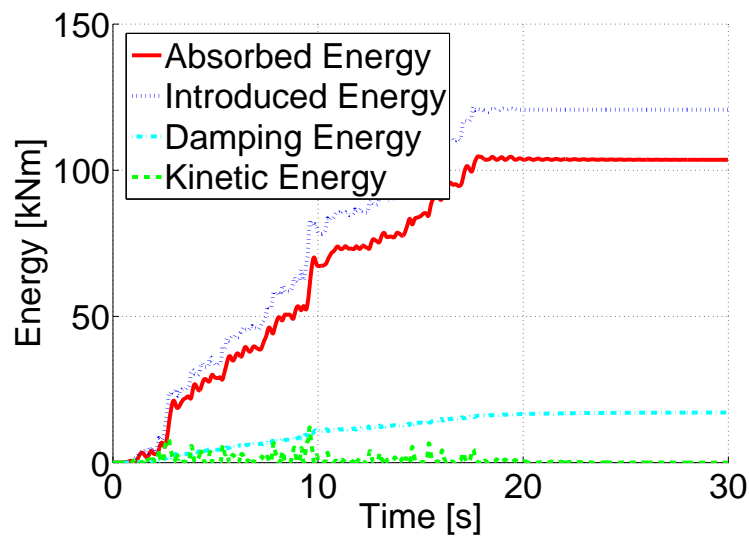
$$E_{ab}(t) = E_{ab}(t - \Delta t) + \frac{1}{2} [\mathbf{x}(t) - \mathbf{x}(t - \Delta t)]^T [\mathbf{F}_r(t - \Delta t) + \mathbf{F}_r(t)] \quad (5.20)$$

- introduced energy up to time  $t$ :

$$E_{in}(t) = E_{in}(t - \Delta t) - \frac{1}{2} [\mathbf{x}(t) - \mathbf{x}(t - \Delta t)]^T \mathbf{M} \mathbf{r} [\ddot{x}_g(t - \Delta t) + \ddot{x}_g(t)] \quad (5.21)$$



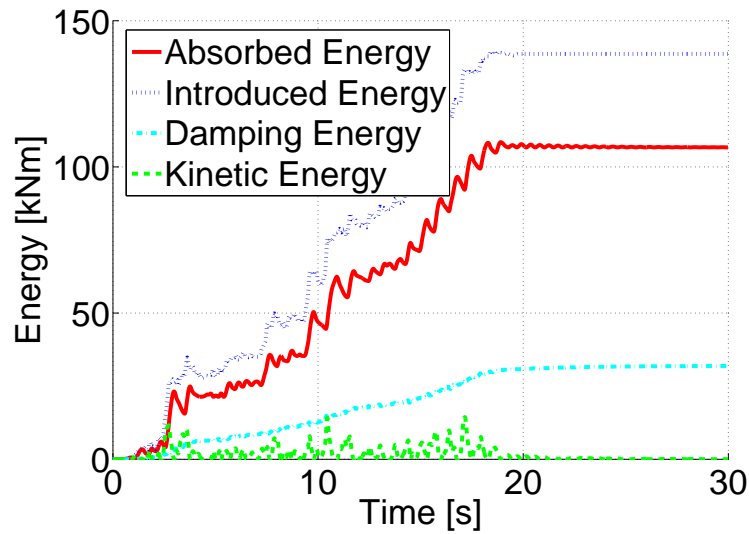
**Figure 5.19:** energy components in a t.h.a. for a linear elastic system.



**Figure 5.20:** energy components in a t.h.a. for an elastoplastic system.

We show in following figures plots of the energy contents versus time of three systems, one linear elastic (in Fig. (5.19)), one elastoplastic (in Fig. (5.20)), and one flag shaped (in Fig. (5.21)), corresponding to the three hysteresis we are considering in the time history analyses.

The energy introduced in the system by the ground motion is a function of the response of the system and differs between the models even if the ground motion is the same. That amount of energy has to be equilibrated at each time by the other forms of energy. Since at the end of the



**Figure 5.21:** energy components in a t.h.a. for a flag-shape system.

seismic excitation the input energy is larger than zero, we expect some dissipation provided by the systems.

Looking at the results and at the equation, it is clear that the kinetic component is a conservative energy contribution, becoming zero at the end of the excitation in all the cases. On the contrary, a damping component express the velocity proportional dissipation, which is a function with an increasing trend characterized by some larger slopes in correspondence of kinetic energy local maxima.

Concerning the absorbed energy, conceptually it is given by the sum of two contribution:

$$E_{ab}(t) = E_{ab,e} + E_{ab,h} \quad (5.22)$$

in which  $E_{ab,e}$  is a conservative component, the one related to the elastic energy stored by the system, which goes to zero when the displacement is zero, and  $E_{ab,h}$  is a hysteretic energy related to the nonlinear behavior of the system and to its unrecoverable deformations.

We are particularly interested in this absorbed energy term because it is representative of the energy demand on structural members during an earthquake.

In the linear elastic system the hysteretic component is zero  $E_{ab,h} = 0$ , therefore the absorbed energy is conservative and it is zero at the end of the ground motion, when the displacement is zero and also the elastic component become zero. In this system the only dissipation is due to the damping contribution which at the end of the seismic excitation has to be equal to the energy introduced in the system.

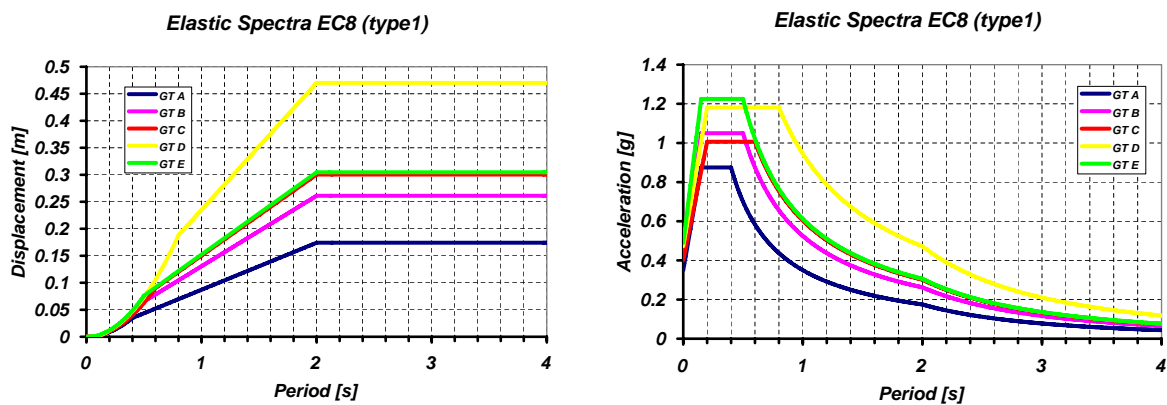
In the elastoplastic system the hysteretic component  $E_{ab,h}$  is significative and provides a large energy dissipation. The elastic component  $E_{ab,e}$  is also different than zero and in this case, due to the fact that can happen to have some residual displacements at the end of the story, it can be

different than zero when the seismic excitation ends.

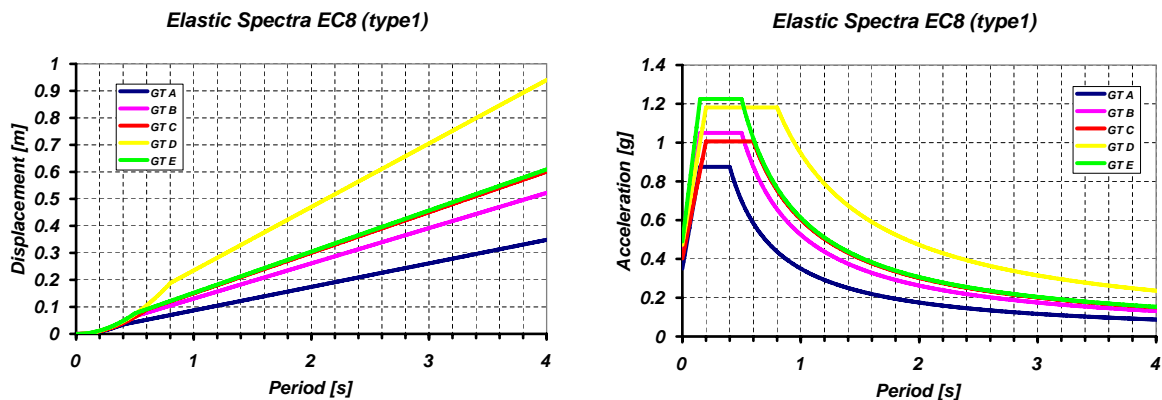
Finally, in the flag-shape hysteresis case, the hysteretic component  $E_{ab,h}$  is still different than zero, even if in theory the dissipation for every cycle is supposed to be smaller than the previous case if the displacement is the same. The elastic component  $E_{ab,e}$  is also different than zero. Nevertheless, in this case the system is nonlinear elastic and the elastic component goes to zero when the excitation finishes. Moreover the effect of the elastic component is more important than in the previous case and this can be noticed looking at the energy line which is more jagged.

In the time history analyses we also compute the effective energy component to be able to estimate the differences in terms of absorbed energy considering the effective hysteresis relations.

### 5.4.2 Ground Motion for the Time History Analyses



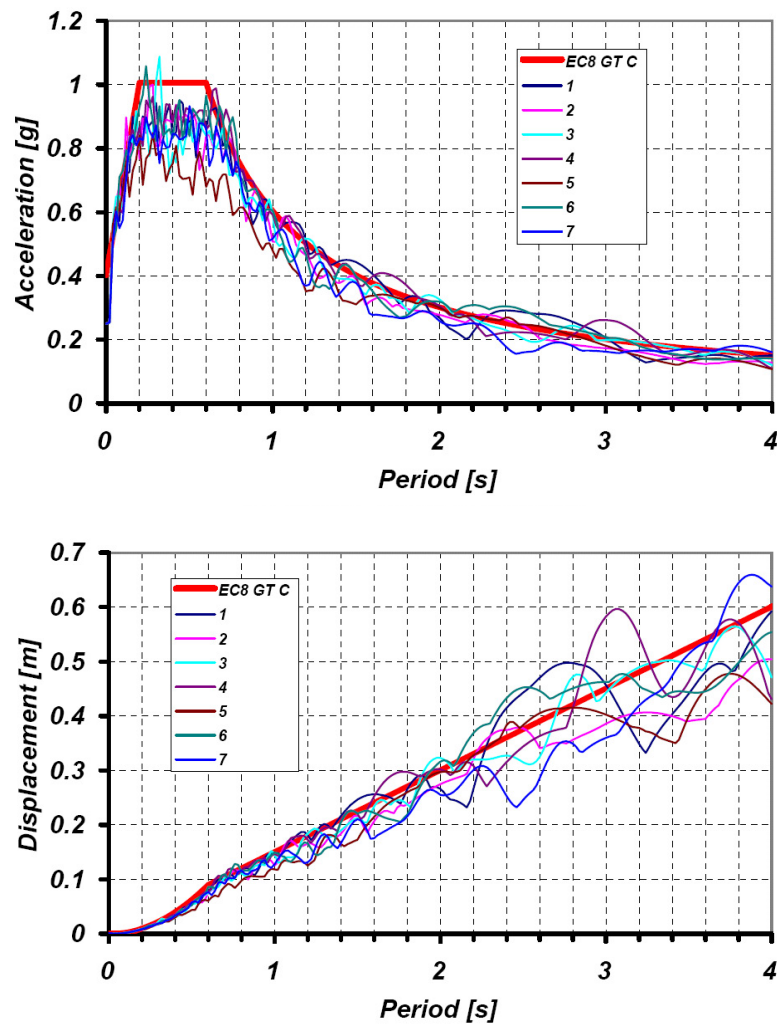
**Figure 5.22:** displacement and acceleration elastic design spectra for  $PGA = 0.35g$ , 5% damping ratio type 1 (far field event) from Eurocode 8.



**Figure 5.23:** displacement and acceleration elastic design spectra for  $PGA = 0.35g$ , 5% damping ratio type 1 (far field event) from Eurocode 8.

Concerning the design spectra of our system we consider the *Eurocode 8* prescriptions (Eurocode8 2003).

The type 1 Eurocode spectra are showed in Fig.(5.22). We can notice that according to these prescriptions the corner period  $T_D$  is equal to  $2s$ . To design an isolated structure using a displacement based approach, this limit is too short. Hence, even if we know that the correct corner period should be estimated as a function of the area local seismicity, we assume to consider the same spectra expression and a corner period longer and equal to  $T_D = 4s$ ; the modified spectra are shown in Fig.(5.23).

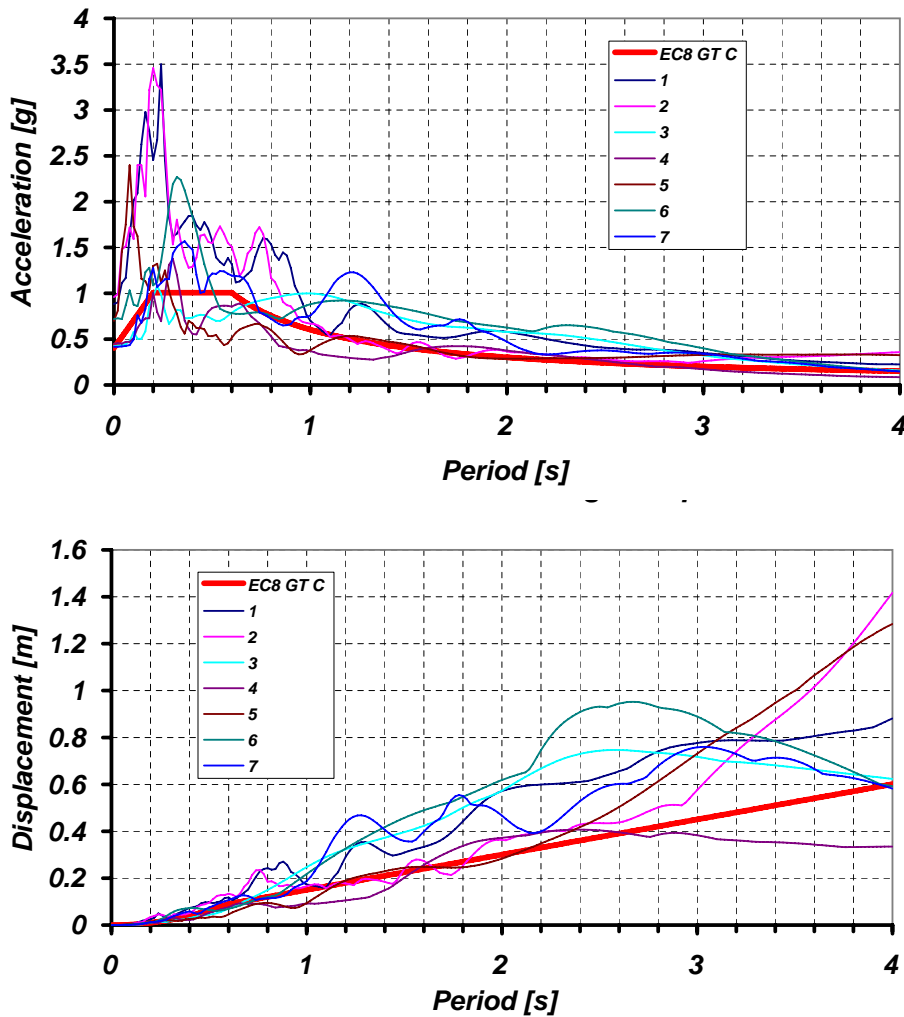


**Figure 5.24:** acceleration and displacement elastic design spectra for spectra compatible artificial ground motions.

The change in the acceleration spectra is very small but the effects of the change in displacement spectra ordinates larger than  $2s$  are significant.

Since we characterize the original isolation system by the effective stiffness and seismic mass of Tab.(5.1), in a rigid superstructure base isolation system design the effective period is:

$$T_e = 2\pi\sqrt{\frac{W}{gK_e}} = 2\pi\sqrt{\frac{1653kN}{9.81\frac{m}{s^2} \cdot 1620kN}} = 2.026s \quad (5.23)$$

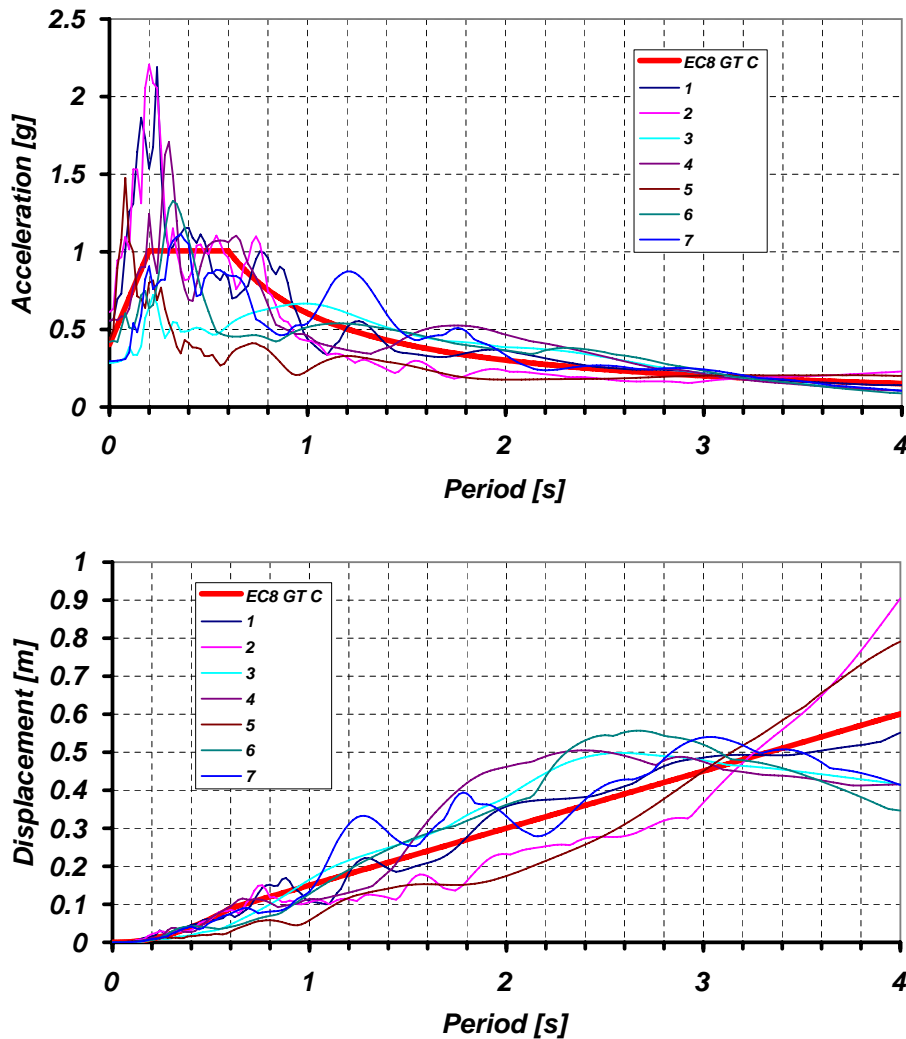


**Figure 5.25:** acceleration and displacement elastic design spectra for original near fault ground motion record.

Moreover, considering a far field event and the damping coefficient of Tab.(5.1), the damping reduction factor is:

$$R_\xi = \eta = \sqrt{\frac{10}{5 + \xi}} = 0.55 \quad (5.24)$$

We assume to be applicable in our case the design spectra of Fig.(5.23) and a soil type *GT C*. For period  $T_e$  we compute the design displacement as the product between the spectral ordinate



**Figure 5.26:** modified acceleration and displacement elastic design spectra for near fault ground motion record.

and the reduction factor:

$$u_d = R_\xi \cdot S_d(T_e) = 0.55 \cdot 0.3m = 0.165m \quad (5.25)$$

which is close to the design displacement reported as a design parameter in Tab.(5.1). Therefore for the analysis we use the design spectra given by the Eurocode 8 expression considering a corner period  $T_D = 4s$ , a  $PGA = 0.35g$  and a soil type  $C$ .

We decide to use several ground motions in the analyses in order to consider the variability of the seismic input. A first set is composed by seven artificial generated ground motions compatible with the design spectra. Those spectra were generated using a research-oriented program, *Simqke* (Carr 2007), considering as a input the design spectra. Comparison between the design spectra and the elastic spectra of the ground motion is shown in Fig.(5.24).

We also want to evaluate responses to need near fault ground motions, to investigate in a suitable way the hysteretic response under particular conditions like pulse loads, which can be quite demanding in nonlinear isolation device comparison. Hence we perform the investigation using seven near fault ground motions.

To get spectra compatible ground motions we have to scale the real near fault records. We perform this in a simplified manner, just multiplying the record for a coefficient equal to the ratio between the design displacement spectra slope to the corner period value and the same slope for the elastic displacement spectra of each record. Original elastic ground motion spectra are shown in Fig.(5.25) and modified ground motion spectra in Fig.(5.26).

We report more details about ground motions used in this research in appendix A.

## **5.5 RIGID SUPERSTRUCTURE APPROACH TIME HISTORY ANALYSES RESULTS**

In the rigid superstructure approach we consider that the isolation system is the only source of stiffness of the system. We refer to the model in Fig.(5.14). In these analyses the superstructure affects only the mass of the system.

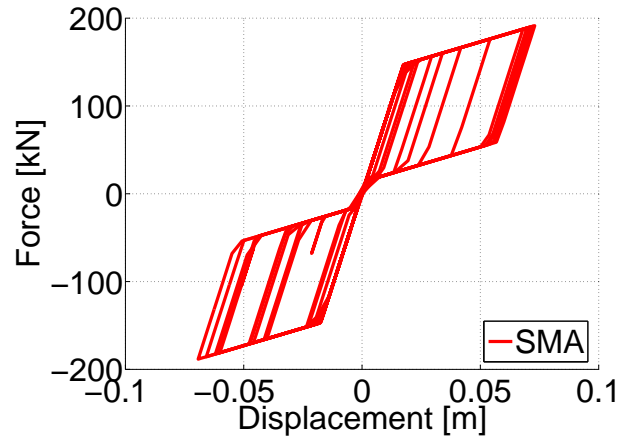
Results from all the analyses in details are reported in appendix B.

### ***5.5.1 Evaluation of Results Considering SMA Model with Largest Dissipation Capability***

In the first set of time history analyses we consider a flag-shape hysteresis characterized by a dissipation capability almost equal to the maximum we can get. We model the SMA isolation hysteresis using a force-displacement relation with a parameter  $\beta = 0.95$ . An example from a THA of this force-displacement relation is shown in Fig.(5.27).

We perform comparisons between flag shaped, elastoplastic and linear elastic systems. We take into account separately the artificial ground motion analysis results and the near fault ground motion analysis results. Even if we perform the base design with the same principles, the displacement demand compared with the design displacement is smaller for artificial ground motions and larger for near fault ground motions in all the models.

Concerning the base shear and displacement, in the elastoplastic and flag shape hysteresis both of them are less than the values for the linear elastic equivalent system. This is an expected result



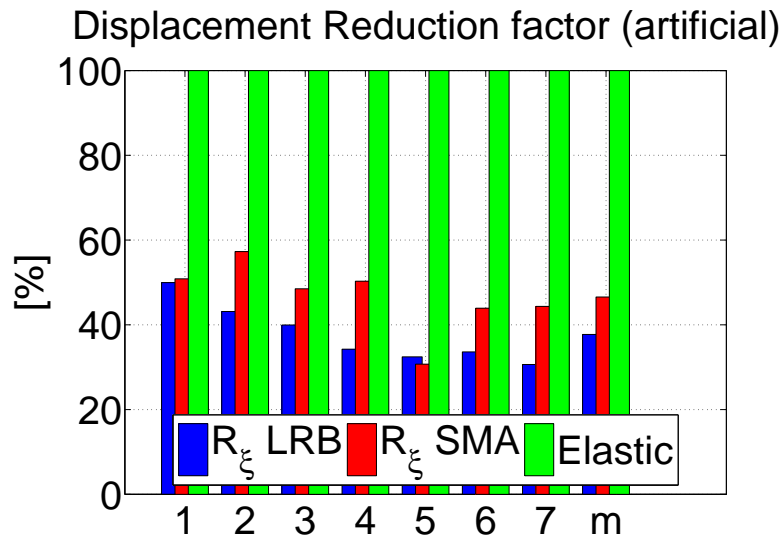
**Figure 5.27:** flag-shape hysteresis from ground motion 5 THA considering parameter  $\beta = 0.95$ .

because the linear elastic model reproduces the isolation system without any energy dissipation. We are interested in the force and displacement reduction factor, which is the ratio between the demand considering the actual hysteresis force-displacement relation with respect to the one given by a linear elastic secant stiffness model; conceptually reduction factor in the analysis conditions represent the effectiveness of the hysteretic energy dissipation.

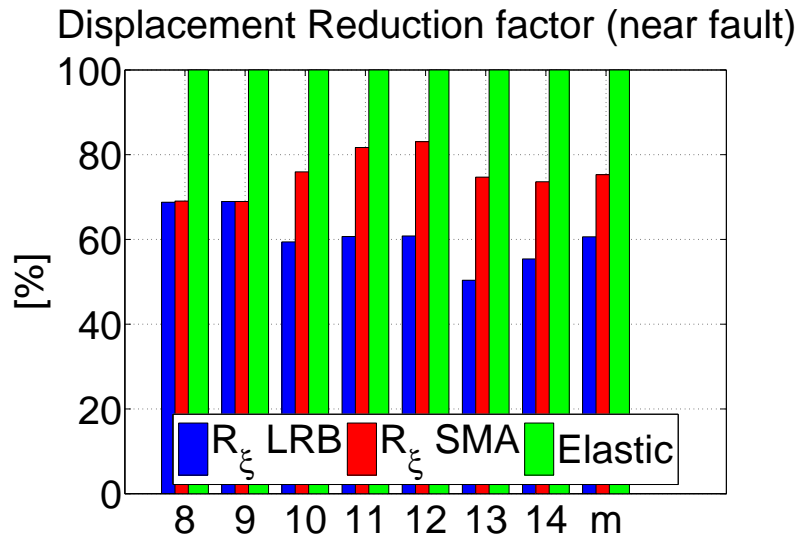
Displacement reduction factors are shown in Fig.(5.28) for artificial ground motions and in Fig.(5.29) for near fault ground motions; force reduction factors are shown in Fig.(5.30) for artificial ground motions and in Fig.(5.31) for near fault ground motions.

The first and most important information we can learn from the comparison is that differences between the lead rubber bearing elastoplastic model and shape memory alloy flag shape model are small if compared with the linear elastic force and displacement demand. This is proved also by Fig.(5.32) and Fig.(5.33), representing the system absorbed energy during the ground motion. The same variable has been plotted also in Fig.(5.34) and Fig.(5.35), normalized respect the input energy because, as shown in Fig.(5.20) and Fig.(5.21), we are interested not only at the absolute value of the absorbed energy but also at the ratio between this and the total input energy. Still the differences are quite small with respect to the fact that the elastoplastic hysteresis is characterized by an area which for the most dissipating case ( $\beta = 0.95$ ) is more than twice of the flag shape one.

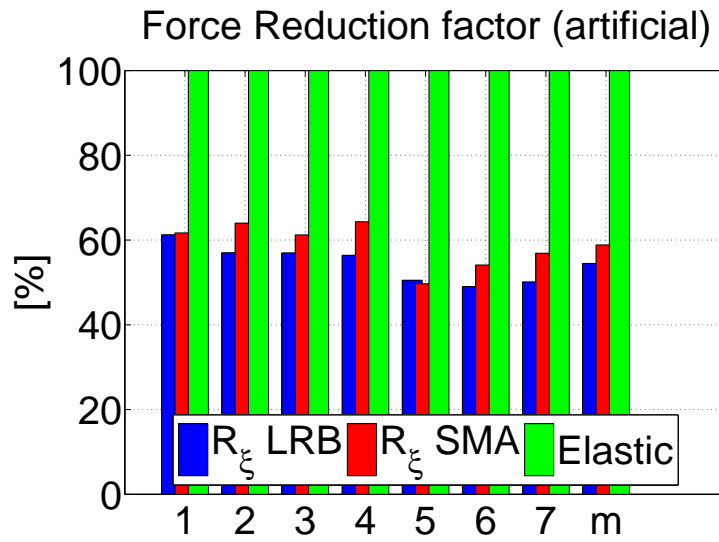
An other issue for isolation bearings is the residual displacement. That is a behavior that is very undesirable in an isolation system device since it leads to the needing of reparation of the system after the seismic event. Of course this problem strongly affects an elastoplastic model, especially when the seismic input is coming from a near fault event, characterized by a pulse-like



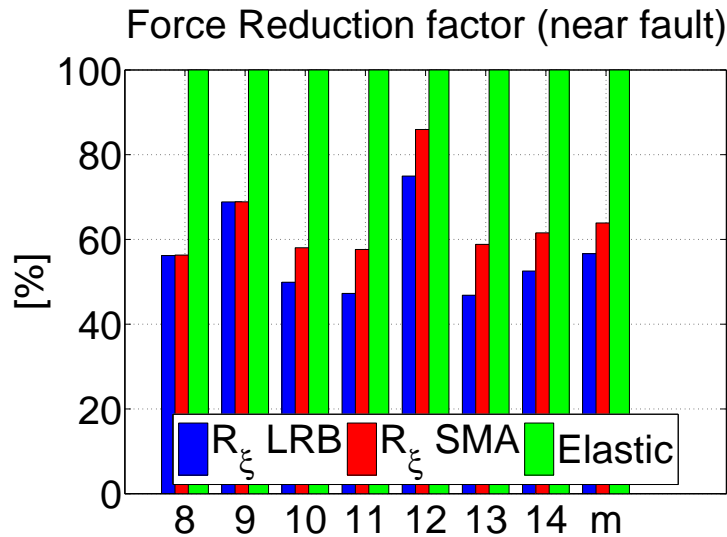
**Figure 5.28:** displacement demand values normalized to the linear elastic displacement demand for artificial ground motions; the last set is the mean value of the previous ones; standard deviation values are  $\sigma_{LRB,u,ar} = 6.96$  and  $\sigma_{SMA,u,ar} = 8.31$ .



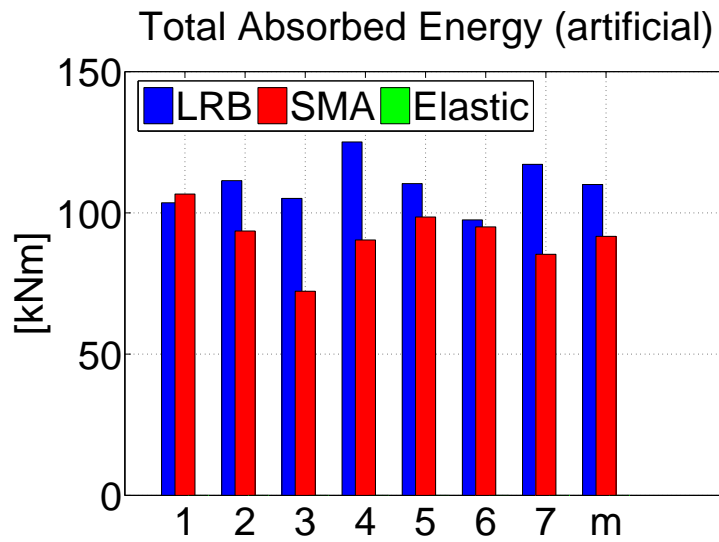
**Figure 5.29:** displacement demand values normalized to the linear elastic displacement demand for near fault ground motions; the last set is the mean value of the previous ones; standard deviation values are  $\sigma_{LRB,u,nf} = 6.70$  and  $\sigma_{SMA,u,nf} = 5.54$ .



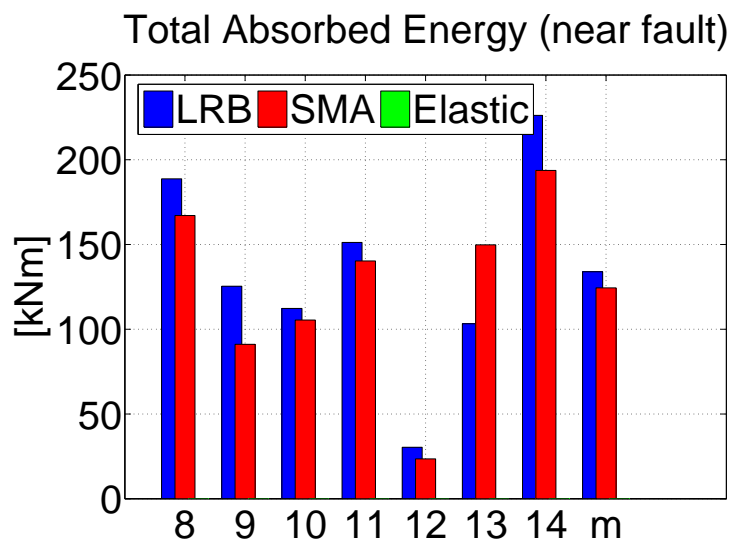
**Figure 5.30:** force demand values normalized to the linear elastic displacement demand for artificial ground motions; the last set is the mean value of the previous ones; standard deviation values are  $\sigma_{LRB,f,ar} = 4.59$  and  $\sigma_{SMA,f,ar} = 5.48$ .



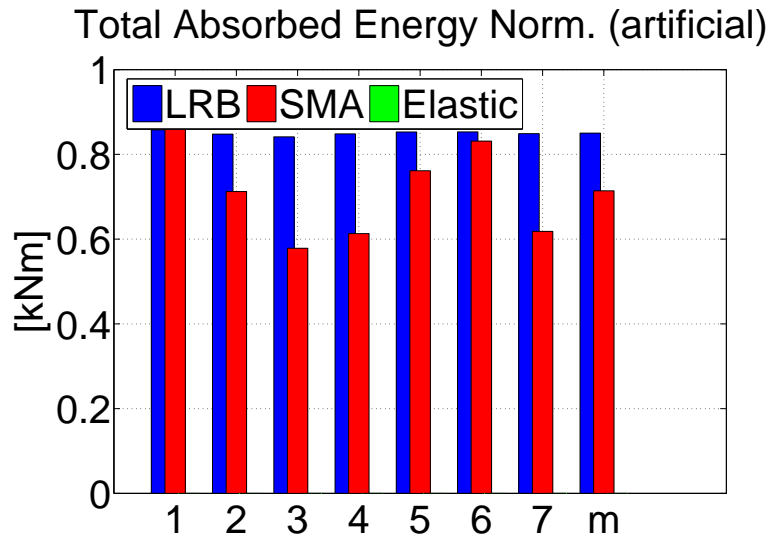
**Figure 5.31:** force demand values normalized to the linear elastic displacement demand for near fault ground motions; the last set is the mean value of the previous ones; standard deviation values are  $\sigma_{LRB,f,nf} = 11.03$  and  $\sigma_{SMA,f,nf} = 10.58$ .



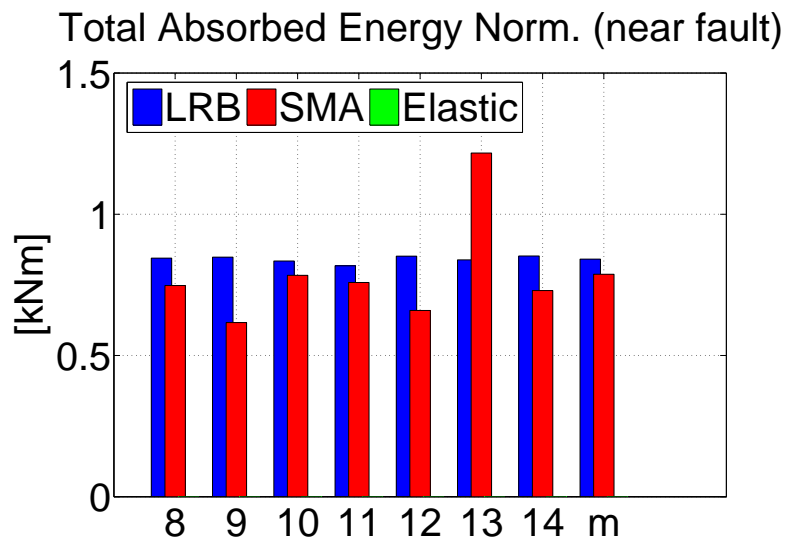
**Figure 5.32:** system absorbed energy for artificial ground motions; the last set is the mean value of the previous ones.



**Figure 5.33:** system absorbed energy for near fault ground motions; the last set is the mean value of the previous ones.



**Figure 5.34:** system absorbed energy normalized respect input energy for artificial ground motions; the last set is the mean value of the previous ones.



**Figure 5.35:** system absorbed energy normalized respect input energy for near fault ground motions; the last set is the mean value of the previous ones.

load. On the other side, the SMA bearing is supposed to perform zero residual displacements. We report the displacement time graph for an artificial ground motion in Fig.(5.36) and for a near field one in Fig.(5.37): in the both of them lead rubber bearing system is characterized by residuals.

However, from the analyses we performed on the elastoplastic model, the residual displacements are not negligible but also not very large as summarized in Fig.(5.38). In general when we consider large magnitude near fault ground motion residuals can be very large.

### ***5.5.2 Evaluation of Result Sensibility to Model Dissipation Ratio***

The flag-shape hysteresis that can be obtained by the SMA superelastic effect (Fig.(4.2)) is not characterized by a dissipation coefficient as large as we have assumed in the previous tests ( $\beta \simeq 1$ ). The usual superelastic hysteresis is characterized by a maximum dissipation parameter of the order of  $\beta \simeq 0.7$ , and this is a function of the material, so the value can also be smaller. We could design a device characterized by a force-displacement flag-shape with a large dissipation coefficient  $\beta$  considering possibility of prestressing shape memory alloy elements. In this case some problems can develop to get a symmetric behavior in tension and in compression. Hence, even if an high dissipation flag shape hysteresis is supposed to perform in theory in the best way, we also want to investigate the differences in response considering different dissipation coefficient responses, eventually closer to actual shape memory alloys superelastic effect parameters.

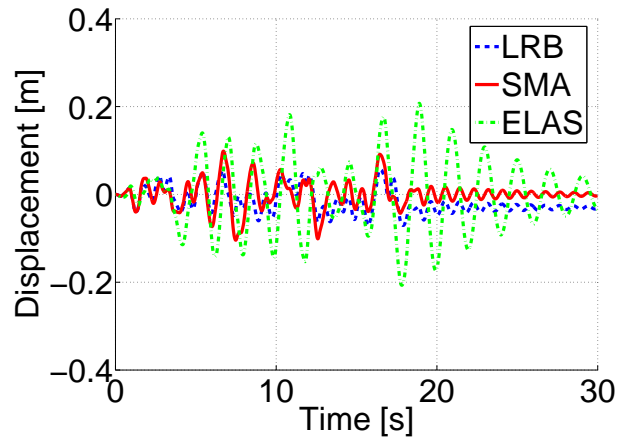
For this purpose, we perform more analyses evaluating the system response if the  $\beta$  factor is smaller. We consider four additional cases, in order to have the dissipation parameter spanning between  $\beta = 0.95$  and  $\beta = 0.15$ .

All the considered hysteresis, in addition with the one from elastoplastic model used for comparison, are shown in Fig.(5.39), Fig.(5.40) and Fig.(5.41).

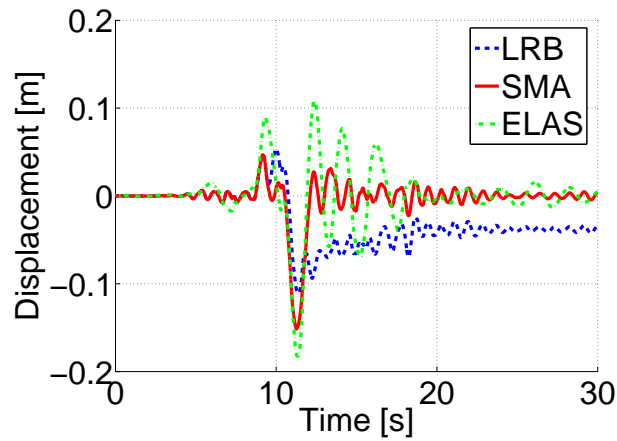
Results in detail are reported in the appendix B in which responses from all the analyses and summaries for every dissipation coefficient are listed. To generalize, it is useful to report a full comparison between the different SMA levels of dissipation and with linear elastic and elastoplastic responses.

Responses in term of displacement demand are reported in Fig.(5.42) and Fig.(5.43) considering the absolute envelope values, in Fig.(5.44) and Fig.(5.45) to take into account the normalized demand respect the linear elastic one.

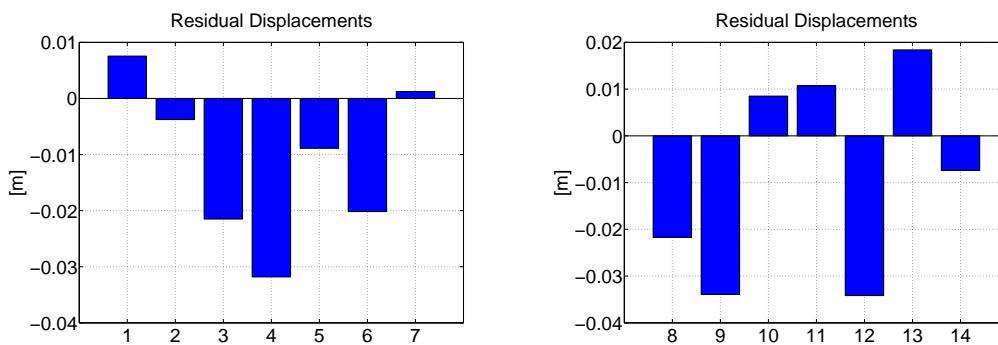
Responses in term of force demand are reported in Fig.(5.46) and Fig.(5.47) considering the absolute envelope values, in Fig.(5.48) and Fig.(5.49) to take into account the normalized demand respect the linear elastic one.



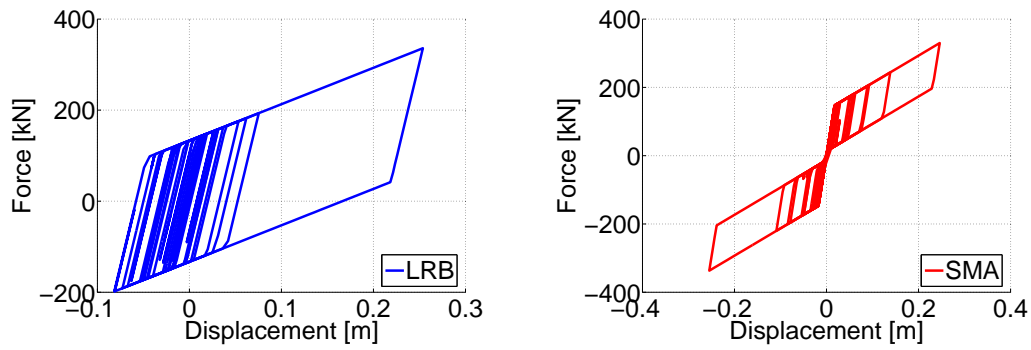
**Figure 5.36:** displacement-time response from an artificial event (ground motion 4).



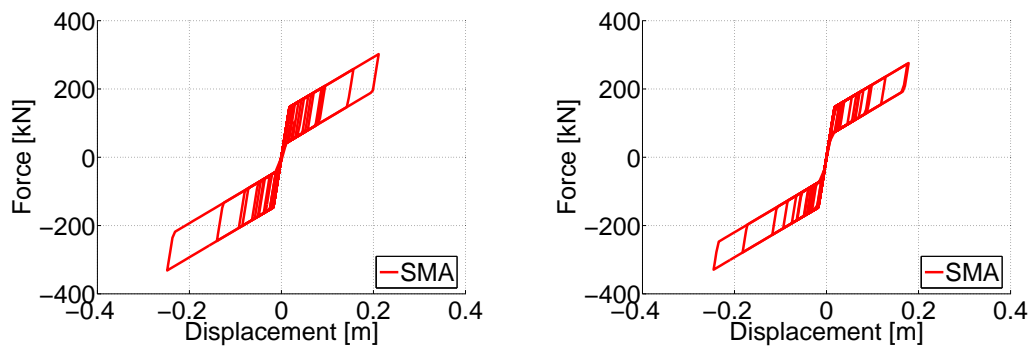
**Figure 5.37:** displacement-time response from an artificial event (ground motion 12).



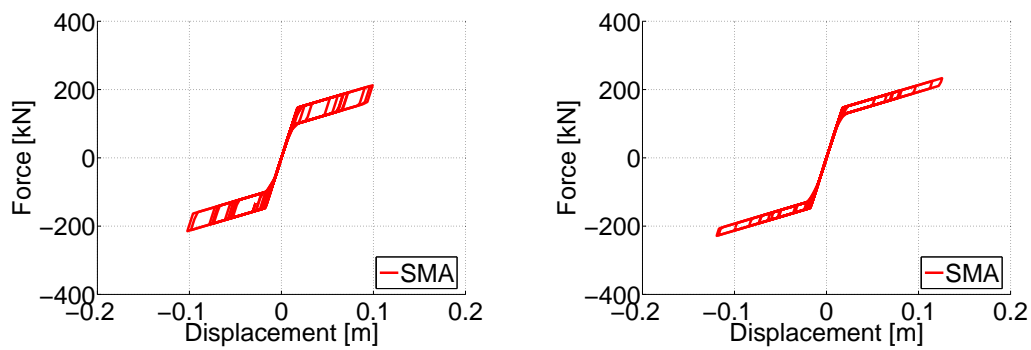
**Figure 5.38:** residual displacements from the artificial (left) and near fault (right) THAs in lead rubber bearing elastoplastic model.



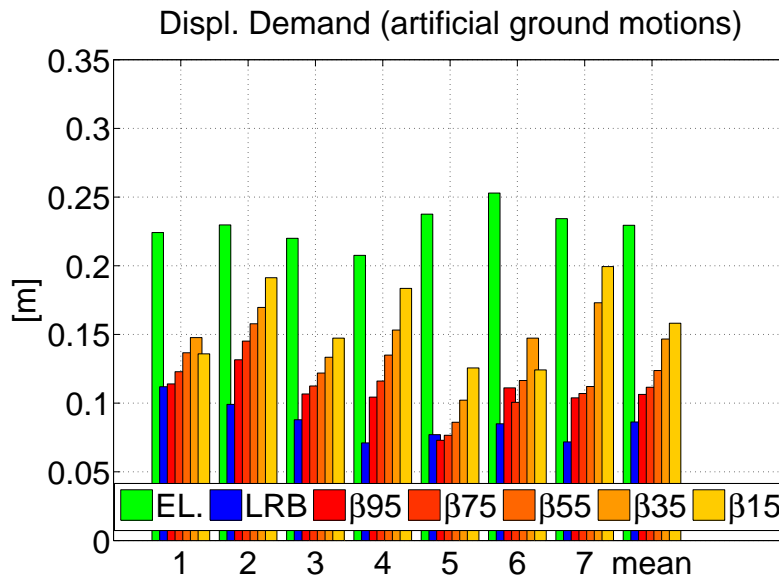
**Figure 5.39:** elastoplastic hysteresis (left) and flag-shape hysteresis (right) considering parameter  $\beta = 0.95$ , from ground motion 8 THA.



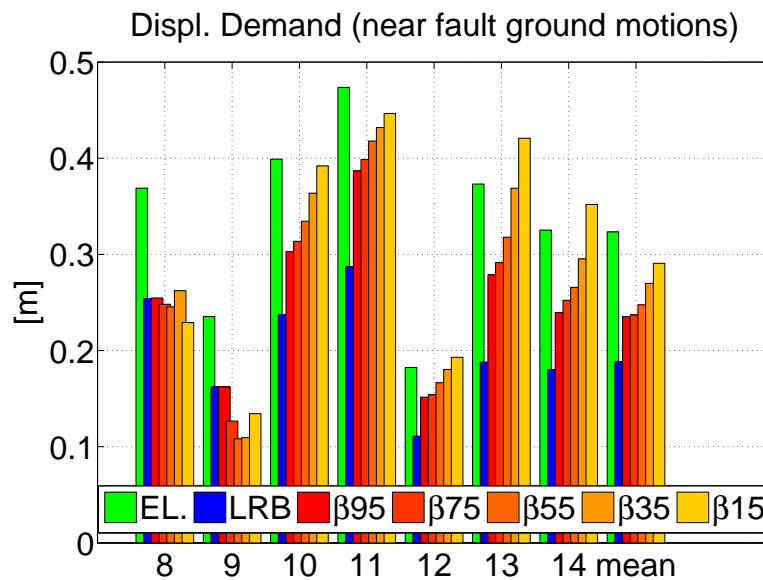
**Figure 5.40:** flag-shape hysteresis considering parameter  $\beta = 0.75$  (left) and flag-shape hysteresis considering parameter  $\beta = 0.55$  (right), from ground motion 8 THA.



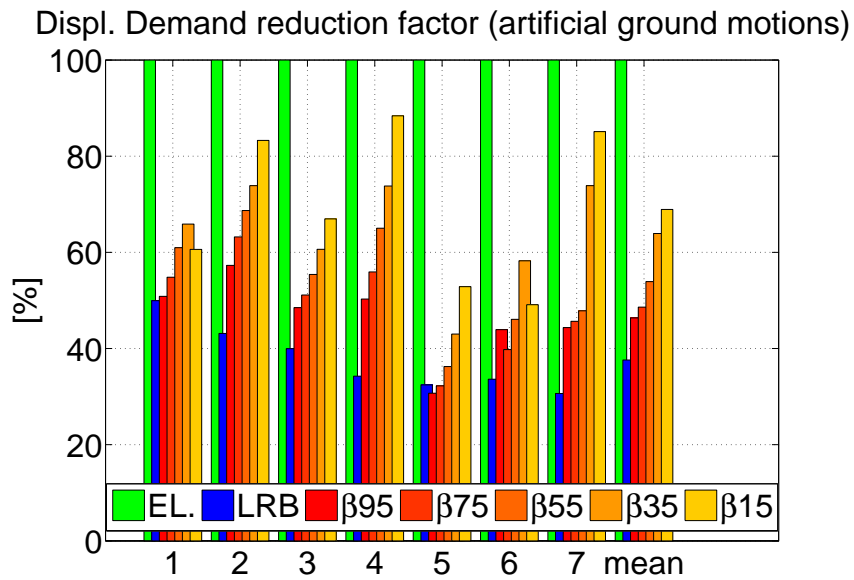
**Figure 5.41:** flag-shape hysteresis considering parameter  $\beta = 0.35$  (left) and flag-shape hysteresis considering parameter  $\beta = 0.15$  (right), from ground motion 5 THA.



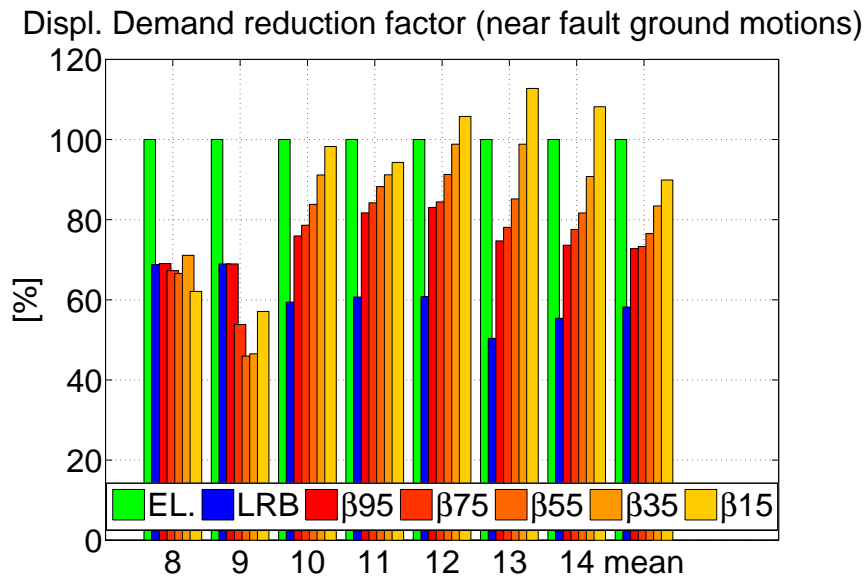
**Figure 5.42:** displacement demand values for different dissipation parameter  $\beta$  for artificial ground motions; the last set is the mean value of the previous ones.



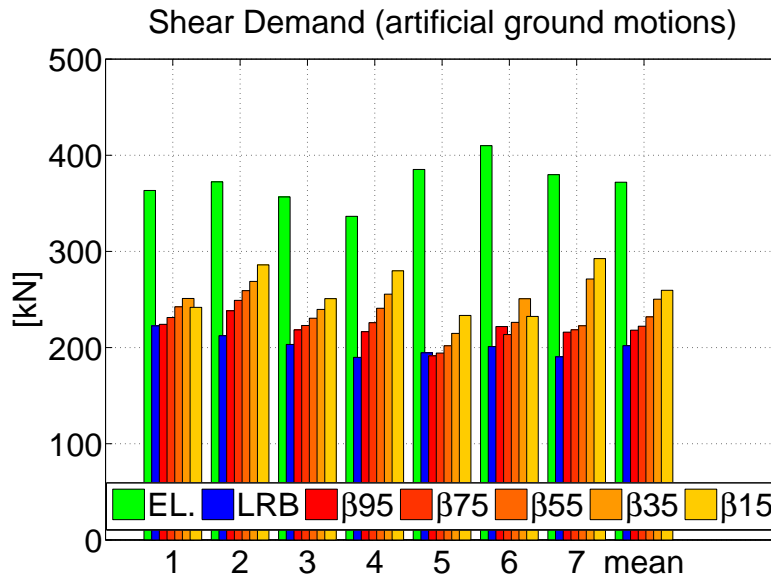
**Figure 5.43:** displacement demand values for different dissipation parameter  $\beta$  for near fault ground motions; the last set is the mean value of the previous ones.



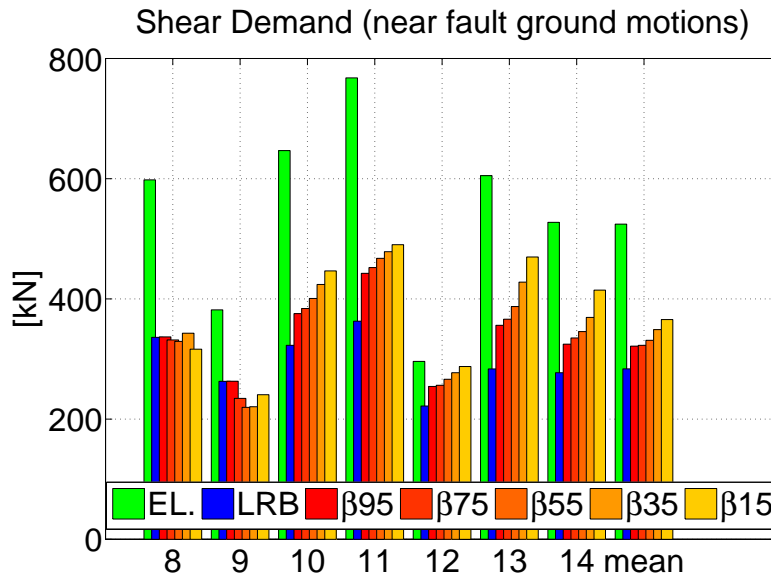
**Figure 5.44:** displacement demand values for different dissipation parameter  $\beta$  normalized to linear elastic system response for artificial ground motions; the last set is the mean value of the previous ones.



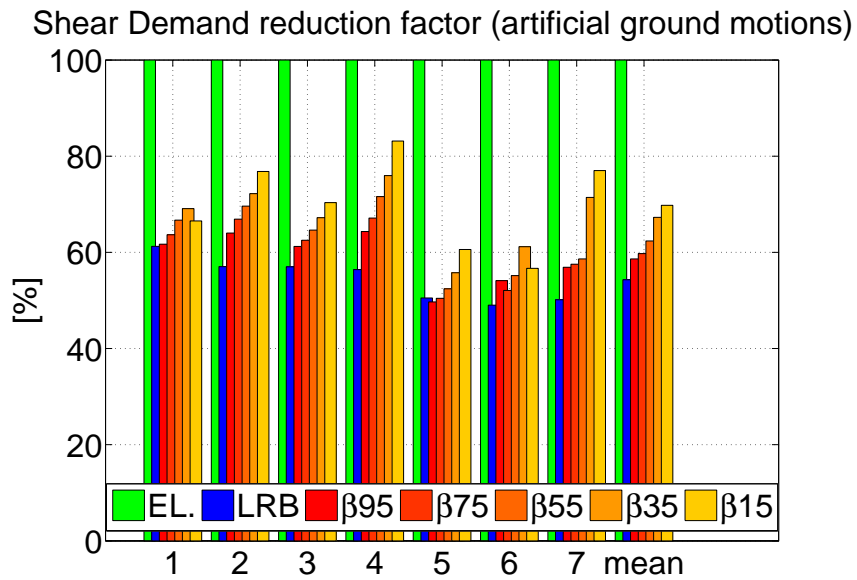
**Figure 5.45:** displacement demand values for different dissipation parameter  $\beta$  normalized to linear elastic system response for near fault ground motions; the last set is the mean value of the previous ones.



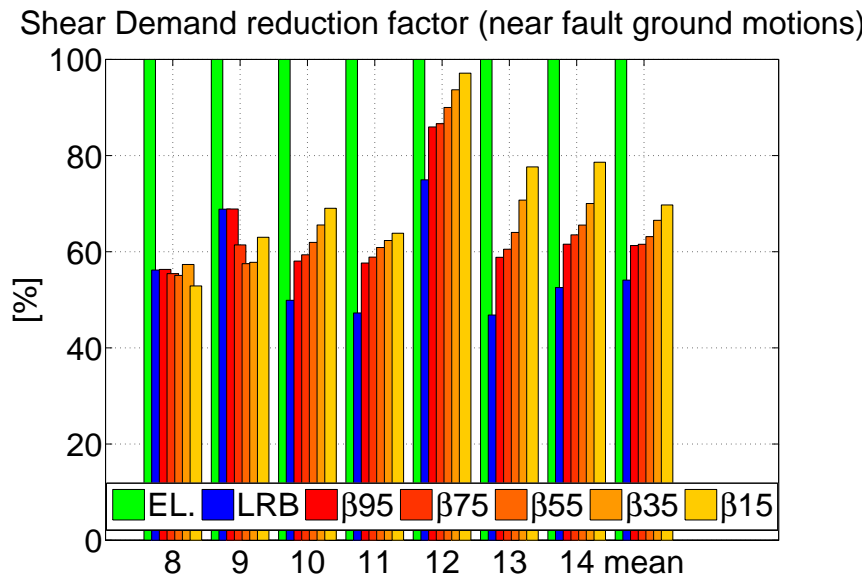
**Figure 5.46:** force demand values for different dissipation parameter  $\beta$  for artificial ground motions; the last set is the mean value of the previous ones.



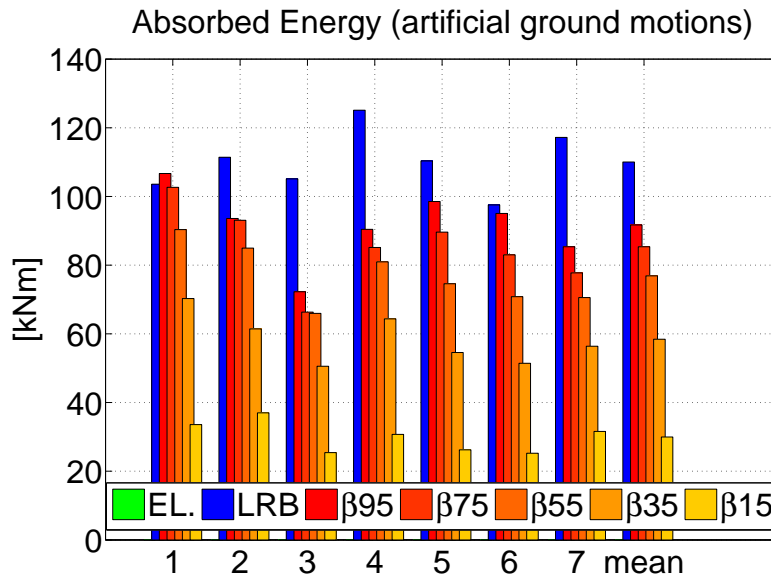
**Figure 5.47:** force demand values for different dissipation parameter  $\beta$  for near fault ground motions; the last set is the mean value of the previous ones.



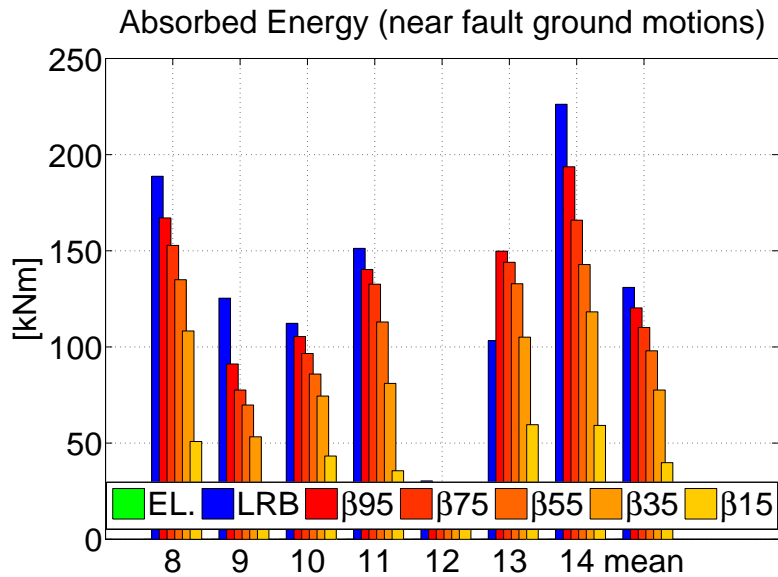
**Figure 5.48:** force demand values for different dissipation parameter  $\beta$  normalized to linear elastic system response for artificial ground motions; the last set is the mean value of the previous ones.



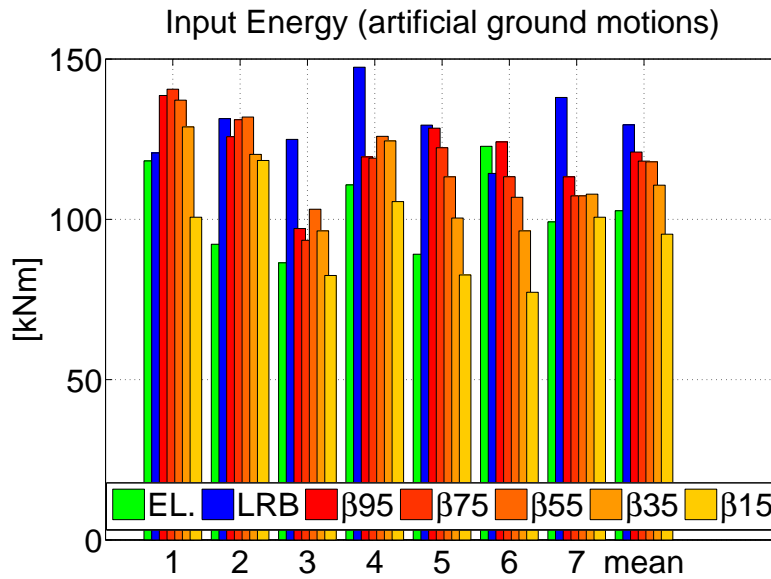
**Figure 5.49:** force demand values for different dissipation parameter  $\beta$  normalized to linear elastic system response for near fault ground motions; the last set is the mean value of the previous ones.



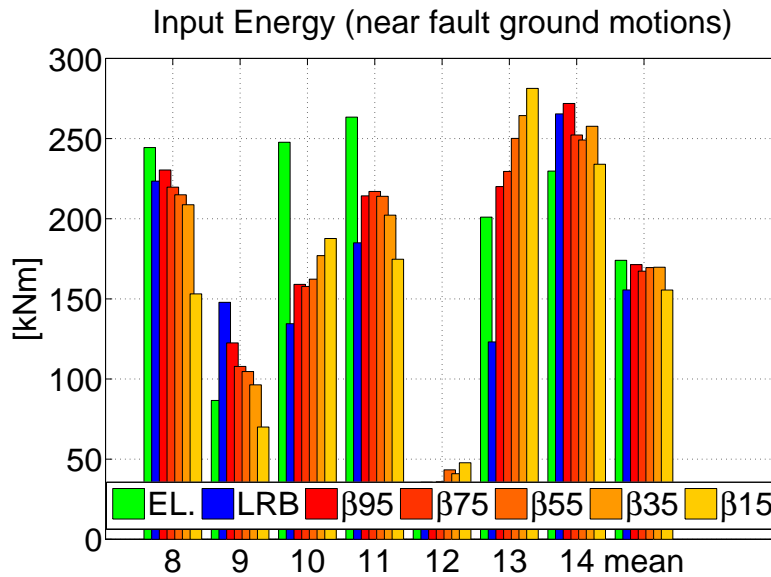
**Figure 5.50:** absorbed energy values for different dissipation parameter  $\beta$  for artificial ground motions; the last set is the mean value of the previous ones.



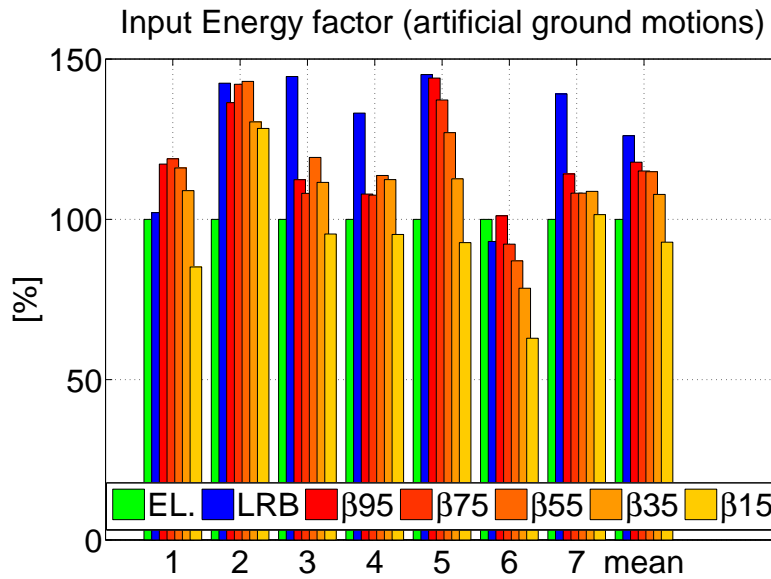
**Figure 5.51:** absorbed energy values for different dissipation parameter  $\beta$  for near fault ground motions; the last set is the mean value of the previous ones.



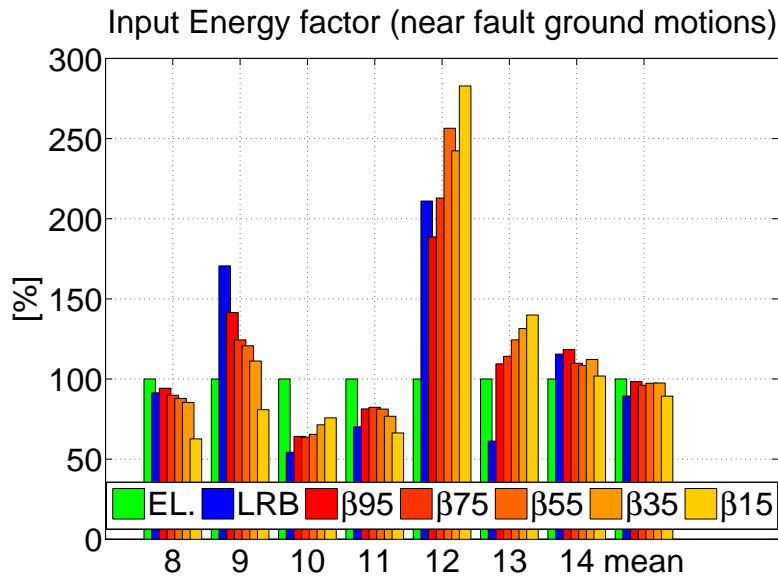
**Figure 5.52:** input energy values for different dissipation parameter  $\beta$  for artificial ground motions; the last set is the mean value of the previous ones.



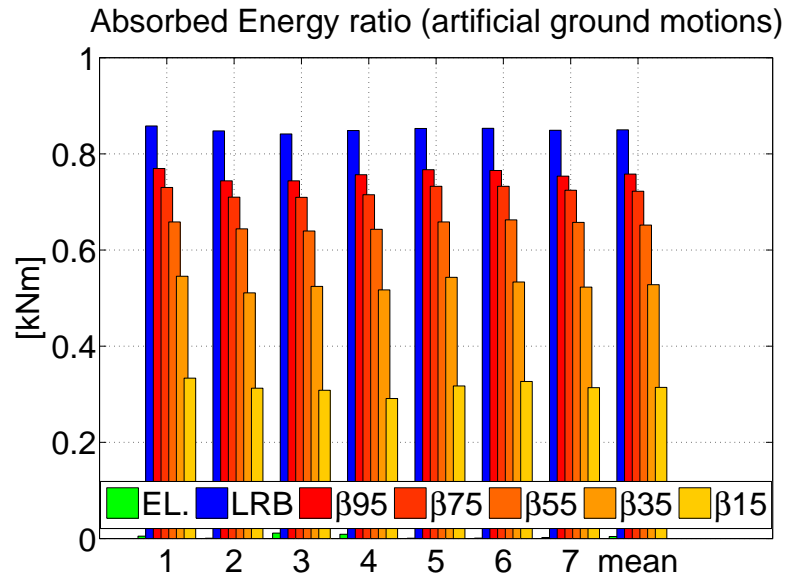
**Figure 5.53:** input energy values for different dissipation parameter  $\beta$  for near fault ground motions; the last set is the mean value of the previous ones.



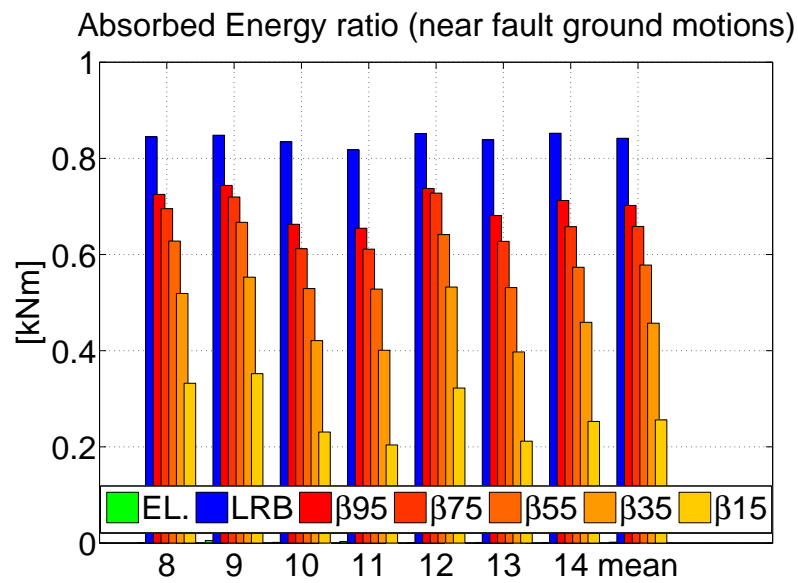
**Figure 5.54:** input normalized energy values for different dissipation parameter  $\beta$  for artificial ground motions; the last set is the mean value of the previous ones.



**Figure 5.55:** input normalized energy values for different dissipation parameter  $\beta$  for near fault ground motions; the last set is the mean value of the previous ones.



**Figure 5.56:** absorbed energy values for different dissipation parameter  $\beta$  normalized respect the input energy for artificial ground motions; the last set is the mean value of the previous ones.



**Figure 5.57:** absorbed energy values for different dissipation parameter  $\beta$  normalized respect the input energy for near fault ground motions; the last set is the mean value of the previous ones.

In general we notice that even changing significantly the dissipation factor and getting a flag shape hysteresis very narrow, the response is not extremely different respect the most dissipating case.

In particular, if we consider the shear demand, it is clear that similarities appear to be more important than differences.

In terms of displacement demand the strong reduction of dissipation increases sensibly the system demand, producing in some near fault events a displacement even larger than the one from linear elastic system. Anyway if we consider the hysteresis with a  $\beta$  value up to 0.55, results are not so different respect the value of  $\beta = 0.95$ .

Considering the hysteresis absorbed energy in Fig.(5.50) and Fig.(5.51), and in particular the values of absorbed energy with normalized with respect the input energy in Fig.(5.56) and Fig.(5.57), we conclude that for the three larger dissipating factors the results are quite close each other and comparable with respect to the elastoplastic case.

Even in the case with the lowest dissipation factor, with a small absorbed energy, the system response is still acceptable. This is due to the simultaneous reduction in absorbed energy and in input energy (given to the system from the seismic excitation) shown in Fig.(5.54), Fig.(5.55), Fig.(5.52) and Fig.(5.53).

As a general conclusion, the response of an idealized SDOF isolation system based on flag shape hysteresis considering different dissipations is quite good and comparable to the actual lead rubber response at least for a dissipation value in the range  $\beta \geq 50\%$ .

Finally, we compare the reduction factors we get from THAs with the ones we compute considering expressions for far field and near field presented in (5.7) and (5.8). Referring to the parameters in Tab.(5.2) and Tab.(5.3), the displacement ductility is  $\mu = 9.25$  and the hardening ratio  $r = 0.05$ . Evaluating different dissipation parameters  $\beta$ , we get the following comparison between reduction from formulas (5.4) and (5.6) and from time history analyses. We use the mean values for artificial and near fault ground motions, as reported in Tab.(5.4) and Tab.(5.5). Concerning the approximated formula for the equivalent viscous damping, we repeat the computations considering either the displacement ductility from the design displacement and the effective ductility from the displacement demand. Conceptually the approaches are very different and the effective ductility values are often sensibly different respect the design ones: nevertheless, differences in the reduction factors are negligible in the two computations. Resulting differences between the simplified expression based on the equivalent viscous damping and results of time history analyses are quite important, especially if related to the fact that it seems inappropriate to use the same reduction both for forces and displacements.

**Table 5.4:** reduction factor coefficients from equivalent damping formulas and THA comparison (artificial ground motions).

<i>Artificial ground motion reduction factors</i>						
	LRB	$\beta = 0.95$	$\beta = 0.75$	$\beta = 0.55$	$\beta = 0.35$	$\beta = 0.15$
eq.s (5.4) and (5.6) (design ductility)	0.45	0.59	0.64	0.70	0.77	0.88
eq.s (5.4) and (5.6) (effective ductility)	0.44	0.58	0.63	0.69	0.77	0.88
displacement - THA	0.37	0.46	0.48	0.53	0.63	0.68
force - THA	0.54	0.58	0.59	0.62	0.67	0.69

**Table 5.5:** reduction factor coefficients from equivalent damping formulas and THA comparison (near fault ground motions).

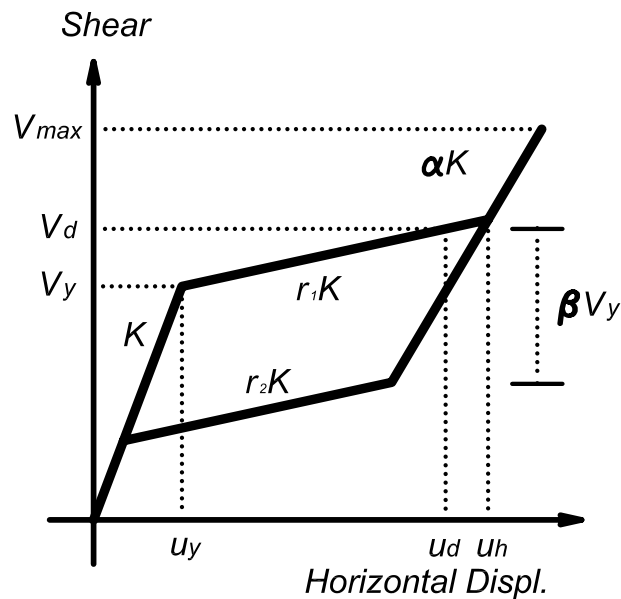
<i>Near Fault ground motion reduction factors</i>						
	LRB	$\beta = 0.95$	$\beta = 0.75$	$\beta = 0.55$	$\beta = 0.35$	$\beta = 0.15$
formulas (5.4) and (5.6) (design ductility)	0.67	0.77	0.80	0.84	0.88	0.93
eq.s (5.4) and (5.6) (effective ductility)	0.67	0.78	0.81	0.84	0.89	0.94
displacement - THA	0.58	0.72	0.73	0.76	0.83	0.89
force - THA	0.54	0.61	0.61	0.63	0.66	0.69

### 5.5.3 Evaluation of Result Sensibility to Second Hardening Effect

We are also interested in evaluating the sensibility of response to the presence of a second hardening branch in the flag-shape hysteresis.

Qualitatively we expect the hardening affects the response reducing and regularizing the displacement demand and in the same time increasing the force demand. At least in theory, the new hardening branch does not affect the dissipation capability of the system. Anyway, it can involve important changes in the equivalent SDOF approach. In particular we are interested in investigate sensibility of system secant stiffness and effective period.

Referring to Fig.(5.1), we consider now a constitutive force displacement relation characterized by an hardening effect at a particular displacement. In this case we consider  $u_h > u_d$ , hence we refer to the condition shown in Fig.(5.58). The parameters we use in the model are summarized in Tab.(5.6). Main parameters are the same of the previous case, reported in Tab.(5.3); in addition we consider a second hardening displacement at a ductility  $\mu_h = 10$ , being the design ductility  $\mu_d = 9.25$ . We assume the third stiffness is the 30% of the initial one and this



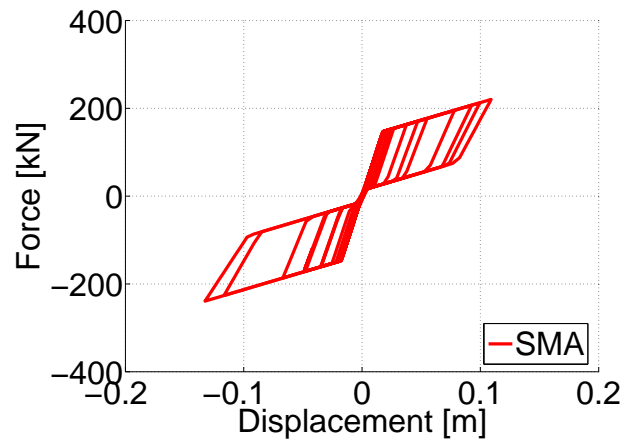
**Figure 5.58:** SMA simplified hysteresis model taking into account second hardening.

affects also the unloading phase after yielding. Since we investigate the effects of hardening not knowing the maximum force demand, at this stage we do not consider any limitation in material strength, so we set the maximum force capability to infinite. Regarding the dissipation, we analyze the same  $\beta$  range values investigated previously. The hysteresis rules we consider as a function of the dissipation parameters are shown in Fig.(5.64), Fig.(5.65) and Fig.(5.66).

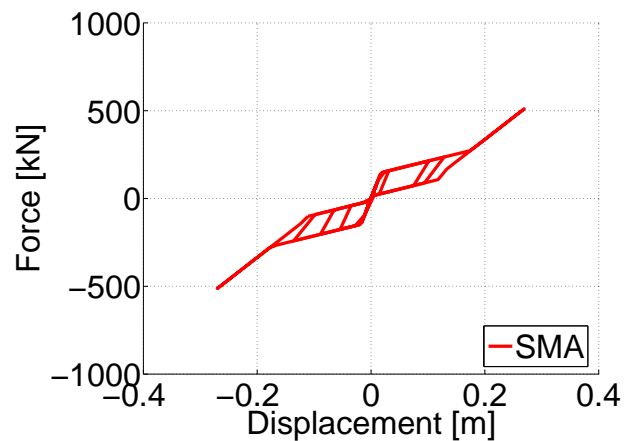
**Table 5.6:** flag-shape model parameters for SMA bearing equivalent to LRB diameter 500 mm [parameters as shown in Fig.(5.58)].

<i>SMA eq. LRB500</i>		
yielding shear	$V_y$	<b>147 kN</b>
design shear	$V_d$	<b>262 kN</b>
yielding displacement	$u_y$	<b>17.5 mm</b>
design displacement	$u_d$	<b>162 mm</b>
second hardening disp.	$u_h$	<b>175 mm</b>
initial stiffness	$k$	<b>8.4 kN/mm</b>
second stiffness $r_1 = r_2 = r$	$rk$	<b>0.8 kN/mm</b>
third stiffness ( $\alpha$ )	$\alpha k$	<b>2.52 kN/mm</b>
ultimate capacity	$V_{max}$	$\infty$
dissipation coefficient for parametric analyses	$\beta_1$	<b>95%</b>
	$\beta_2$	<b>75%</b>
	$\beta_3$	<b>55%</b>
	$\beta_4$	<b>35%</b>
	$\beta_5$	<b>15%</b>

In theory, force and displacement demand of the system is not supposed to exceed the plateau ( $\mu_d < \mu_h$ ), therefore the force displacement relation should be similar to the previous ones.



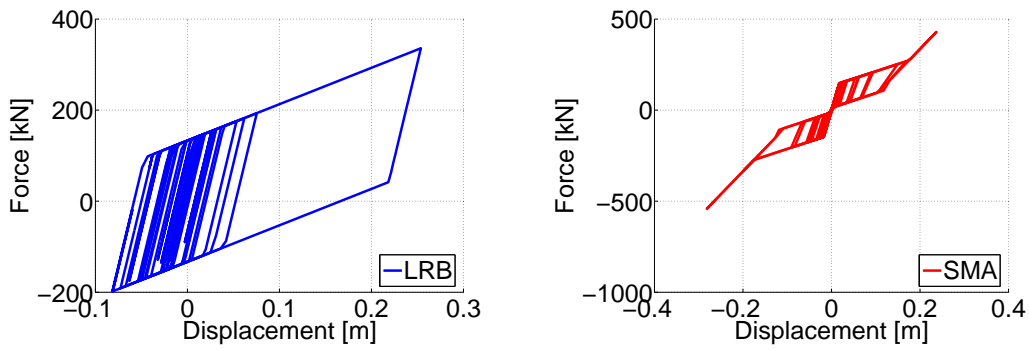
**Figure 5.59:** flag-shape hysteresis from ground motion 2 THA considering parameter  $\beta = 0.95$ .



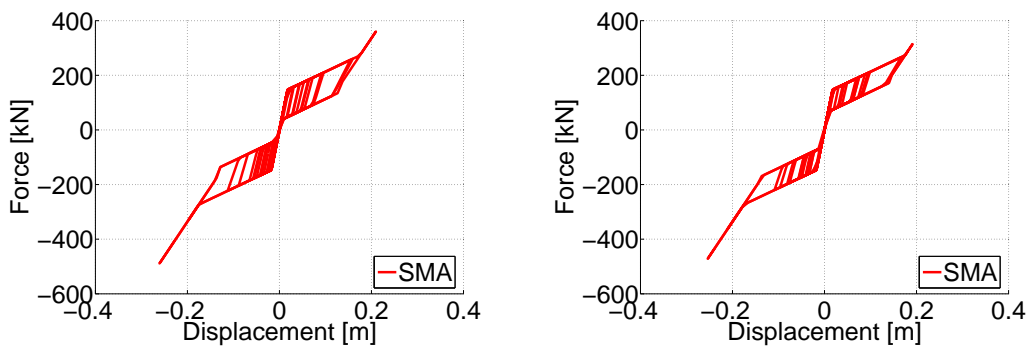
**Figure 5.60:** flag-shape hysteresis from ground motion 13 THA considering parameter  $\beta = 0.95$ .

Nevertheless, since we also consider near fault event, characterized by most irregular response due either by the energy content and by the approximated way they have been reduced, we take into account more complex situations in which the demand can be larger. This resulted also in previous analyses, because the near fault ground motion responses are more severe, characterized usually by larger displacements; we can show this comparing results from Fig.(5.42) with those in Fig.(5.43).

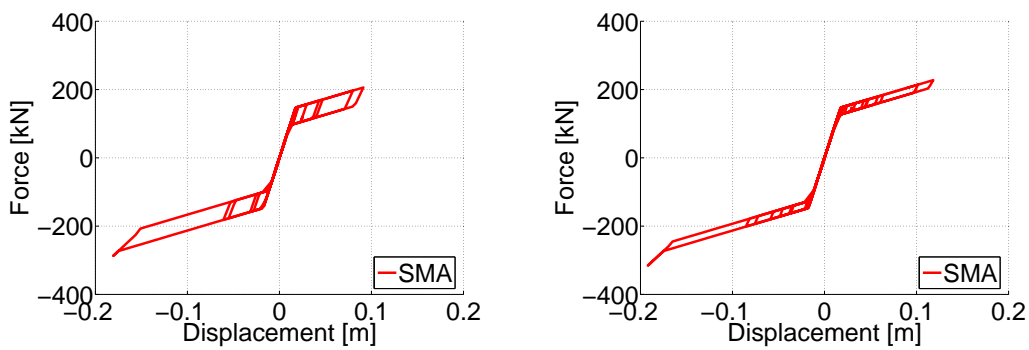
Artificial ground motion system response is quite regular, giving almost the same results than



**Figure 5.61:** elastoplastic hysteresis (left) and flag-shape hysteresis with second hardening (right) considering parameter  $\beta = 0.95$ , from ground motion 8 THA.



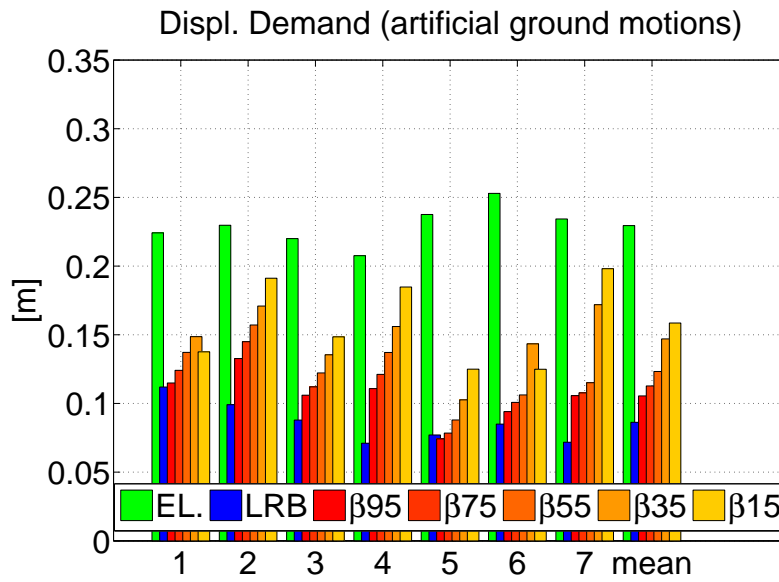
**Figure 5.62:** flag-shape hysteresis with second hardening considering parameter  $\beta = 0.75$  (left) and  $\beta = 0.55$  (right), from ground motion 8 THA.



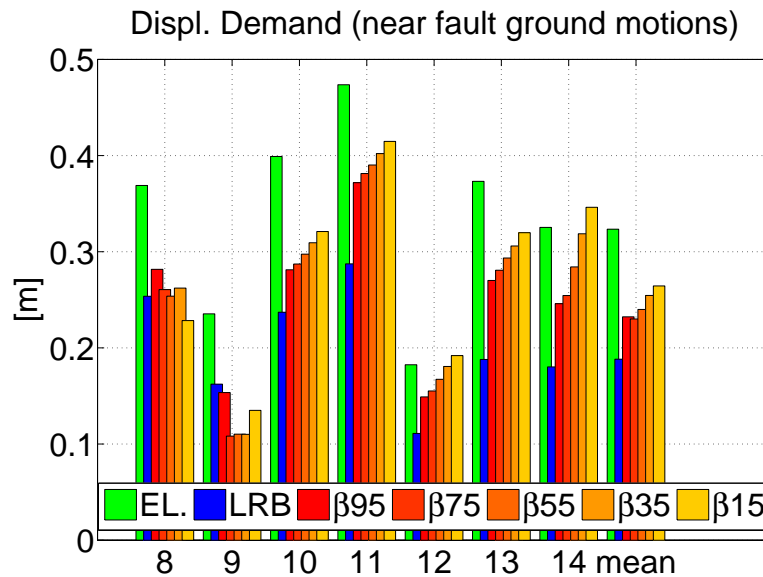
**Figure 5.63:** flag-shape hysteresis with second hardening considering parameter  $\beta = 0.35$  (left) and  $\beta = 0.15$  (right), from ground motion 12 THA.

in the previous cases, except the little difference in unloading branch stiffness (Fig.(5.59)). On the contrary, when we consider near fault ground motion, system often reaches the second hardening branch, as shown in Fig.(5.60). In some specific cases the design force is exceeded by almost the 100%.

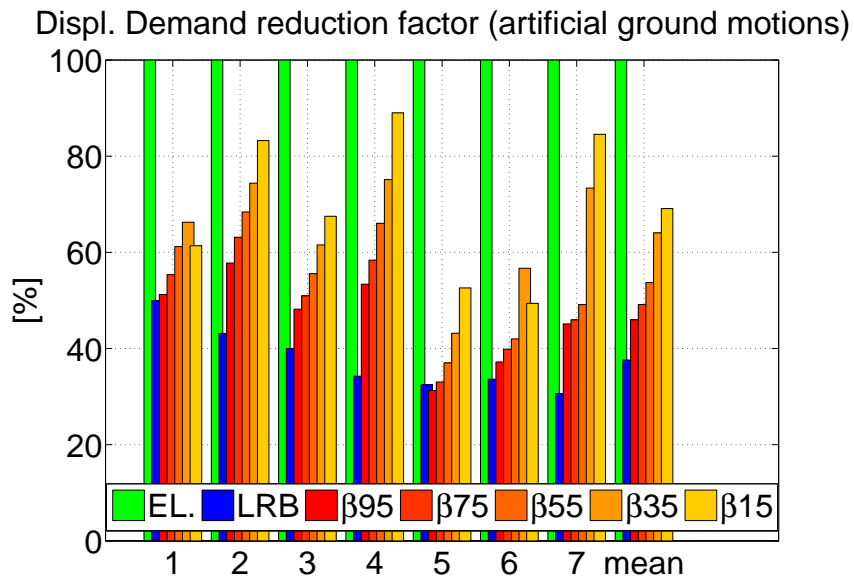
A summary of the THA results in terms of displacements considering also a second stiffness branch is shown in Fig.(5.64), Fig.(5.65), Fig.(5.66) and Fig.(5.67). The response in terms of force envelope is shown in Fig.(5.68), Fig.(5.69), Fig.(5.70) and Fig.(5.71). The absorbed energy graphs are shown in Fig.5.72 and Fig.(5.73).



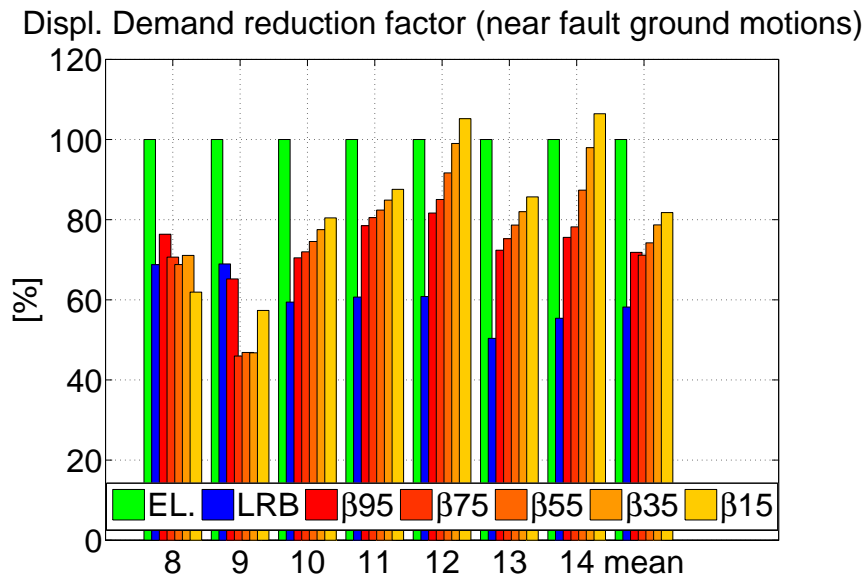
**Figure 5.64:** displacement demand values for different dissipation parameter  $\beta$  considering second hardening for artificial ground motions; the last set is the mean value of the previous ones.



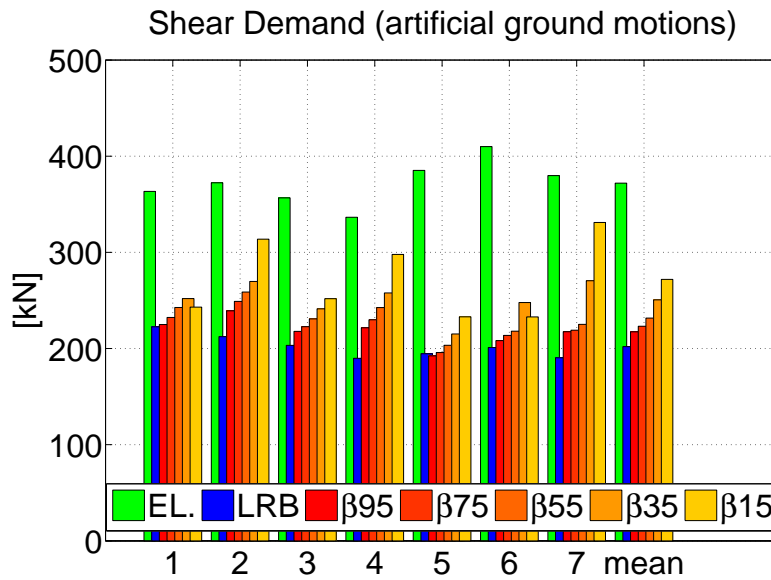
**Figure 5.65:** displacement demand values for different dissipation parameter  $\beta$  considering second hardening for near fault ground motions; the last set is the mean value of the previous ones.



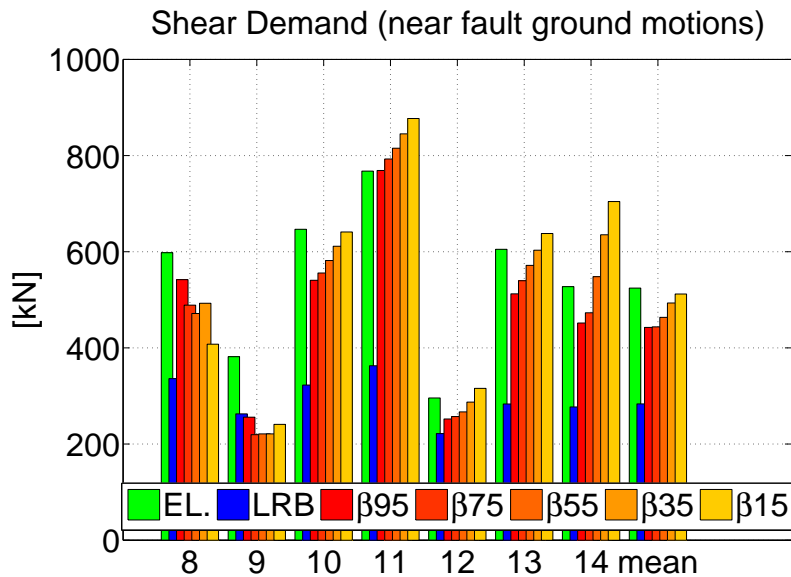
**Figure 5.66:** displacement demand values for different dissipation parameter  $\beta$  considering second hardening normalized to linear elastic system response for artificial ground motions; the last set is the mean value of the previous ones.



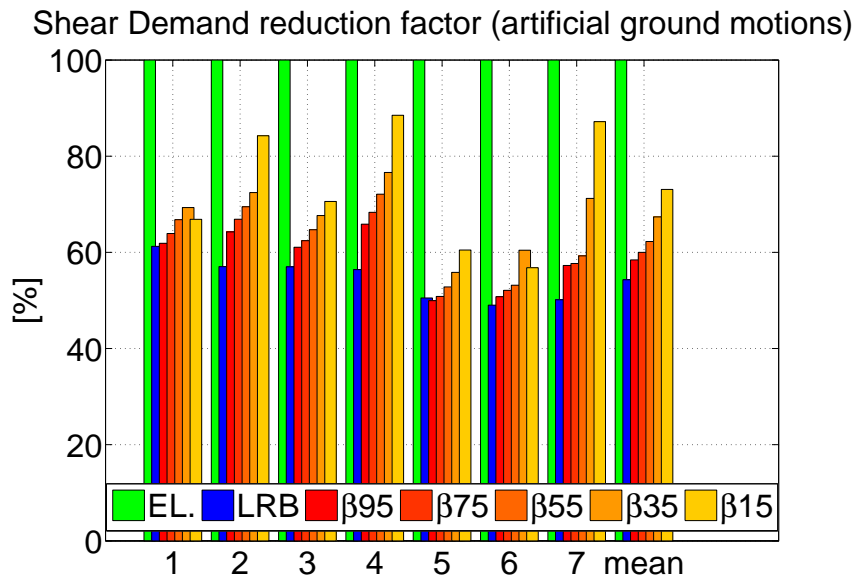
**Figure 5.67:** displacement demand values for different dissipation parameter  $\beta$  considering second hardening normalized to linear elastic system response for near fault ground motions; the last set is the mean value of the previous ones.



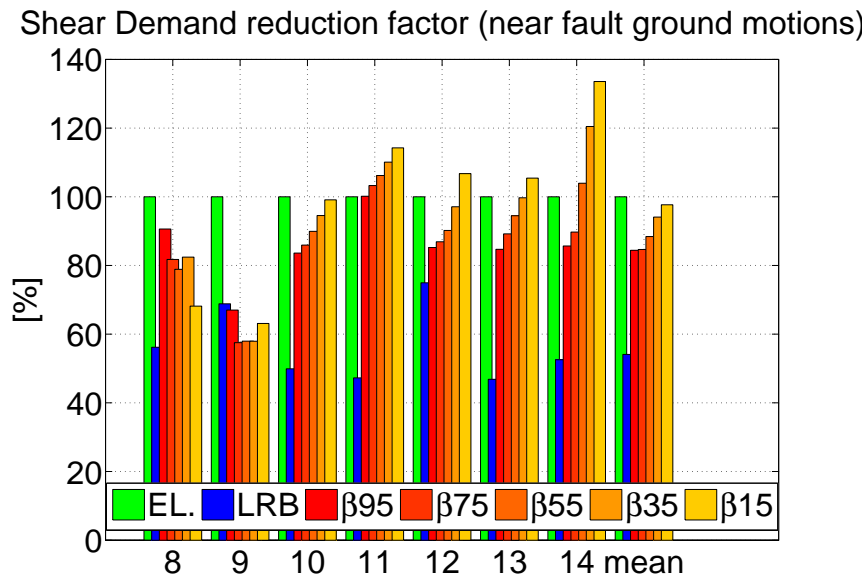
**Figure 5.68:** force demand values for different dissipation parameter  $\beta$  considering second hardening for artificial ground motions; the last set is the mean value of the previous ones.



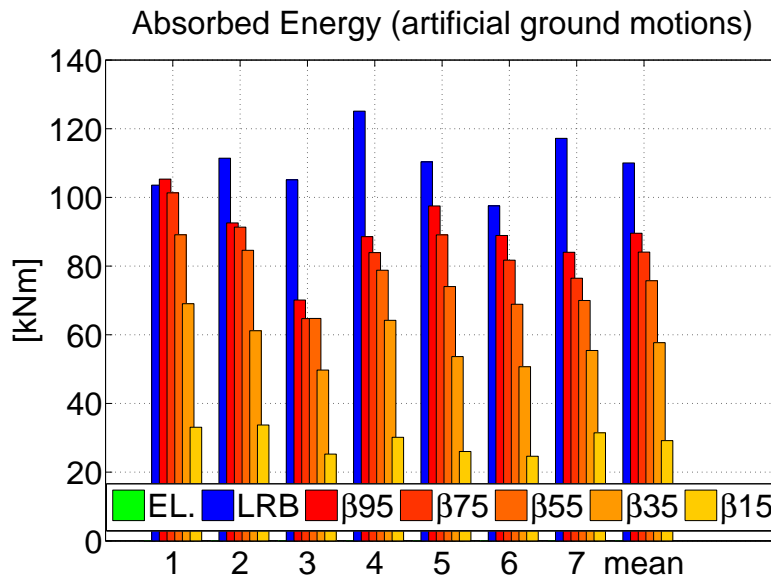
**Figure 5.69:** force demand values for different dissipation parameter  $\beta$  considering second hardening for near fault ground motions; the last set is the mean value of the previous ones.



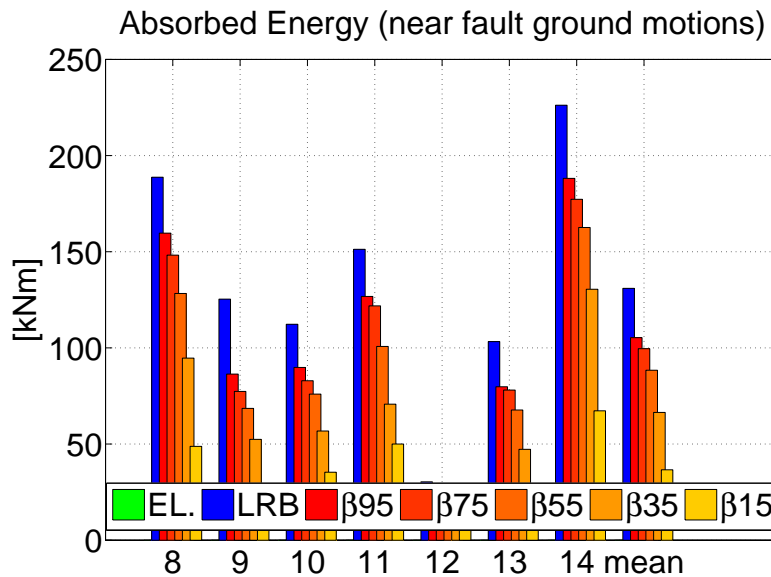
**Figure 5.70:** force demand values for different dissipation parameter  $\beta$  considering second hardening normalized to linear elastic system response for artificial ground motions; the last set is the mean value of the previous ones.



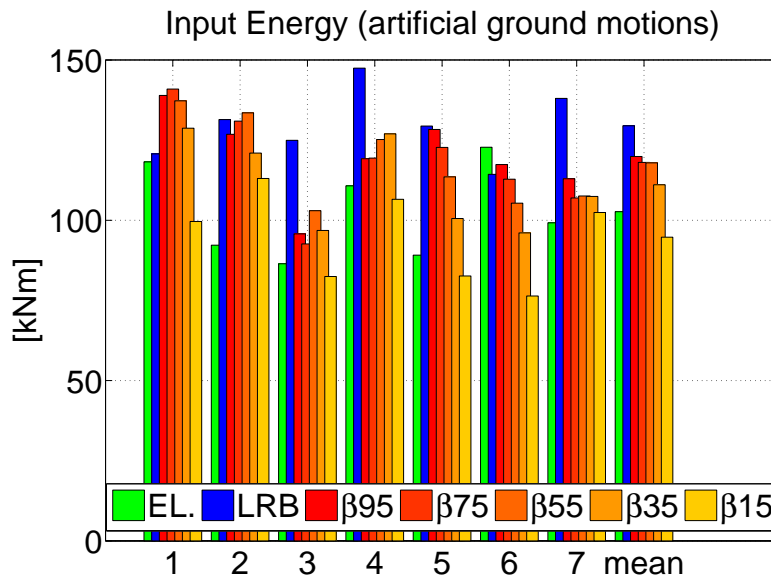
**Figure 5.71:** force demand values for different dissipation parameter  $\beta$  considering second hardening normalized to linear elastic system response for near fault ground motions; the last set is the mean value of the previous ones.



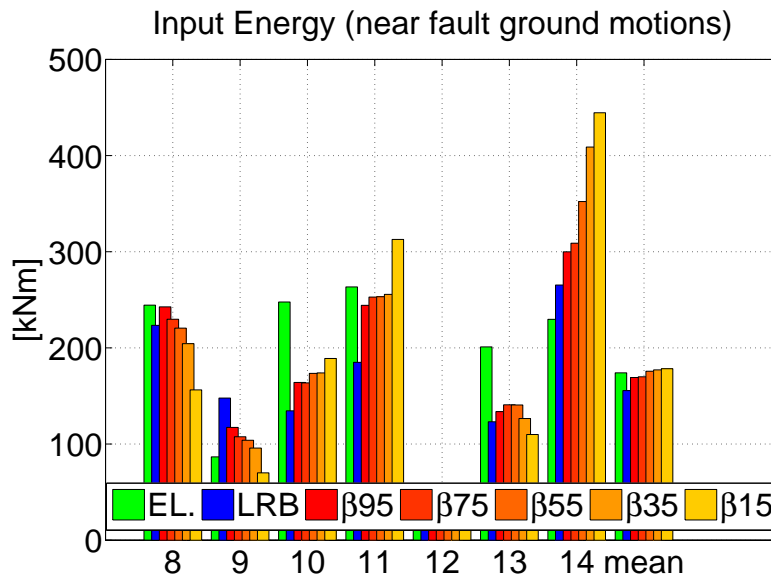
**Figure 5.72:** absorbed energy values for different dissipation parameter  $\beta$  considering second hardening for artificial ground motions; the last set is the mean value of the previous ones.



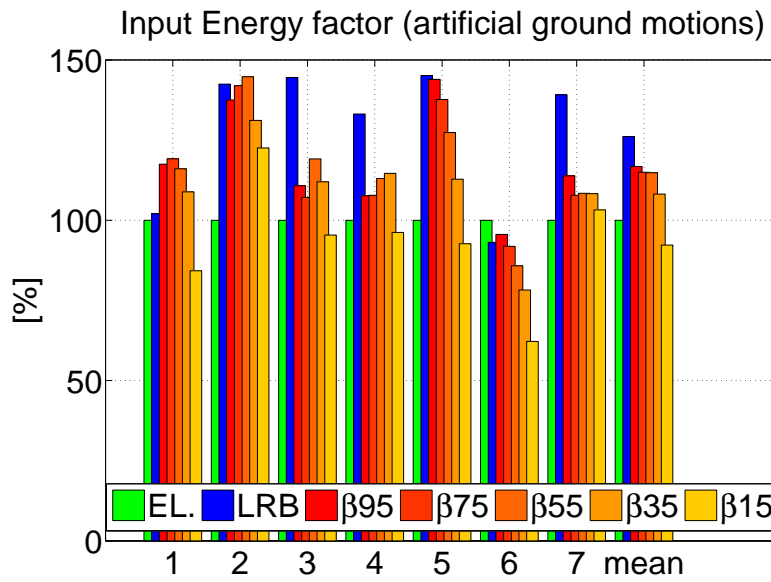
**Figure 5.73:** absorbed energy values for different dissipation parameter  $\beta$  considering second hardening for near fault ground motions; the last set is the mean value of the previous ones.



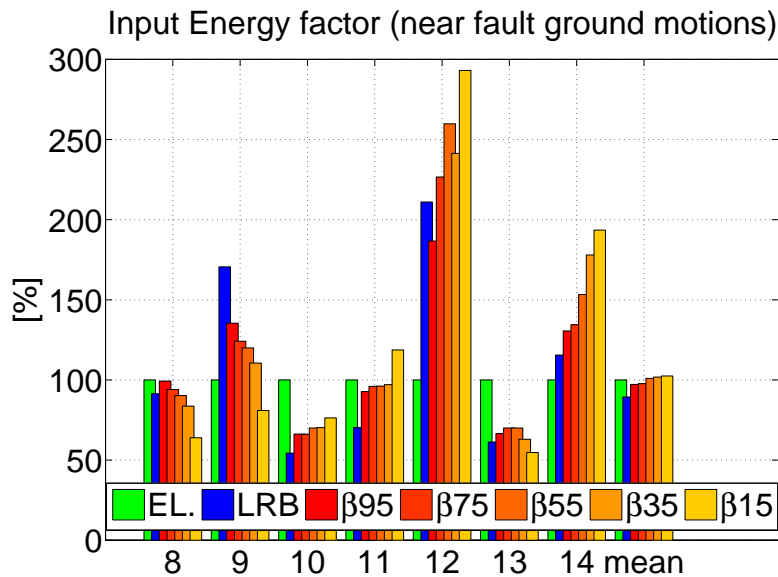
**Figure 5.74:** input energy values for different dissipation parameter  $\beta$  considering second hardening for artificial ground motions; the last set is the mean value of the previous ones.



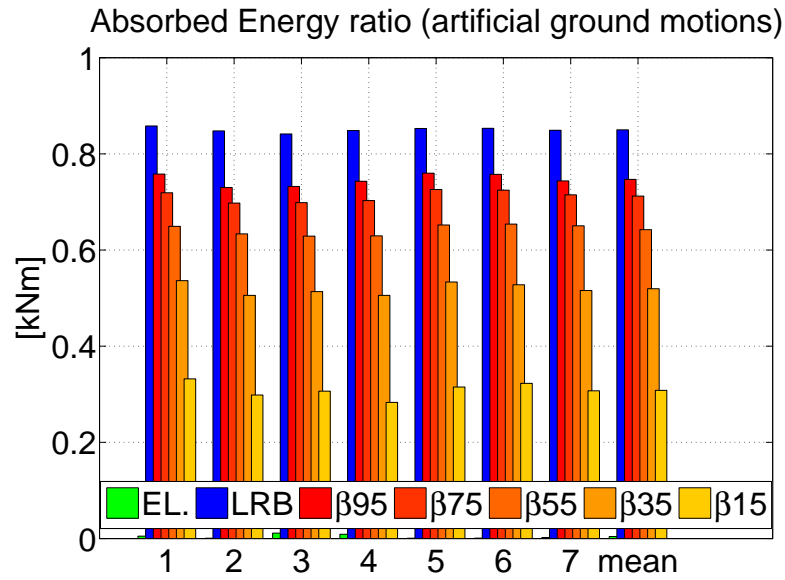
**Figure 5.75:** input energy values for different dissipation parameter  $\beta$  considering second hardening for near fault ground motions; the last set is the mean value of the previous ones.



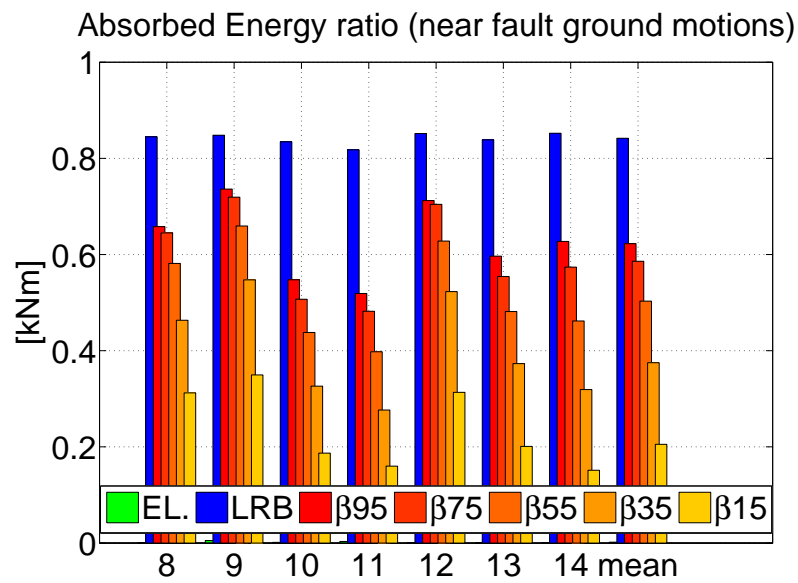
**Figure 5.76:** input normalized energy values for different dissipation parameter  $\beta$  considering second hardening for artificial ground motions; the last set is the mean value of the previous ones.



**Figure 5.77:** input normalized energy values for different dissipation parameter  $\beta$  considering second hardening for near fault ground motions; the last set is the mean value of the previous ones.



**Figure 5.78:** absorbed energy values for different dissipation parameter  $\beta$  normalized respect the input energy for artificial ground motions; the last set is the mean value of the previous ones.



**Figure 5.79:** absorbed energy values for different dissipation parameter  $\beta$  normalized respect the input energy for near fault ground motions; the last set is the mean value of the previous ones.

General analysis of results leads to following conclusion for the main response variables:

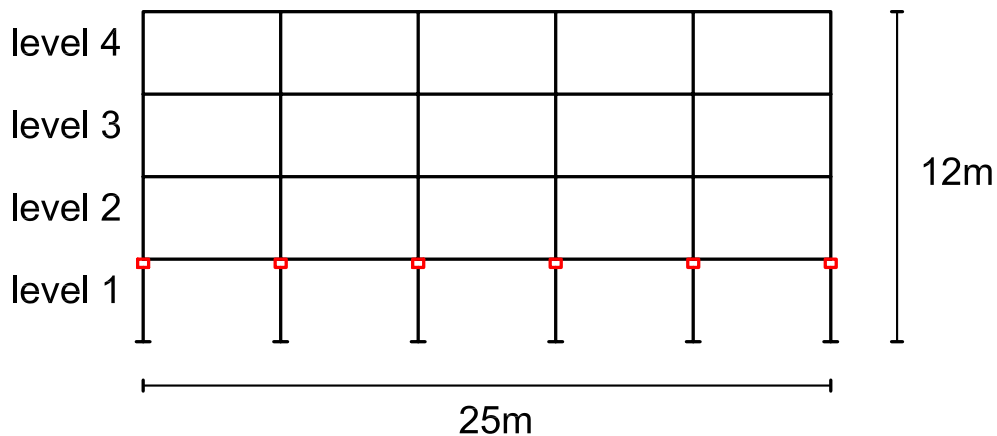
- Displacements
  - artificial ground motions: the response is almost the same of the previous case, differences are negligible as can be seen from the comparison between Fig.(5.42) and Fig.(5.64);
  - near fault ground motions: presence of second hardening branch regularizes the displacement demand of different dissipation models; this means that, merely in terms of displacement demand, the response of low dissipation SMA models is closer to the one of large dissipation for the same ground motion; in general for low dissipation systems the displacement is lower with respect to the case without second hardening as turns out from comparison between Fig.(5.44) and Fig.(5.66).
- Forces
  - artificial ground motions: from comparison between Fig.(5.46) and Fig.(5.68) differences are small and affect only the low dissipation model analyses;
  - near fault ground motions: comparing Fig.(5.46) with Fig.(5.68) we conclude that, when we consider the second hardening, the shear demand is sensibly higher with respect to the normal flag-shape model. These large force demand is related to the displacements regularization noted in the previous section; even if in terms of displacement differences are small, it turns out that in terms of forces they are very important.
- Absorbed energy
  - in terms of absorbed energy there are no differences between the second hardening model and the normal one because hardening is just a linear elastic force-displacement relation without any dissipation.
- Input energy
  - artificial ground motions: from comparison between Fig.(5.52) and Fig.(5.74) differences are very small;
  - near fault ground motions: comparing Fig.(5.53) with Fig.(5.75) differences are important between the two model and in general, if the shear demand increases, also the input energy significantly increases, especially for low dissipation models; anyway that is not a general conclusion because in some cases input energy decreases.

Regarding the evaluation of second hardening effects in force-displacement relation we can conclude that there are several disadvantages in having a structural behavior based on an excursion in the second hardening branch of the constitutive relation. This is a potential cause of structural force demand increasing up to a high level and reaching the material strength limit. Therefore the goal in the design process of the superelastic device is to avoid any excursion to second hardening force-displacement range.

## 5.6 FLEXIBLE SUPERSTRUCTURE APPROACH TIME HISTORY ANALYSES RESULTS

We also perform time history analysis comparisons considering flexible superstructure to investigate the isolation system effectiveness when the superstructure deformability is not negligible. We consider a simplified design procedure for a base isolated building to get a structural configuration compatible with the original isolator characteristics. In particular we look for a structure in which the fundamental period is close enough considering the isolated and the not-isolated case.

### 5.6.1 Simplified Design Procedure Structure



**Figure 5.80:** geometric outline of the frame system we are considering for the flexible superstructure approach.

The structure we analyze is shown in Fig.(5.80). We take into account a plane frame with five bays spanning 5 meters each and four levels being the interstorey height 3 meters.

The isolation system is located at the first level, so the first floor is fixed with the foundations and the first slab is rigid and isolated from the first level of columns and foundations. The

design philosophy is to isolate the upper stories, which are supposed to resist the seismic event elastically and to design the first storey to resist to the maximum load without plastic damage, assuming rigid foundations. We design to have two column sections: the first is assigned in the first level, the fixed one with stiff large dimension elements; the second column section is assigned in the upper levels and it is smaller. The beam section is constant in all the levels and it is small to provide the required flexibility to the superstructure. The geometric properties are summarized in Tab.(5.7).

**Table 5.7:** frame model geometric properties.

<b><i>Test Frame Properties</i></b>		
Materials		
Concrete Elastic Modulus	$E$	25000 <i>MPa</i>
Concrete Poisson Modulus	$\nu$	10000 <i>MPa</i>
Beams		
Depth	$d_b$	0.40 <i>m</i>
Width	$w_b$	0.25 <i>m</i>
1 <sup>st</sup> level Columns		
Depth	$d_{1c}$	0.80 <i>m</i>
Width	$w_{1c}$	0.80 <i>m</i>
upper level Columns		
Depth	$d_{uc}$	0.40 <i>m</i>
Width	$w_{uc}$	0.30 <i>m</i>

We model the isolation system considering a spring element, like in the previous SDOF system analysis. We assume lumped masses in the beam-column intersections and we compute them to get in the tributary area of every device the design isolator seismic combination weight. The only exception is in the external column isolators, where the mass is one half of the design one. In the internal beam column joints we assign a weight of  $413kN$ , while in the external ones the weight is  $207kN$ . Hence in the internal columns, considering four times (the number of levels) the acting weight, we get the same design load reported in the isolator device design parameters of Tab.(5.1).

The non-isolated structure is characterized by a fundamental mode of vibration period equal to 1.07 seconds, and a summary of the not isolated building modal informations is reported in Tab.(5.8).

Modeling the isolation system with an equivalent linear secant stiffness using parameters in Tab.(5.1), we get the modal properties reported in Tab.(5.9).

**Table 5.8:** modal properties from not isolated structure analysis.

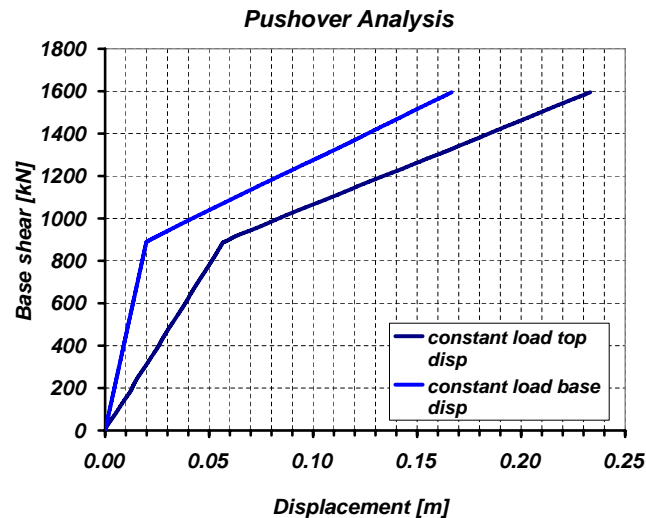
<i>Not Isolated Modal Frame Properties</i>		
Mode Number	Vibration Period	Participating Mass
1	1.07s	69%
2	0.33s	10%
3	0.18s	3%
4	0.09s	16%

**Table 5.9:** modal properties from isolated structure analysis.

<i>Isolated Modal Frame Properties</i>		
Mode Number	Vibration Period	Participating Mass
1	2.14s	98.3%
2	0.58s	1.6%

Obviously, in the isolated case the first mode of vibration consists in the relative movement of the upper levels on the base isolated system and the other modal contributions are negligible. Since the fundamental period elongation from the not-isolated to the isolated case is about the 100%, we can consider the superstructure as a flexible element. Moreover, the natural period computed based on the secant stiffness of 2.14 seconds corresponds to a design Eurocode 8 soil C displacement spectra ordinate of about 0.31 meters (Fig.(5.23)), and if we consider the reduction factor due to lead rubber bearing hysteresis equal to 0.55 (as reported in (5.24)), we get a design displacement of about 0.17 meters which is very close to the value in (5.25).

Before conducting the time history analyses we investigated structural properties through a pushover analysis. The applied load pattern is constant with the height of the building; it represents the first mode of vibration which is characterized by a displacement occurring mainly at the isolation level. The system capacity curve, governed by the isolation properties, is the same for both the isolation solutions, the lead rubber one and the shape memory alloy one. In fact we consider the same initial stiffness and the same hardening; therefore there is no difference when the structure is subjected to monotonically increasing lateral load. In the analysis, we evaluate displacements in two points of control, one at the top of the structure and one at the first slab level. When we consider the base shear and the first slab level displacement, we are taking into account the behavior of the isolation system alone. Comparing the latest with the top slab displacement curve, we investigate the real flexibility of the superstructure and the displacement given by its contribution. The capacity curves from pushover analysis are shown in Fig.(5.81). We increase maximum base force till reaching the double of the yielding force. This maximum



**Figure 5.81:** capacity curve from pushover analysis of the structure; a uniform lateral load has been considered and two displacement control points have been taken into account, one at the base of the superstructure and one at the top of it.

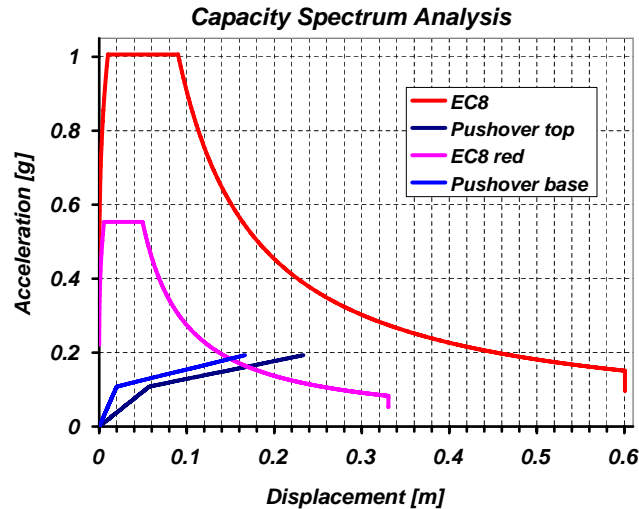
force produces a maximum drift equal to 1.94% in this structure.

**Table 5.10:** base shear and control point displacements from pushover analysis.

<b>Pushover Frame Analysis</b>		
yielding base shear	$V_{y \text{ base}}$	882 kN
yielding 1 <sup>st</sup> level displacement	$D_{y \text{ base}}$	0.020 m
yielding 4 <sup>th</sup> level displacement	$D_{y \text{ top}}$	0.056 m
superstructure displacement	$D_{y \text{ ss}}$	0.036 m
ratio of ss. displ. over total	$\Delta_{y \text{ ss}}$	66%
maximum Base Shear	$V_{\text{max base}}$	1600 kN
maximum 1 <sup>st</sup> level displacement	$D_{\text{max base}}$	0.167 m
maximum 4 <sup>th</sup> level displacement	$D_{\text{max top}}$	0.233 m
superstructure displacement	$D_{\text{max ss}}$	0.066 m
ratio of ss. displ. over total	$\Delta_{\text{max ss}}$	28%

In both the curves of Fig.(5.81), the yielding point is due to yielding in the isolation system. Pushover analysis results are summarized in Tab.(5.10).

The capacity spectrum analysis considering the two pushover curves and the design Eurocode 8 displacement acceleration spectra is shown in Fig.(5.82). If we consider the reduction factor given by the hysteretic damping of the lead rubber bearing, the design displacement of the system results between 0.160 and 0.175 meters, which corresponds to the actual LRB isolator design value.



**Figure 5.82:** capacity spectrum analysis: simulated design frame pushover curve compared with the design spectra at 5% damping and reduced considering the coefficient in (5.24).

### 5.6.2 Time History Analysis Isolation System Modeling

We perform time history analyses using as a seismic input the same ground motions we used previously (appendix A). The analyses of single degree of freedom has demonstrated that the structural behavior is better if the hardening effect in the flag shape hysteresis rule is avoided. Hence we perform analysis considering the same model described in Tab.(5.3) and Fig.(5.5), with no second hardening and considering the different dissipation parameter values  $\beta$  reported in Tab.(5.6). Then we carry on a results comparison.

Considering the same procedure we described in section 5.4 (b) we investigate the isolator device behavior given by the following force-displacement relations:

- elastoplastic (Fig.(5.16)), to reproduce the lead rubber bearing system;
- flag-shape (Fig.(5.17)), for the equivalent shape memory alloy hysteresis;
- linear elastic (Fig.(5.18)), to compare the previous responses with the equivalent secant isolation system stiffness.

An important issue in this context is the global structural damping evaluation. We want to take into account explicitly in the equation of motion only the viscous component of the isolation devices. In fact THAs are supposed to gain estimation of hysteretic dissipations.

The model in this case is more complex with respect to the SDOF because we have to take into

account the isolation system and superstructure contributions. We assume the superstructure to be characterized by a 5% equivalent viscous damping.

In the case of linear elastic modeling for the isolation devices, we consider a 5% damping ratio in all the modes. To compare the results, we have to take into account the same damping contribution also in the other models, so we compute the same percentage for elastoplastic and flag shape models also, referred to the secant stiffness to the design displacement. Given the initial stiffness of the nonlinear models, to use the 5% ratio of the secant stiffness is equivalent than to assume a 2.2% ratio of the initial stiffness of the isolation device. Unfortunately, in this case we have to combine it with the super structure damping; we decide to use a weighted sum of it to take into account all the flexibility sources in the structural first mode. According to (3.14), at the isolator design displacement, we have:

$$\begin{aligned}
 \xi_{e,sys} &= \frac{\xi_{e,is} \Delta_{d,is} + \xi_{e,ss} \Delta_{d,ss}}{\Delta_{d,is} + \Delta_{d,ss}} = \\
 &= \frac{\xi_{e,is} D_{max\ base} + \xi_{e,ss} D_{max\ ss}}{D_{max\ top}} = \\
 &= \frac{2.2 \cdot 0.167 + 5 \cdot 0.066}{0.233} = 3
 \end{aligned} \tag{5.26}$$

in which  $\Delta_{d,is}$  and  $\Delta_{d,ss}$  are respectively the design displacement of the isolation system and of the superstructure and we approximate them considering the values  $D_{max\ base}$  and  $D_{max\ ss}$  from the pushover analysis to the design displacement;  $\xi_{e,is}$  and  $\xi_{e,ss}$  are respectively the damping coefficient of the isolation system and of the superstructure. From the (5.26) the system viscous damping for the first mode is equal to 3% of the critical one, still computed on the initial stiffness. Hence we perform analyses of lead rubber bearing frame isolated system and of shape memory alloys device frame isolated system considering the value  $\xi_{e,sys} = 3\%$  in the fundamental mode.

### 5.6.3 Evaluation of Results considering different SMA Dissipation Capabilities

To investigate response of flexible superstructure system we report results in term of floor shear, floor displacement and acceleration demand. They are summarized in this sections and reported in more detail in appendix C. We did not normalize results to make possible a comparison between the different storey level responses.

- Displacements.

The first comparison concerns displacements at different floor levels. Of course the lateral

displacement occurs almost only in the isolation system level; therefore the interstorey drift is quite small in all the time history tests in the higher levels.

As we have noticed before, the near fault ground motions are usually more severe than artificial ground motions. Also in storey displacement comparison between artificial ground motions in Fig.(5.83) and near fault ground motions in Fig.(5.84), we notice that the mean displacement demands in the near field time histories are larger. Moreover the standard deviations in the near fault event is significantly larger than in the artificial ground motion case (Fig.(5.89)), showing a large dispersion of results in the near event responses.

Test results confirm that the displacement demand is larger in equivalent secant stiffness linear elastic system than in nonlinear hysteresis models. The reduction which takes into account of the hysteretic dissipation with respect the secant linear model is larger for artificial ground motion but important also for near fault events. Displacement reduction factor increases with the increase of the floor level number. Concerning the elastoplastic and flag-shape model comparison, responses are not very different at least for the higher range of SMA dissipation parameters. Obviously large dissipating flag shape hysteresis models performs better than the less dissipating ones, but if the flag shape dissipation factor  $\beta$  is at least about  $\beta \simeq 50\%$ , the maximum displacement demand in flag-shape model is similar to the one of lead rubber bearing isolation device.

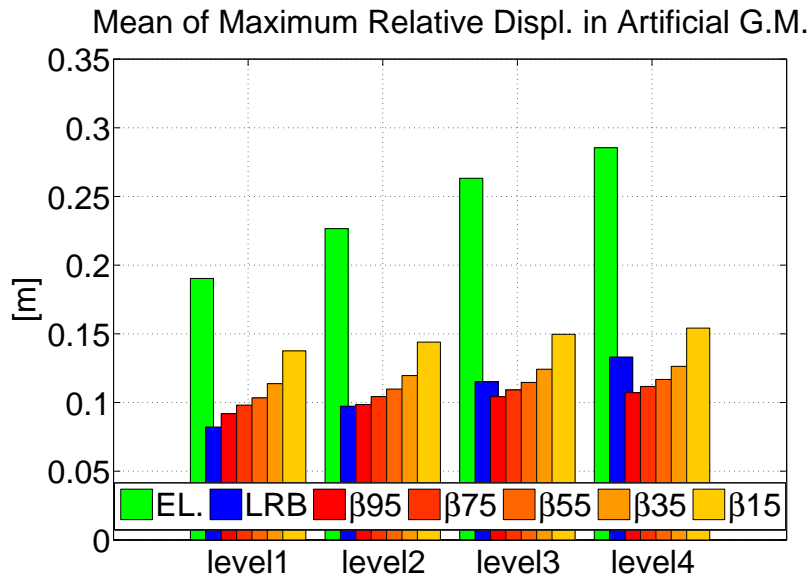
- Accelerations.

Seismic isolation reduces the acceleration demand at the storey levels with respect the not-isolated structure. Regarding the model comparison anyway, the nonlinear hysteresis models turns out to produce larger mean accelerations than the linear elastic secant stiffness model. However, still there are not big differences between lead rubber bearing and SMA hysteresis, considering all the range of dissipating values, either in artificial ground motion floor acceleration envelopes (Fig.(5.85)) and in near fault ones (Fig.(5.86)). The comparison is completed with the standard deviation plots in Fig.(5.90) which prove a larger scatter in the near fault events.

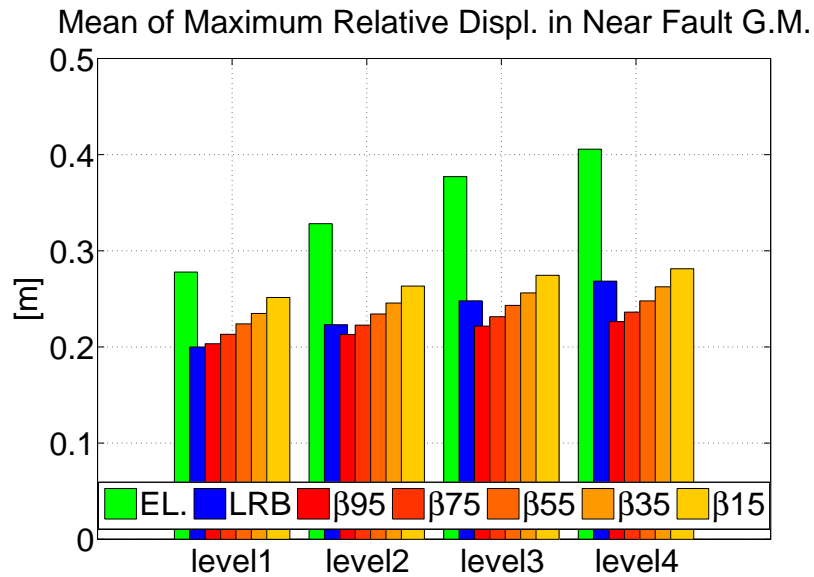
- Shear values.

In terms of mean values of floor shear, we can notice that main values are not very different considering the linear, the elastoplastic and the flag-shape models. While the linear model response values are characterized by a well defined decrease of floor shear demand increasing with the height, in the nonlinear cases decreasing is still present but differences are less evident. Therefore in the nonlinear cases the shear demand at different floors is closer to an intermediate value in all the levels. We can notice this aspect either in artificial ground motions (Fig.(5.87)) and near fault ones (Fig.(5.88)). Because of this we cannot define a real reduction factor, at least considering the mean of the shear demand over the different ground motions. Anyway we still can state that differences between flag

shape and elastoplastic model are quite small and also the differences in decreasing the SMA dissipation are quite small and flag shape hysteresis are well performing for a large range of  $\beta$  values, at least larger than 50%.



**Figure 5.83:** maximum relative displacement demand mean values from artificial ground motions.



**Figure 5.84:** maximum relative displacement demand mean values from near fault ground motions.

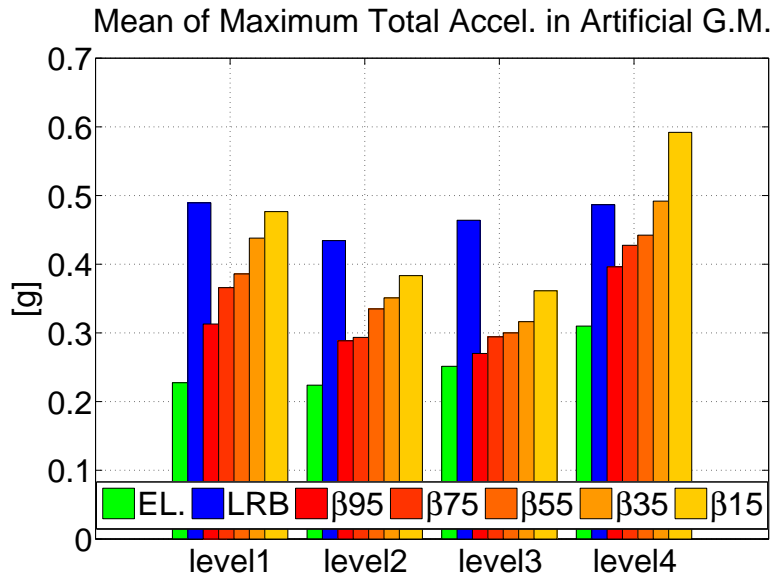


Figure 5.85: maximum total acceleration demand mean values from artificial ground motions.

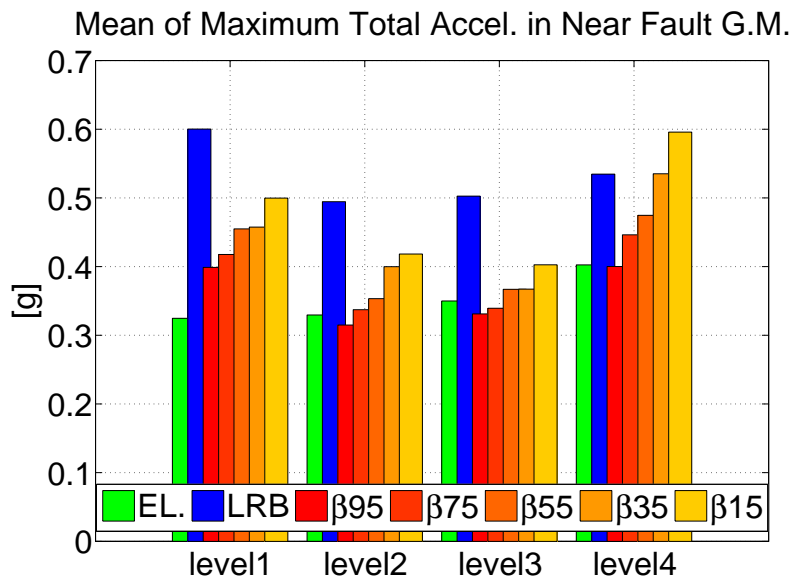


Figure 5.86: maximum total acceleration demand mean values from near fault ground motions.

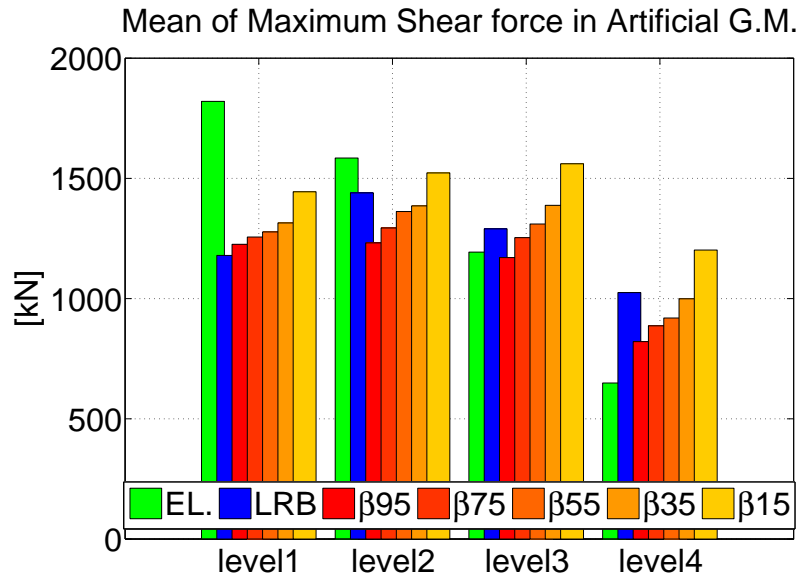


Figure 5.87: maximum shear demand mean values from artificial ground motions.

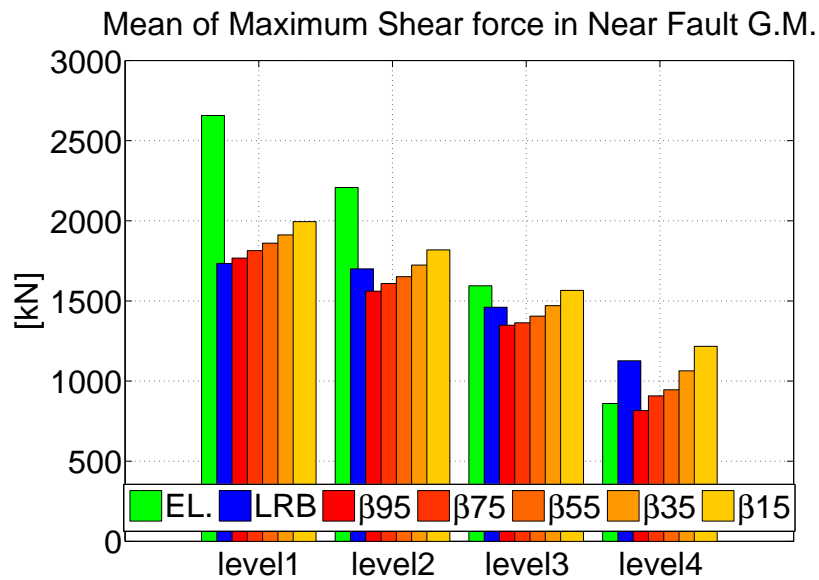
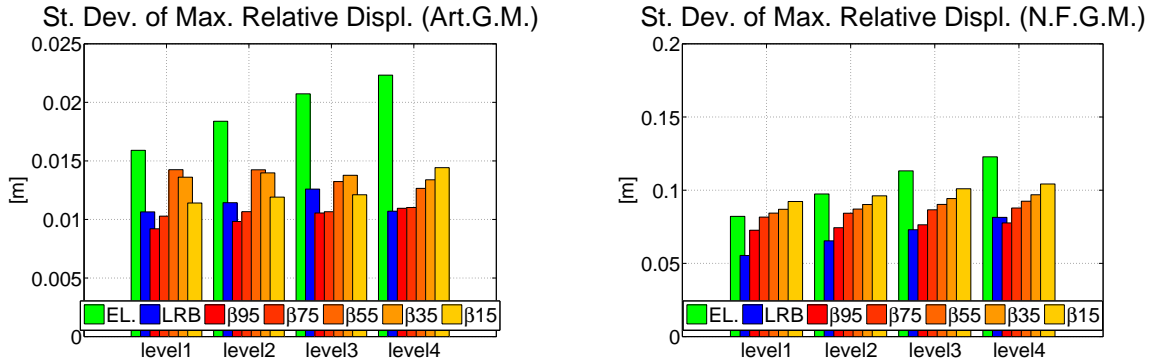
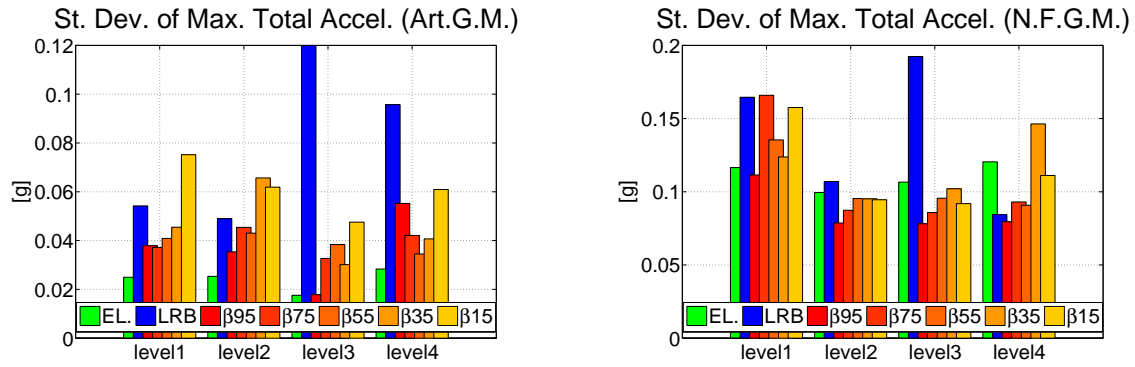


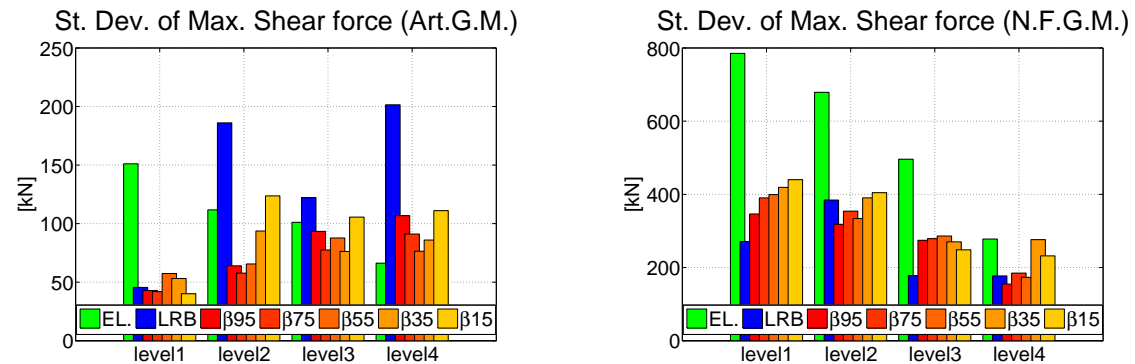
Figure 5.88: maximum shear demand mean values from near fault ground motions.



**Figure 5.89:** maximum relative displacement demand standard deviation values from artificial (left) and near fault (right) ground motions.



**Figure 5.90:** maximum acceleration floor demand standard deviation values from artificial (left) and near fault (right) ground motions.



**Figure 5.91:** maximum shear demand standard deviation values from artificial (left) and near fault (right) ground motions.

## 5.7 TIME HISTORY ANALYSIS RESULT EVALUATION

Main issues and conclusions from the comparison of rigid and flexible superstructure model analysis results considering the linear, the elastoplastic and the flag-shaped isolators are summarized in the following subsections.

### 5.7.1 *Dissipation Capability and Influence in Reducing Force and Displacement Demand*

If we computed the reduction factor of displacements and forces based on the hysteresis area estimation, we would find out the flag shape hysteresis is significantly more demanding compared with the elastoplastic model. In fact, time history analyses demonstrates that differences are present, but they are not as big as estimated using the hysteretic area based approach. In particular, considering either the single degree of freedom and the multiple degree of freedom analyses, displacement and force demand of a shape memory alloy device is close to the one of lead rubber bearing system and also the energy dissipation is almost the same, regardless the big differences in hysteretic area.

We find analogous results considering the effective absorbed energy from the time history analyses: considering also the energetic approach differences between elastoplastic and flag shape model are less important than expected.

We verified that these conclusions are valid not only for the more dissipating flag-shaped model, but also for smaller dissipation flag shape hysteresis provided that the beta parameter is at least in the order of  $\beta \simeq 50\%$ . In practise this mean that even if the dissipation parameter is keep in a level characteristic of the shape memory alloy not prestressed, results are still quite good.

### 5.7.2 *Recentering Capability*

Shape memory alloy based technology system is characterized by zero residual displacement. This is an important advantage for damage mitigation in structural seismic design if compared with the lead rubber bearing systems with elastoplastic model. Test have underlined that residuals are always affecting the lead rubber bearing devices, more or less significantly.

The application of shape memory alloys to the isolation device is able to carry out an important shear and provide recentering capacity just considering the superelastic effect.

Moreover shape memory alloys could be the source of an additional contribution if an existing recentering force was not enough and we needed to retrofit the devices after the seismic event.

### ***5.7.3 Displacement Limitation Considering the Second Hardening effect***

Shape memory alloy superelastic effect is characterized by a second hardening branch at a particular displacement corresponding to the end of the transformation process. In theory this hardening is useful to limit the maximum displacements if the effective seismic load is greater than the design one.

Nevertheless numeric tests demonstrate that the limitation in displacement leads to severe structural demand in terms of forces. Hence from time history analyses it is preferable to avoid a design that may have an excursion in the second hardening displacement range. The large increase in force demand is also related to the assumption of not considering material strength limit.

Even if it were preferable to avoid second hardening excursion for real device design, it represents a safety effect in limiting excessive displacements which can lead to instability collapse in real structure. Therefore hardening is useful for the ultimate limit state design purpose.

## 6. CONCLUSIONS

An investigation about the feasibility of shape memory alloy technology application to seismic isolation devices has been performed.

The evaluation of responses data from time history analyses was considered the most suitable method to study the problem. We have compared behavior of a model representing a conventional lead rubber bearing device with the behavior of a shape memory technology device and of an equivalent linear elastic model. They were characterized by the same secant stiffness and strength with respect the LRB device but different hysteresis. The flag shape model analyses were parametric, considering different values of dissipation capacity.

Results show that the overall behavior of the isolation system characterized by the flag-shape hysteresis is close to the response of isolation system with elastoplastic one. This is true for many values of dissipation in the flag shape model and for both rigid and flexible superstructure condition. In particular, reduction factors in terms of displacements and forces of LRB and SMA models with respect to linear elastic secant model response are quite close for medium-large SMA dissipation capability. Also in terms of absorbed energy over input energy ratio differences are small.

Given these results, the conclusion of this investigation is that the SMA application in seismic isolation is possible and can lead to several advantages.

SMA devices are characterized by energy dissipation. Numerical investigations have demonstrated that it is comparable, for its influence on the response, to the dissipation of actual highly dissipating devices.

Moreover SMA devices have good recentering capability, either because of the superelastic effect, which has been taken into account in this work, or because of the shape memory effect, that can provide a further restoring force if for any reason some residuals are still present.

Possible applications of SMAs in isolating bearing systems are relative to dissipating-recentering additional element for any other bearings, existing or new. Hence in theory we are considering a quite flexible device characterized by large range of application. For instance we can think to apply this kind of restrainer to rubber bearing, in substitution of the lead component, or in friction pendulous system to be able to control not only the horizontal displacement, eventually provide a recentering force if the gravity is not enough to be larger than the friction, but also it could be possible to control the possible uplift.

After this preliminary investigation, the main effort has to be focused in evaluating the real technology to reach a lateral force base shear like the one we are taking into account. Many issues have to be considered, in particular we are aware of the difficulty of getting this large displacement capacity from a SMA manufactured element and to guarantee a multi-direction good hysteresis behavior, taking into account the economically efficiency of a device of this kind, in order not to make advantages in the behavior negligible respect to device cost increase.

## REFERENCES

- Ates, S., A. A. Dumanoglu, and A. Bayraktara (2005). Stochastic response of seismically isolated highway bridges with friction pendulum systems to spatially varying earthquake ground motions. *Engineering Structures* 27, 1843–1858.
- Carr, A. J. (2007). *Ruamoko Manual Volume 4: User Guide to Associated Programs*. Department of Civil Engineering, University of Canterbury, ChristChurch, New Zealand.
- Casarotti, C. (2004, July). *Bridge Isolation and Dissipation Devices: state of the art review of seismic response and modelling of modern seismic isolation and dissipation devices*. Master Thesis, European School for Advanced Studies in Reduction of Seismic Risk (ROSE School), University of Pavia, Italy.
- Chopra, A. K. (2006). *Dynamics of Structures. Theory and Applications to Earthquake Engineering, Third Edition*. Prentice-Hall, Upper Saddle River, New Jersey.
- Christopoulos, C. (2004). Frequency-response of flag-shaped sdof hysteretic systems. *Journal of Engineering Mechanics* 130, 894–903.
- Christopoulos, C. and A. Filiatrault (2006). *Principles of Passive Supplemental Damping and Seismic Isolation*. IUSS Press, Pavia.
- Clough, R. W. and J. Penzien (1993). *Dynamics of Structures*. McGraw-Hill, New York.
- Desroches, R. and B. Smith (2003). Shape memory alloys in seismic resistant design and retrofit: a critical review of their potential and limitations. *Journal of Earthquake Engineering* 7, 1–15.
- Dwairi, H. M., M. J. Kowalsky, and J. M. Nau (2007). Equivalent damping in support of direct displacement-based design. *Journal of Earthquake Engineering* 11, 512–530.
- Eurocode8 (2003). Design of structures for earthquake resistance, part i: General rules, seismic actions and rules for buildings. *pre-ENV 1998-1*.
- Grant, D. N., C. A. Blandon, and M. J. N. Priestley (2005). *Modelling Inelastic Response in Direct Displacement Based Design*. IUSS Press, Pavia.
- Gulkan, P. and M. Sozen (1974). Inelastic response of reinforced concrete structures to earthquake motion. *ACI Journal* 71, 604–610.

- Iwan, W. and N. Gates (1979). Estimating earthquake response of simple hysteretic structures. *Journal of Engineering Mechanics Division* 105, 391–405.
- Jacobsen, L. S. (1930). Steady forced vibrations as influenced by damping. *ASME Transaction* 52, 169–181.
- Jacobsen, L. S. (1960). Damping on composite structures. In *Proceedings of the II World Conference of Earthquake Engineering*, Tokyo and Kyoto, Japan, pp. 1029–1044.
- Jain, S. K. and S. K. Thakkar (2005). Experimental investigations on laminated rubber bearings. *JBulletin of Earthquake Engineering* 3, 129–136.
- Jennings, P. C. (1968). Equivalent viscous damping for yielding structures. *Journal of Earthquake Engineering* 94, 103–116.
- Kaounides, L. (1995). Advanced materials - corporate strategies for competitive advantages in the 1990s. *FT Management Reports*, 2557–2573.
- Kwan, W. and S. Billington (2003). Influence of hysteretic behavior on equivalent period and damping of structural systems. *Journal of Earthquake Engineering* 129, 576–585.
- Miranda, E. and Y. Lin (2003). Non-iterative equivalent linear method for displacement-based design. In *Proceedings of the XIII World Conference of Earthquake Engineering*, Number 3422, Vancouver, Canada.
- Naeim, F. and J. M. Kelly (1999). *Design of Seismic Isolated Structures. From Theory to Practice*. John Wiley and Sons, New York.
- Priestley, M. J. N., G. M. Calvi, and M. J. Kowalsky (2007). *Displacement-Based Seismic Design of Structures*. IUSS Press, Pavia.
- Priestley, M. J. N. and J. R. T. Tao (1993). Seismic response of precast-prestressed concrete frames with partially debonded tendons. *PCI Journal* 38, 58–69.
- Ramirez, O. M., M. C. Costantinou, J. D. Gomez, A. S. Whittaker, and C. Z. Chrysostomou (2002). Evaluation of simplified methods of analysis of yielding structures with damping systems. *Earthquake Spectra* 18, 501–530.
- Rosenblueth, E. and I. Herrera (1964). On a kind of hysteretic damping. *Journal of the Engineering Mechanical Division, ASCE* 90, 37–48.
- Shibata, A. and M. Sozen (1976). Substitute structure method for seismic design in rc. *Journal of the Structural Division, ASCE* 102, 1–18.
- Skinner, R. I., W. H. Robinson, and G. H. McVerry (1993). *An Introduction to Seismic Isolation*. John Wiley and Sons, Chichester.
- Song, G., N. Ma, and H.-N. Li (2006). Applications of shape memory alloys in civil structures. *Engineering Structures* 28, 1266–1274.

- Strnadel, B., S. Ohashi, H. Ohtsuka, T. Ishihara, and S. Miyazaki (1995). Cyclic stress-strain characteristics of ti-ni and ti-ni-cu shape memory alloys. *Materials Science and Engineering*, 148–156.
- Takeda, T., M. Sozen, and N. Nielsen (1970). Substitute structure method for seismic design in rc. *Journal of the Structural Division, ASCE* 96, 2557–2573.
- Tsai, C. S., T. Chiang, B. Chen, and S. Lin (2003). An advanced analytical model for high damping rubber bearings. *Journal of the Earthquake Engineering and Structural Dynamics* 32, 1373–1387.
- Tsai, C. S., P. Lu, W. Chen, T. Chiang, C. Yang, and Y. Lin (2008). A finite element formulation and shaking table tests of direction-optimized-friction-pendulum system. *Engineering Structures*.

## A. GROUND MOTION RECORDS USED IN THE TIME HISTORY ANALYSES

### A.1 ARTIFICIAL GROUND MOTION GENERATION

The artificial ground motion have been generated using the research oriented program *Simqke* (Carr 2007), considering as a target design spectra the Eurocode8 type 1 soil C spectra for a  $PGA = 0.35g$  (Eurocode8 2003).

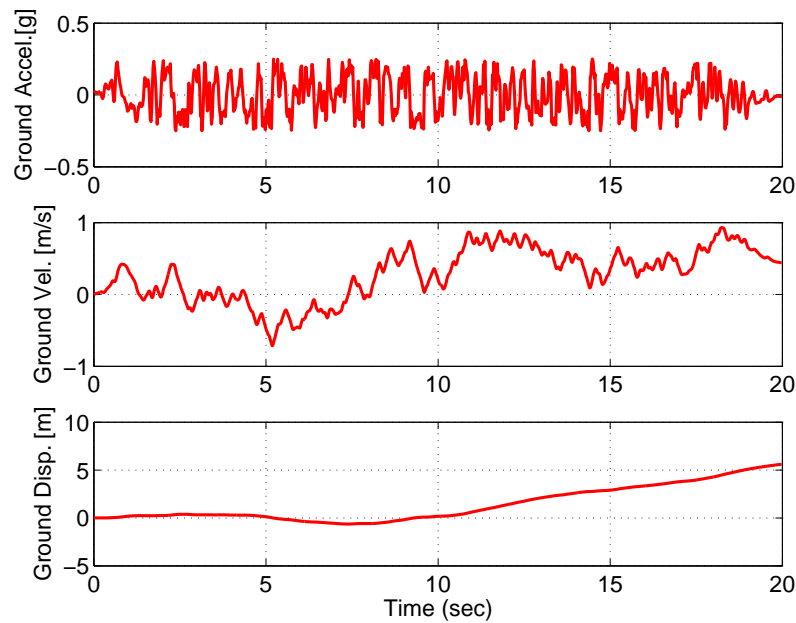
The parameter we use for the generation, common to all the ground motions are listed in Tab.(A.1). To produce different ground motion then we just use different *seed* numbers.

**Table A.1:** artificial ground motion generation parameters.

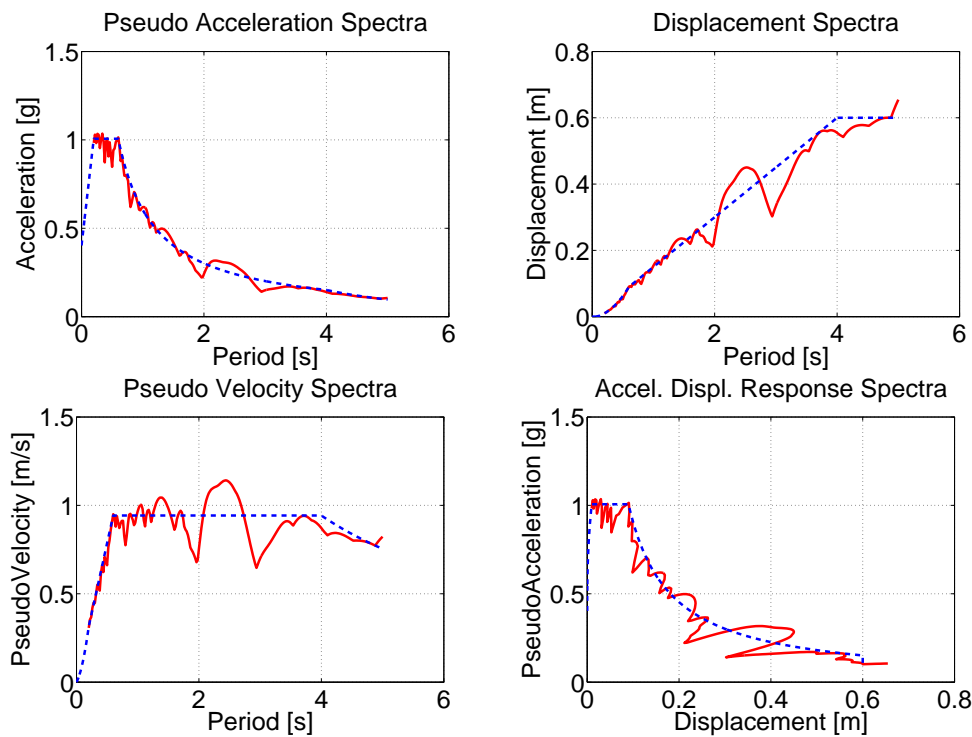
<i>Simqke generation parameters</i>		
Envelope parameters: trapezoidal		
minimum period of simulation	$T_s$	<b>0.1 s</b>
maximum period of simulation	$T_l$	<b>4.0 s</b>
acceleration duration	<b>DUR</b>	<b>20.0 s</b>
acceleration rise time	<b>TRISE</b>	<b>2.0 s</b>
acceleration level time	<b>TLVL</b>	<b>15 s</b>
time step for accelerogram	<b>DELTA</b>	<b>0.02 s</b>
maximum acceleration	<b>AGMX</b>	<b>0.25 g</b>
damping ratio	<b>DAMP</b>	<b>5 %</b>

The generated ground motions with their respective spectra are listed in the following subsections.

### A.1.1 Ground motion 1

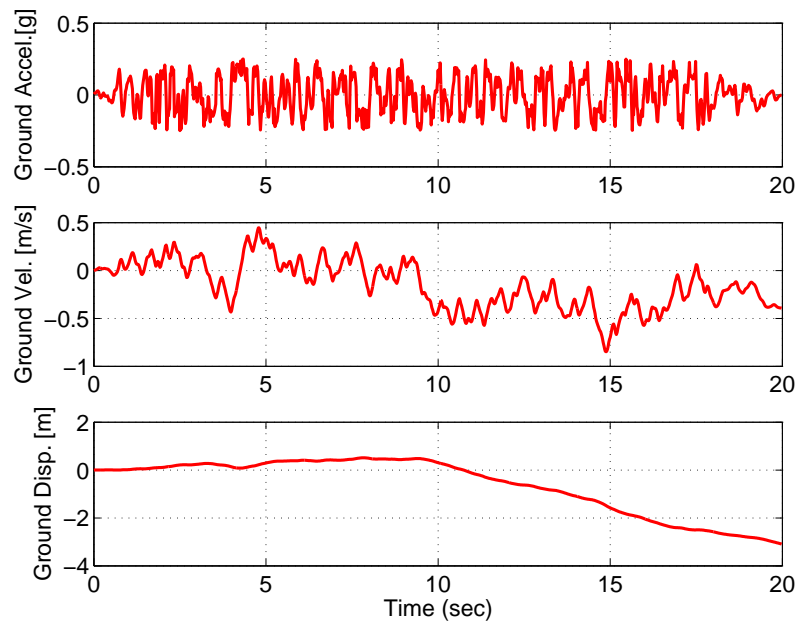


**Figure A.1:** ground motion 1.

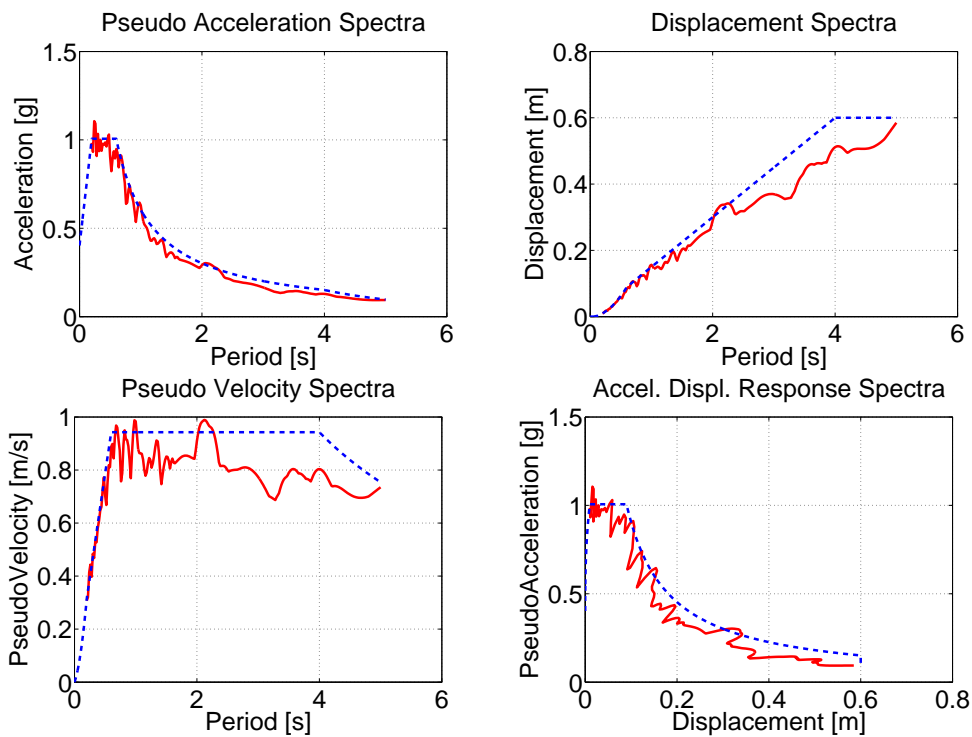


**Figure A.2:** ground motion 1 spectra: pseudo-acceleration spectra (top-left), displacement spectra (top-right), velocity spectra (bottom-left), acceleration-velocity (bottom-right); figures report also comparison with design spectra (dashed line).

### A.1.2 Ground motion 2

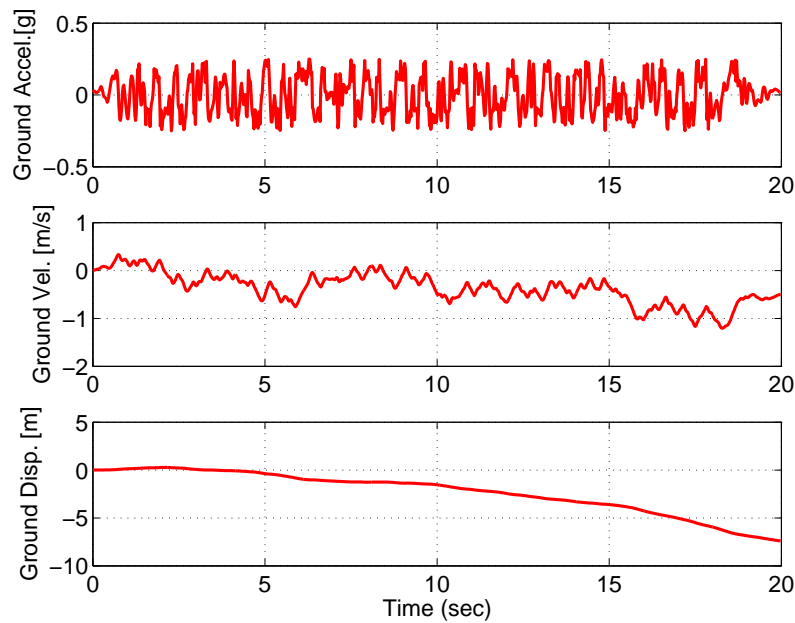


**Figure A.3:** ground motion 2.

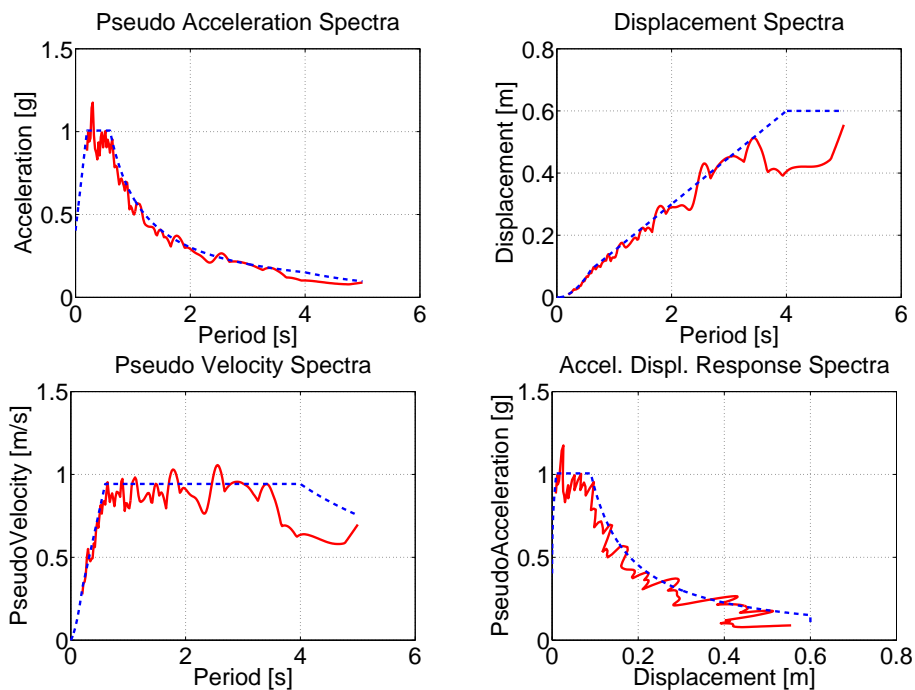


**Figure A.4:** ground motion 2 spectra: pseudo-acceleration spectra (top-left), displacement spectra (top-right), velocity spectra (bottom-left), acceleration-velocity (bottom-right); figures report also comparison with design spectra (dashed line).

### A.1.3 Ground motion 3

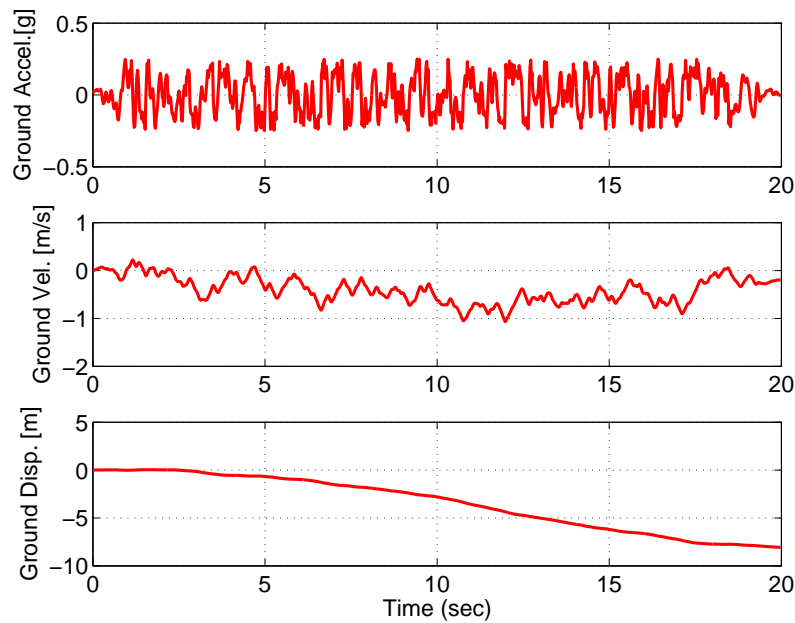


**Figure A.5:** ground motion 3.

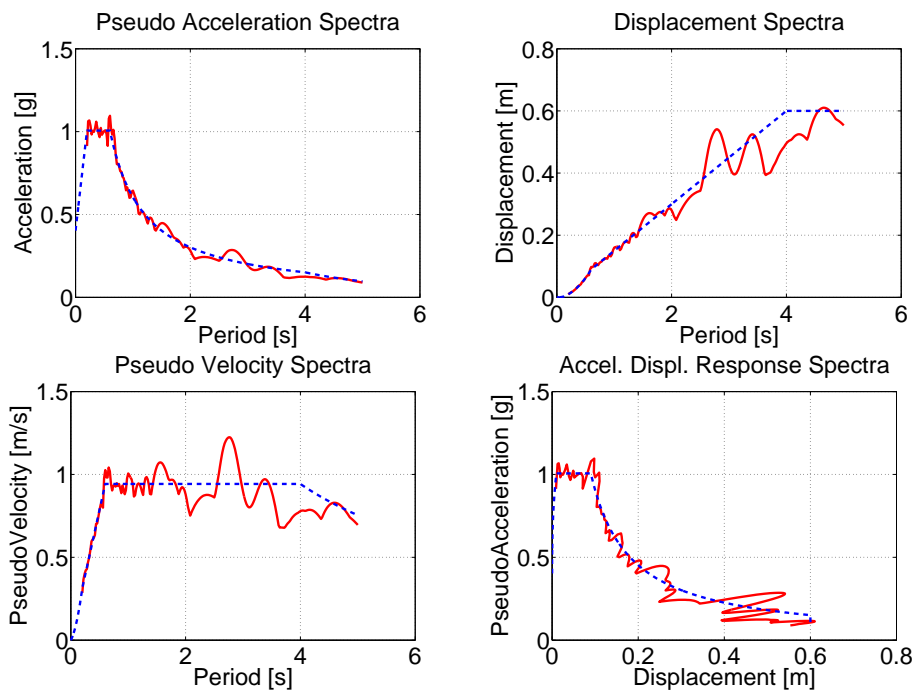


**Figure A.6:** ground motion 3 spectra: pseudo-acceleration spectra (top-left), displacement spectra (top-right), velocity spectra (bottom-left), acceleration-velocity (bottom-right); figures report also comparison with design spectra (dashed line).

### A.1.4 Ground motion 4

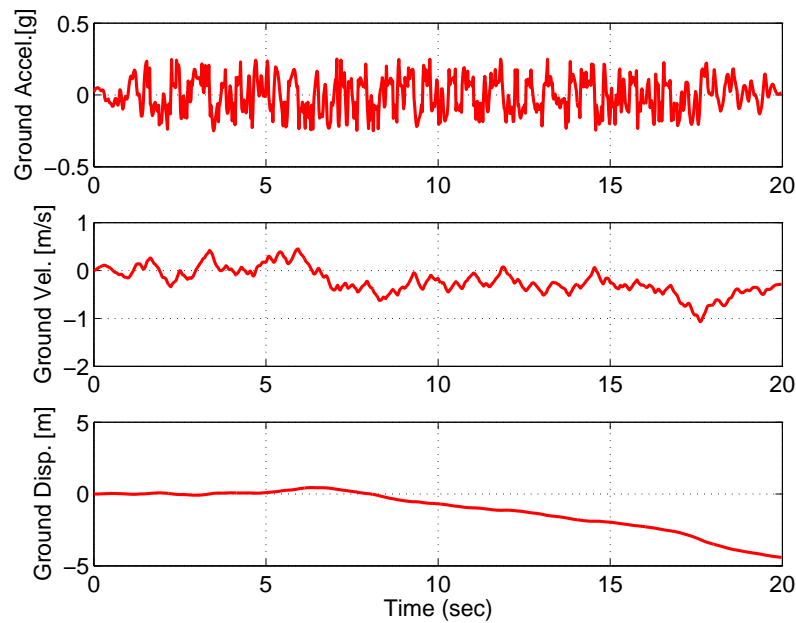


**Figure A.7:** ground motion 4.

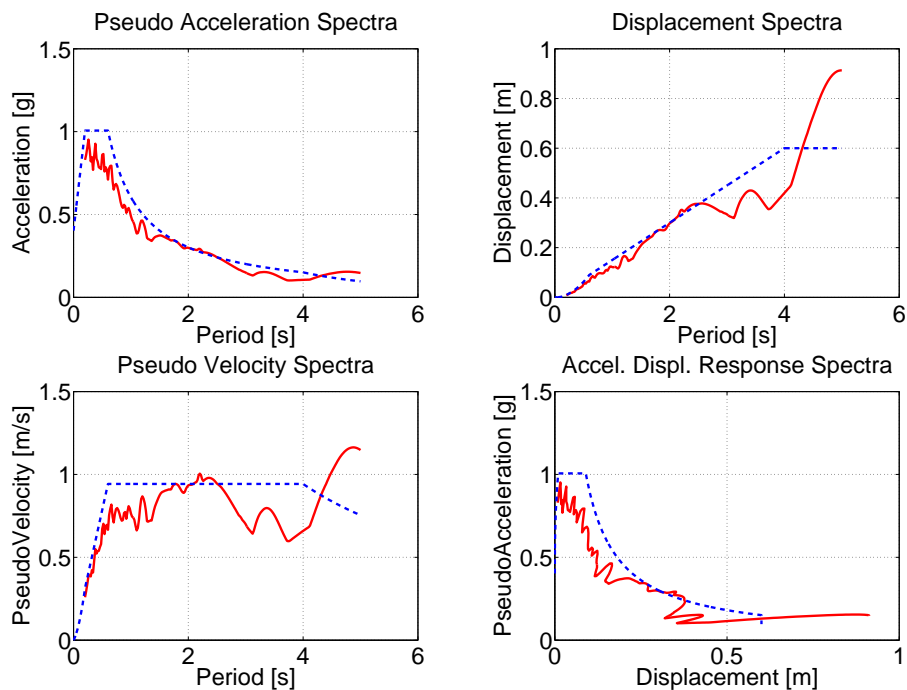


**Figure A.8:** ground motion 4 spectra: pseudo-acceleration spectra (top-left), displacement spectra (top-right), velocity spectra (bottom-left), acceleration-velocity (bottom-right); figures report also comparison with design spectra (dashed line).

### A.1.5 Ground motion 5

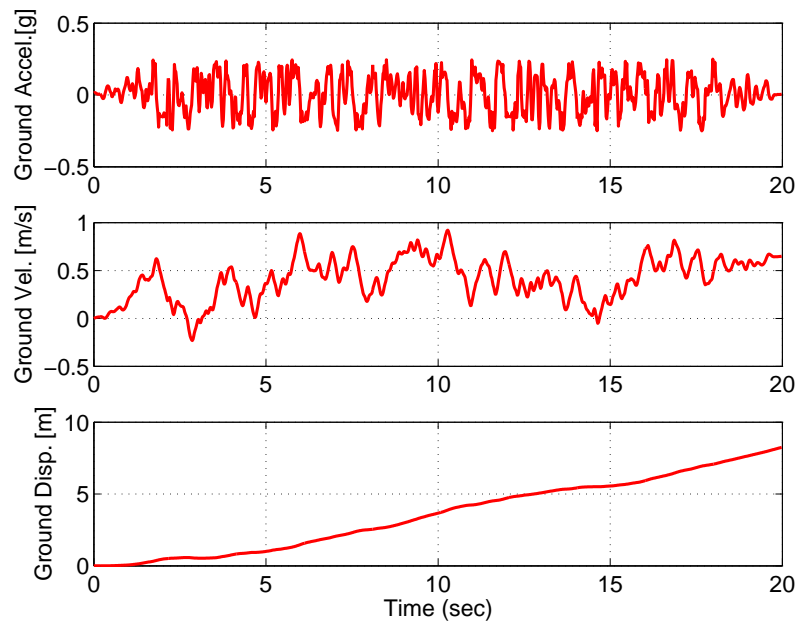


**Figure A.9:** ground motion 5.

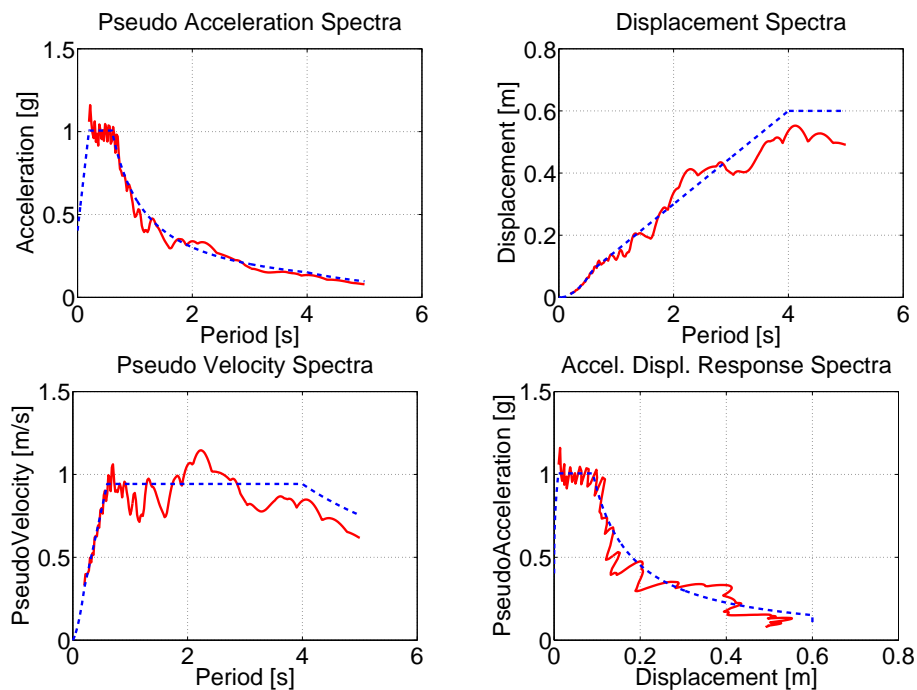


**Figure A.10:** ground motion 5 spectra: pseudo-acceleration spectra (top-left), displacement spectra (top-right), velocity spectra (bottom-left), acceleration-velocity (bottom-right); figures report also comparison with design spectra (dashed line).

### A.1.6 Ground motion 6

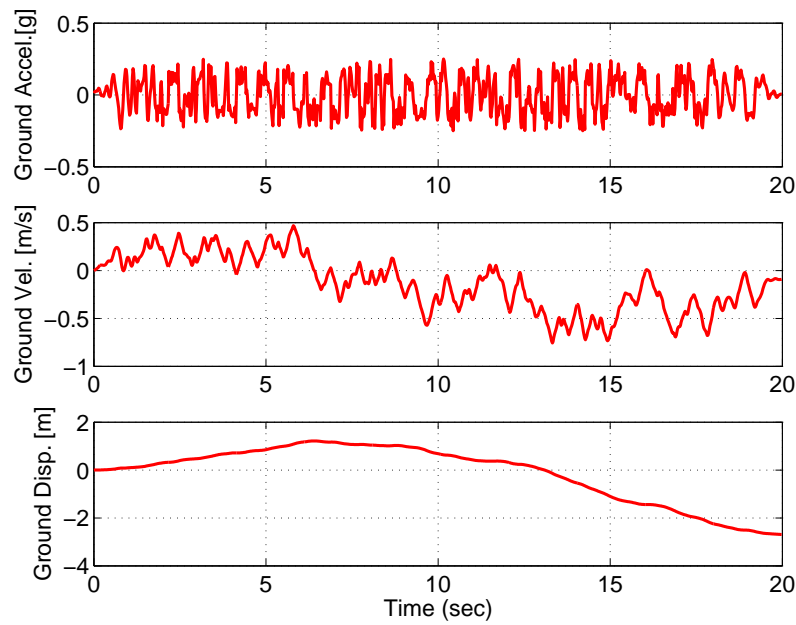


**Figure A.11:** ground motion 6.

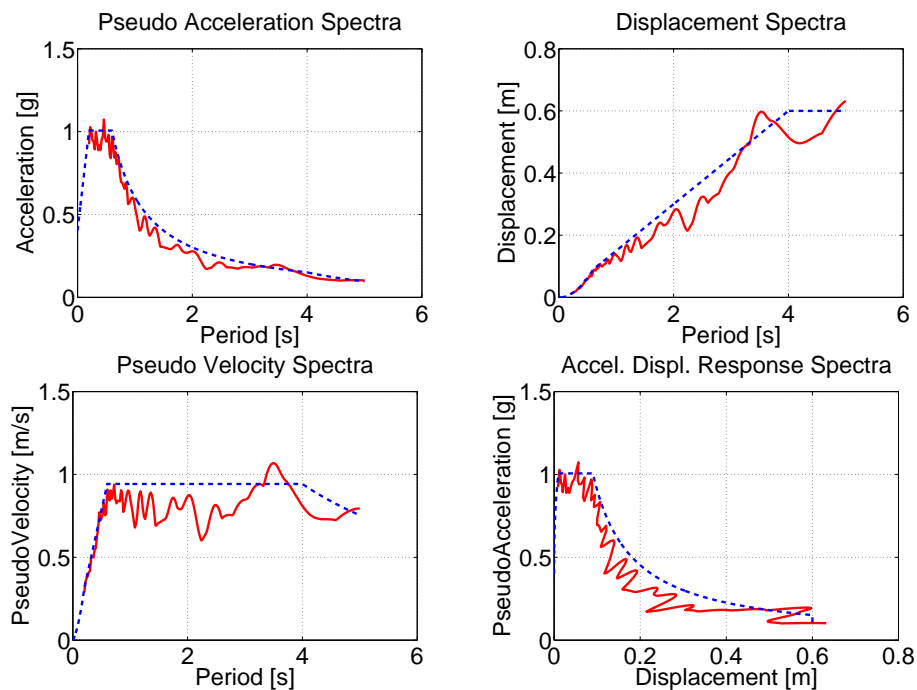


**Figure A.12:** ground motion 6 spectra: pseudo-acceleration spectra (top-left), displacement spectra (top-right), velocity spectra (bottom-left), acceleration-velocity (bottom-right); figures report also comparison with design spectra (dashed line).

### A.1.7 Ground motion 7



**Figure A.13:** ground motion 7.



**Figure A.14:** ground motion 7 spectra: pseudo-acceleration spectra (top-left), displacement spectra (top-right), velocity spectra (bottom-left), acceleration-velocity (bottom-right); figures report also comparison with design spectra (dashed line).

## A.2 NEAR FIELD GROUND MOTION SCALING

Concerning the near field ground motions, we chose seven accelerograms which are those in Tab.(A.2).

**Table A.2:** near field ground motions.

G.M.#	Earthquake	Date	Location	Comp.	PGA [g]	PGV [m/s]	PGD [m]
8	Tabas	16 Sep 78	Tabas stat.	FN	0.900	1.100	0.513
9	Tabas	16 Sep 78	Tabas stat.	FP	0.977	1.058	0.752
10	Erzinican	13 Mar 92	Meteor. stat.	FN	0.432	1.192	0.423
11	Erzinican	13 Mar 92	Meteor. stat.	FP	0.457	0.581	0.295
12	Landers	28 Giu 92	Lucerne	FN	0.713	1.360	2.298
13	Northridge	17 Jan 94	Olive View	FN	0.732	1.222	0.310
14	Kobe	16 Jan 95	Tato	FP	0.424	0.637	0.233

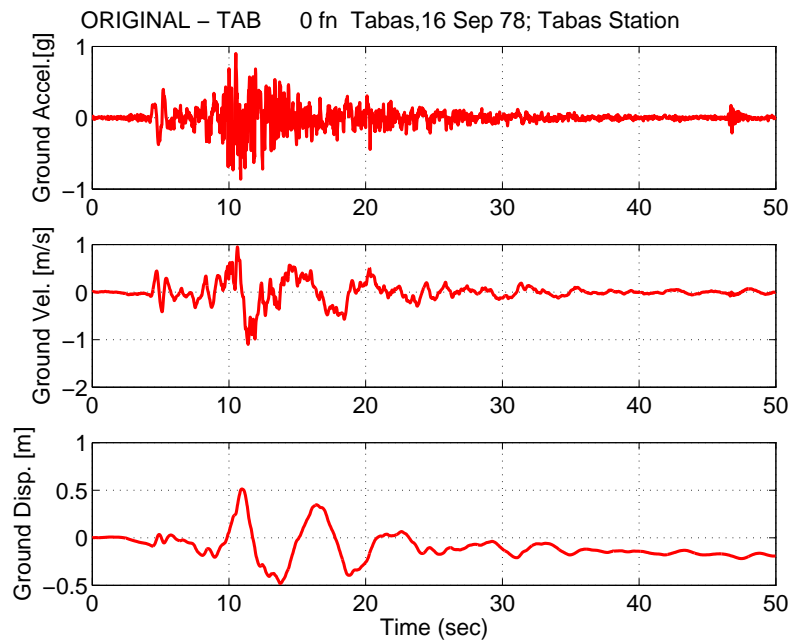
To use those ground motions, we scale them in a very simplified manner, just multiplying the record for a coefficient equal to the ratio between the design displacement spectra slope to the corner period value and the same slope for the elastic displacement spectra of each record. Scaling factors are reported in the Tab.(A.3). Obviously this procedure does not guarantee that for

**Table A.3:** near field ground motions scaling factors.

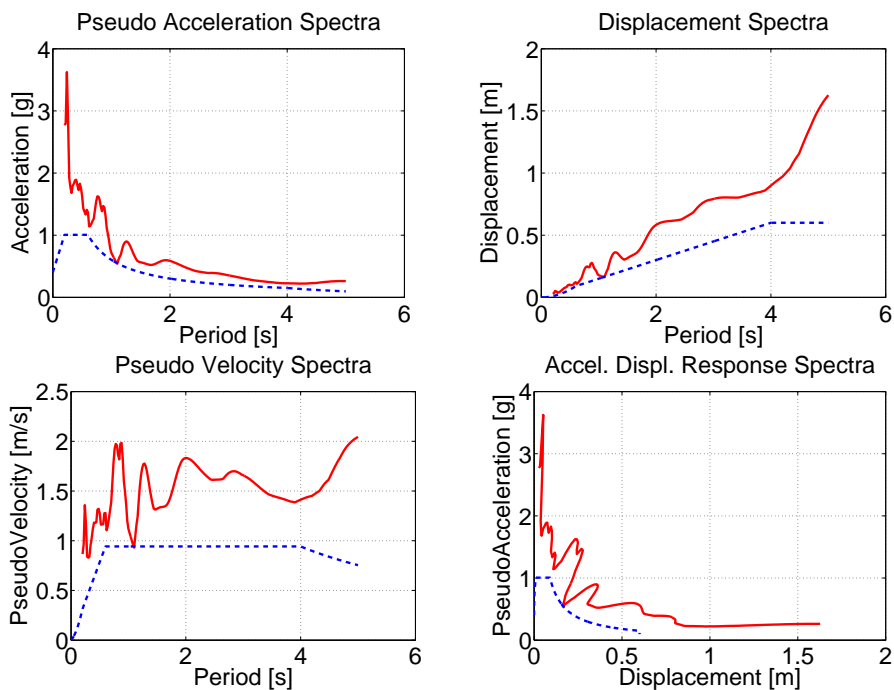
G.M. #	Eartquake	Scaling factor	PGA [g]	PGV [m/s]	PGD [m]
8	Tabas	0.6257	0.563	0.689	0.321
9	Tabas	0.6382	0.624	0.675	0.480
10	Erzinican	0.6672	0.288	0.795	0.282
11	Erzinican	1.2406	0.567	0.721	0.365
12	Landers	0.6161	0.439	0.838	1.416
13	Northridge	0.5847	0.428	0.714	0.181
14	Kobe	0.7109	0.302	0.453	0.165

the period of interest the spectra ordinates of the ground motion are close to the design spectra. Therefore, the near fault ground motion are supposed to be more severe than the artificial ones. In the following subsection, the ground motions are reported with their spectra.

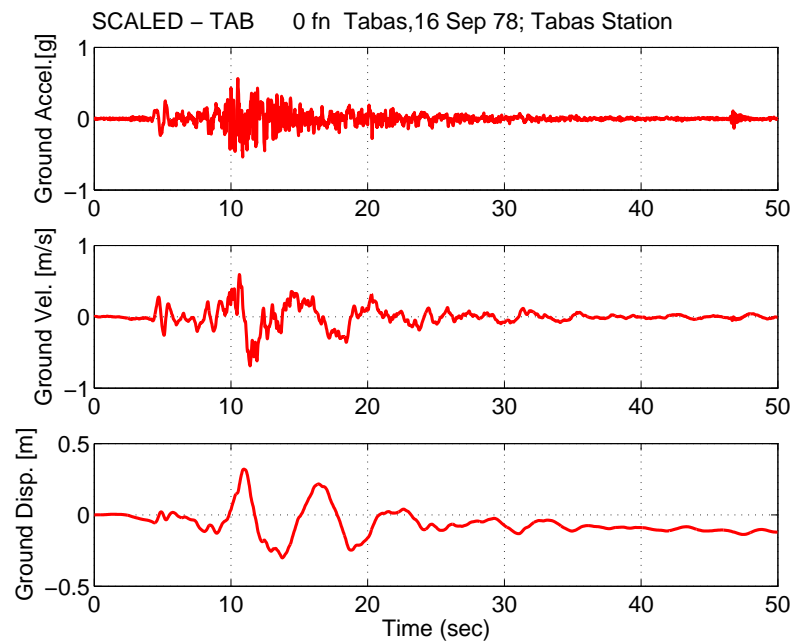
### A.2.1 Ground motion 8



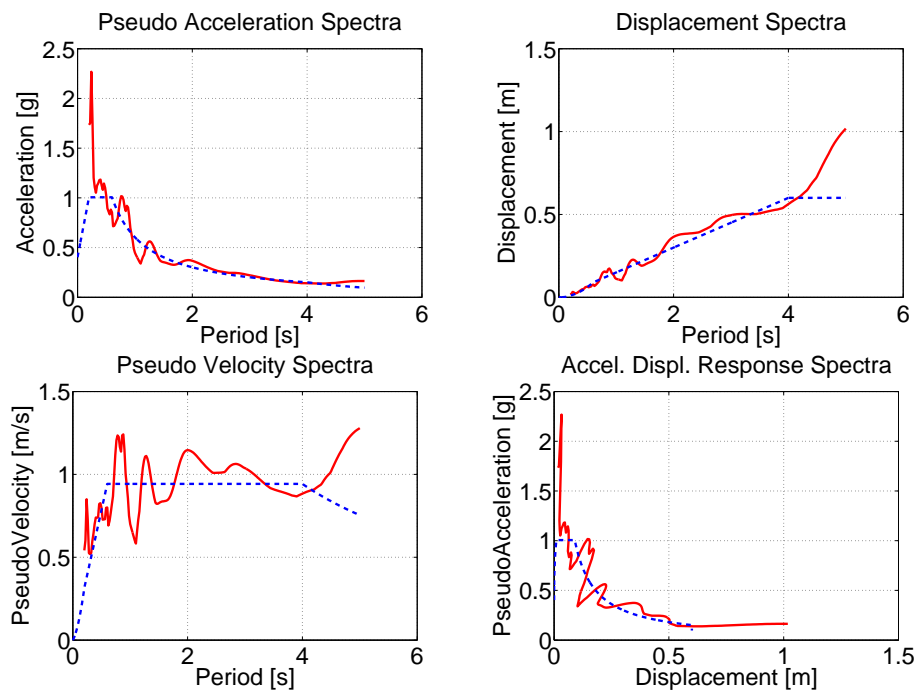
**Figure A.15:** original ground motion 8.



**Figure A.16:** original ground motion 8 spectra: pseudo-acceleration spectra (top-left), displacement spectra (top-right), velocity spectra (bottom-left), acceleration-velocity (bottom-right); figures report also comparison with design spectra (dashed line).



**Figure A.17:** scaled ground motion 8.



**Figure A.18:** scaled ground motion 8 spectra: pseudo-acceleration spectra (top-left), displacement spectra (top-right), velocity spectra (bottom-left), acceleration-velocity (bottom-right); figures report also comparison with design spectra (dashed line).

### A.2.2 Ground motion 9

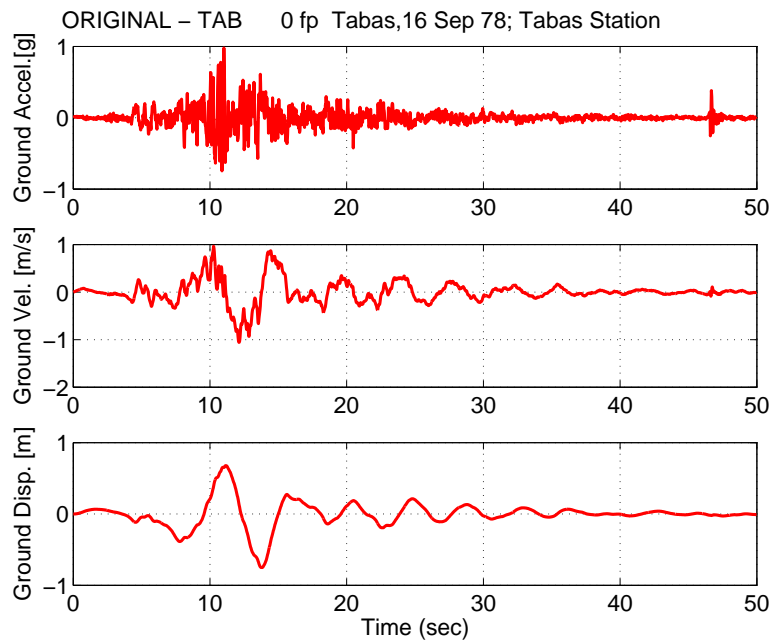


Figure A.19: original ground motion 9.

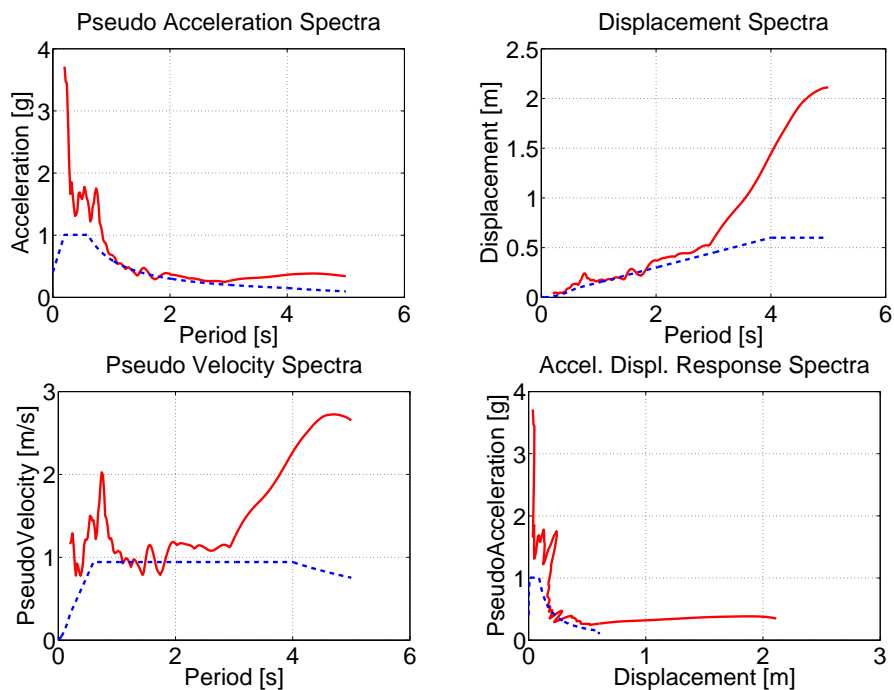
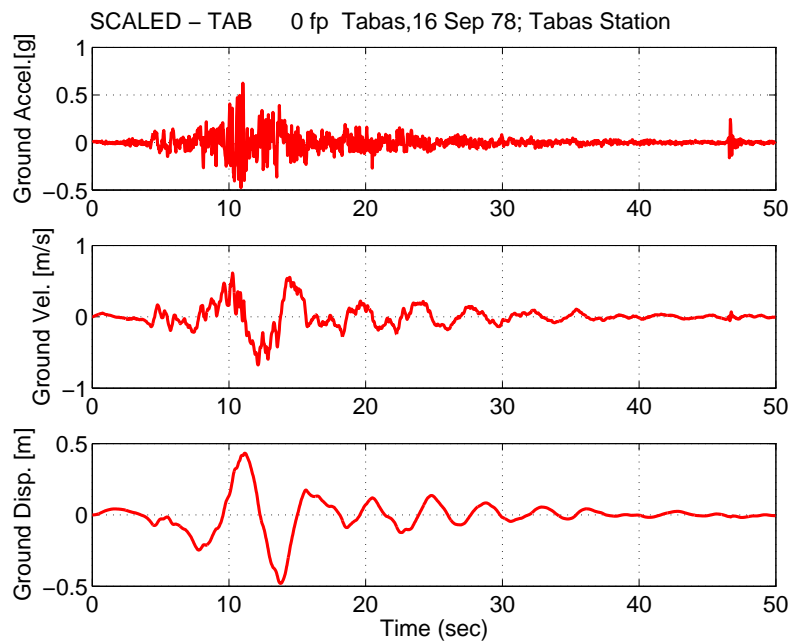
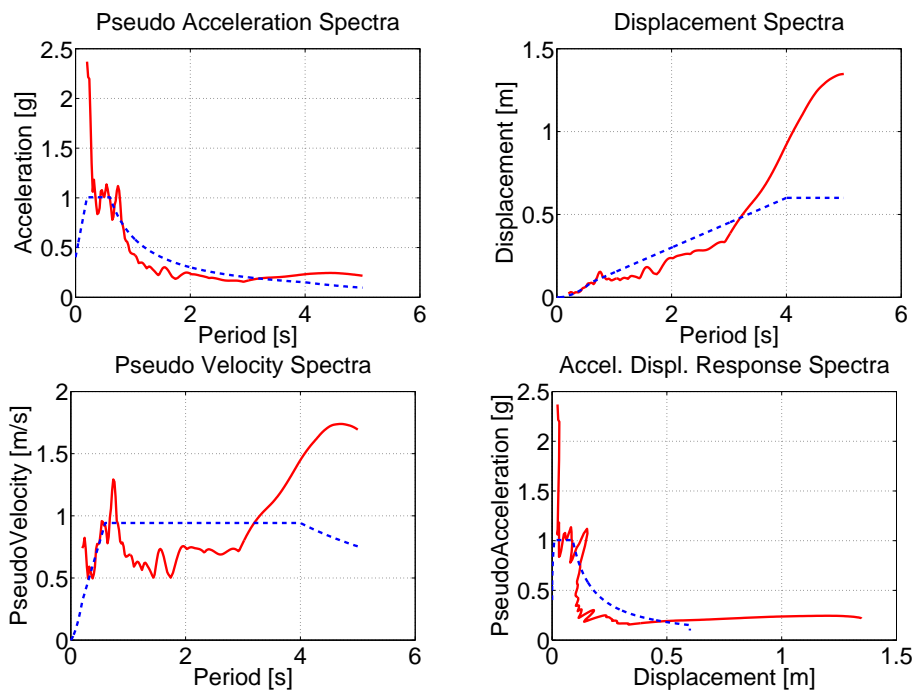


Figure A.20: original ground motion 9 spectra: pseudo-acceleration spectra (top-left), displacement spectra (top-right), velocity spectra (bottom-left), acceleration-velocity (bottom-right); figures report also comparison with design spectra (dashed line).



**Figure A.21:** scaled ground motion 9.



**Figure A.22:** scaled ground motion 9 spectra: pseudo-acceleration spectra (top-left), displacement spectra (top-right), velocity spectra (bottom-left), acceleration-velocity (bottom-right); figures report also comparison with design spectra (dashed line).

### A.2.3 Ground motion 10

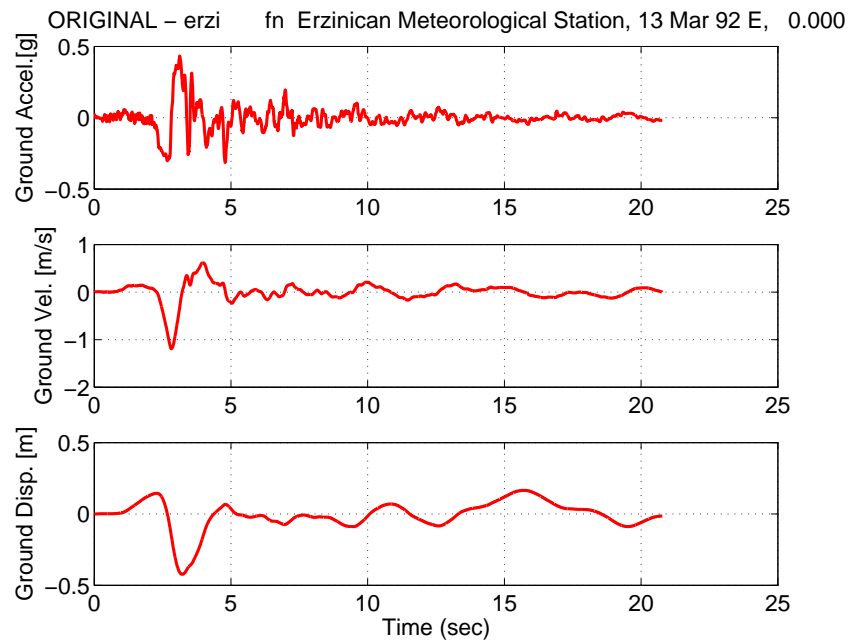


Figure A.23: original ground motion 10.

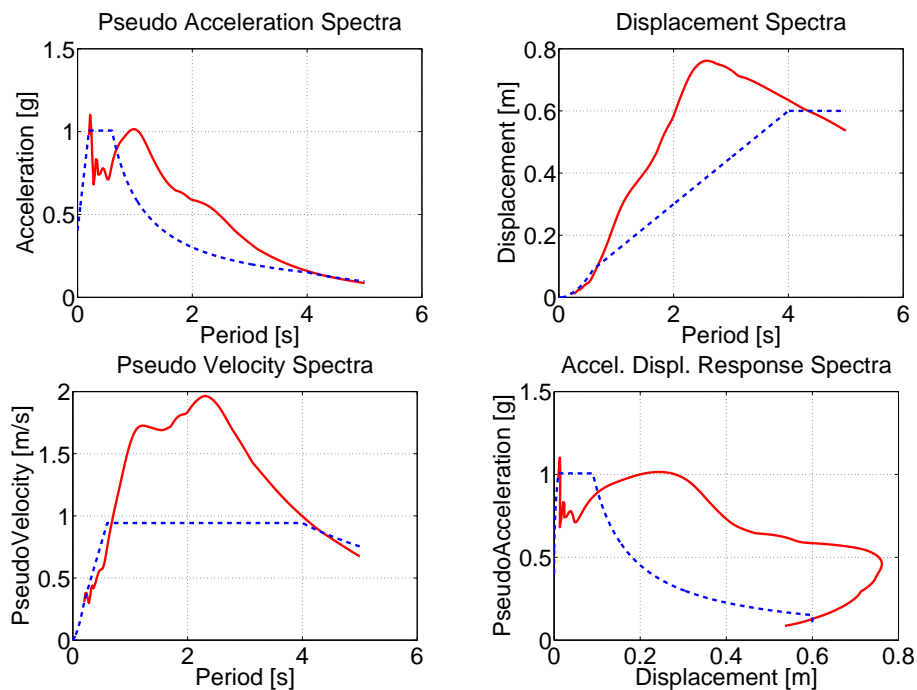
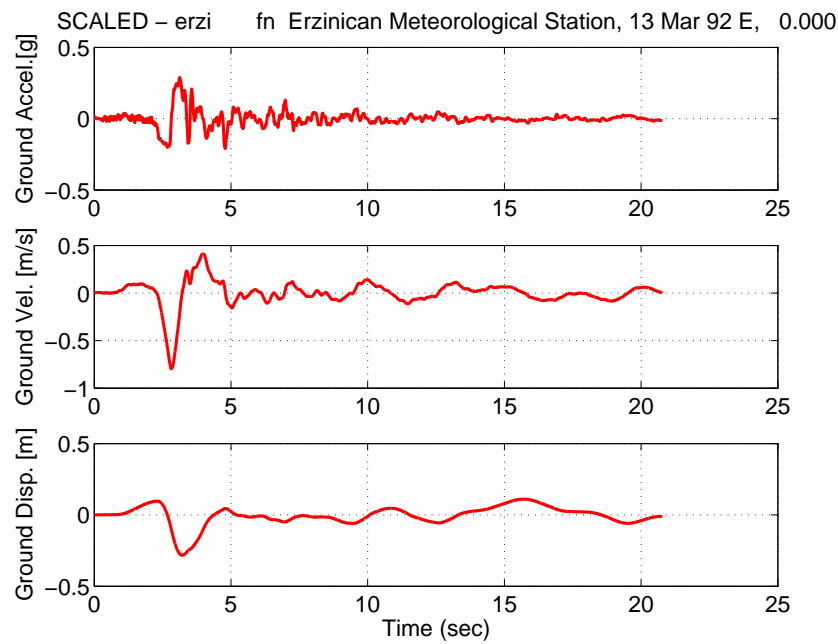
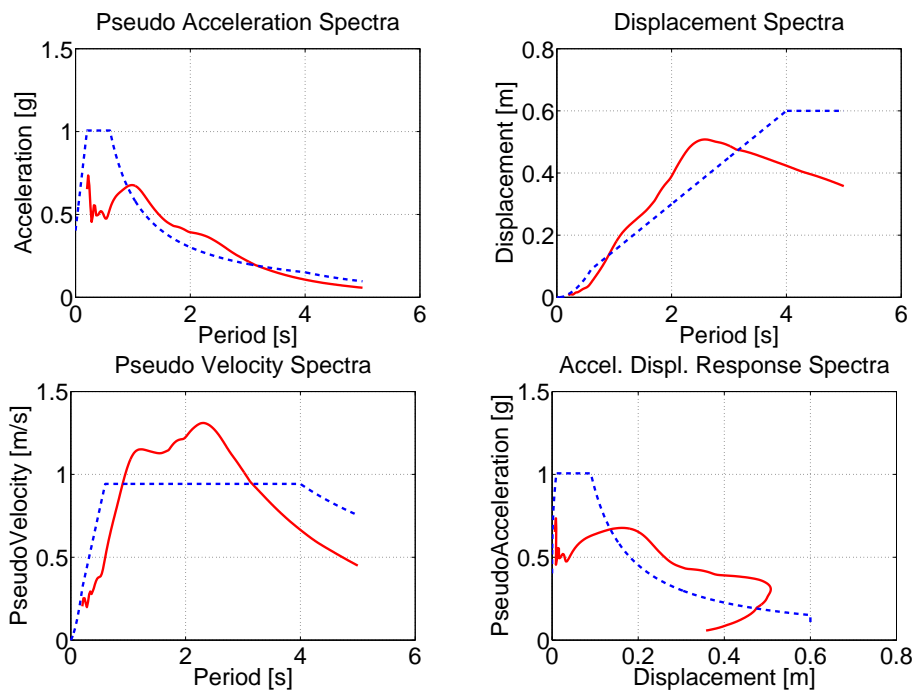


Figure A.24: original ground motion 10 spectra: pseudo-acceleration spectra (top-left), displacement spectra (top-right), velocity spectra (bottom-left), acceleration-velocity (bottom-right); figures report also comparison with design spectra (dashed line).



**Figure A.25:** scaled ground motion 10.



**Figure A.26:** scaled ground motion 10 spectra: pseudo-acceleration spectra (top-left), displacement spectra (top-right), velocity spectra (bottom-left), acceleration-velocity (bottom-right); figures report also comparison with design spectra (dashed line).

### A.2.4 Ground motion 11

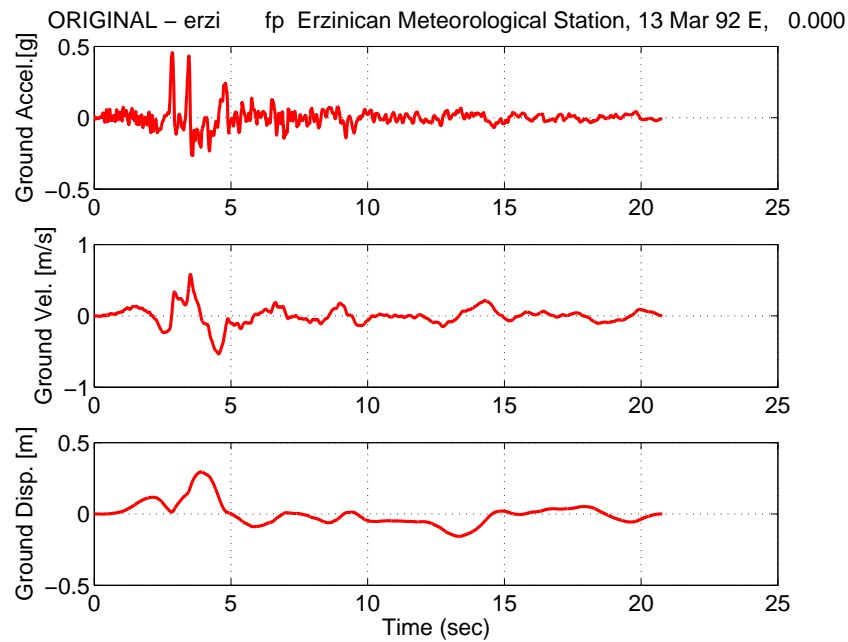


Figure A.27: original ground motion 11.

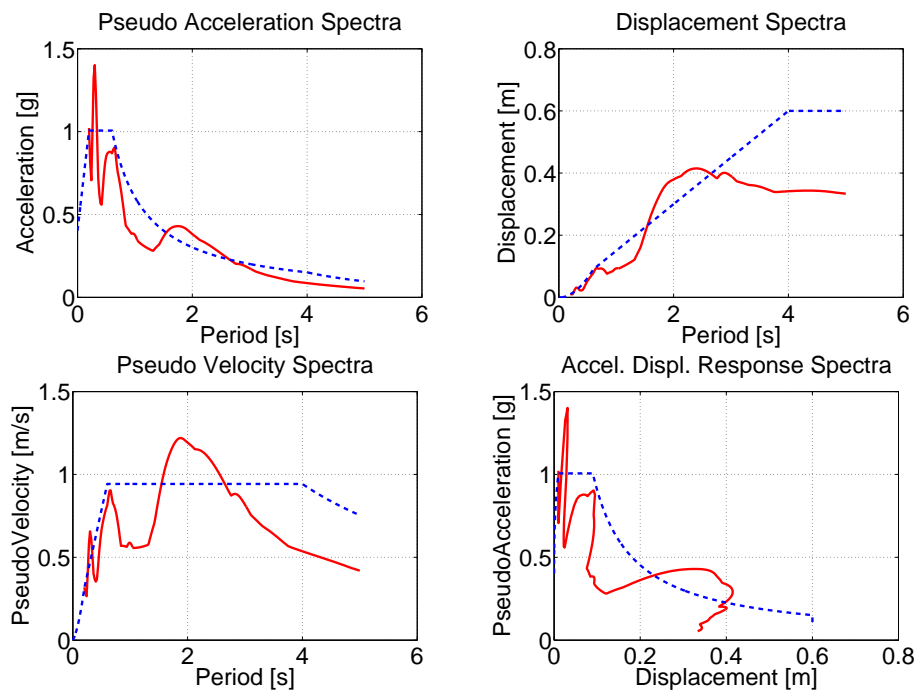
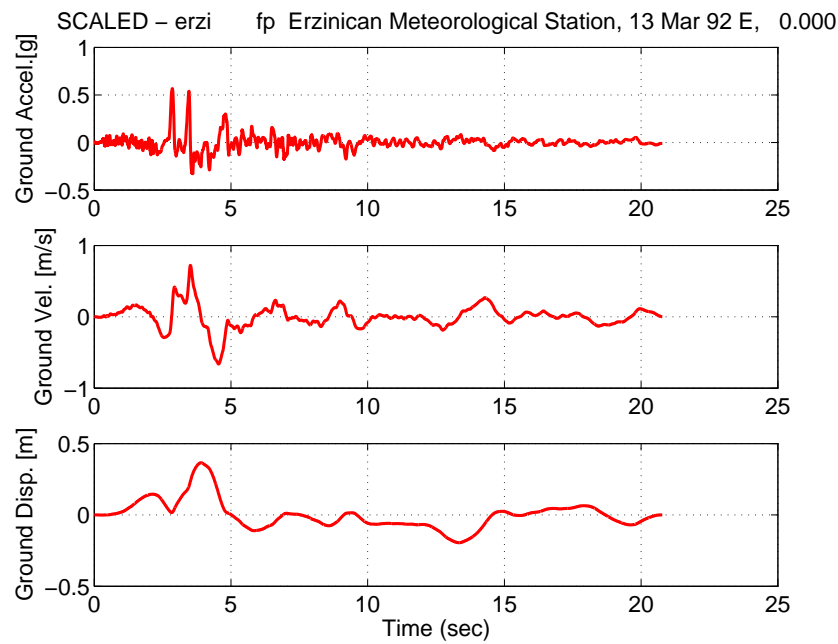
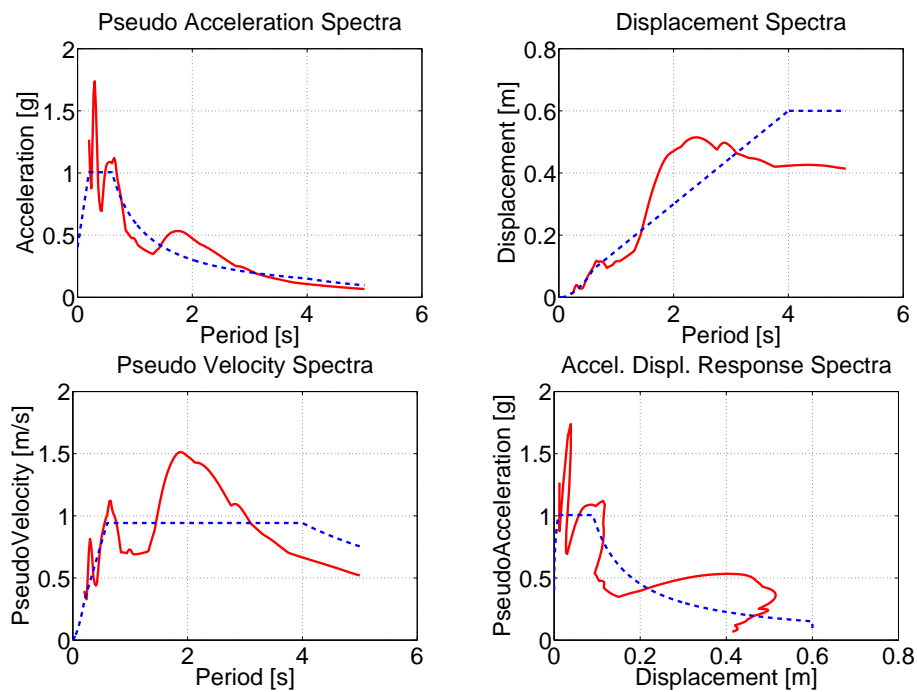


Figure A.28: original ground motion 11 spectra: pseudo-acceleration spectra (top-left), displacement spectra (top-right), velocity spectra (bottom-left), acceleration-velocity (bottom-right); figures report also comparison with design spectra (dashed line).

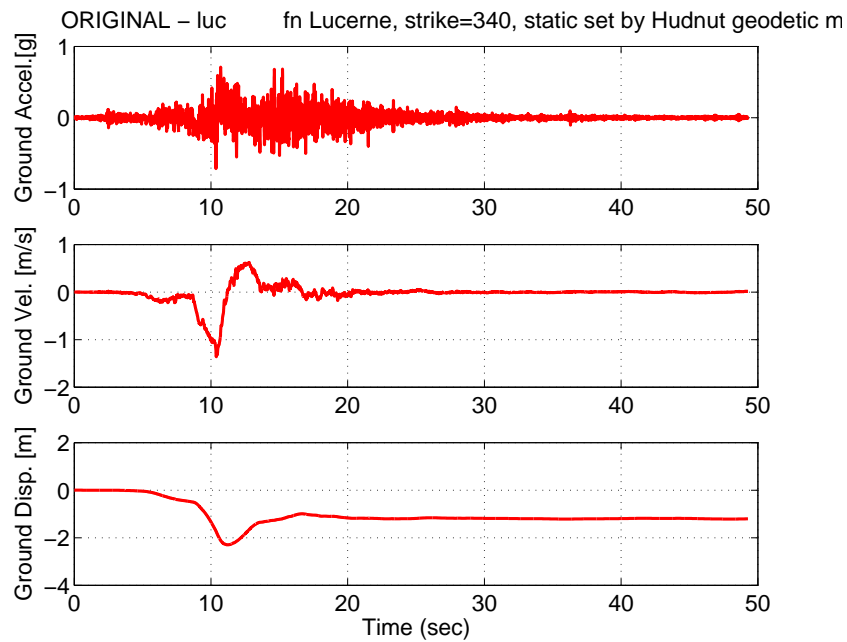


**Figure A.29:** scaled ground motion 11.

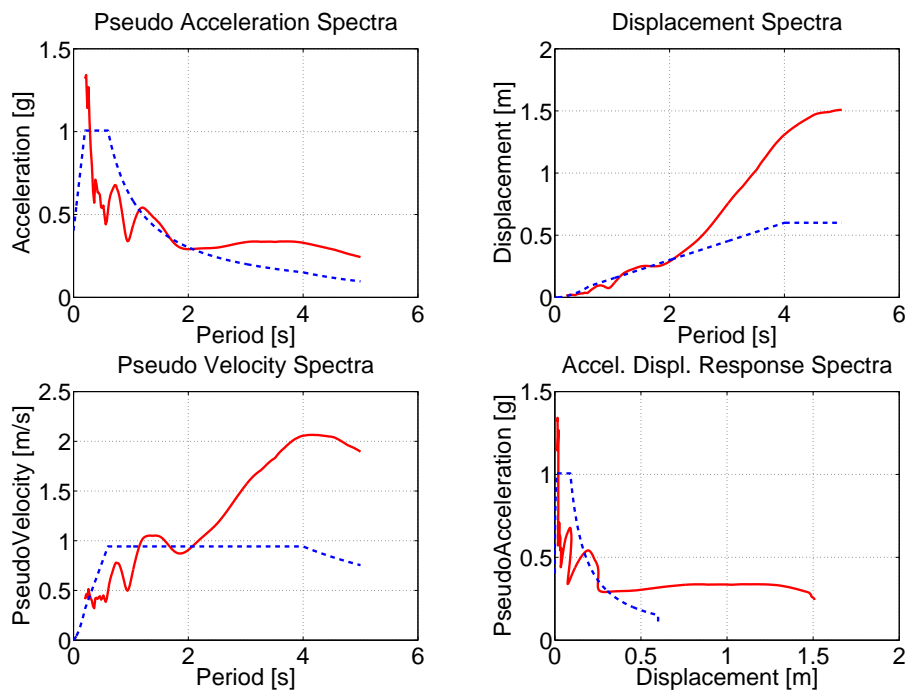


**Figure A.30:** scaled ground motion 11 spectra: pseudo-acceleration spectra (top-left), displacement spectra (top-right), velocity spectra (bottom-left), acceleration-velocity (bottom-right); figures report also comparison with design spectra (dashed line).

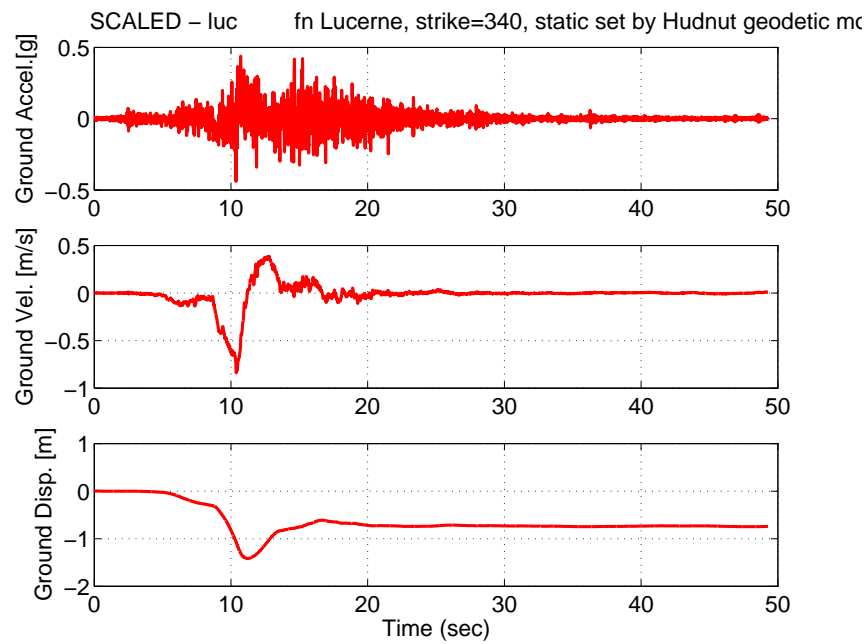
### A.2.5 Ground motion 12



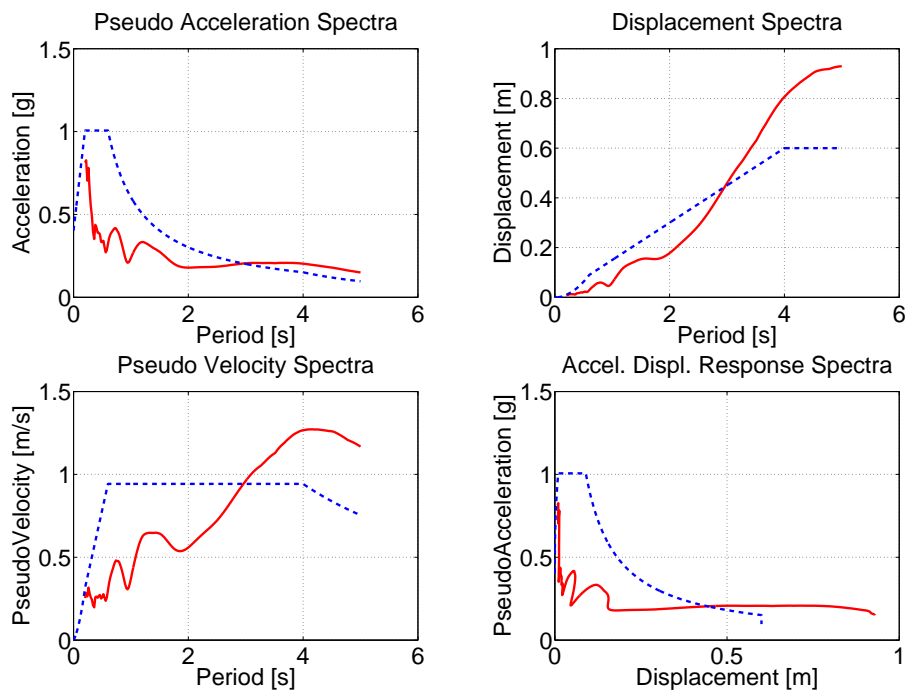
**Figure A.31:** original ground motion 12.



**Figure A.32:** original ground motion 12 spectra: pseudo-acceleration spectra (top-left), displacement spectra (top-right), velocity spectra (bottom-left), acceleration-velocity (bottom-right); figures report also comparison with design spectra (dashed line).

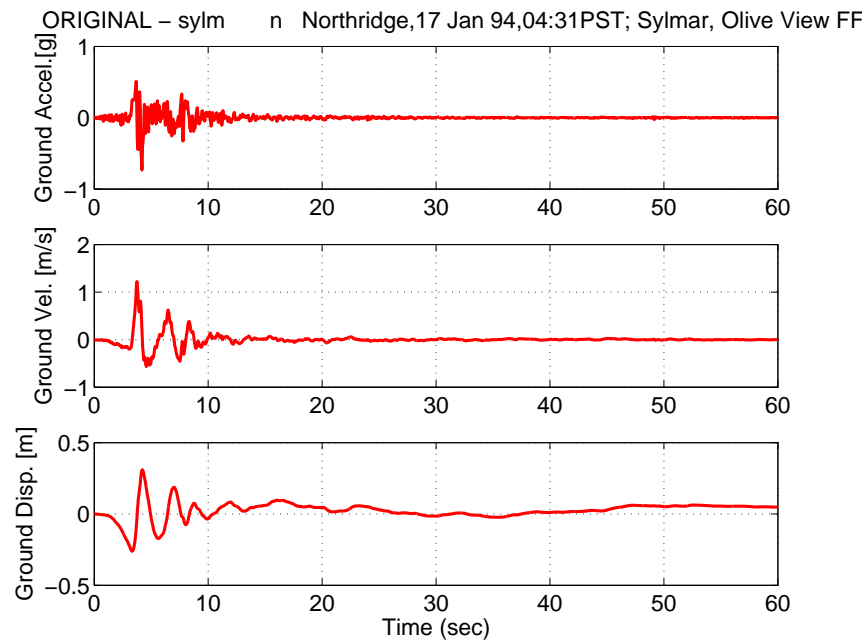


**Figure A.33:** scaled ground motion 12.

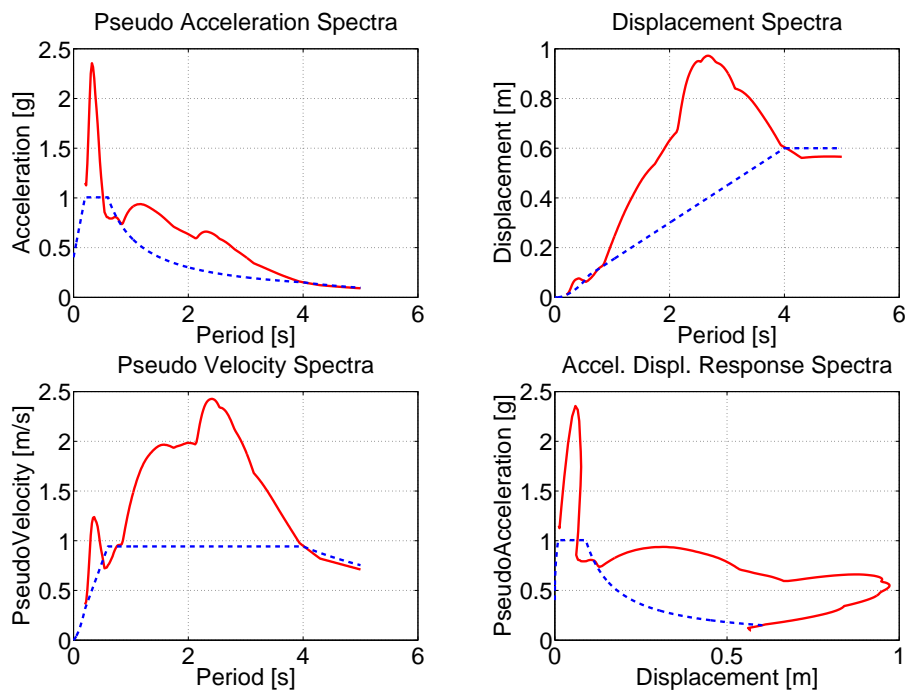


**Figure A.34:** scaled ground motion 12 spectra: pseudo-acceleration spectra (top-left), displacement spectra (top-right), velocity spectra (bottom-left), acceleration-velocity (bottom-right); figures report also comparison with design spectra (dashed line).

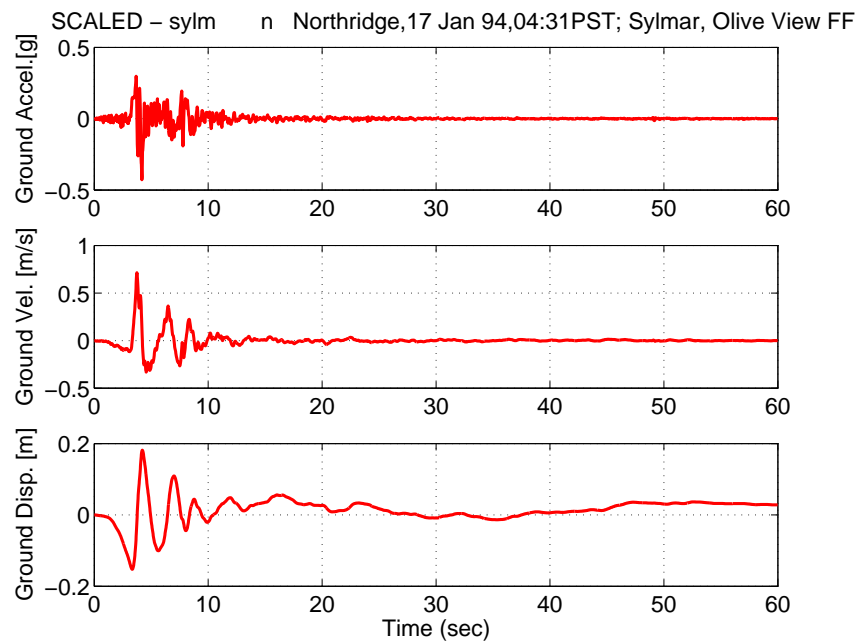
### A.2.6 Ground motion 13



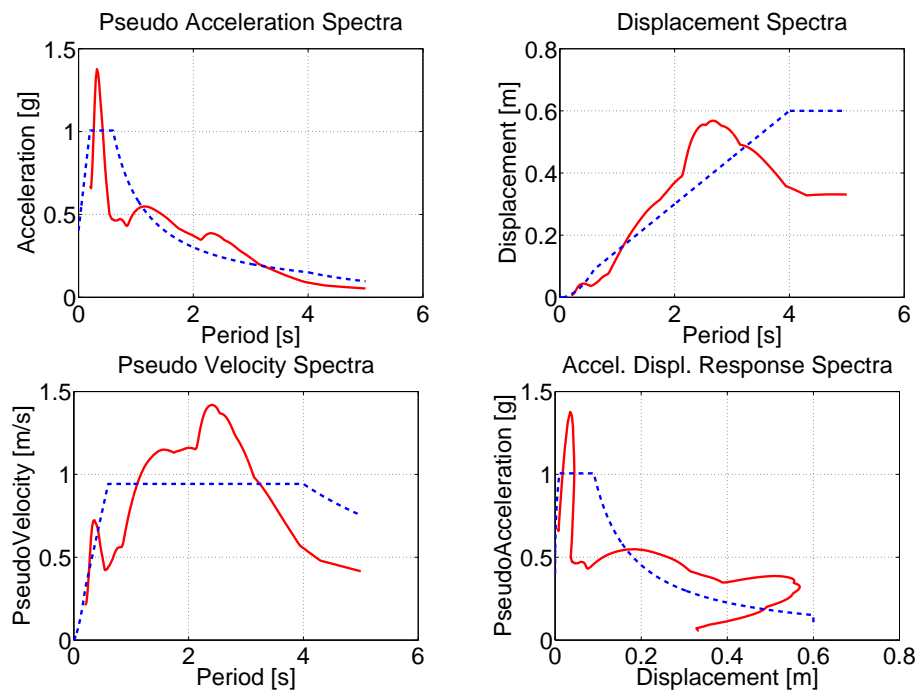
**Figure A.35:** original ground motion 13.



**Figure A.36:** original ground motion 13 spectra: pseudo-acceleration spectra (top-left), displacement spectra (top-right), velocity spectra (bottom-left), acceleration-velocity (bottom-right); figures report also comparison with design spectra (dashed line).

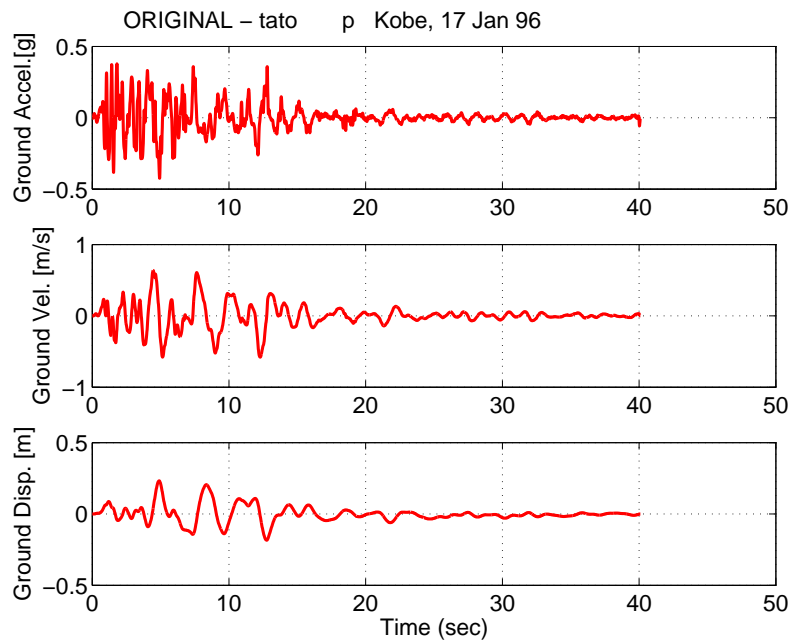


**Figure A.37:** scaled ground motion 13.

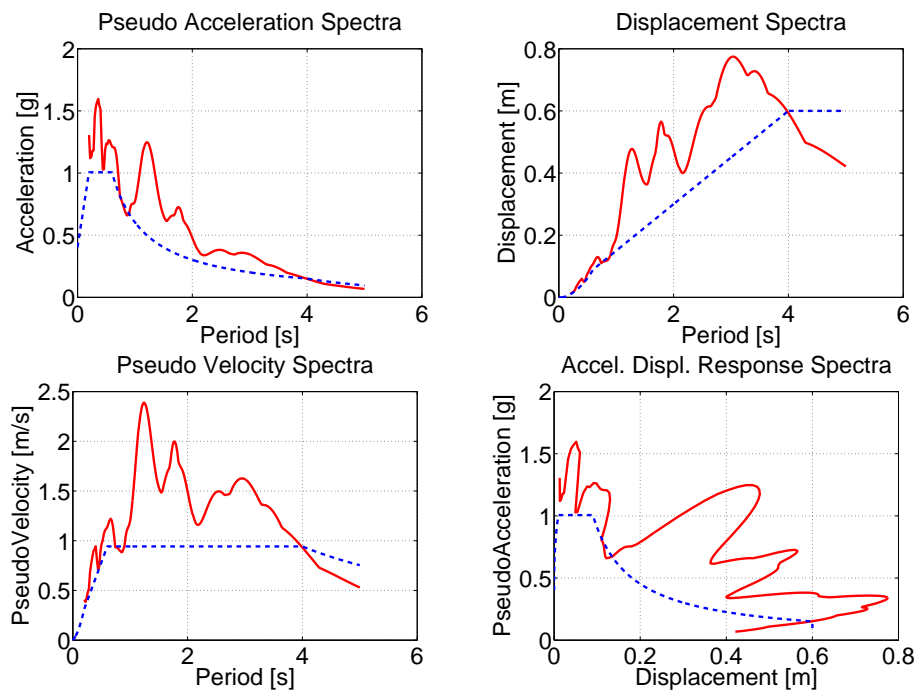


**Figure A.38:** scaled ground motion 13 spectra: pseudo-acceleration spectra (top-left), displacement spectra (top-right), velocity spectra (bottom-left), acceleration-velocity (bottom-right); figures report also comparison with design spectra (dashed line).

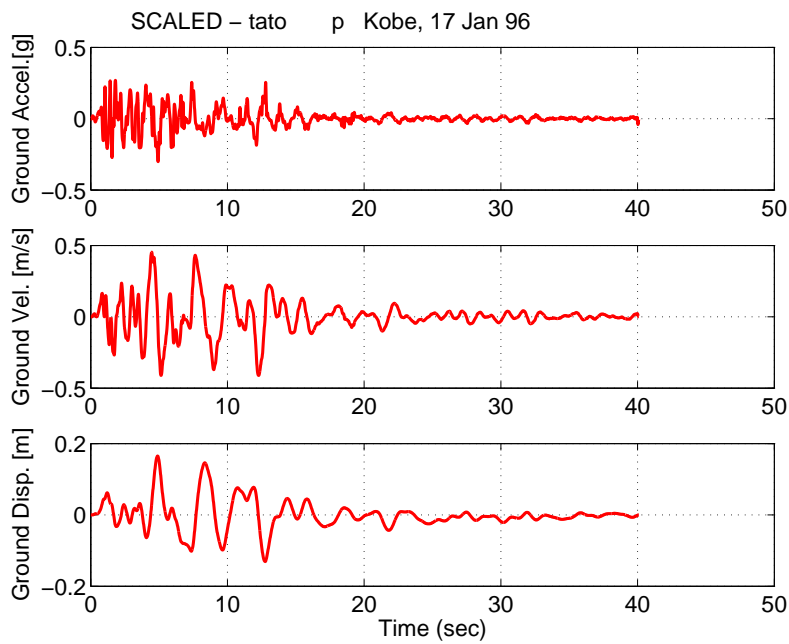
### A.2.7 Ground motion 14



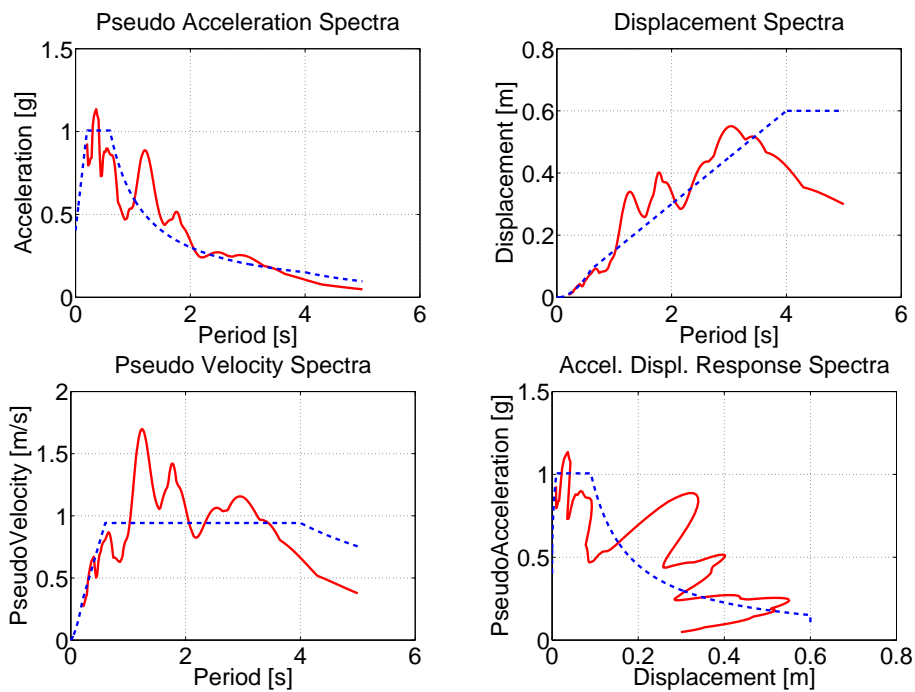
**Figure A.39:** original ground motion 14.



**Figure A.40:** original ground motion 14 spectra: pseudo-acceleration spectra (top-left), displacement spectra (top-right), velocity spectra (bottom-left), acceleration-velocity (bottom-right); figures report also comparison with design spectra (dashed line).



**Figure A.41:** scaled ground motion 14.

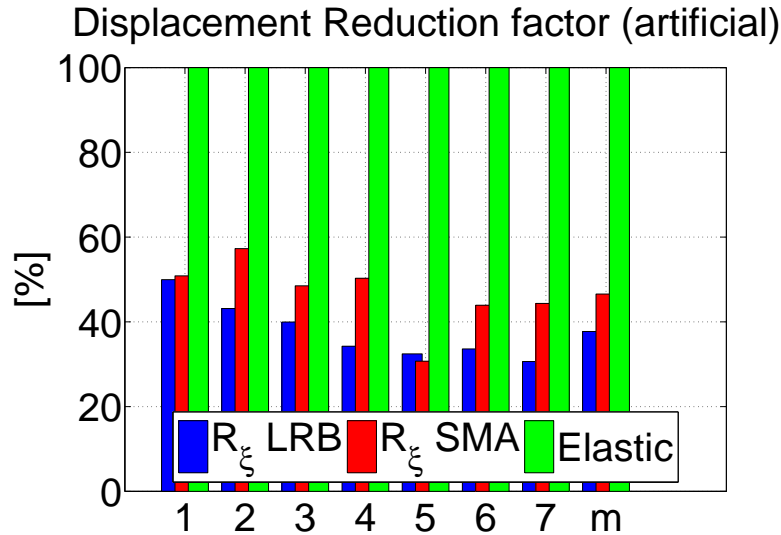


**Figure A.42:** scaled ground motion 14 spectra: pseudo-acceleration spectra (top-left), displacement spectra (top-right), velocity spectra (bottom-left), acceleration-velocity (bottom-right); figures report also comparison with design spectra (dashed line).

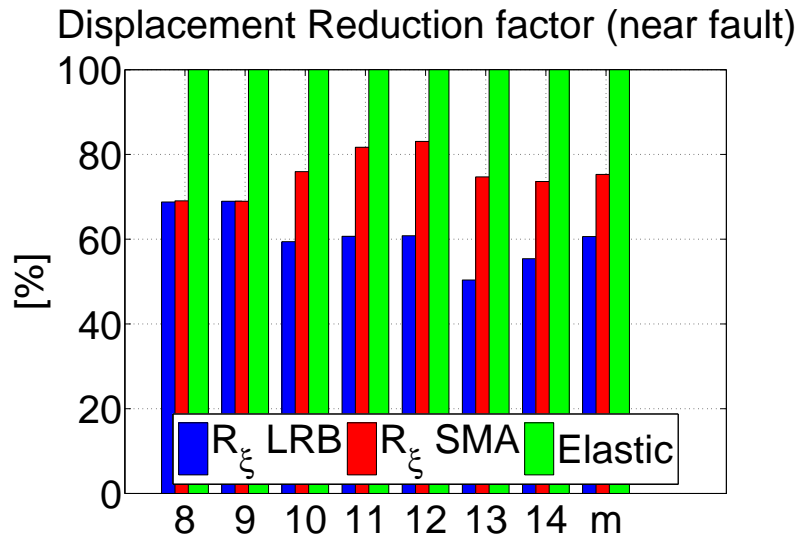
## **B. RIGID SUPERSTRUCTURE TIME HISTORY RESULTS SUMMARY**

## B.1 NO SECOND HARDENING MODEL

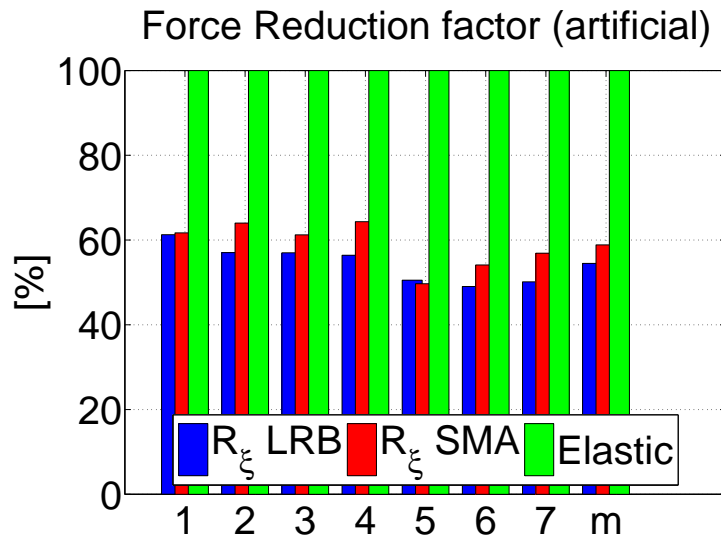
### B.1.1 $\beta = 0.95$



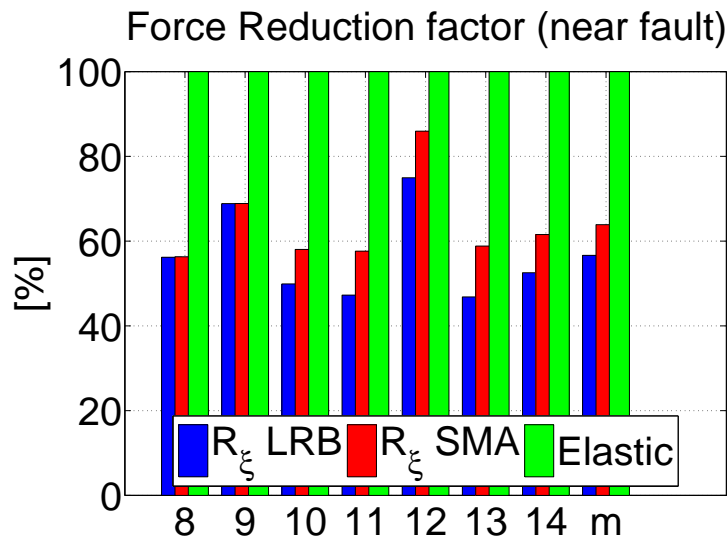
**Figure B.1:** displacement demand values normalized to the linear elastic displacement demand for artificial ground motions; the last set is the mean value of the previous ones; standard deviation values are  $\sigma_{LRB,u,ar} = 6.96$  and  $\sigma_{SMA,u,ar} = 8.31$ .



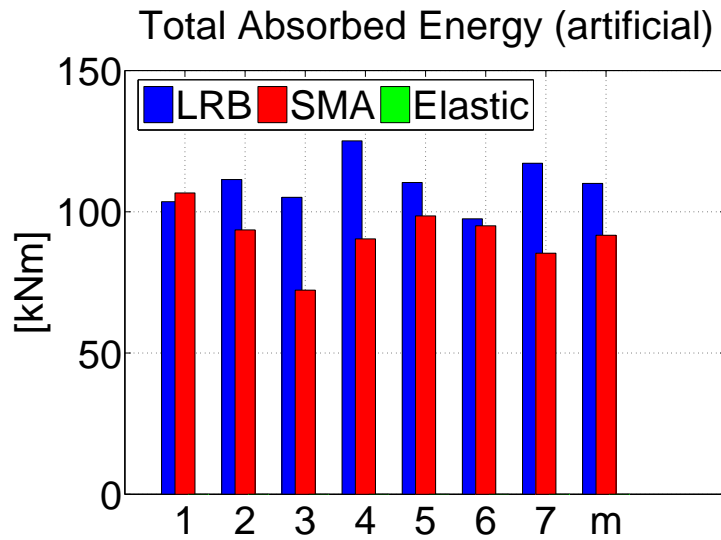
**Figure B.2:** displacement demand values normalized to the linear elastic displacement demand for near fault ground motions; the last set is the mean value of the previous ones; standard deviation values are  $\sigma_{LRB,u,nf} = 6.70$  and  $\sigma_{SMA,u,nf} = 5.54$ .



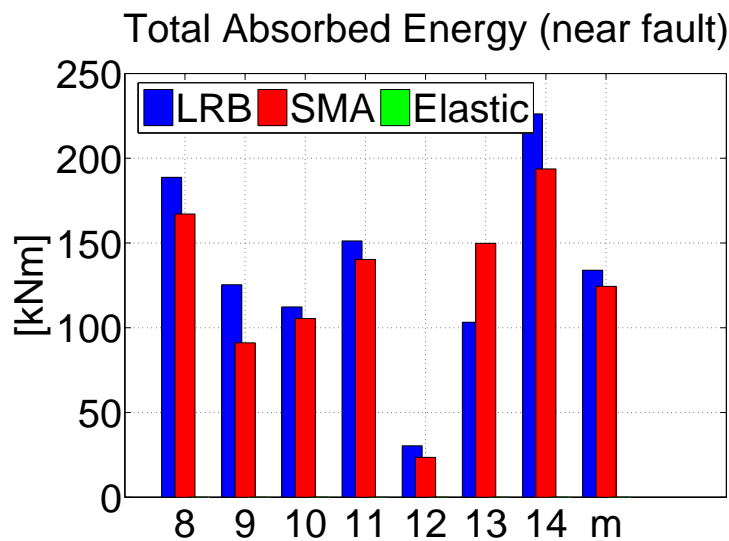
**Figure B.3:** force demand values normalized to the linear elastic displacement demand for artificial ground motions; the last set is the mean value of the previous ones; standard deviation values are  $\sigma_{LRB,f,ar} = 4.59$  and  $\sigma_{SMA,f,ar} = 5.48$ .



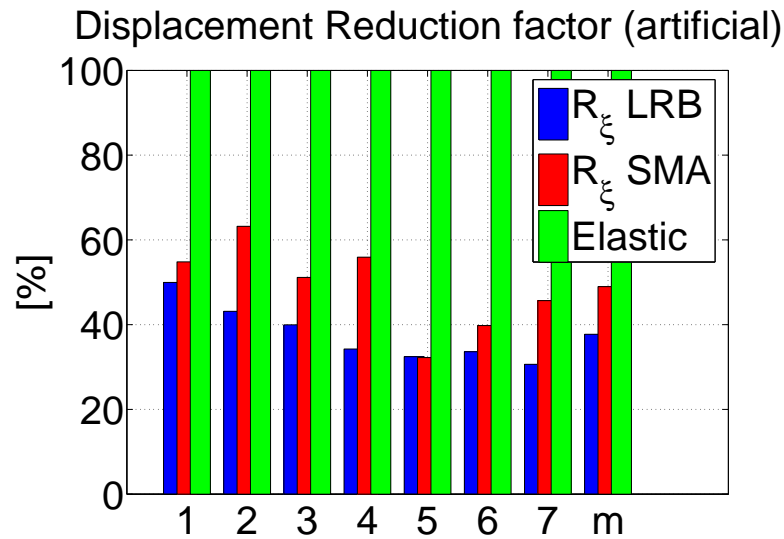
**Figure B.4:** force demand values normalized to the linear elastic displacement demand for near fault ground motions; the last set is the mean value of the previous ones; standard deviation values are  $\sigma_{LRB,f,nf} = 11.03$  and  $\sigma_{SMA,f,nf} = 10.58$ .



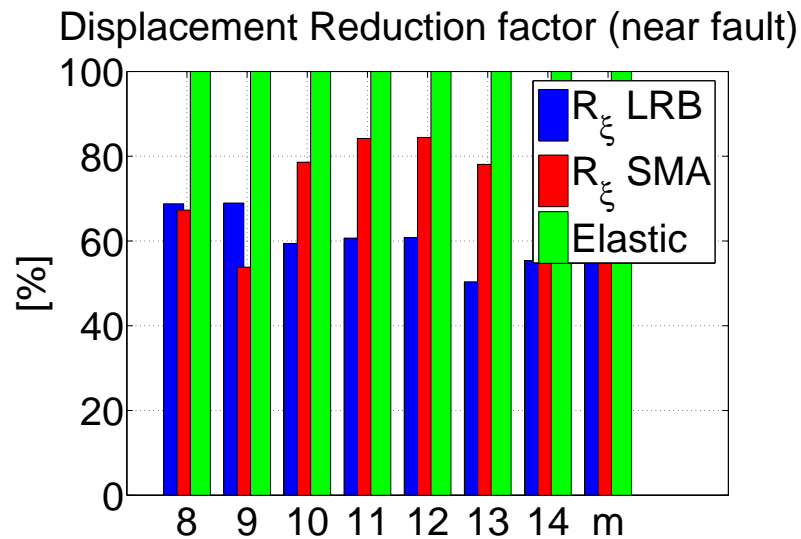
**Figure B.5:** system absorbed energy for artificial ground motions; the last set is the mean value of the previous ones.



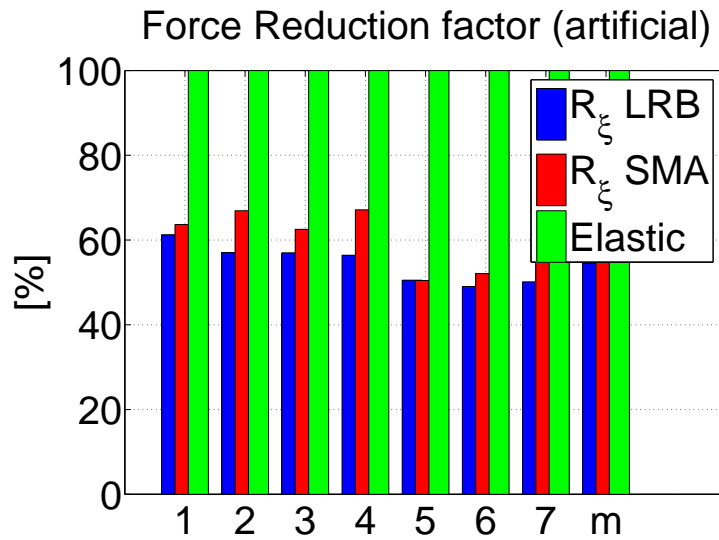
**Figure B.6:** system absorbed energy for near fault ground motions; the last set is the mean value of the previous ones.

**B.1.2**  $\beta = 0.75$ 


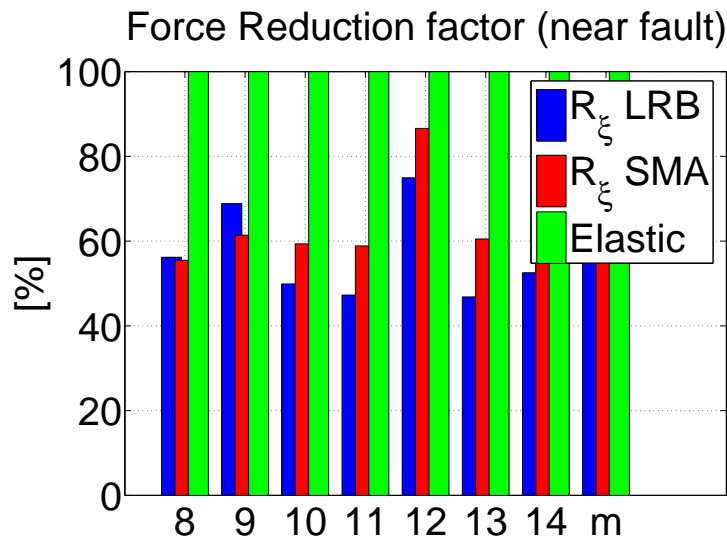
**Figure B.7:** displacement demand values normalized to the linear elastic displacement demand for artificial ground motions; the last set is the mean value of the previous ones; standard deviation values are  $\sigma_{LRB,u,ar} = 6.96$  and  $\sigma_{SMA,u,ar} = 10.53$ .



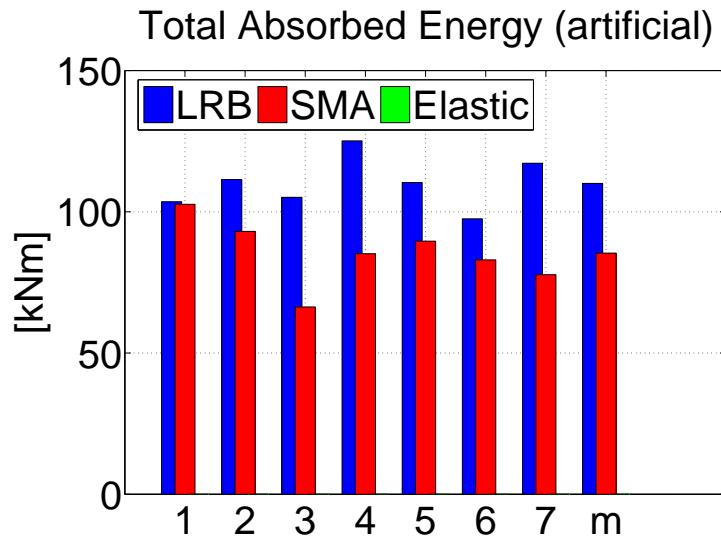
**Figure B.8:** displacement demand values normalized to the linear elastic displacement demand for near fault ground motions; the last set is the mean value of the previous ones; standard deviation values are  $\sigma_{LRB,u,nf} = 6.70$  and  $\sigma_{SMA,u,nf} = 10.88$ .



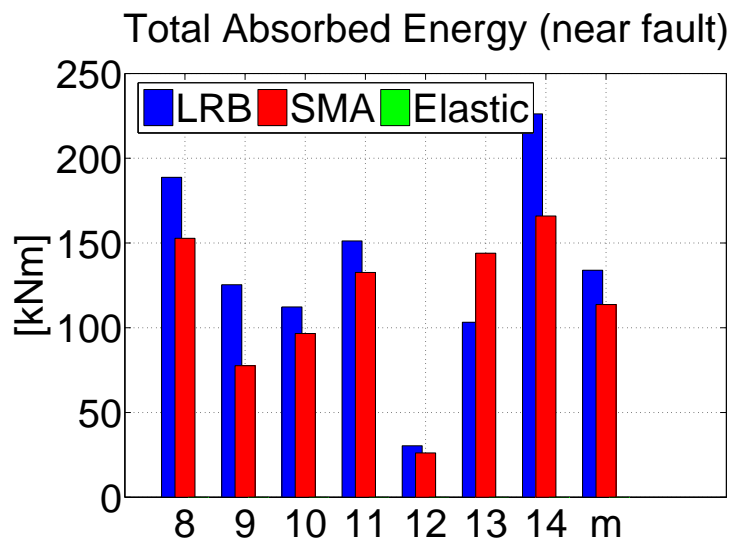
**Figure B.9:** force demand values normalized to the linear elastic displacement demand for artificial ground motions; the last set is the mean value of the previous ones; standard deviation values are  $\sigma_{LRB,f,ar} = 4.59$  and  $\sigma_{SMA,f,ar} = 6.81$ .



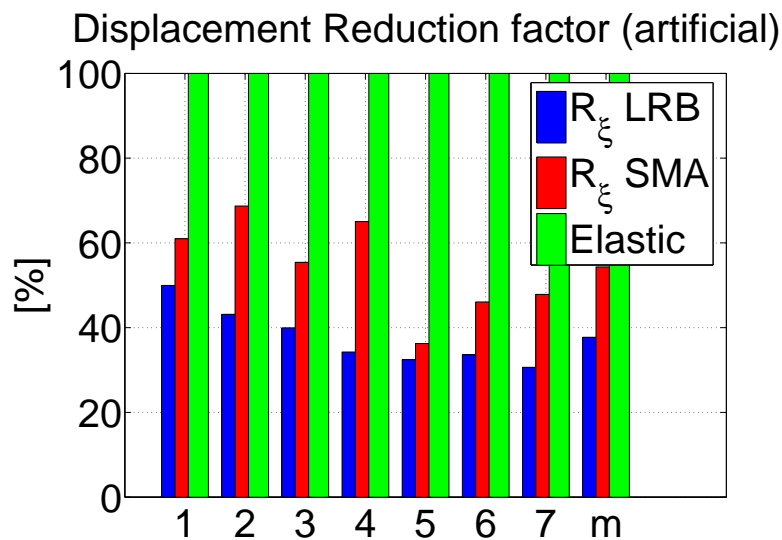
**Figure B.10:** force demand values normalized to the linear elastic displacement demand for near fault ground motions; the last set is the mean value of the previous ones; standard deviation values are  $\sigma_{LRB,f,nf} = 11.03$  and  $\sigma_{SMA,f,nf} = 10.41$ .



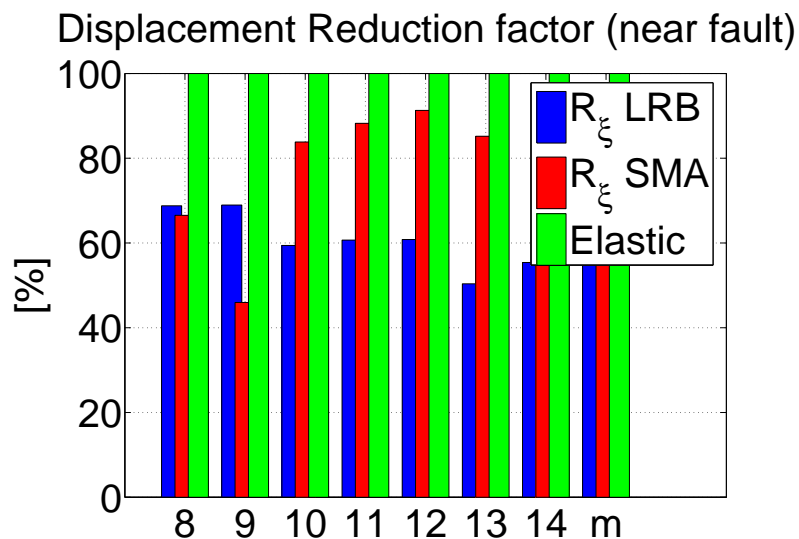
**Figure B.11:** system absorbed energy for artificial ground motions; the last set is the mean value of the previous ones.



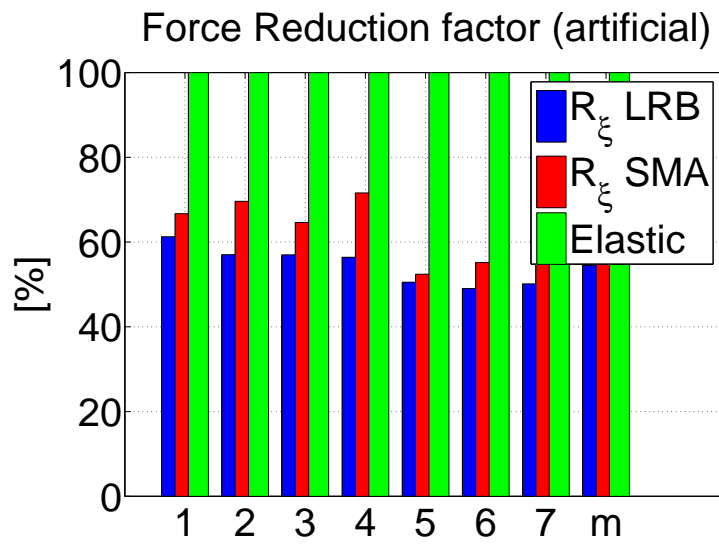
**Figure B.12:** system absorbed energy for near fault ground motions; the last set is the mean value of the previous ones.

**B.1.3**  $\beta = 0.55$ 


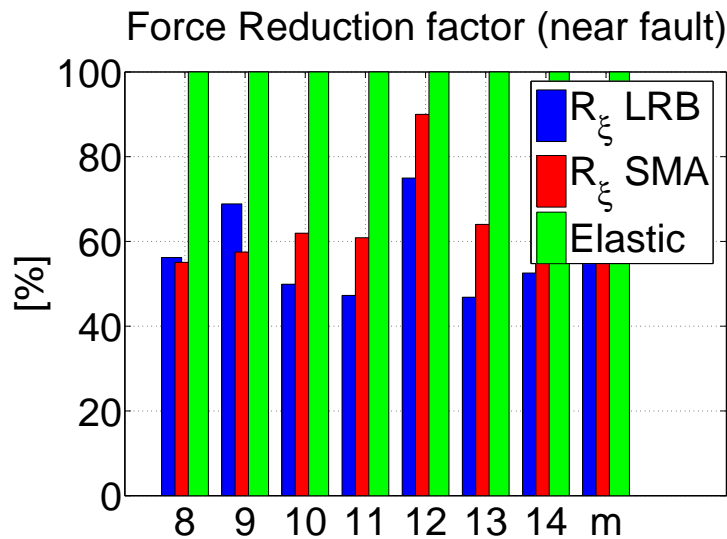
**Figure B.13:** displacement demand values normalized to the linear elastic displacement demand for artificial ground motions; the last set is the mean value of the previous ones; standard deviation values are  $\sigma_{LRB,u,ar} = 6.96$  and  $\sigma_{SMA,u,ar} = 11.57$ .



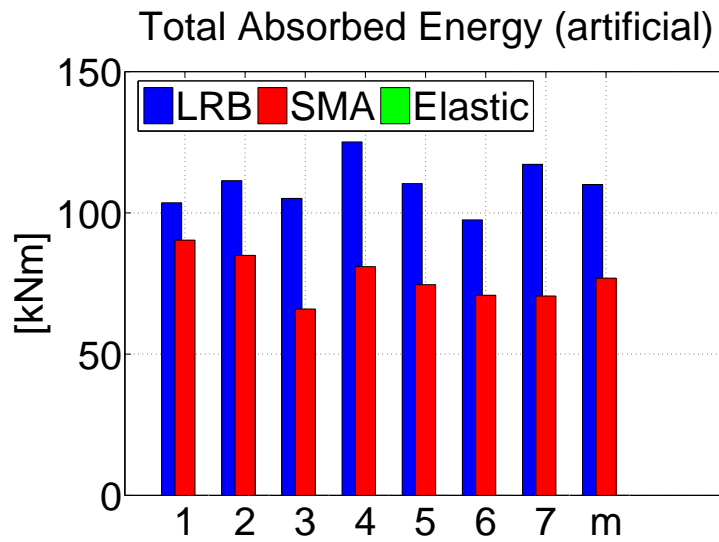
**Figure B.14:** displacement demand values normalized to the linear elastic displacement demand for near fault ground motions; the last set is the mean value of the previous ones; standard deviation values are  $\sigma_{LRB,u,nf} = 6.70$  and  $\sigma_{SMA,u,nf} = 16.00$ .



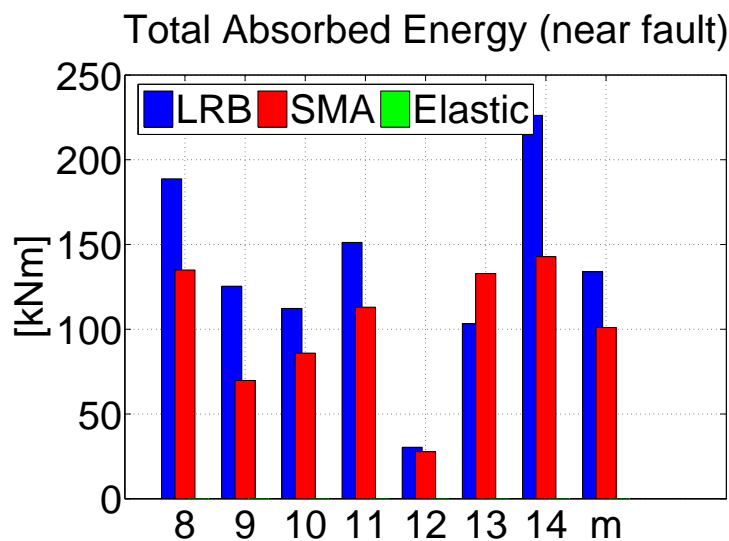
**Figure B.15:** force demand values normalized to the linear elastic displacement demand for artificial ground motions; the last set is the mean value of the previous ones; standard deviation values are  $\sigma_{LRB,f,ar} = 4.59$  and  $\sigma_{SMA,f,ar} = 7.36$ .



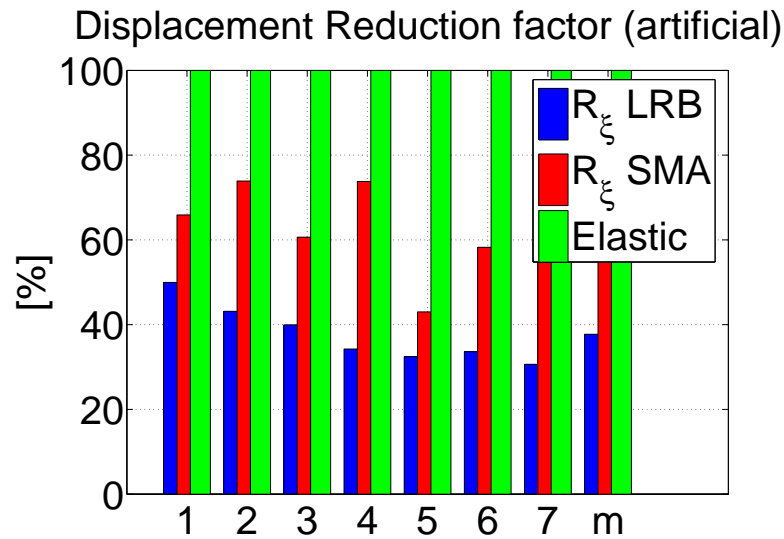
**Figure B.16:** force demand values normalized to the linear elastic displacement demand for near fault ground motions; the last set is the mean value of the previous ones; standard deviation values are  $\sigma_{LRB,f,nf} = 11.03$  and  $\sigma_{SMA,f,nf} = 11.59$ .



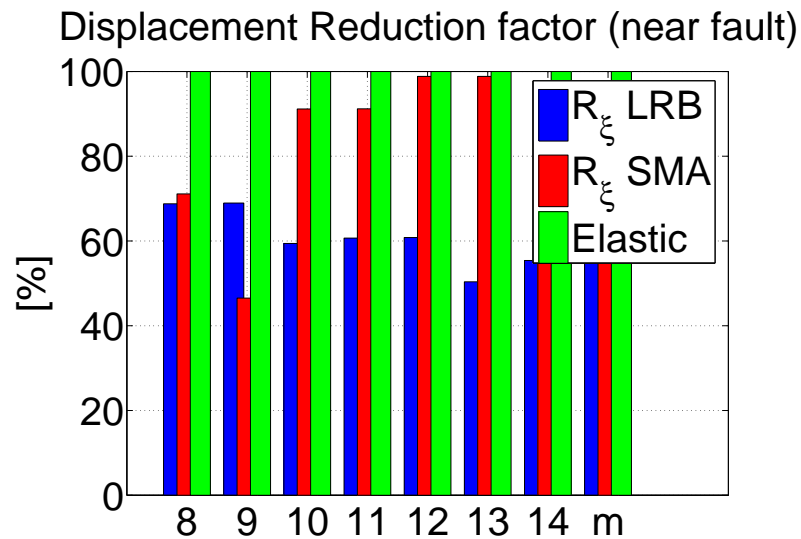
**Figure B.17:** system absorbed energy for artificial ground motions; the last set is the mean value of the previous ones.



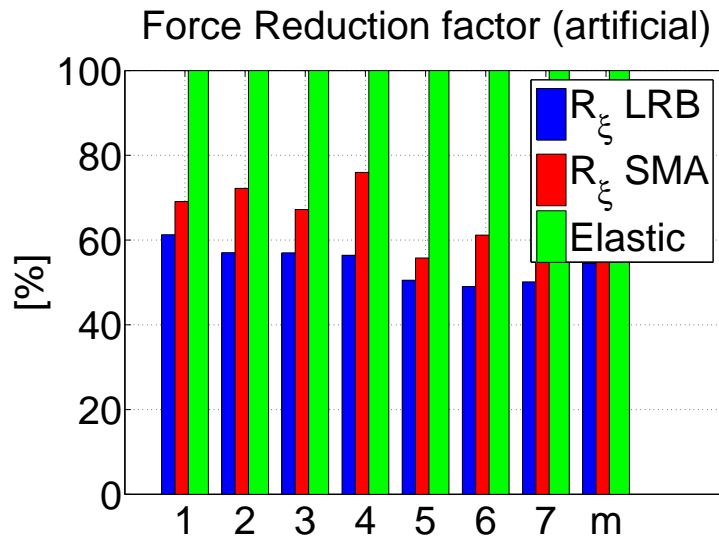
**Figure B.18:** system absorbed energy for near fault ground motions; the last set is the mean value of the previous ones.

**B.1.4**  $\beta = 0.35$ 


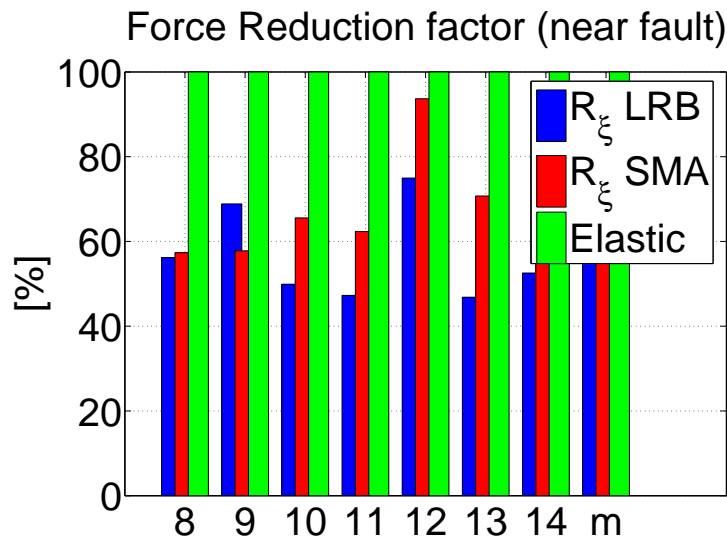
**Figure B.19:** displacement demand values normalized to the linear elastic displacement demand for artificial ground motions; the last set is the mean value of the previous ones; standard deviation values are  $\sigma_{LRB,u,ar} = 6.96$  and  $\sigma_{SMA,u,ar} = 11.39$ .



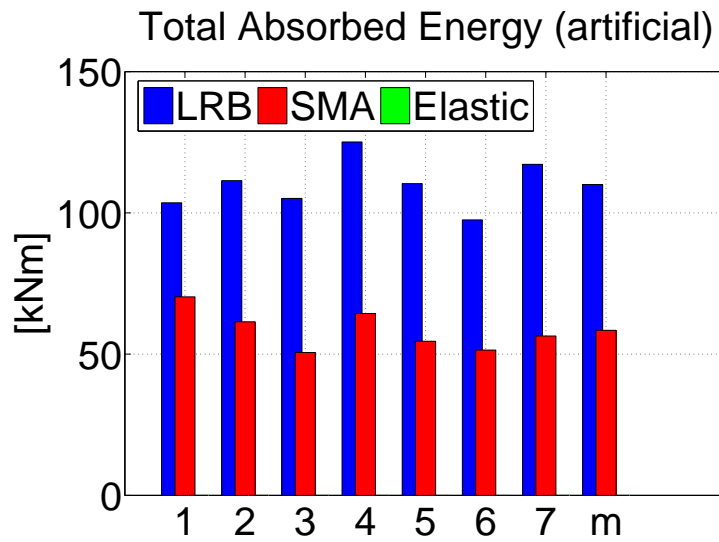
**Figure B.20:** displacement demand values normalized to the linear elastic displacement demand for near fault ground motions; the last set is the mean value of the previous ones; standard deviation values are  $\sigma_{LRB,u,nf} = 6.70$  and  $\sigma_{SMA,u,nf} = 18.97$ .



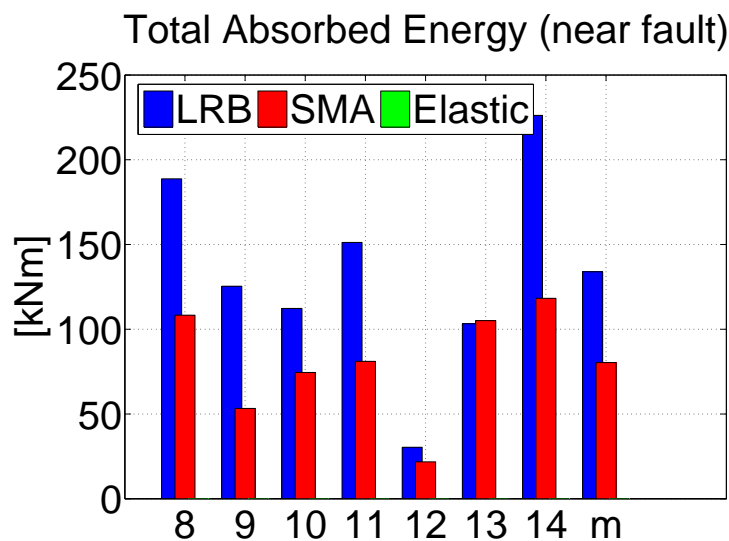
**Figure B.21:** force demand values normalized to the linear elastic displacement demand for artificial ground motions; the last set is the mean value of the previous ones; standard deviation values are  $\sigma_{LRB,f,ar} = 4.59$  and  $\sigma_{SMA,f,ar} = 6.94$ .



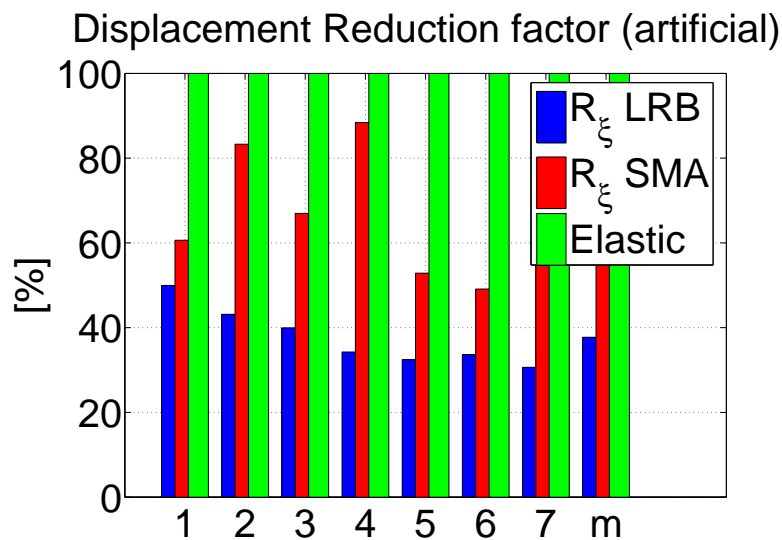
**Figure B.22:** force demand values normalized to the linear elastic displacement demand for near fault ground motions; the last set is the mean value of the previous ones; standard deviation values are  $\sigma_{LRB,f,nf} = 11.03$  and  $\sigma_{SMA,f,nf} = 12.42$ .



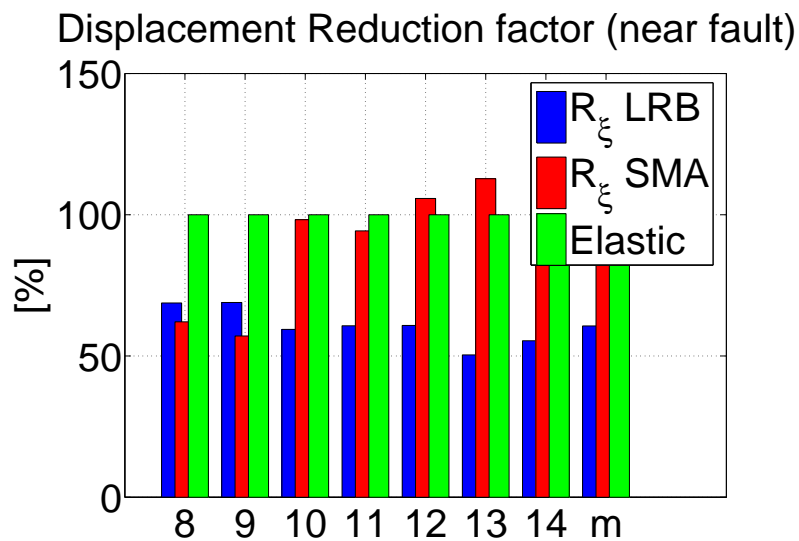
**Figure B.23:** system absorbed energy for artificial ground motions; the last set is the mean value of the previous ones.



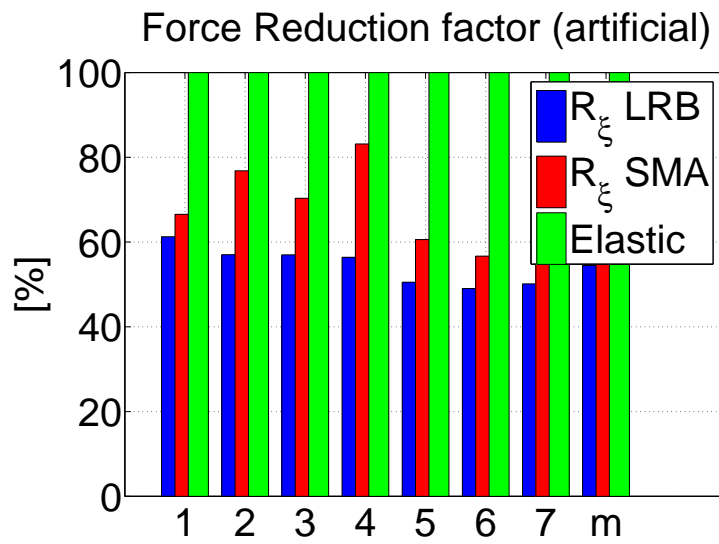
**Figure B.24:** system absorbed energy for near fault ground motions; the last set is the mean value of the previous ones.

**B.1.5**  $\beta = 0.15$ 


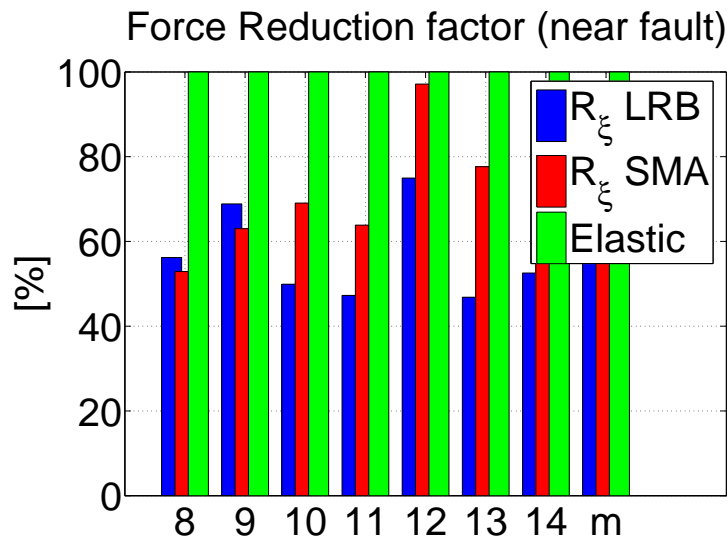
**Figure B.25:** displacement demand values normalized to the linear elastic displacement demand for artificial ground motions; the last set is the mean value of the previous ones; standard deviation values are  $\sigma_{LRB,u,ar} = 6.96$  and  $\sigma_{SMA,u,ar} = 16.16$ .



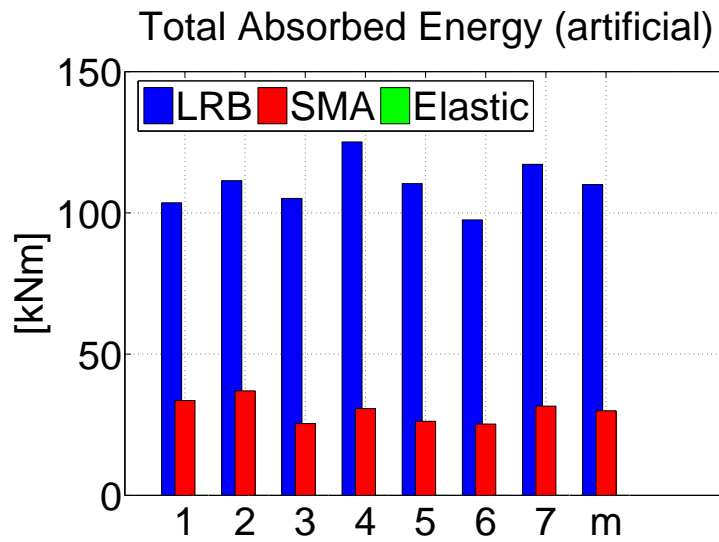
**Figure B.26:** displacement demand values normalized to the linear elastic displacement demand for near fault ground motions; the last set is the mean value of the previous ones; standard deviation values are  $\sigma_{LRB,u,nf} = 6.70$  and  $\sigma_{SMA,u,nf} = 22.48$ .



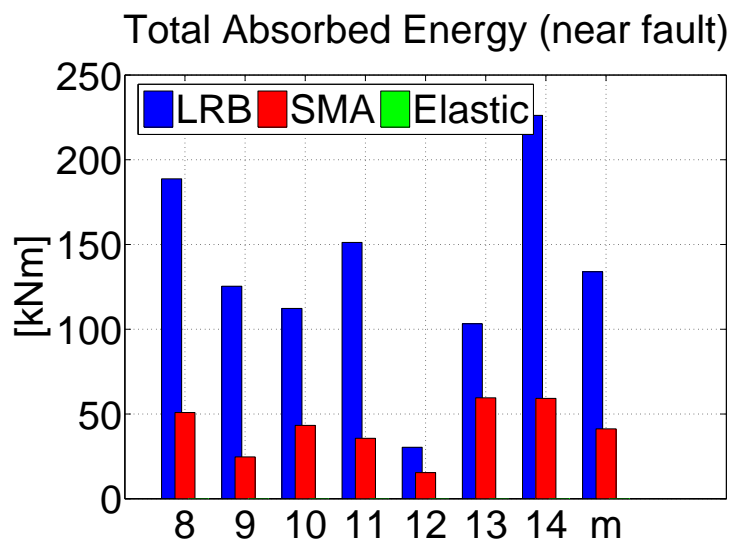
**Figure B.27:** force demand values normalized to the linear elastic displacement demand for artificial ground motions; the last set is the mean value of the previous ones; standard deviation values are  $\sigma_{LRB,f,ar} = 4.59$  and  $\sigma_{SMA,f,ar} = 9.54$ .



**Figure B.28:** force demand values normalized to the linear elastic displacement demand for near fault ground motions; the last set is the mean value of the previous ones; standard deviation values are  $\sigma_{LRB,f,nf} = 11.03$  and  $\sigma_{SMA,f,nf} = 14.30$ .



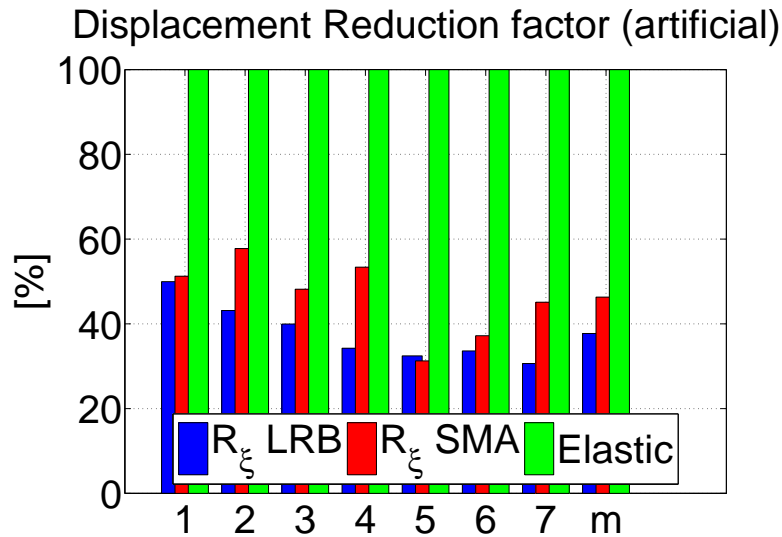
**Figure B.29:** system absorbed energy for artificial ground motions; the last set is the mean value of the previous ones.



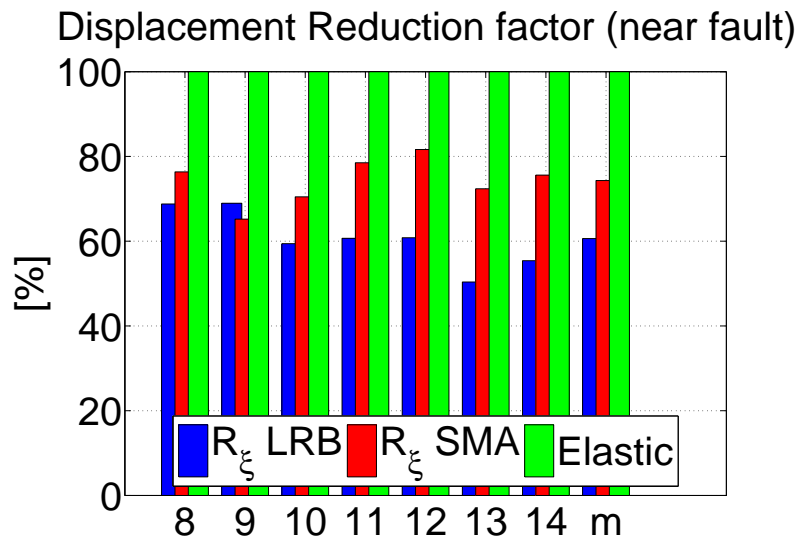
**Figure B.30:** system absorbed energy for near fault ground motions; the last set is the mean value of the previous ones.

## B.2 SECOND HARDENING MODEL

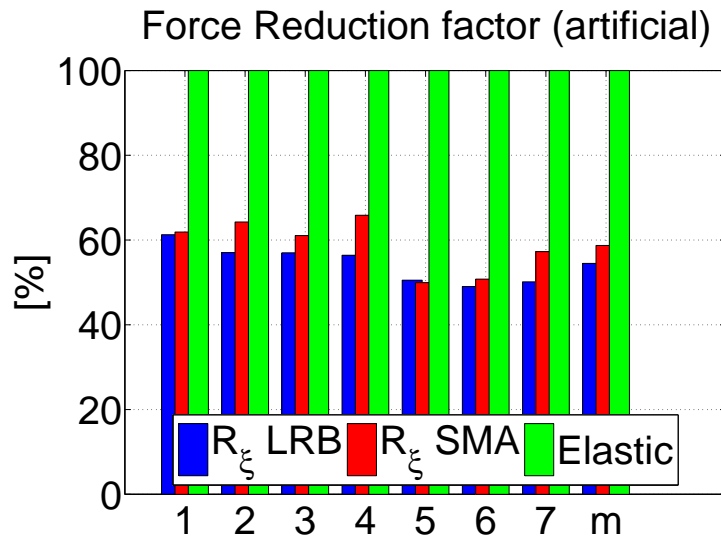
### B.2.1 $\beta = 0.95$



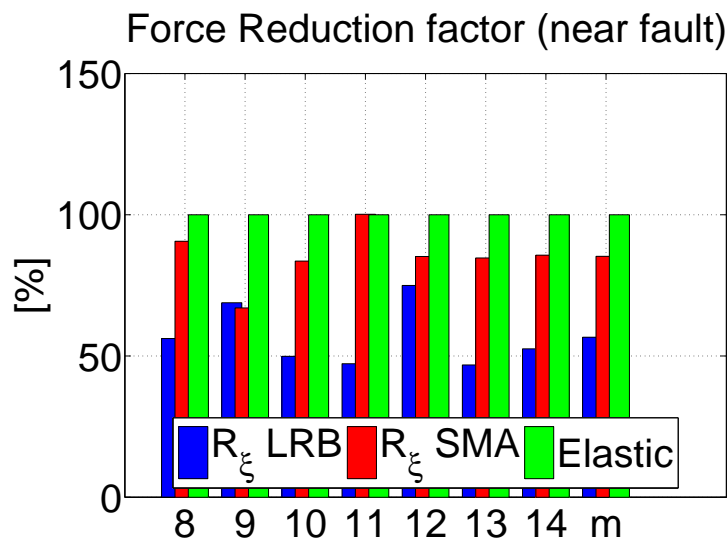
**Figure B.31:** displacement demand values normalized to the linear elastic displacement demand for artificial ground motions; the last set is the mean value of the previous ones.



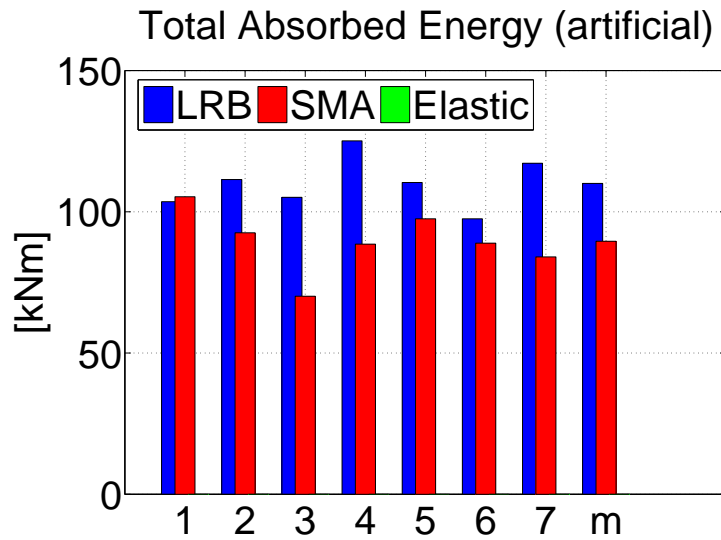
**Figure B.32:** displacement demand values normalized to the linear elastic displacement demand for near fault ground motions; the last set is the mean value of the previous ones.



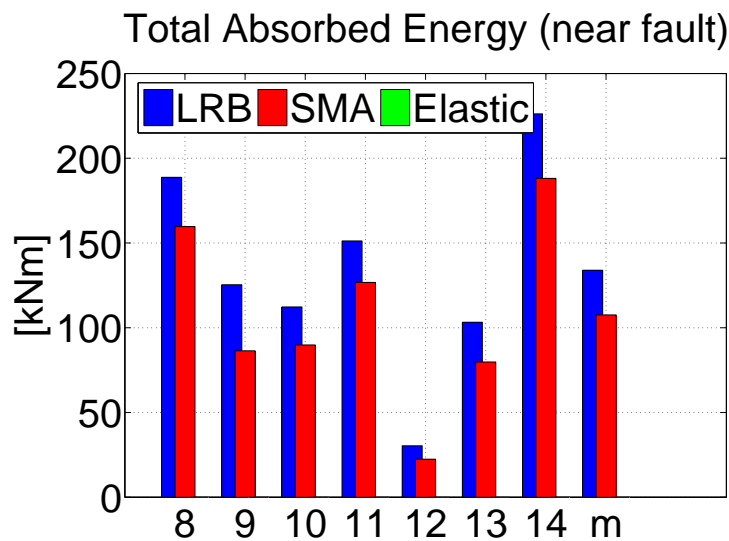
**Figure B.33:** force demand values normalized to the linear elastic displacement demand for artificial ground motions; the last set is the mean value of the previous ones.



**Figure B.34:** force demand values normalized to the linear elastic displacement demand for near fault ground motions; the last set is the mean value of the previous ones.

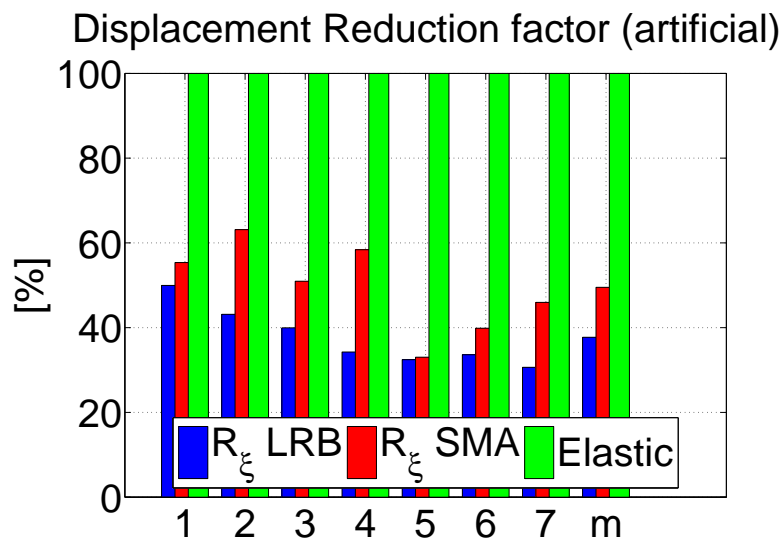


**Figure B.35:** system absorbed energy for artificial ground motions; the last set is the mean value of the previous ones.

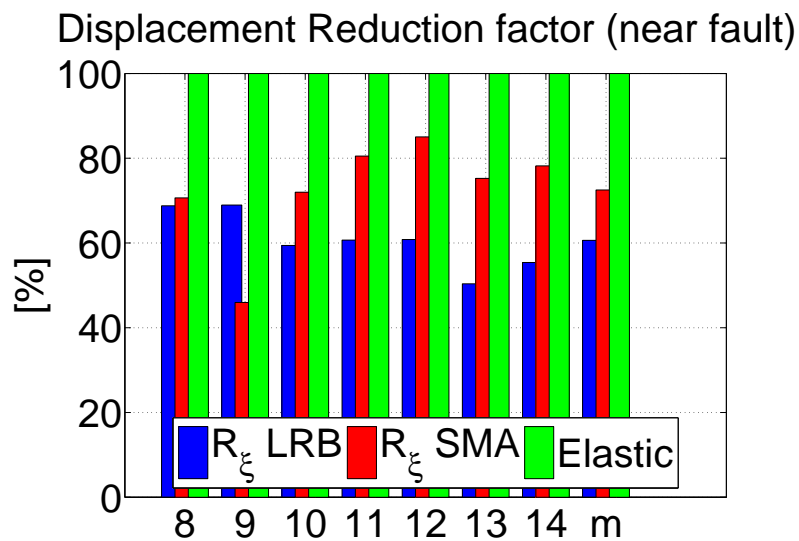


**Figure B.36:** system absorbed energy for near fault ground motions; the last set is the mean value of the previous ones.

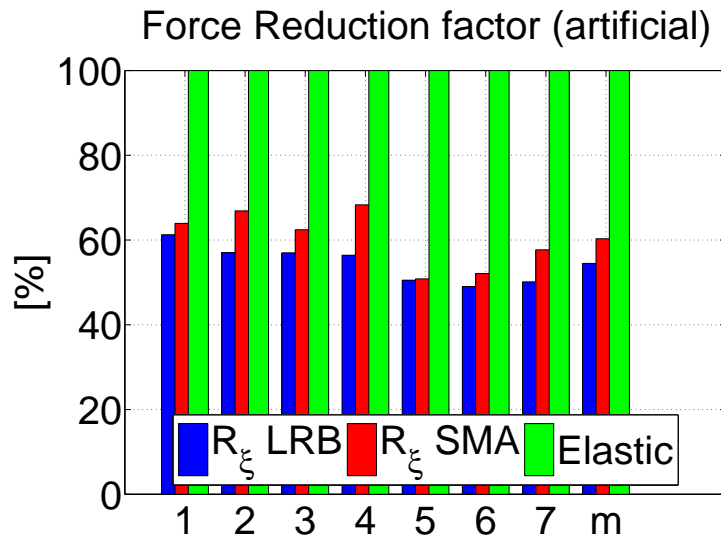
**B.2.2**  $\beta = 0.75$



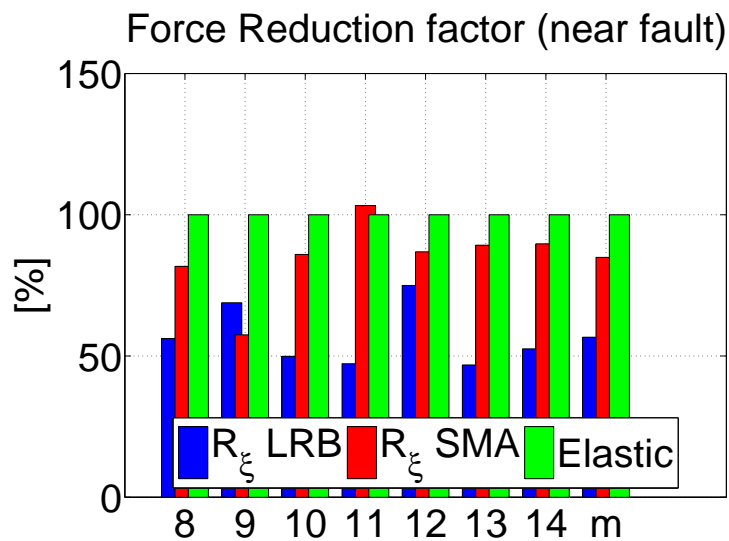
**Figure B.37:** displacement demand values normalized to the linear elastic displacement demand for artificial ground motions; the last set is the mean value of the previous ones.



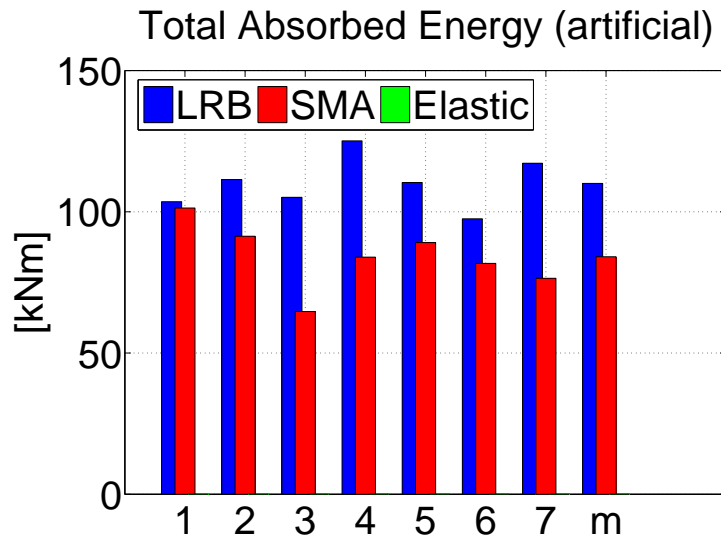
**Figure B.38:** displacement demand values normalized to the linear elastic displacement demand for near fault ground motions; the last set is the mean value of the previous ones.



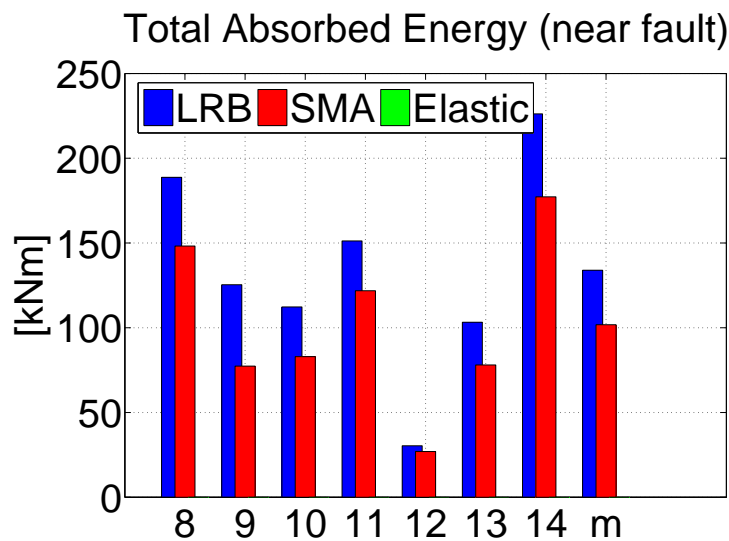
**Figure B.39:** force demand values normalized to the linear elastic displacement demand for artificial ground motions; the last set is the mean value of the previous ones.



**Figure B.40:** force demand values normalized to the linear elastic displacement demand for near fault ground motions; the last set is the mean value of the previous ones.

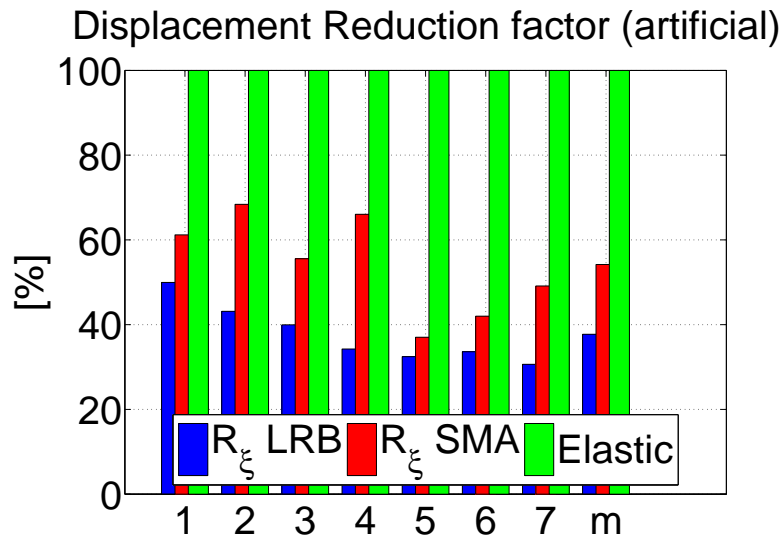


**Figure B.41:** system absorbed energy for artificial ground motions; the last set is the mean value of the previous ones.

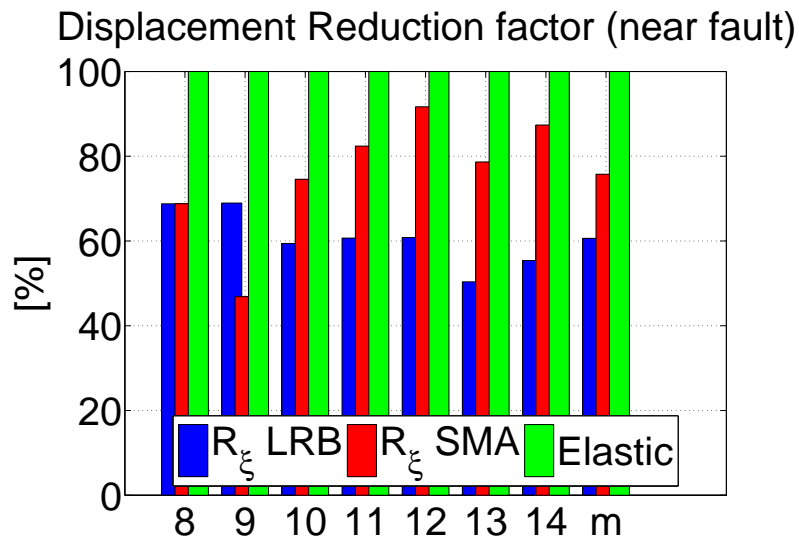


**Figure B.42:** system absorbed energy for near fault ground motions; the last set is the mean value of the previous ones.

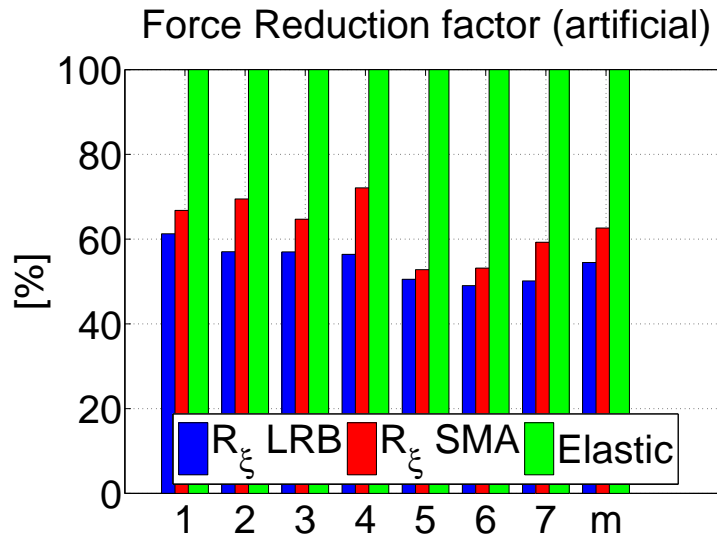
**B.2.3**  $\beta = 0.55$



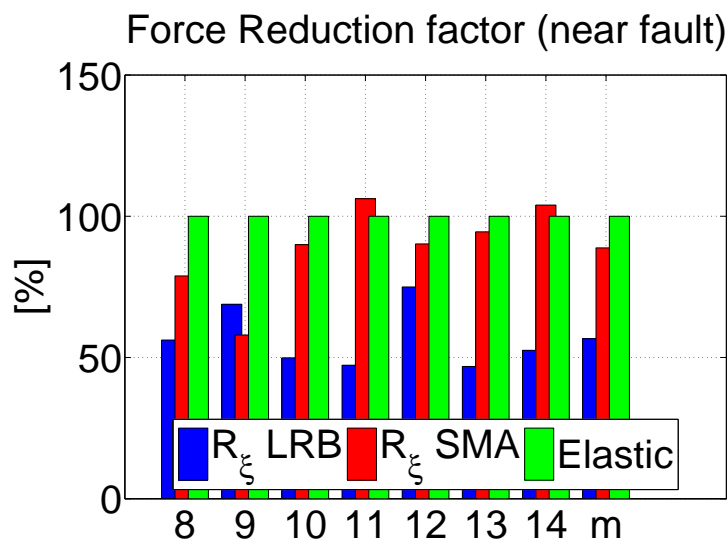
**Figure B.43:** displacement demand values normalized to the linear elastic displacement demand for artificial ground motions; the last set is the mean value of the previous ones.



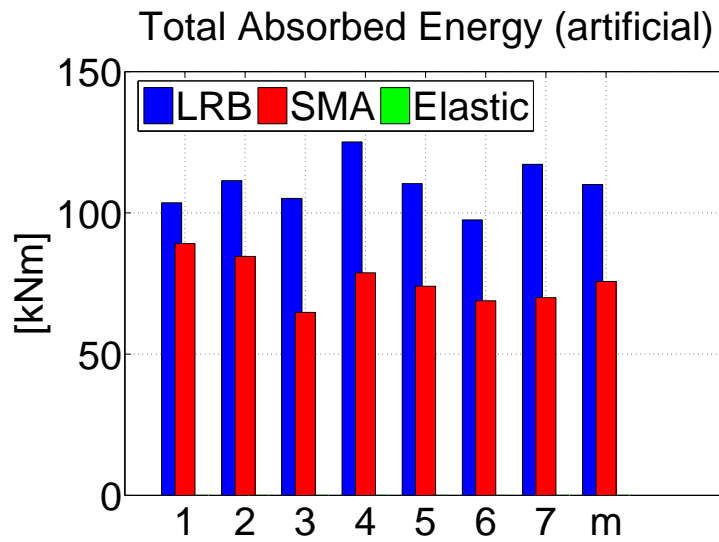
**Figure B.44:** displacement demand values normalized to the linear elastic displacement demand for near fault ground motions; the last set is the mean value of the previous ones.



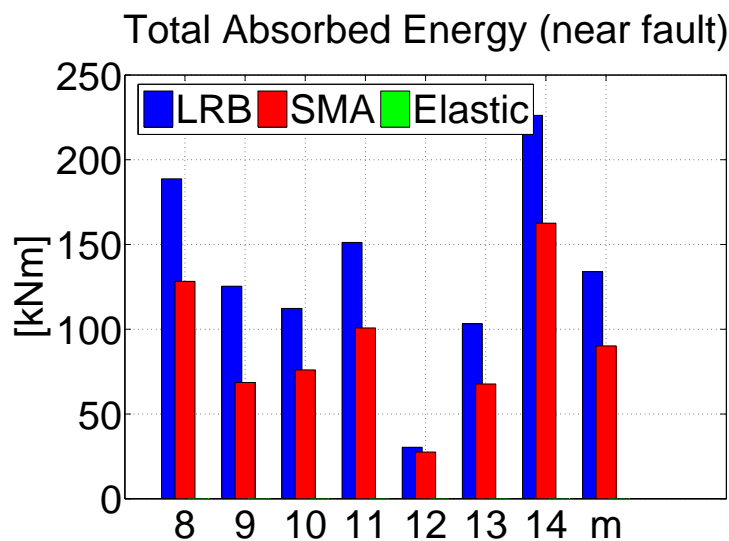
**Figure B.45:** force demand values normalized to the linear elastic displacement demand for artificial ground motions; the last set is the mean value of the previous ones.



**Figure B.46:** force demand values normalized to the linear elastic displacement demand for near fault ground motions; the last set is the mean value of the previous ones.

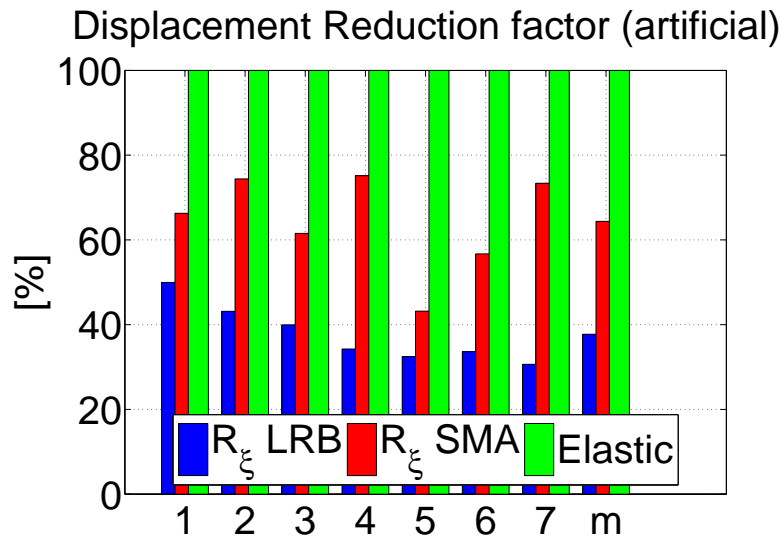


**Figure B.47:** system absorbed energy for artificial ground motions; the last set is the mean value of the previous ones.

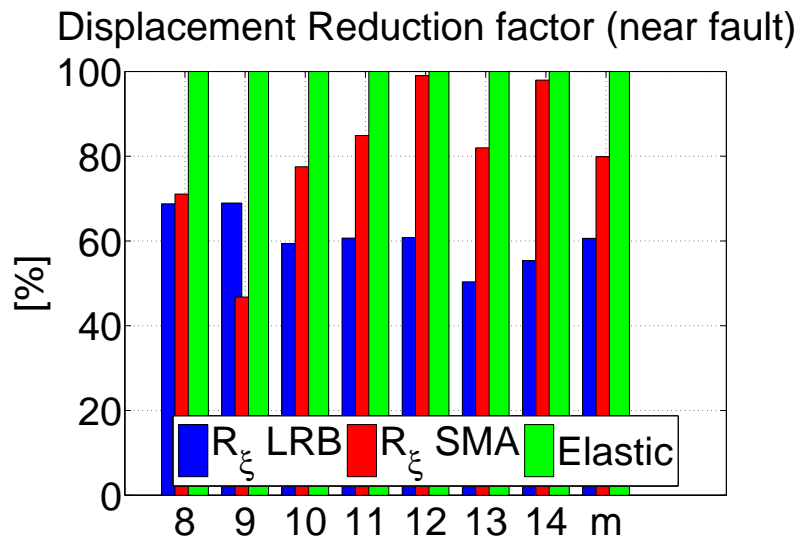


**Figure B.48:** system absorbed energy for near fault ground motions; the last set is the mean value of the previous ones.

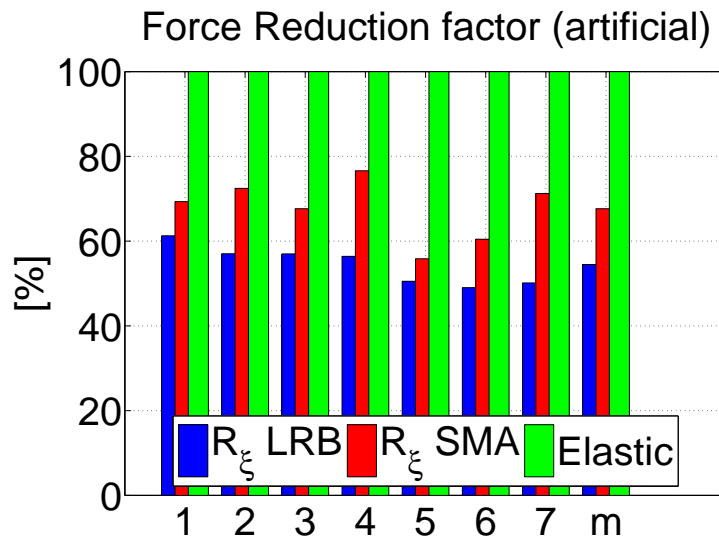
**B.2.4**  $\beta = 0.35$



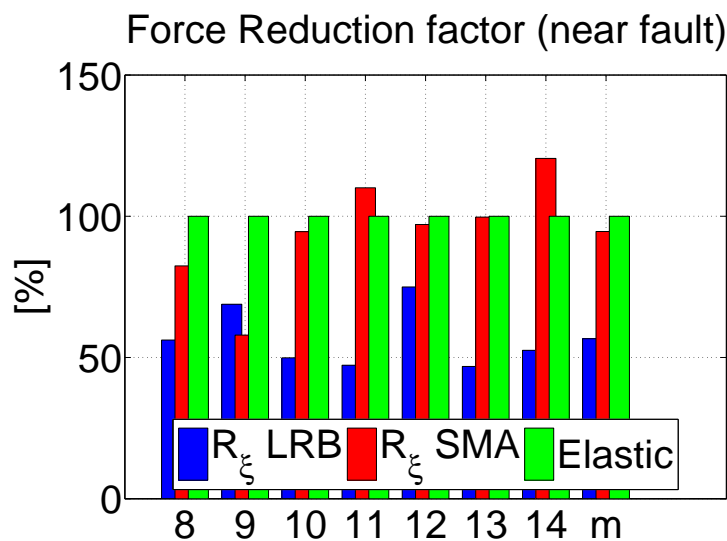
**Figure B.49:** displacement demand values normalized to the linear elastic displacement demand for artificial ground motions; the last set is the mean value of the previous ones.



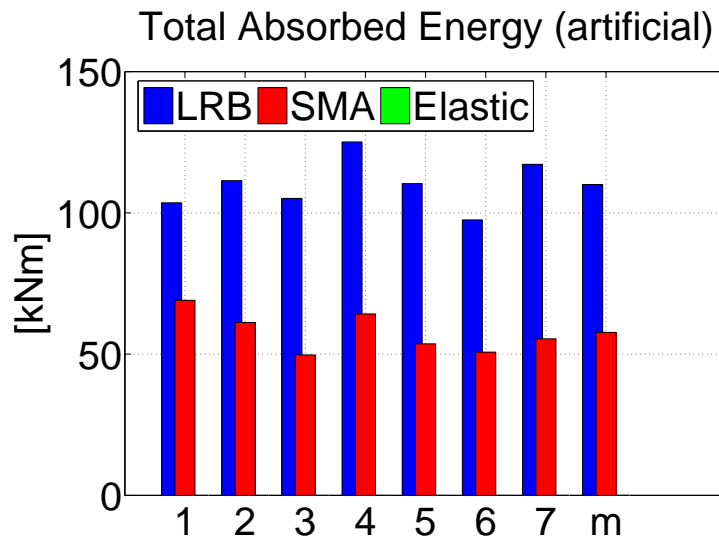
**Figure B.50:** displacement demand values normalized to the linear elastic displacement demand for near fault ground motions; the last set is the mean value of the previous ones.



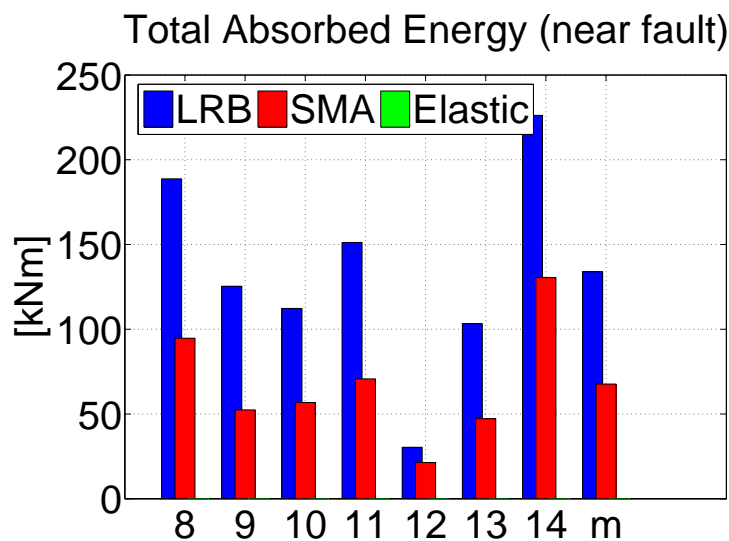
**Figure B.51:** force demand values normalized to the linear elastic displacement demand for artificial ground motions; the last set is the mean value of the previous ones.



**Figure B.52:** force demand values normalized to the linear elastic displacement demand for near fault ground motions; the last set is the mean value of the previous ones.

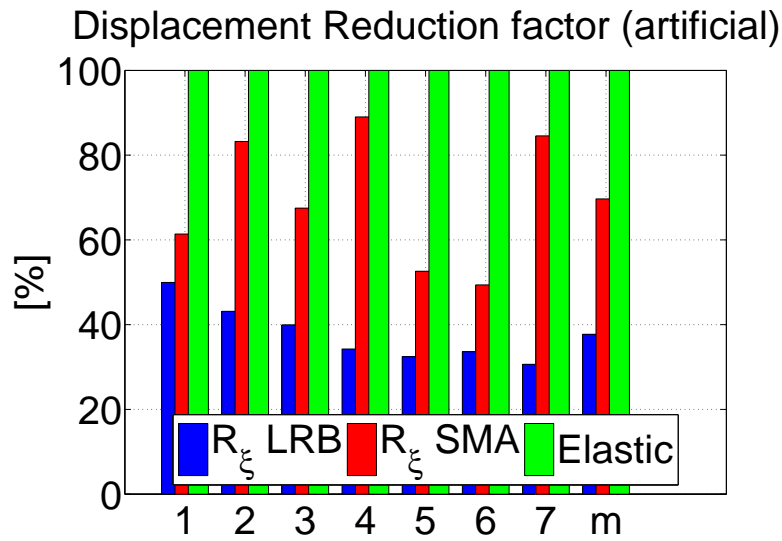


**Figure B.53:** system absorbed energy for artificial ground motions; the last set is the mean value of the previous ones.

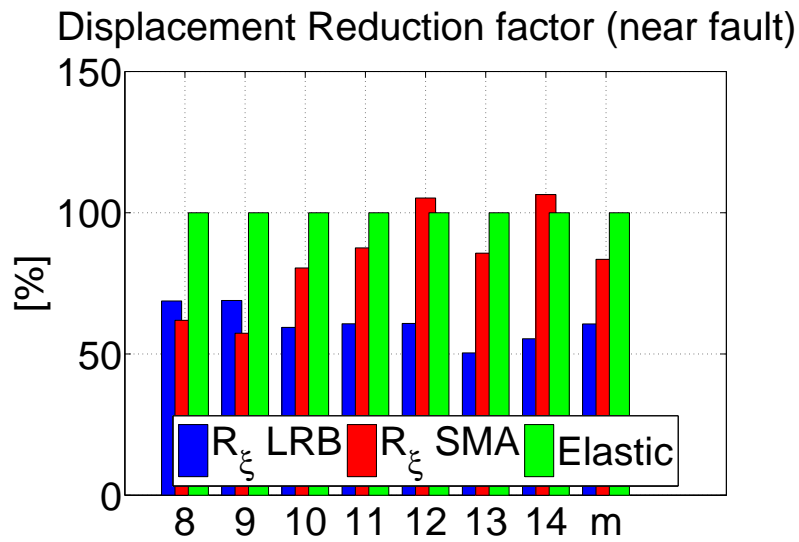


**Figure B.54:** system absorbed energy for near fault ground motions; the last set is the mean value of the previous ones.

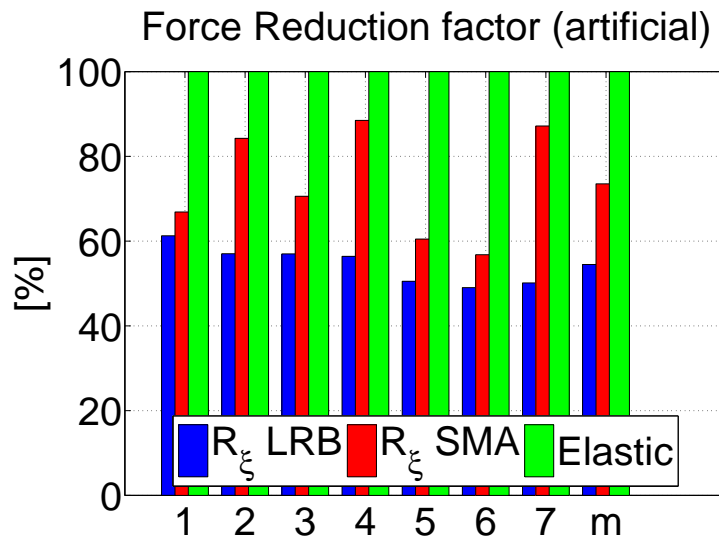
**B.2.5**  $\beta = 0.15$



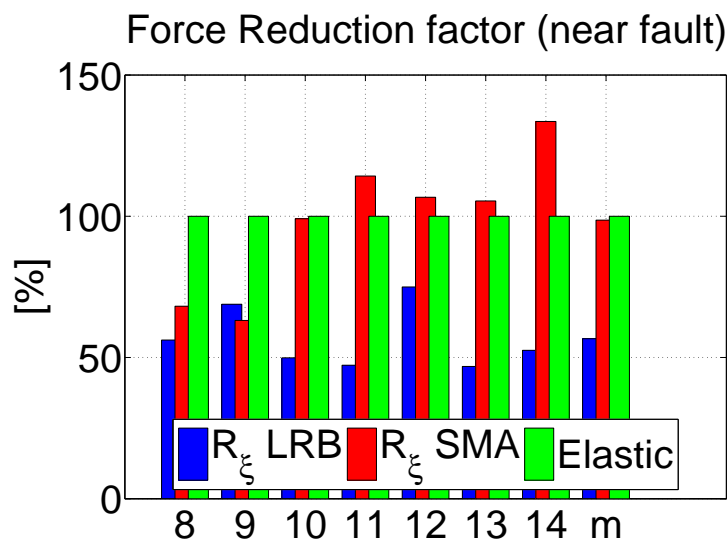
**Figure B.55:** displacement demand values normalized to the linear elastic displacement demand for artificial ground motions; the last set is the mean value of the previous ones.



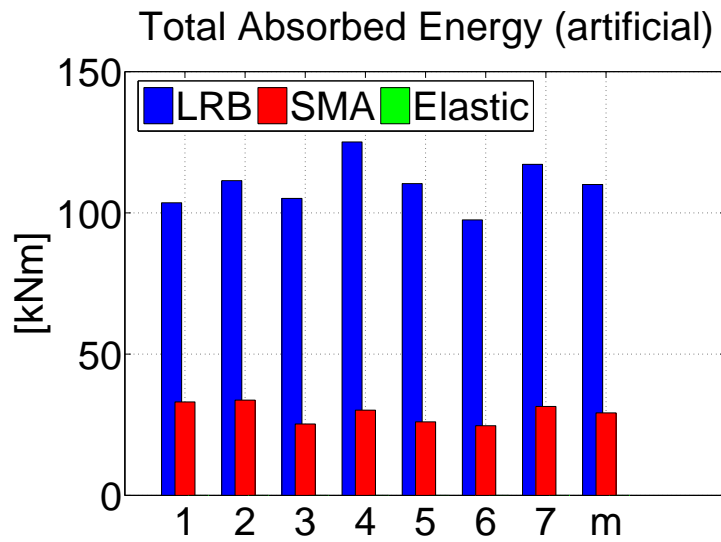
**Figure B.56:** displacement demand values normalized to the linear elastic displacement demand for near fault ground motions; the last set is the mean value of the previous ones.



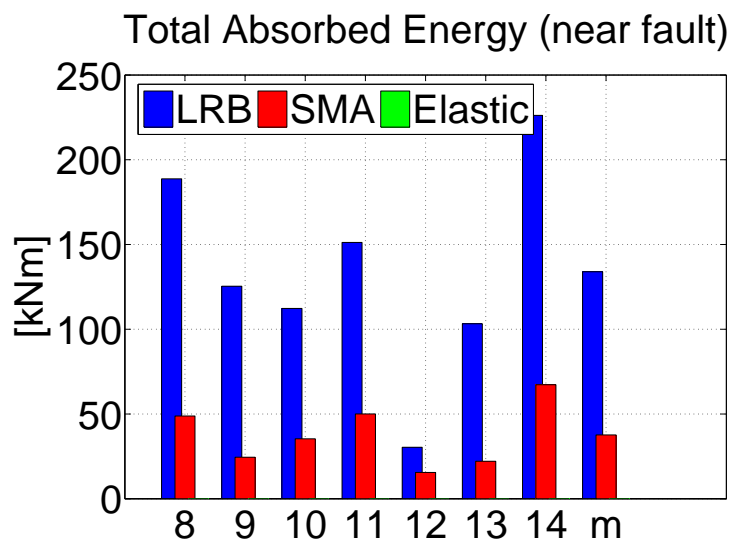
**Figure B.57:** force demand values normalized to the linear elastic displacement demand for artificial ground motions; the last set is the mean value of the previous ones.



**Figure B.58:** force demand values normalized to the linear elastic displacement demand for near fault ground motions; the last set is the mean value of the previous ones.



**Figure B.59:** system absorbed energy for artificial ground motions; the last set is the mean value of the previous ones.



**Figure B.60:** system absorbed energy for near fault ground motions; the last set is the mean value of the previous ones.

## **C. FLEXIBLE SUPERSTRUCTURE TIME HISTORY RESULTS SUMMARY**

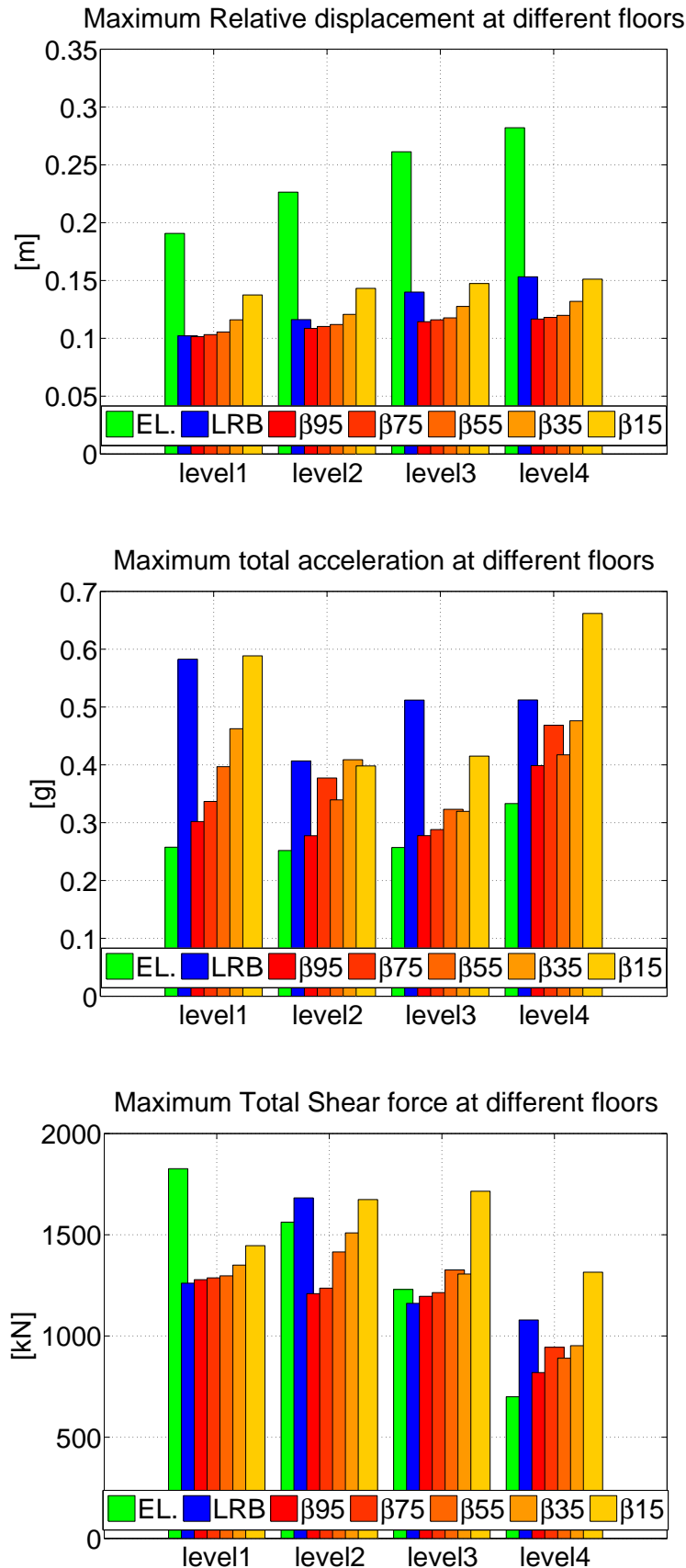


Figure C.1: ground motion 1 results (artificial).

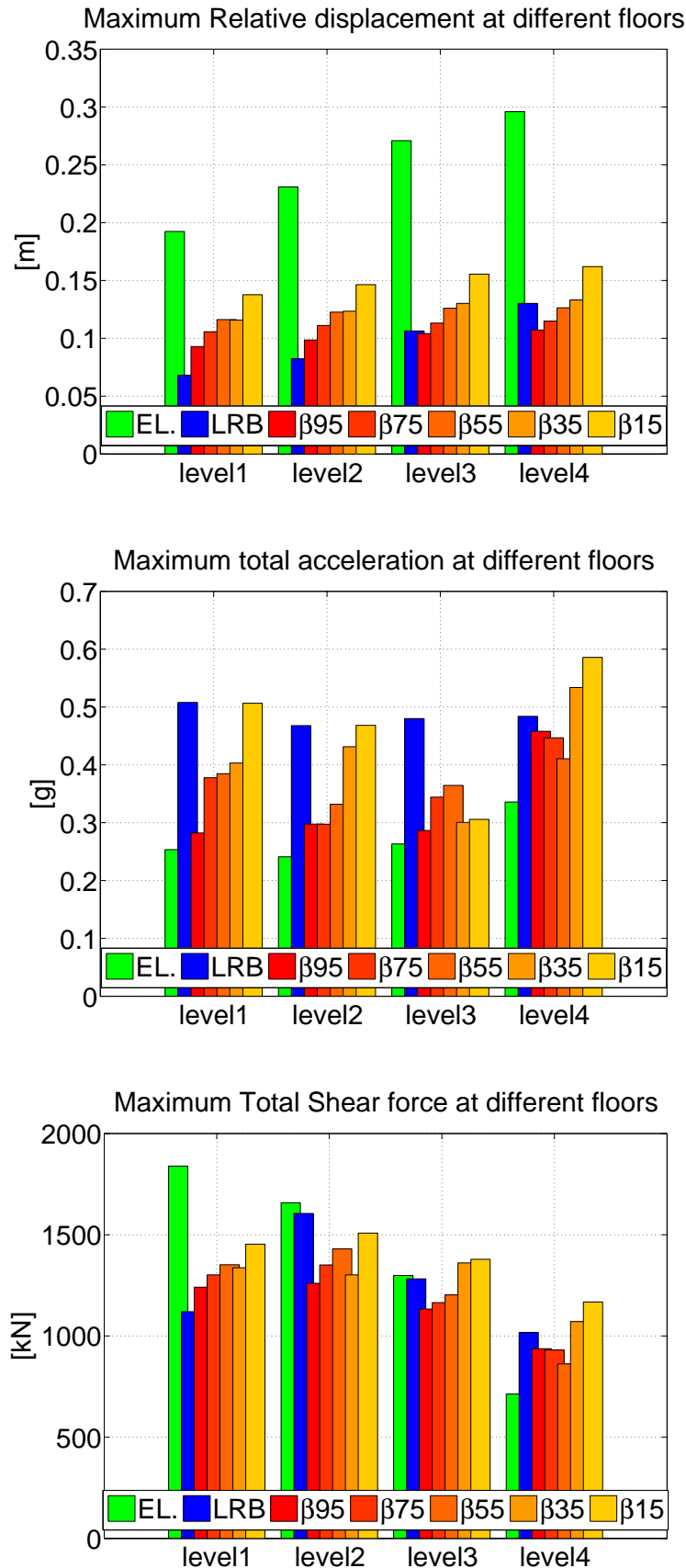


Figure C.2: ground motion 2 results (artificial).

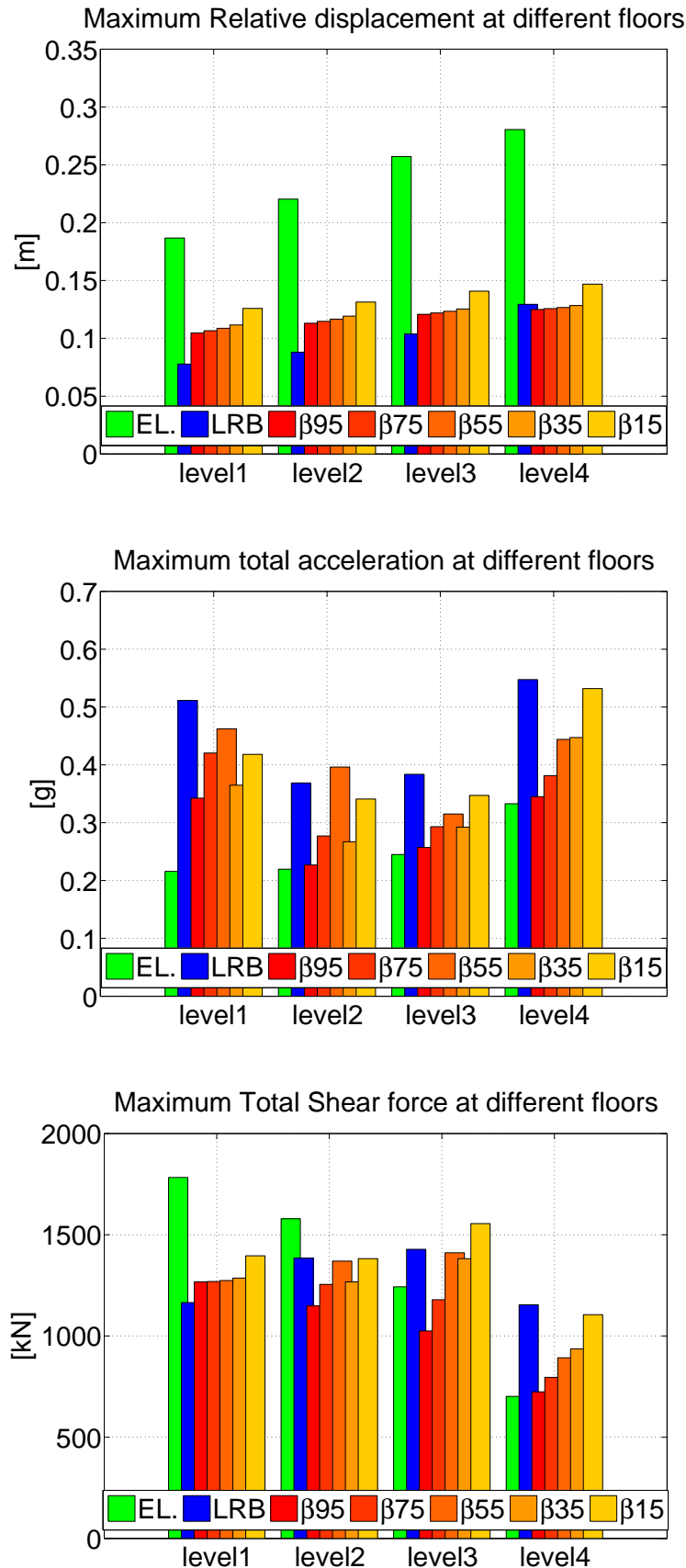


Figure C.3: ground motion 3 results (artificial).

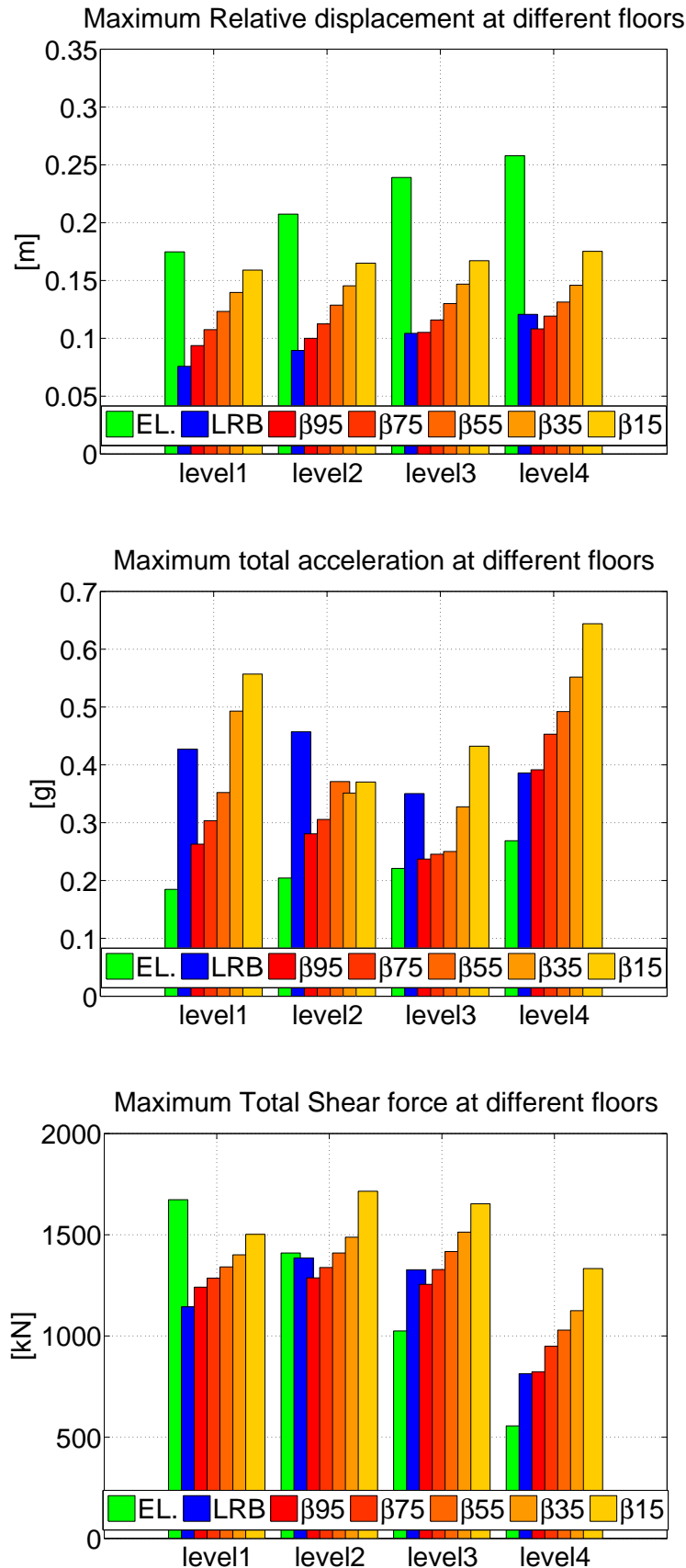


Figure C.4: ground motion 4 results (artificial).

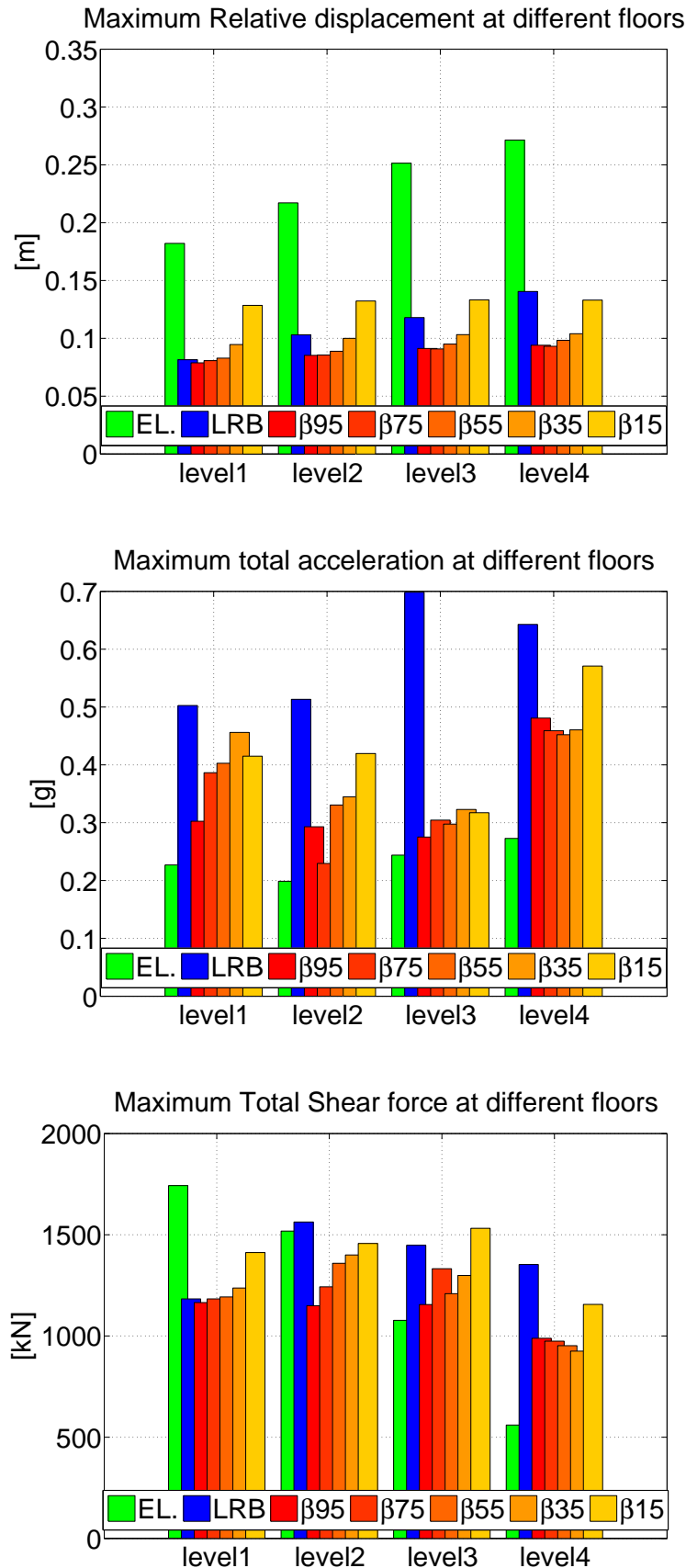


Figure C.5: ground motion 5 results (artificial).

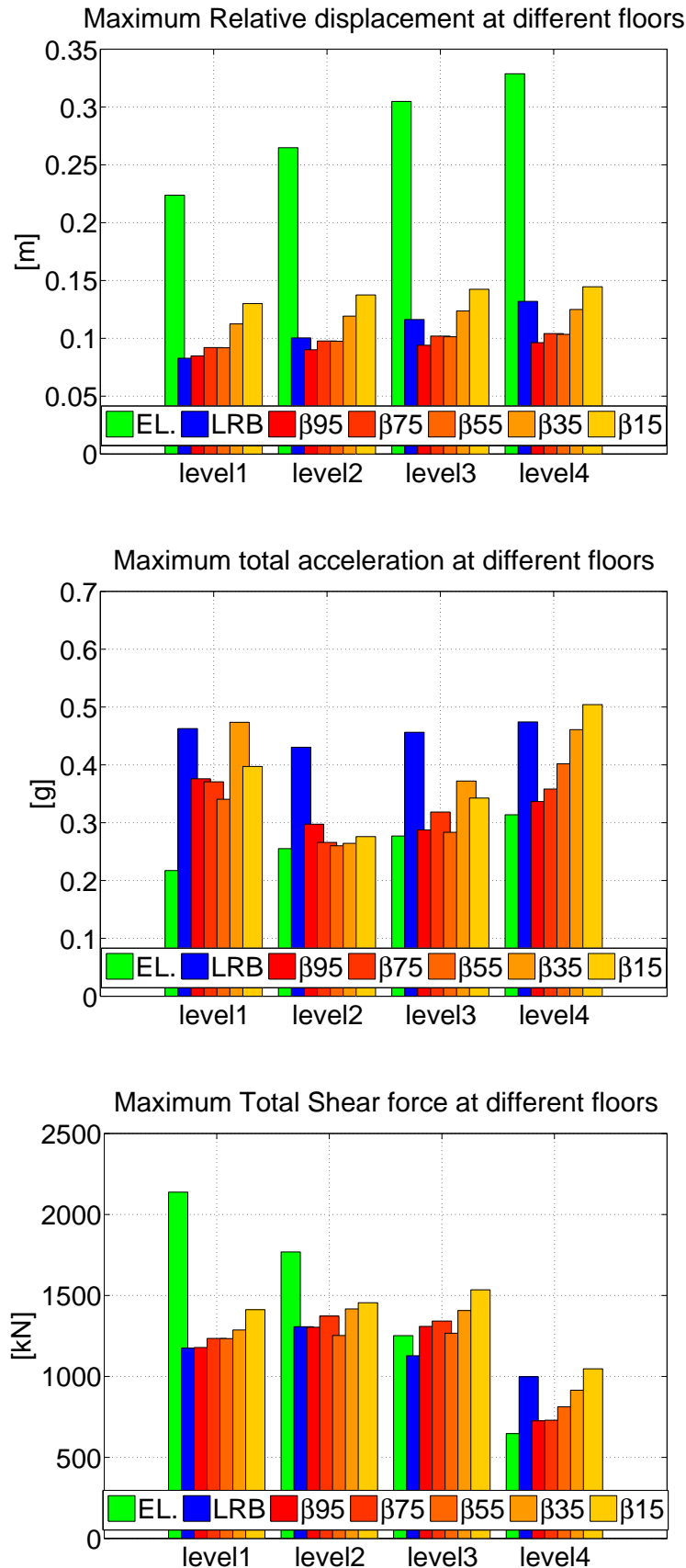


Figure C.6: ground motion 6 results (artificial).

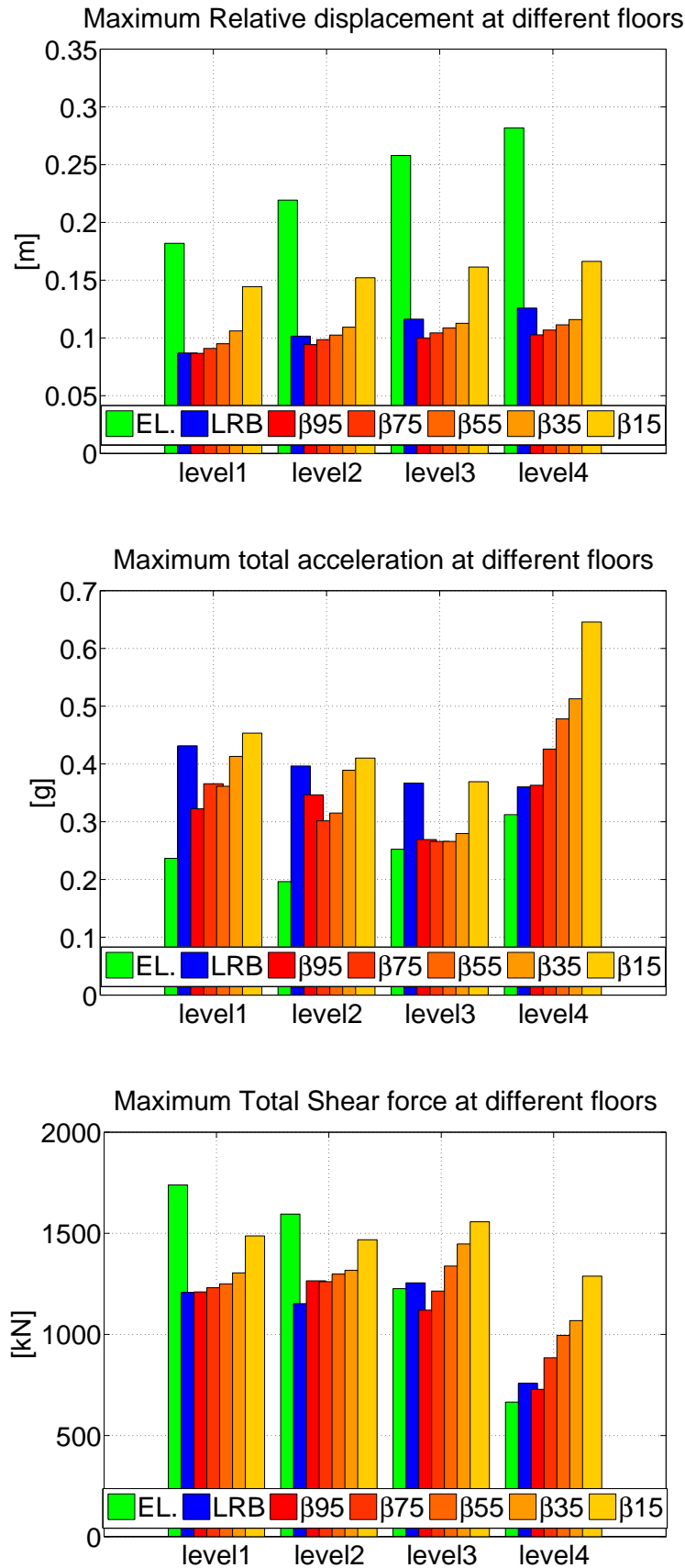


Figure C.7: ground motion 7 results (artificial).

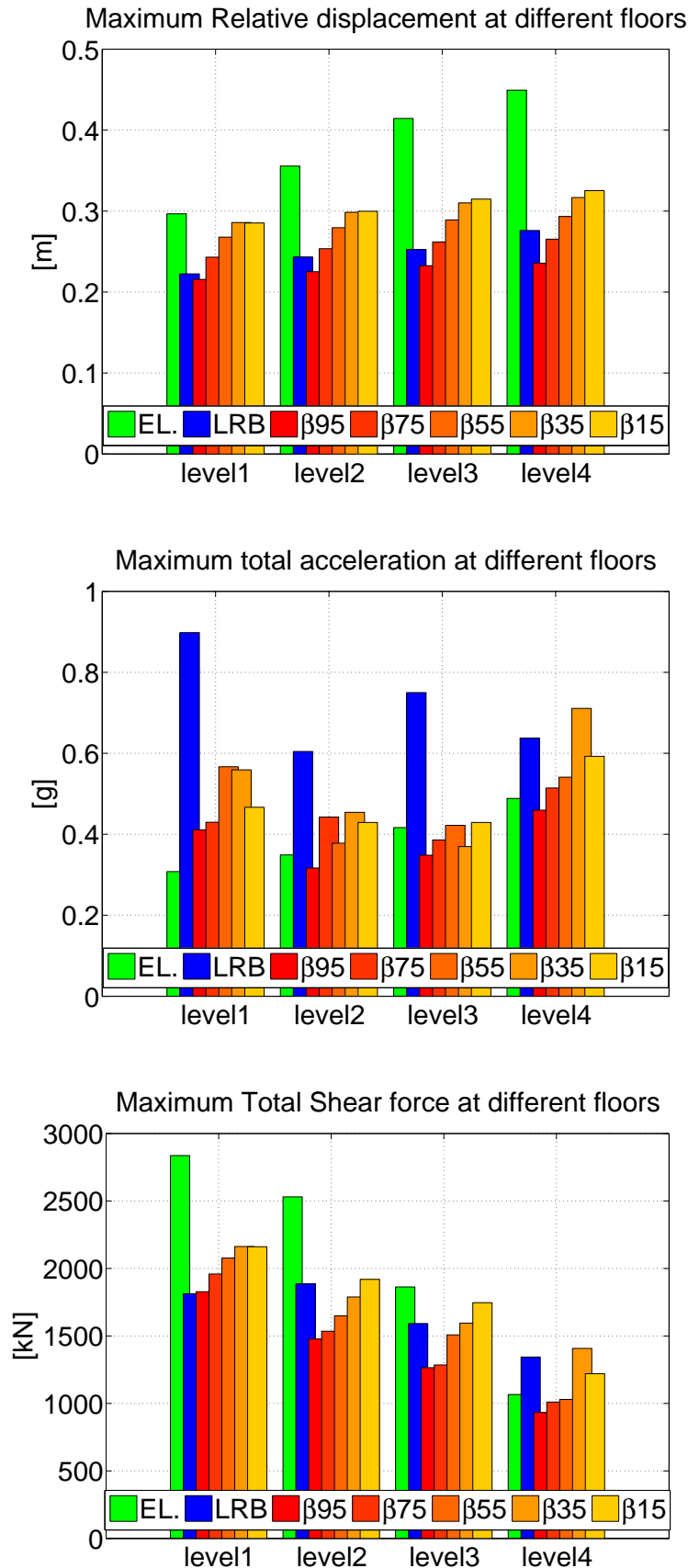


Figure C.8: ground motion 8 results (near fault).

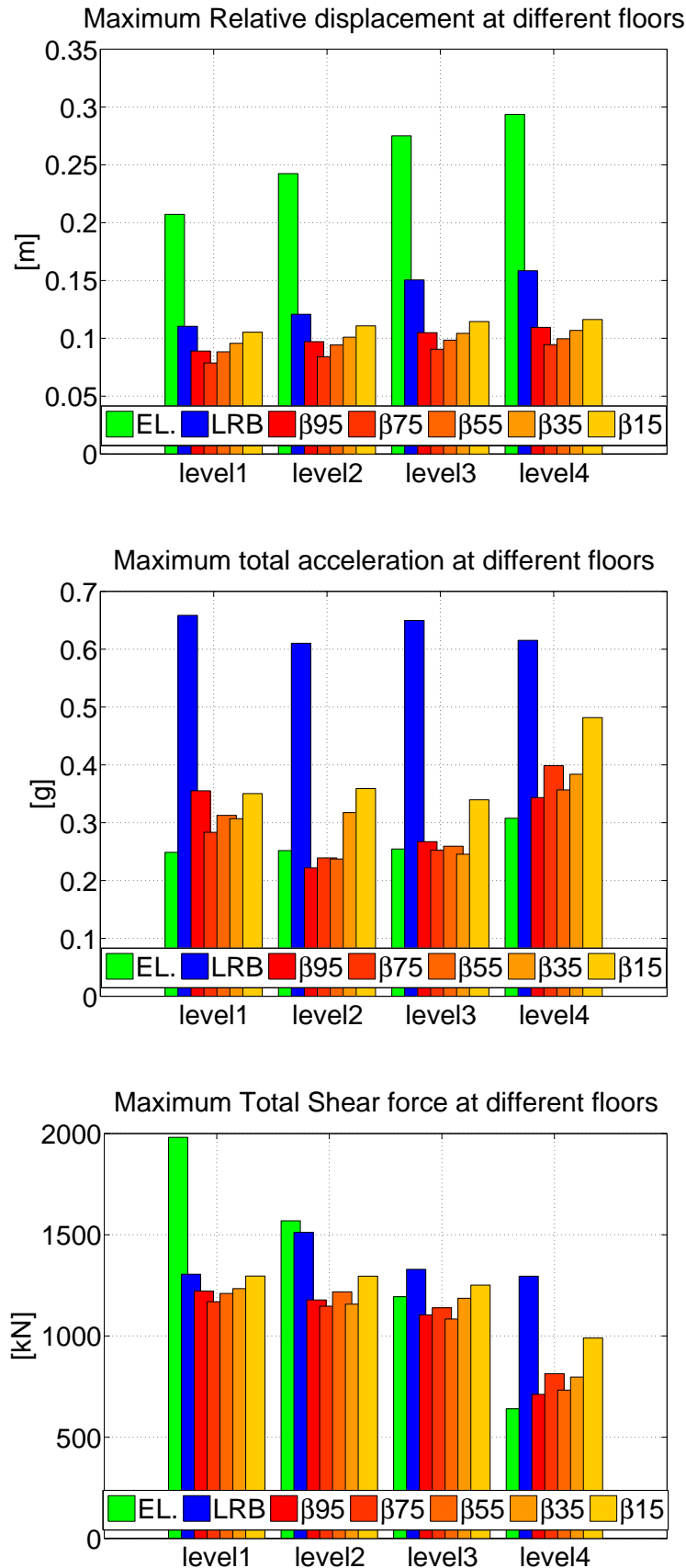


Figure C.9: ground motion 9 results (near fault).

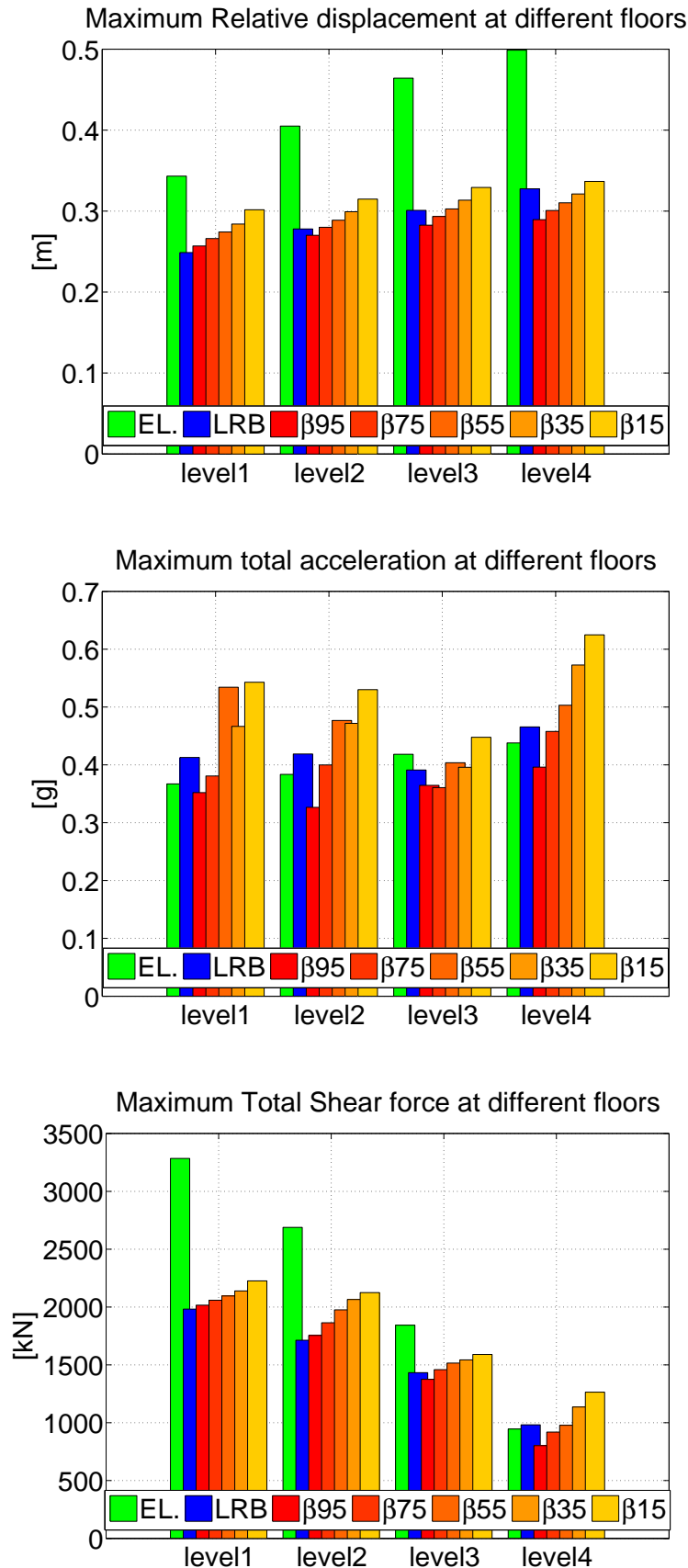


Figure C.10: ground motion 10 results (near fault).

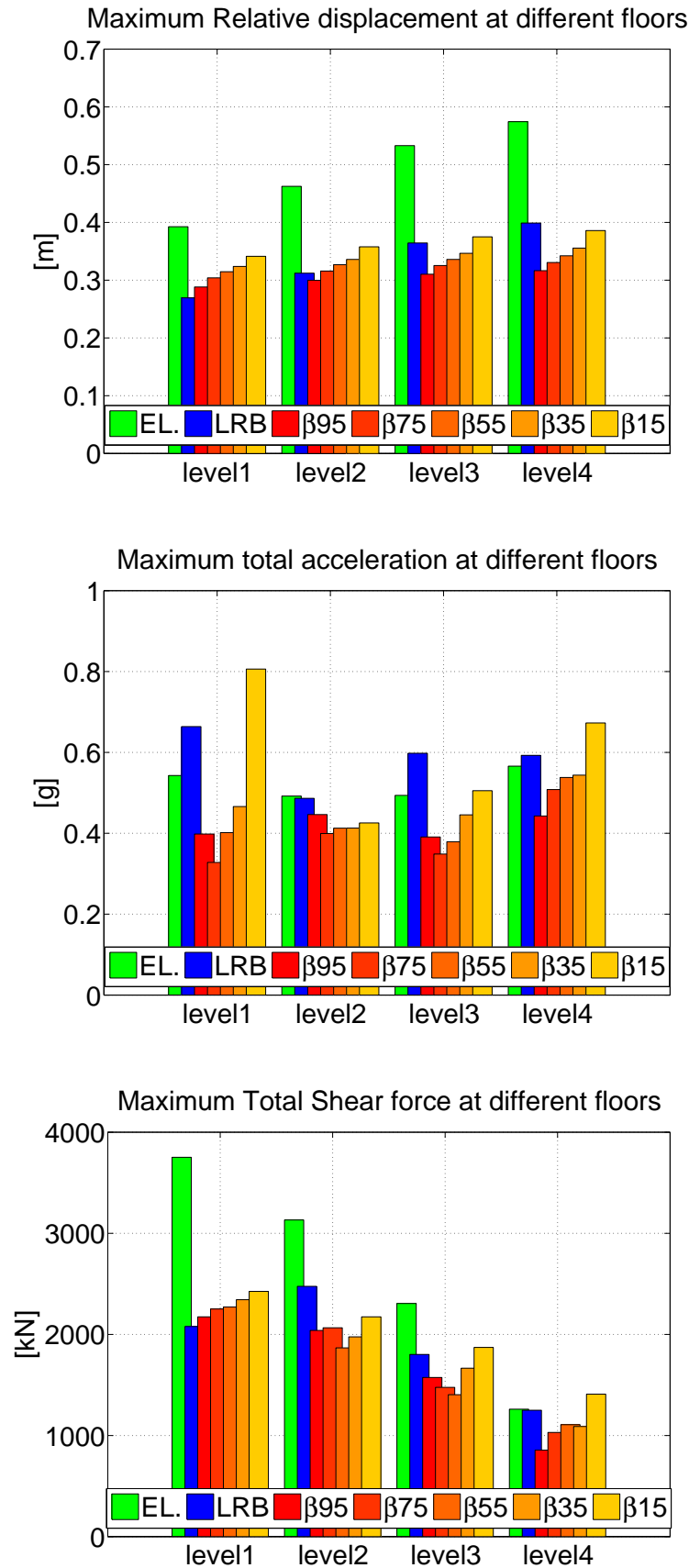


Figure C.11: ground motion 11 results (near fault).

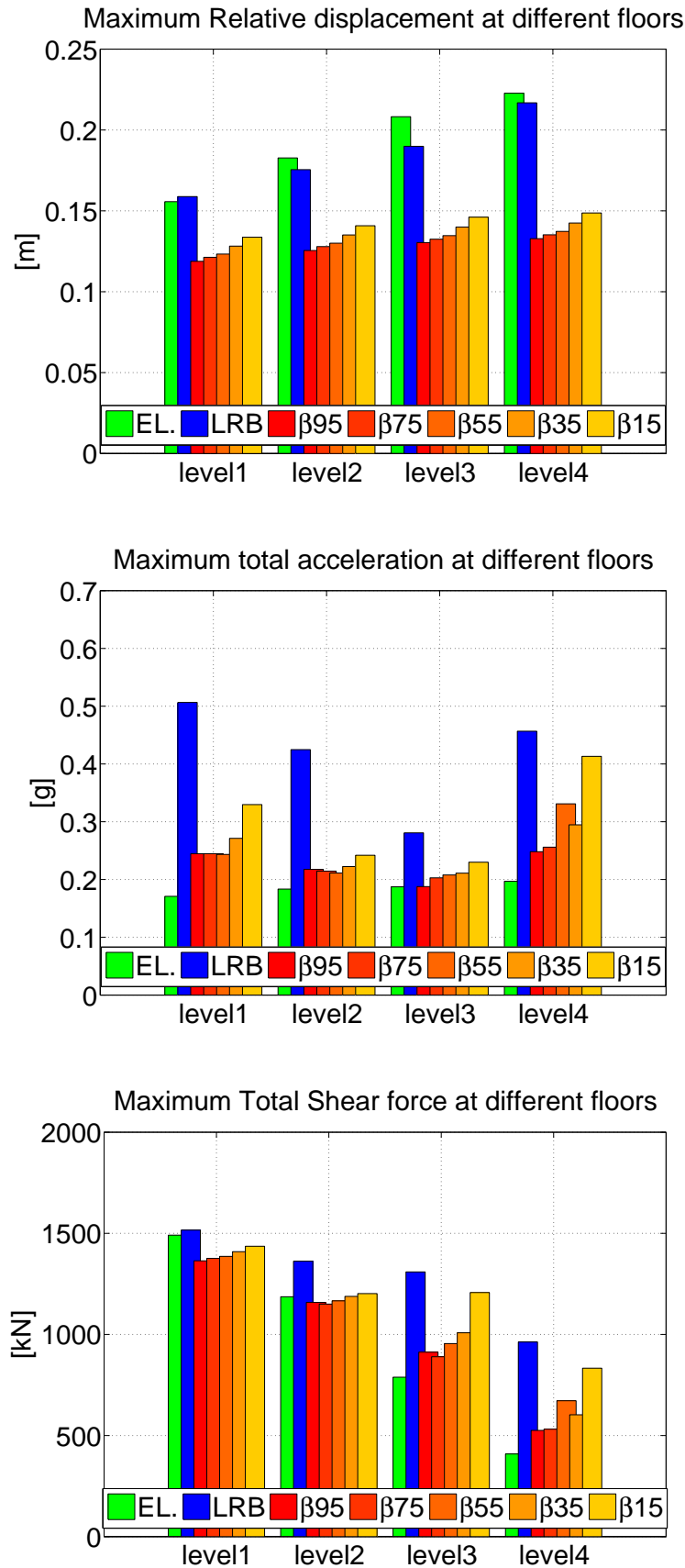


Figure C.12: ground motion 12 results (near fault).

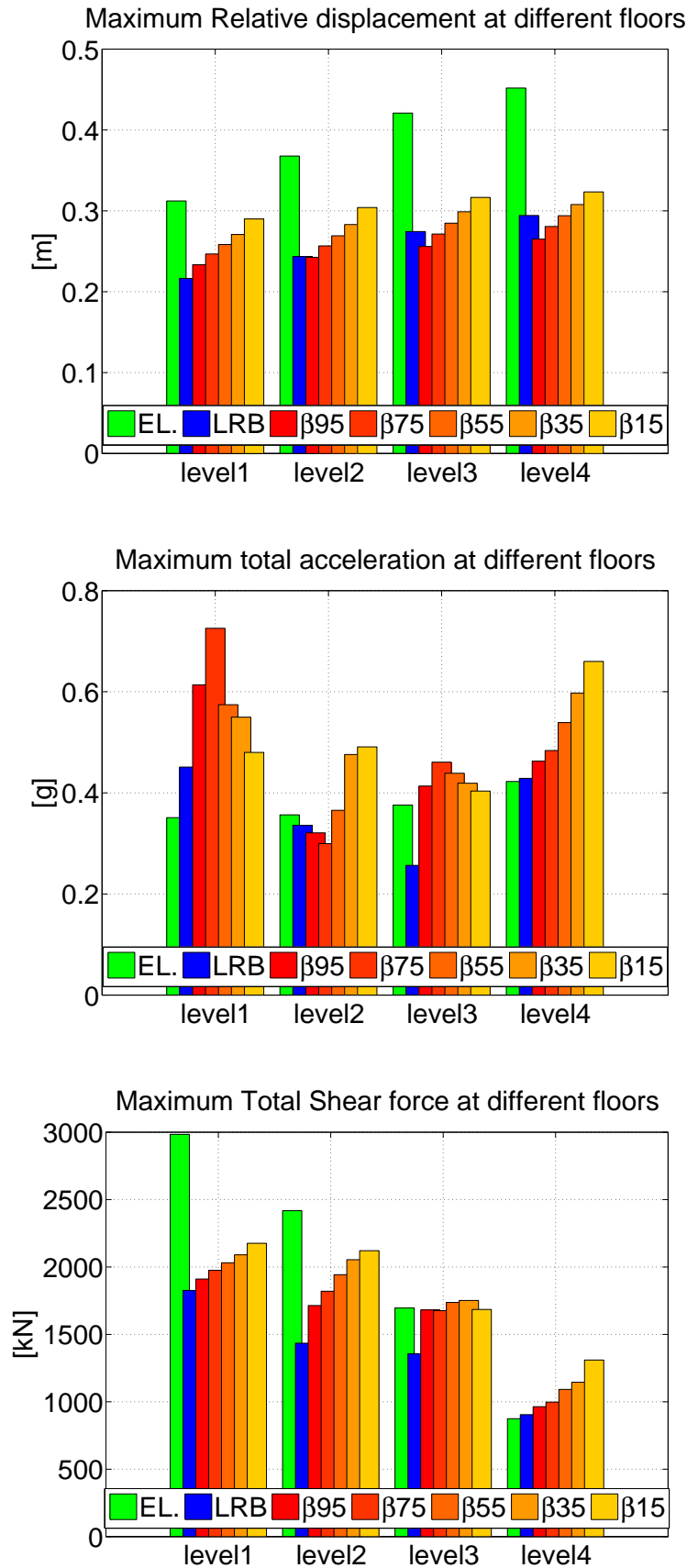


Figure C.13: ground motion 13 results (near fault).

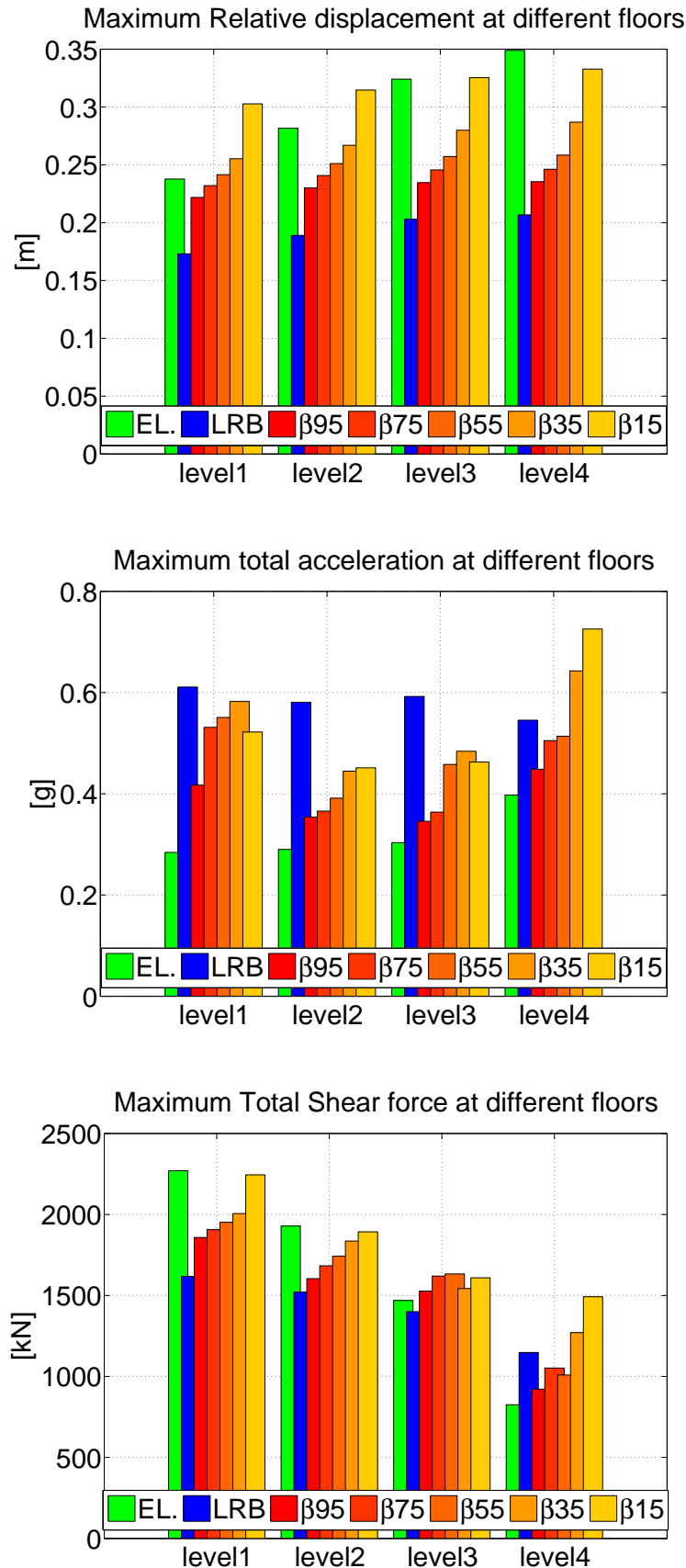


Figure C.14: ground motion 14 results (near fault).